# Mathematical modelling of biological systems and derivation of macroscopic models

Diane Peurichard

## To cite this version:

Diane Peurichard. Mathematical modelling of biological systems and derivation of macroscopic models. Mathematics [math]. Université toulouse 3 Paul Sabatier, 2015. English. NNT : . tel-01276777v1

**HAL Id: tel-01276777**

**https://hal.science/tel-01276777v1**

Submitted on 20 Feb 2016 (v1), last revised 5 Apr 2016 (v2)

# THÈSE

En vue de l'obtention du

## DOCTORAT DE L'UNIVERSITÉ DE TOULOUSE

**Délivré par :** *l'Université Toulouse 3 Paul Sabatier (UT3 Paul Sabatier)*

**Présentée et soutenue le** *8/07/2015* **par :**

**Diane Peurichard**

## MODELISATION MATHEMATIQUE DES SYSTEMES BIOLOGIQUES ET DERIVATION DE MODELES MACROSCOPIQUES

**JURY**

| | | |
|---|---|---|
| Louis Casteilla | Professeur d'université | Co-directeur de thèse |
| Christian Schmeiser | Professeur d'université | Rapporteur |
| Magali Ribot | Maître de conférence | Rapporteur |
| Christophe Besse | Professeur d'université | Examinateur |
| Pauline Lafitte | Professeur d'université | Examinateur |
| Fanny Delebecque | Maître de conférence | Co-directeur de thèse |
| Pierre Degond | Professeur d'université | Directeur de thèse |

**École doctorale et spécialité :**
*MITT : Domaine Mathématiques : Mathématiques appliquées*
**Unité de Recherche :**
*Institut Mathématiques de Toulouse*
**Directeur(s) de Thèse :**
*Pierre Degond* , *Fanny Delebecque*
**Rapporteurs :**
*Christian Schmeiser* et *Magali Ribot*

# Remerciements

Je remercie chaleureusement mon directeur Pierre Degond de m'avoir offert l'opportunité de travailler sur ce sujet passionnant et original dans le cadre de mon stage de master puis de cette thèse. Son savoir, ses précieux conseils et son enthousiasme permanent m'ont permis de m'épanouir pleinement dans le monde des mathématiques pour la biologie. Durant ces trois années, il m'a donné l'opportunité d'être indépendante tout en étant présent, et je ne le remercierai jamais assez de m'avoir permis de travailler à ses côtés à l'Imperial College de Londres pendant 8 mois. Une des grandes forces de son enseignement a été de m'apprendre à prendre du recul sur des résultats théoriques ou techniques complexes pour en extraire une réalité physique. Pour toutes ses raisons et bien d'autres encore, cette expérience sous sa direction a été très enrichissante et valorisante. Je tiens à remercier également toutes les personnes que j'ai rencontrées et qui ont été essentielles à la progression de ce travail. A commencer par ma co-directrice Fanny Delebecque, qui a toujours su se rendre disponible quand j'en avais besoin et qui m'a donné de nombreux conseils tout au long de ces trois années. Son soutien et ses suggestions ont étés précieux pour l'avancement de cette thèse. Du côté des biologistes, je remercie grandement Louis Casteilla qui a bien voulu codiriger cette thèse. Son ouverture au monde des mathématiques a permis cette collaboration très enrichissante et multidisciplinaire, et m'a apporté de nombreuses connaissances en biologie des tissus. Je remercie par ailleurs son équipe, composée notamment d'Anne Lorsignol et de Corinne Barreau qui m'ont ouvert les portes de leur laboratoire d'imagerie et m'ont fait découvrir un peu plus l'univers de la biologie.

Durant cette thèse, j'ai eu l'incroyable opportunité de voyager et de collaborer avec plusieurs chercheurs. Je remercie Xavier Descombes de m'avoir accueillie pendant une semaine dans son laboratoire et de m'avoir fait découvrir de nouvelles techniques de traitement d'images. Mon séjour d'un mois à l'Université d'Arizona m'a permis de rencontrer Sebastien Motsch, avec qui ce fut un grand plaisir de travailler. Sa gentillesse, son enthousiasme et sa détermination ont été plus qu'appréciés et nos débats intenses (sur tous types de sujets) ont été plus que motivants. J'espère pouvoir continuer de fructueuses collaborations avec lui. Je remercie par ailleurs Hayat de sa gentillesse et de son accueil chaleureux qui ont grandement participés à rendre ce séjour plus qu'agréable. Durant mes séjours à l'Imperial, j'ai eu l'occasion de rencontrer des collègues formidables tels que Hui, Benjamin, Frédérique, Francesco, Marina, Yanghong. Je remercie Stephan pour nos discussions et nos parties de squash endiablées. Merci à José Carillo pour nos réunions et ses conseils avisés (ainsi que son café formidable!). Je remercie les organisateurs de séminaires m'ayant donné l'occasion de présenter mes travaux: Sepideh Mirrahimi, Yanlan Mao, Claudia Negulescu, Sebastien Motsch, Raluca

Eftimie et j'en passe. Je tiens à remercier Christian Schmeiser et Magalie Ribot d'avoir accepté de rapporter ce manuscrit, ainsi que Pauline Lafitte, Christophe Besse, Fanny Delebecque Louis Casteilla et Pierre Degond d'avoir accepté de faire partie du jury.

Je souhaite encore remercier tous mes collègues de l'IMT avec qui je n'ai pas passé autant de temps que je l'aurai voulu. Je pense à Claire B, Claire D, Pierre, Niels (un jour peut-être on le fera ce projet de jeux combinatoires?), Laurent, ainsi que mes cobureaux Anne-Charline, Anais, Vittorio, Alexandra et Leilah. Je remercie Janani, Delphine et Celine de s'être occupées toujours très efficacement des questions administratives.

Je ne serais pas là ou j'en suis sans ma précieuse team de l'INSA (et autres), qui m'ont notamment permis de littéralement m'envoyer en l'air à un moment ou j'en avais vraiment besoin (et oui je l'ai osée celle la). Je pense évidemment à Lola, Valentine, Léna, Pierre, Elo et Marine, mais encore Laure, Greg, Thomas, Babwe (oui, jusqu'ici ce surnom), Blaise, César, Aurel, Blanchon, Magali, Ben, Adri, Jimmy, et ceux que j'aurai oublié. Car je n'oublie pas d'où je viens et qui m'a aidé quand j'en ai eu besoin: un grand merci à Géraldine, qui a grandement contribué à mon intérêt pour les mathématiques et Elina qui m'a redonné un souffle dans les moments de faiblesse.

Je tiens évidemment à remercier toute ma famille qui m'a soutenue dans cette entreprise. Je ne sais comment remercier mes parents pour tout ce qu'ils nous ont donnés. Merci à mon père, mon inconditionnel allié des grands débats (grâce à notre esprit logique c'est bien évident), de m'avoir fait faire mes premiers pas informatiques sur disquettes pour Amstrad 6128, et merci à ma mère, mon soutien moral absolu, de m'avoir montré à la Mc Gyver qu'avec un ciseau et un carton on pouvait construire un flipper (sans exagérer bien sûr). Merci à vous deux de nous avoir offert cette éducation que je prendrai en exemple. Merci de nous avoir laissé la liberté de faire nos choix tout en nous faisant les remettre en question, nous permettant ainsi d'être épanouis et indépendants dans nos domaines respectifs. Dans la continuité, j'en viens à remercier mes frangins, ces deux énergumènes si différents et dont je suis si fière. Merci à mon grand frère, générateur de discussions politiques enflamées aux repas de famille, de me responsabiliser et me rappeler à la réalité de notre monde, et merci à mon petit frère de me faire rêver et voyager en m'emmenant dans son monde d'artiste plein de poésie.

Finalement, je fais le plus gros remerciement à Aurore qui m'a toujours soutenue dans les bons comme dans les mauvais moments, et qui a réussi à me supporter malgrè le rythme de vie loin de tout repos engendré par ce travail de thèse. Merci d'être toujours là, et j'espère que ce n'est que le début d'une grande aventure!

## Abstract (version française)

Dans cette thèse, nous nous intéressons aux mécanismes en jeux dans l'auto-organisation d'agents dans les systèmes biologiques. Ces systèmes complexes sont formés d'un grand nombre d'individus intéragissant à différentes échelles (moléculaire, génomique, cellulaire), et s'auto-organisant pour former et maintenir des structures complexes fonctionnelles (telles que les organes).

Dans un premier temps (travail en collaboration avec l'équipe de biologistes de Louis Casteilla), nous utilisons le tissu adipeux comme modèle et nous nous intéressons à l'étude de l'émergence de structures cellulaires de forme lobulaire dans un réseau organisé de fibres. Dans ce but, nous introduisons un modèle de cellules intéragissant avec la matrice extra-cellulaire composée d'éléments de fibres. Nous développons une méthode de traitement d'images permettant d'extraire des données quantitatives à partir des images biologiques, afin de comparer quantitativement les expériences numériques et biologiques. Nous sommes alors capables de montrer la concordances des données du modèle avec les données extraites de tissus réels. Une analyse approfondie de l'influence des paramètres du modèle sur les résultats numériques nous permet de montrer que l'émergence de structures biologiquement cohérentes peut être reproduite par un modèle basé essentiellement sur des règles mécaniques entre les cellules et le réseau de fibres de collagène. L'originalité de ce modèle réside dans l'utilisation d'une méthode de minimisation pour décrire le mouvement des agents. Cette approche nous permet de modéliser des structures géométriques complexes (comme des réseaux de fibres) par un ensemble d'unités élémentaires connectées, les connections étant traitées comme des contraintes à l'aide de fonctionnelles simples. Cette nouveauté a donné lieu à d'autres types de modèles, comme (i) un modèle pour la formation de tissus épithéliaux, dans lequel les cellules épithéliales de géométrie complexe sont modélisées par un ensemble de sphères 2D connectées et (ii) un modèle pour l'auto-organisation de la vascularisation dans un milieu poreux. Dans ce dernier, le réseau vasculaire est modélisé par un ensemble de tubes connectés.

Afin d'obtenir un modèle macroscopique nous permettant d'étudier le tissu adipeux dans sa globalité, nous nous concentrons ensuite sur le réseau de fibres, et dérivons un modèle macroscopique de fibres interconnectées et sujettes à une force d'alignement en ses points d'attache. Nous obtenons formellement la limite quand le nombre de particules tend vers l'infini, et montrons que nous otbenons un système fermé de deux équations: une pour la distribution à une particule (décrivant la probabilité de trouver une fibre à un endroit donné pour une orientation donnée) et la seconde pour la distribution des liens de fibres. L'originalité de notre résultat réside dans le fait qu'aucune hypothèse supplémentaire sur le modèle n'est nécessaire pour obtenir la fermeture du système. L'évolution de la distribution des liens de fibres, reliée à la distribution à deux particules, est entièrement décrite par une équation non linéaire.

La limite hydrodynamique de l'équation cinétique nous amène à l'obtention d'un modèle macroscopique pour le réseau de fibres. Cette limite est obtenue à l'aide de techniques non conventionnelles dûes à un manque d'équation de conservation pour le système étudié. Nous obtenons finalement un système de deux équations: (i) une équation de continuité décrivant l'évolution de la densité de fibres, et (ii) une équation parabolique non linéaire décrivant l'évolution de l'orientation locale moyenne des fibres. Dans le cas d'une densité homogène de fibres, nous prouvons l'existence de solutions à l'équation (ii).

Finallement (travail en collaboration avec S. Motsch), nous nous sommes intéressés à l'influence d'intéractions de type répulsion cellules-cellules dans un modèle simple de croissance tumorale. Dans ce travail, nous voulons étudier comment des intéractions de type congestion modifient les propriétés d'invasion (vitesse, forme...) d'une masse croissante de cellules. La dynamique microscopique présente des caractéristiques intéressantes comme la formation d'ondes progressives que le modèle macroscopique dérivé ne capture pas. Nous montrons que ceci est dû au fait que les masses de Dirac ne sont pas stables pour l'équation macroscopique, expliquant la différence de solutions entre le modèle microscopique et macroscopique. Nous proposons une version modifiée de l'équation macroscopique que nous sommes capables de relier à la dynamique cellulaire, et montrons la bonne correspondance entre les deux modèles.

**Mots clés:** Biologie mathématique, modélisation, modèles individus-centrés, théorie cinétique, modèles macroscopiques, étude asymptotique

## Abstract (english version)

In this thesis, we want to understand the mechanisms involved in the self-organization of agents in biological systems. These complex systems involve a large number of different entities interacting at different scales (molecular, genomic, cellular) and self-organizing to create and maintain complex and functional structures (such as organs).

First, (work in collaboration with L. Casteilla and his team (StromaLab)) we use adipose tissue as a biological model and aim at studying the formation of lobular cell structures surrounded by an organized fiber network. To this aim, we introduced a new individual based model for cells interacting with extra-cellular-matrix fiber elements. We implemented an image processing methodology to enable the quantitative comparison between numerical and biological experiments, and showed a good correspondance between the model and the data. We performed a parametric analysis on the role of the model parameters on the numerical structures observed, and prove that the emergence of biologically relevant structures can be explained by simple mechanical interactions between the cells and the collagen fibers. The originality of this model mainly relies in the use of a minimization method to describe individual motion. By this mean, complex geometrical structures such as fiber networks can be modeled as sets of connected elementary units, which connections are seen as constraints through the use of functionals. This novelty has been used to build other types of models, such as (i) a model for epithelial tissue formation, in which the complex geometry of epithelial cells is described by a set of connected spheres (work in progress), and (ii) a model for self-organization of vascularization from a porous media flow, where the vascular network is modeled as a set of elementary connected segments (work in progress).

In order to obtain a macroscopic model and gain insight into the global dynamics of a fiber network as described by our individual based model (interconnected elements with alignment interactions), we then performed a derivation of a kinetic model for fibers, closely linked to the microscopic one. We were able to entirely describe the fiber one-particle distribution function evolution thanks to the fiber two-particle distribution function (which describes the fiber connections). The originality of our result lies in the fact that no additional hypothesis on the model is required to obtain a closure relation for the fiber two-particle distribution function, which is entirely described by a non linear equation.

The hydrodynamic limit of the kinetic equation led us to a macroscopic model for fiber links. Using non conventional techniques because of the lack of conservation equations, we were able to obtain a continuity equation for the fiber density and a non linear conservative equation for the fiber mean orientation. This equation is a non linear elliptic equation and we were able to show existence of solutions by using methods of functional analysis.

Finally (work in collaboration with S. Motsch), we used cell-cell interactions to produce an individual based model for brain tumor invasion. We were interested in the role of cell-cell interactions in the invasion properties (speed, geometry...) of a growing mass of cells. The asymptotic behavior of solutions to the kinetic model derived from the microscopic one had interesting features such as the convergence towards dirac deltas that remains to be theoretically proved. We proposed a modified expression for the potential kernel to take into account congestion features and performed a hydrodynamic limit of the modified kinetic model. The numerical simulations of the macroscopic model obtained have shown the relevance of the macroscopic model to describe the microscopic dynamics at large scale.

**Key words:** Mathematical biology, Modelisation, Individual based models, Kinetic theory, Macroscopic models, Asymptotic study

# Contents

**Introduction générale** **10**
1 Motivations . . . 10
2 Le Tissu Adipeux . . . 11
3 Modèles mathématiques . . . 13
4 Vue générale du projet . . . 15
5 Contributions des travaux . . . 19
6 Résultats . . . 21

**General Introduction** **33**
7 Motivations . . . 33
8 The Adipose Tissue . . . 34
9 Models . . . 35
10 Overview of the project . . . 37
11 Contributions of the work . . . 41
12 Results . . . 43

**1 An Individual Based Model for Adipose tissues** **58**
1 Significance statement . . . 59
2 Introduction . . . 59
3 Results . . . 61
4 Discussion . . . 69
5 Materials . . . 71
6 Supporting Information . . . 73

**2 Macroscopic model** **101**
1 Introduction . . . 102
2 Individual Based Model . . . 106
3 Derivation of a kinetic model . . . 111
4 Scaling . . . 114
5 Large scale limit . . . 123
6 Homogeneous fiber distribution . . . 133

7 Conclusion . . . . . . . . . . 138
8 Appendix A . . . . . . . . . . 142
9 Appendix B . . . . . . . . . . 150

**3 Numerical simulations of the macroscopic model 154**
1 Introduction . . . . . . . . . . 155
2 Microscopic model and mean-field limit . . . . . . . . . . 157
3 Macroscopic derived model . . . . . . . . . . 164
4 Micro-Macro comparison . . . . . . . . . . 175
5 Conclusion . . . . . . . . . . 181
6 Appendix A . . . . . . . . . . 185
7 Appendix B . . . . . . . . . . 190
8 Appendix C . . . . . . . . . . 193
9 Appendix D . . . . . . . . . . 197

**4 A model for tumor growth 199**
1 Introduction . . . . . . . . . . 200
2 Short range repulsion: I . . . . . . . . . . 201
3 Short range repulsion: II . . . . . . . . . . 208
4 Repulsion and cell division . . . . . . . . . . 213
5 Conclusion . . . . . . . . . . 213
6 Appendix A . . . . . . . . . . 220
7 Appendix B . . . . . . . . . . 221

**5 Extensions 222**
1 A model for vasculogenesis . . . . . . . . . . 222
2 A model for ballistic aggregation . . . . . . . . . . 230

# Introduction(version française)

## 1 Motivations

Dans cette thèse, nous nous intéressons à l'étude des mécanismes en jeux dans l'auto organisation des systèmes biologiques. Ces systèmes complexes sont formés d'un grand nombre d'individus s'auto-organisant pour former des structures complexes (telles que des organes). Nous cherchons à comprendre quels sont les mécanismes et agents principaux qui mènent à la morphogénèse et homéostasie des tissus et lesquels sont secondaires à cette organisation. L'auto-organisation d'agents dans les systèmes biologiques a donné lieu à de nombreuses études mais reste encore largement inconnue [2]. Il est très difficile de déterminer quels mécanismes individuels mènent à l'apparition de structures complexes à l'échelle du tissu entier. Cette difficulté provient du fait que les interactions sont de plusieurs types (génomique, cellulaire, moléculaire, mécaniques) et se font à différentes échelles. Afin de mieux comprendre ces problèmes, une approche naturelle est de développer un modèle mathématique. En effet, la construction d'un modèle biologiquement adéquat permet de tester des hypothèses sur l'émergence et le maintien de structures fonctionnelles et d'explorer différents scénarios. La modélisation mathématique a pour autre avantage clef d'être développée dans un cadre général, ce qui permet à un même modèle d'être utilisé pour étudier différents problèmes physiques ou biologiques. Un modèle pourra valider une hypothèse sur des interactions si les solutions numériques obtenues sont en adéquation avec les structures observées dans les systèmes réels. Cependant, il faut noter qu'un modèle mathématique n'a pas pour but de reproduire fidèlement la réalité, mais seulement d'aider à la compréhension d'un phénomène observé. De plus, il est souvent difficile d'avoir accès/de mesurer des faits biologiques, rendant difficile la comparaison des données expérimentales avec les résultats du modèle. Ainsi, la construction d'un modèle mathématique requiert des expériences biologiques, des techniques avancées de segmentation et de traitement d'images, de l'analyse de données expérimentales etc. Finalement, la confrontation des résultats du modèle à une réalité biologique est délicate pour deux raisons. Premièrement, les résultats expérimentaux sont sujets à des bruits aléatoires dûs aux instruments de mesures et aux conditions expérimentales, et peuvent donc varier d'une expérience à une autre. De plus, le nombre d'expériences est limité tandis qu'un modèle requiert un grand nombre de paramètres.

Dans notre étude, nous considérons le tissu biologique comme un système écologique engageant un nombre réduit d'agents et d'interactions. Nous prenons l'exemple du tissu adipeux qui est le principal réservoir d'énergie de l'organisme et qui joue un rôle fondamental dans la régulation du poids et de l'énergie.

# 2 Le Tissu Adipeux

Il existe deux types de tissus adipeux jouant des rôles distincts et complémentaires: le tissu adipeux blanc (WAT) et le brun (BAT). Le WAT est composé principalement d'adipocytes blancs qui stockent le surplus d'énergie de l'organisme. Au contraire, le BAT est composé d'adipocytes bruns dont la couleur est due à une irrigation plus dense comparé au WAT. Le BAT est spécialisé dans la thermogénèse adaptative: sa fonction principale est de transférer l'énergie des nutriments en chaleur. Dans notre étude, nous nous intéressons au premier type de tissu adipeux: le WAT. Il est composé d'adipocytes matures (gouttes de lipides), de préadipocytes (leur précurseurs) et d'une fraction de stroma vasculaire contenant du sang, des cellules endothéliales et des macrophages. Un extrait de tissu adipeux extrait d'une souris mature saine (expériences faites au StromaLab) est montré en Figure 1. Le tissu adipeux inguinal entier de la souris est prélevé, fixé dans de l'agarose et coupé en tranches. Les tranches sont traitées par un colorant lipophile fluorescent rouge (CD34-BODIPY) (travail de spécialistes ed l'ITAV). Dans la Figure 1, les adipocytes apparaissent en rouge, les cellules souches en vert et la matrice extra-cellulaire (ECM) en bleu. Cette image montre qu'à l'équilibre, le tissu adipeux mature est composé d'adipocytes regroupés en formes spécifiques, nommées lobules, et entourés d'une matrice extra-cellulaire organisée.

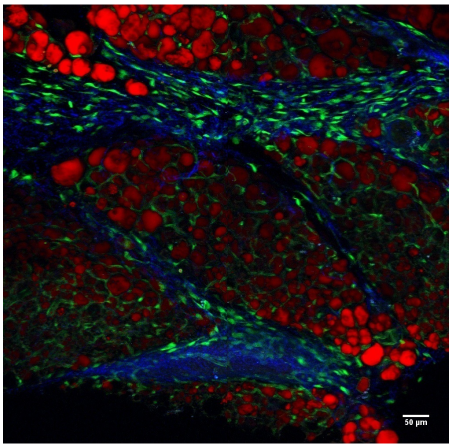

Figure 1: Image 2D Image d'un tissu adipeux sous-cutané extrait d'une souris saine. CD34-Bodipy-Second harmonics / visualization IMARIS.

En influençant le statut physiologique et le devenir des cellules précurseures, le métabolisme est un facteur important de l'adipogénèse. Dans ce contexte, la vascularisation apporte des nutriments et de l'oxygène. L'innervation contrôle les cellules immatures et les processus de régénération . En draînant des métabolites telles que le $CO_2$, le flux sanguin participe à la formation de niches, de gradients et à l'activité cellulaire. D'un autre côté, l'ECM et les cellules régénératives de l'ECM (myofibroblastes) jouent un rôle majeur dans l'homéostasie du tissu adipeux : elles créent des contraintes mécaniques, servent de points d'attache aux cellules, et participent à la migration cellulaire en donnant une directionalité au mouvement des cellules. Par leur capacité à se différencier et devenir des cellules fonctionnelles du tissu (adipocytes), les cellules souches sont un autre déterminant clef dans la morphogénèse et homéostasie des tissus adipeux.

Tous ces éléments chimiques, biologiques et mécaniques jouent des rôles différents et complémentaires dans l'émergence et le maintien de structures fonctionnelles des tissus. Cependant, les prendre tous en compte amènerait à des modèles trop complexes et difficiles à interpréter. Notre travail donne, dans le cas des tissus adipeux, des modèles simplifiés mettant en jeux un nombre réduit d'agents et d'interactions .

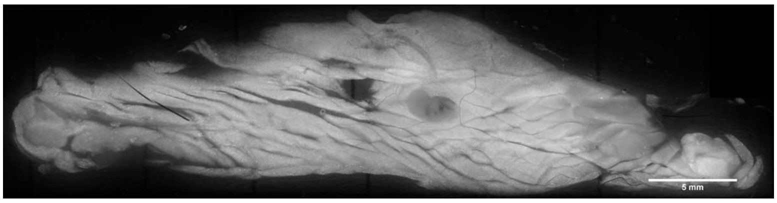

Figure 2: Image 2D Image d'un tissu adipeux inguinal entier extrait d'une souris saine.

Pour finir, comme montré en Figure 2 (extrait de tissu adipeux entier), il est à noter que le niveau d'organisation en lobules varie selon la zone de tissu observée. Si les structures lobulaires sont organisées et distinctes dans la partie supérieure, les groupements de cellules sont désorganisés et plus allongés dans la partie inférieure. Nous sommes donc amenés à développer des modèles décrivant une dynamique à plusieurs échelles : (i) une échelle microscopique pour étudier le tissu à l'échelle des cellules et (ii) une échelle macroscopique pour étudier l'organisation à l'échelle du tissu entier.

# 3 Modèles mathématiques

Comme expliqué précédemment, nous avons besoin dans notre étude de considérer une dynamique à plusieurs échelles: à l'échelle des cellules et du tissu entier. Pour la première, nous sommes amenés à développer un modèle individu-centré (IBM) qui permet de décrire la dynamique de chaque agent et chaque intéraction. Pour obtenir un modèle à une échelle plus grande, nous avons besoin de développer un modèle macroscopique.

## 3.1 Modèles Individu-centrés

La majorité des modèles développés pour adresser une question biologique sont des modèles dits 'individus-centrés'. L'avantage principal de ce type de modèles réside dans le fait qu'ils permettent de décrire chaque individu à l'aide de variables qui lui sont propres telles que sa position, vitesse, forme etc. Ces modèles permettent de décrire précisément les différentes interactions entre agents à l'aide de fonctionnelles définies à partir de règles heuristiques venant de la réalité biologique. Ils décrivent en effet l'évolution des variables de manière discrète ou continue. Dans les systèmes dynamiques, les agents peuvent être auto-propulsés ou sujets à des forces mécaniques induisant un mouvement. Dans ce dernier cas, les équations du mouvement sont déduites de lois physiques comme le principe fondamental de la dynamique ou la minimisation d'une énergie par exemple.

De nombreux modèles individus centrés ont été proposés pour décrire les intéractions et les agents en jeux dans l'auto-organisation de systèmes biologiques. On se propose içi de donner un bref aperçu de modèles présents dans la littérature.

Quand il s´ agit de modéliser un système impliquant une organisation de structures cellulaires et fibreuses, les principales intéractions peuvent être de trois types: (i) cellules-cellules, (ii) cellules-fibres ou (iii) fibres-fibres. Les modèles basés sur des intéractions de type (i) [4] sont développés pour comprendre l'emergence de structures cellulaires et modélisent la croissance tumorale par exemple. Ils supposent souvent que le déplacement des cellules est indépendant de la nature du mileu dans lequel elles évoluent. De nombreux travaux [5] ont montré que le déplacement des agents dans un milieu fibreux pouvait être trés différent de celui dans un milieu homogène. Ainsi, de nombreux modèles mathématiques ont été proposés pour comprendre le rôle d'interactions de type (ii) dans la morphogénèse tissulaire. La littérature autour de cette question peut être divisée en trois grands types d'intéractions: (a) des intéractions de type chimiques ( [7, 9] ), où le déplacement des cellules suit la présence de gradients chimiques dans le milieu, (b) des modèles de transport ([9, 10, 12, 13]) où la matrice extra-cellulaire donne de l'information directionnelle au mouvement cellulaire [13]), ou (c) des modèles de type mécanique [8] où les cellules exercent et subissent une tension sur l'ECM.

Enfin, de nombreux auteurs ont étudié l'influence d'interactions de type fibres-fibres (iii) sur la morphogénèse [14, 15]. Différentes approches sont généralement employées pour modéliser les structures de fibres: la première consiste à développer un modèle discret en temps et en espace pour les fibres et les ponts de fibres (par exemple [16, 18, 19]). Le réseau de fibres peut être encore traité comme un matériau viscoélastique [20], un milieu poreux [21], un fluide visqueux [12] ou un gel actif [22]. Finalement, dans [14], les auteurs présentent un modèle individu-centré pour un réseau de fibres d'actine, où les fibres sont vues comme des particules et l'action des liens de fibres est modélisé par des interactions moyennes.

## 3.2 Modèles macroscopiques

Car les IBM décrivent le mouvement de chaque cellule et l'effet de chaque intéraction, ils deviennent rapidement lourds en temps de calcul. Pour des systèmes composés de plusieurs millions d'individus, il est donc plus efficace de développer un modèle continu qui considère la masse d'agents dans son ensemble. Les modèles macroscopiques décrivent l'évolution de cette masse, et ont donc un coût de calcul indépendant de la taille du système [31, 28]. Les modèles macroscopiques ont aussi pour avantage d'être analysés théoriquement. Nous disposons d'un cadre mathématique permettant de démontrer et prédire le comportement des solutions du modèle. Au contraire, pour les IBM, peu de résultats théoriques sont disponibles et la plupart des travaux sont empiriques. Cependant, les modèles macroscopiques engendrent une perte d'information à l'échelle de l'individu. Afin de garder au mieux la description au niveau microscopique, il est donc important de relier aussi rigoureusement que possible les deux visions, càd dériver un modèle macroscopique à partir d'un modèle microscopique. Le passage de l'un à l'autre s'effectue par changement d'échelle en temps et en espace [33]. Le modèle macroscopique ainsi construit décrira la dynamique du modèle microscopique de départ à grande échelle de temps et d'espace, et sera ainsi étroitement lié à une dynamique mesurable expérimentalement. Etablir rigoureusement un modèle macroscopique de son IBM est la tâche centrale de la théorie cinétique [32, 32, 34, 35]. Cependant, certaines techniques classiques ne sont pas applicables à cause de la nature des interactions entre agents, i.e (i) le manque d'équations de conservations (ii) l'apparence d'équilibres multiples et de transitions de phases ou encore (iii) la perte de propriété de propagation du chaos due à l'apparence de corrélations. Cependant, une théorie récente d'Invariant Collisionels Généralisés (GCI) [29, 30, 23, 37] a été développée, et permet d'obtenir une limite macroscopique pour des systèmes avec des nombres réduits de lois de conservation.

## 4 Vue générale du projet

Dans cette thèse, nous voulons comprendre les mécanismes en jeu dans la morphogénèse des tissus adipeux. Dans ce but, nous avons suivi la méthodologie indiquée en Diagramme 3. En collaboration étroite avec une équipe de biologistes du StromaLab et de spécialistes du laboratoire d'imagerie de l'ITAV, nous avons d'abord construit un modèle IBM à partir de règles heuristiques données par la réalité biologique (chap I). Le but de ce modèle était de montrer que l'auto-organisation de cellules et de fibres en structures cellulaires de forme lobulaires dans un réseau de fibres organisé pouvait être reproduite par un modèle simple construit principalement sur des règles mécaniques.

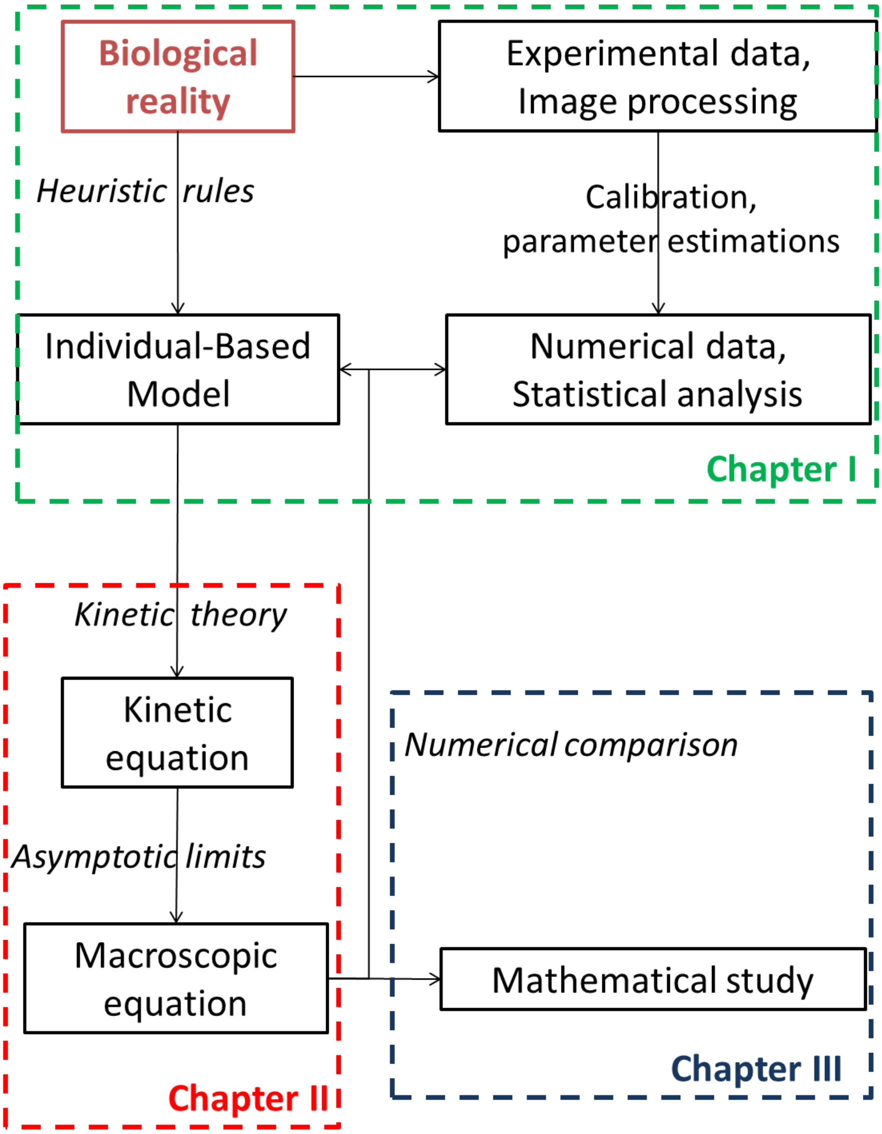

Figure 3: Un diagramme de l'utilisation de la modélisation mathématique pour répondre à une question biologique. A partir de règles heuristiques extraites du système réel, un modèle individu-centré est développé. Une analyse statistique des structures couplées à un processus de traitement d'images permet de calibrer les données expérimentales des données du modèle, permettant une première validation du modèle mathématique. En utilisant les concepts de la théorie cinétique, un modèle cinétique est développé, et sa limite asymptotique amène à un modèle macroscopique. Ce dernier peut alors être étudié analytiquement et numériquement et comparé à son IBM correspondant.

Le modèle individu centré proposé dans ce chapitre a été qualitativement et quantitativement comparé aux données expérimentales, et montre un bon accord avec les observations extraites des tissus réels. La confrontation des résultats du modèle aux données réelles a été réalisée dans le cadre d'un projet multidisciplinaire impliquant biologistes, spécialistes du traitement d'images et mathématiciens.

Afin de modéliser le tissu à grande échelle, nous avons ensuite développé un modèle mesoscopique puis dérivé un modèle macroscopique à partir du modèle IBM du chapitre I, en utilisant des techniques de la théorie cinétique. Nous nous sommes d'abord concentrés sur le réseau de fibres et voulions obtenir un modèle pour des fibres ayant la possibilité de se lier et de se détacher, sujettes à un potentiel extérieur et s'alignant en ses points d'attache. Afin de capturer les effets de la dynamique microscopique sur les structures à grande échelle, le modèle macroscopique a été lié le plus rigoureusement possible à son IBM. La dérivation d'un modèle macroscopique est présentée au chapitre II, où nous dérivons d'abord un modèle cinétique pour un réseau complexe de fibres inter-connectées, puis introduisons une approximation de diffusion sur ce modèle pour parvenir à un modèle continu. Le modèle cinétique apporte une description statistique de son IBM correspondant, en décrivant l'évolution temporelle de la distribution de probabilités en espace et orientation des fibres individuelles. Nous obtenons un système fermé à deux équations décrivant l'évolution de deux fonctions de distribution : la distribution de probabilités des fibres et celle de leur points d'attache. Nous considérons ensuite un régime où le processus d'attachement/de détachement des fibres est quasi-instantané, ce qui nous permet d'exprimer la fonction de distribution des liens de fibres en fonction de celle des fibres individuelles.

Comme la dérivation du modèle macroscopique est seulement formelle, la correspondance des deux formulations (modèle continu et IBM) doit être confirmée par des simulations numériques et des preuves mathématiques. Ceci est l'objet du chapitre III, où nous présentons une première étude du modèle macroscopique. Dans ce chapitre, nous prouvons d'abord l'existence de solutions à l'équation continue dans le cas d'une distribution homogène de fibres et sous réserve de conditions structurelles du potentiel extérieur. Nous nous intéressons ensuite aux propriétés des solutions, et analysons numériquement le profil des solutions stationnaires. Nous montrons que le modèle macroscopique fait apparaître un phénomène de flambement dépendant des paramètres du modèle et de la force appliquée au réseau, ce qui nous permet de déduire des premières propriétés mécaniques de notre modèle macroscopique. Nous comparons ensuite numériquement les profils des solutions du modèle continu et du modèle microscopique, et montrons une bonne concordance entre les deux modèles.

Les chapitres IV et V sortent du contexte des tissus adipeux. Le chapitre IV est le résultat d'un travail en collaboration avec S. Motsch, où nous nous intéressons à l'effet de contraintes de congestion sur les propriétés (forme, vitesse..) d'une masse croissante de cellules. Les contraintes de non recouvrement entre cellules sont omniprésentes dans les modèles de mouvement collectif et, plus particulièrement, dans les modèles de croissance tumorale. Elles consistent à considérer que seulement un nombre fini d'agents peut occuper un certain espace à un temps donné. Ceci peut être utilisé pour modéliser des fluides incompressibles par exemple. Nous proposons en premier lieu un modèle individus-centré pour des cellules - représentées par des sphères 2D- se déplaçant de manière aléatoire et interagissant à travers des forces de non recouvrement. Nous dérivons un modèle continu de cet IBM, et montrons que le modèle macroscopique ne capture pas les mêmes effets que le modèle individu-centré de départ. Nous montrons que cette différence est dûe au fait que les masses de Dirac ne sont pas stables pour le modèle macroscopique. Afin de relier les deux visions, nous proposons alors une version modifiée du modèle macroscopique que nous sommes capables de relier avec la dynamique microscopique. Ce modèle montre une bonne correspondance avec l'IBM.

Pour finir, le chapitre V présente les extensions de nos travaux. Dans une première partie, nous présentons les travaux (en cours) effectués avec P. Degond et B. Aymard sur la modélisation de la vasculogénèse. Dans ce modèle, quatre acteurs sont considérés : les capillaires, le flux sanguin, l'oxygène et le tissu. Le but de cette étude est de construire un modèle hybride dans lequel l'oxygène est décrit par des variables macroscopiques (le flux et la pression), et le réseau de capillaires comme un ensemble d'éléments discrets. La connexion avec nos travaux réside dans la modélisation du réseau capillaire qui est analogue à notre traitement de la matrice extra-cellulaire du modèle du chapitre I.

Le second modèle est un travail en cours avec M. Ferreira, P. Degond et S. Motsch et a pour but de modéliser l'agrégation balistique. L'idée sous-jacente de ce travail, commune avec notre travail sur les tissus adipeux, est de modéliser des structures de géométrie complexes comme un ensemble d'unités élémentaires de géométrie simple (par exemple des sphères 2D) connectées. Comme point de départ, nous présentons un modèle d'agrégation pour des sphères 2D auto propulsées se connectant quand elles s'entre-choquent. Le but est d'étudier le type de structures obtenues à l'équilibre avec un tel processus de recrutement.

# 5 Contributions des travaux

## 5.1 Sur la dérivation d'un modèle microscopique pour le tissu adipeux

Le modèle que nous avons développé dans le cadre de la morphogénèse des tissus adipeux a été le fruit d'une collaboration étroite avec l'équipe de biologistes de L. Casteilla (StromaLab), et d'une équipe de spécialistes du traitement de l'image à l'ITAV. Nous avons d'abord construit un IBM biologiquement significatif décrivant l'organisation de cellules dans une matrice extra-cellulaire composée de fibres. L'originalité de notre travail réside dans l'hypothèse que cette auto-organisation peut être reproduite par un modèle engageant un nombre réduit d'agents et d'interactions. Nous avons conduit une analyse quantitative approfondie sur les structures numériques et les données expérimentales pour tester différentes hypothèses sur l'émergence de structures lobulaires de cellules dans les tissus adipeux. Munis d'une méthode de traitement d'images que nous avons développée ainsi que de descripteurs appropriés pour les structures cellulaires et fibreuses, nous avons été en mesure de montrer la correspondance entre les résultats du modèle et les données expérimentales. Ce modèle montre que l'auto-organisation d'agents dans les tissus adipeux peut être le résultat de règles mécaniques impliquant un nombre réduit d'entités.

D'un point de vue biologique et à notre connaissance, c'est la première fois qu'un modèle mathématique est développé et confronté à des données biologiques pour comprendre les mécanismes d'auto-organisation des tissus adipeux. Notre modèle suggère, étonnamment, que la vascularisation pourrait être secondaire dans la formation de lobules dans les tissus adipeux.

D'un point de vue mathématique, ce travail suggère que des structures géométriques complexes comme des réseaux inter-connectés de fibres peuvent être modélisées comme un ensemble d'unités élémentaires de géométrie simple connectées, ces connexions vues comme des contraintes à travers l'utilisation de fonctionnelles simples. Cette nouveauté a été utilisée pour construire d'autres modèles comme (i) un modèle pour la vasculogénèse, où le réseau vasculaire est modélisé comme un ensemble de segments connectés, et (ii) un modèle d'agrégation balistique, où des cellules de forme complexe sont modélisées par un ensemble de sphères connectées. Ces travaux sont présentés en chapitre V.

## 5.2 Sur la dérivation d'un modèle continu pour un réseau complexe de fibres interconnectées

La deuxième partie de cette thèse a porté sur la dérivation d'un modèle macroscopique à partir du modèle microscopique introduit en première partie. Dans ce but, nous avons d'abord dérivé un modèle cinétique basé sur les intéractions fibres-fibres. Le challenge était de réussir à obtenir une description macroscopique d'un milieu constitué d'une multitude de fibres ayant la possibilité de se lier et sujettes à des forces extérieures. Dans un premier temps, la dérivation d'un modèle cinétique nous a conduit à une équation décrivant l'évolution de la distribution de fibres individuelles (i.e la probabilité de trouver une fibre dans un certain endroit du domaine), mais aussi à une équation décrivant l'évolution de la distribution à deux particules (i.e la probabilité de trouver deux fibres liées à un certain endroit du domaine). Ainsi, le mouvement des fibres seules pouvait être décrit en fonction de la fonction de distribution à deux particules, elle-même entièrement déterminée grâce à un système de fermeture simple ne demandant pas d'hypothèse supplémentaire sur le modèle.

A l'aide de techniques récentes non conventionnelles [23] dûes au manque de lois de conservation pour ce système, nous avons pu obtenir formellement la limite à grande échelle du modèle cinétique, dans un régime d'attachement/détachement de liens de fibres quasi-instantané. Dans ce régime, nous obtenons un système de deux équations : une équation classique de continuité décrivant l'évolution de la densité de fibres ainsi qu'une équation non linéaire décrivant leur orientation moyenne. L'étude analytique complète du modèle macroscopique obtenu reste un problème ouvert. Nous avons premièrement obtenu l'existence de solutions dans un cadre simplifié, puis nous nous sommes concentrés sur les simulations numériques du modèle macroscopique. Ces questions sont présentées en chapitre III.

## 5.3 Modèle macroscopique pour un réseau complexe de fibres : existence de solutions et simulations numériques.

Dans ce chapitre, nous proposons une première analyse théorique et numérique du modèle macroscopique du chapitre II. Nous étudions le cas où la densité de fibres est homogène, et prouvons l'existence de solutions sous hypothèse structurelle pour le potentiel extérieur. Les simulations numériques du modèle macroscopique font apparaître un phénomène de flambage, permettant de déduire des propriétés physiques du modèle macroscopique de fibres. Nous proposons ensuite une première comparaison numérique entre le modèle continu et son IBM correspondant. Nous montrons que la distribution de l'orientation moyenne locale des fibres est en bon accord avec la distribution théorique prédite par le modèle macroscopique. En particulier, nous sommes en mesure de calculer le paramètre d'ordre du système à partir des expériences numériques du modèle microscopique. Nous montrons ensuite que dans un certain régime de paramètres, nous obtenons une bonne correspondance entre les structures des deux modèles. Cette étude préliminaire est proposée comme une première validation de la dynamique macroscopique par comparaison aux prédictions du modèle IBM.

### 5.4 Amélioration dún modèle de croissance tumorale

Une application directe de notre travail a consisté à introduire notre dynamique cellulaire dans un modèle de croissance tumorale. Ce travail, fait en collaboration avec S. Motsch, a consisté à enrichir un modèle existant en incluant des intéractions cellules-cellules afin d'étudier l'influence de contraintes de congestion dans un modèle de diffusion. Au cours de cette étude, nous avons été amenés à dériver un modèle macroscopique de croissance tumorale, et à effectuer une comparaison entre le modèle microscopique et macroscopique. Ce travail nous a permis d'approfondir l'étude de l'influence d'interactions de type cellules-cellules sur la forme et l'évolution de structures cellulaires.

## 6 Résultats

### 6.1 Chap. I : Modèle individu centré pour l'auto-organisation dans les tissus adipeux

Dans ce chapitre, nous introduisons un modèle pour la morphogénèse des tissus adipeux. Les expériences biologiques montrent qu'à l'équilibre, le tissu adipeux est composé d'adipocytes groupés en formes lobulaires entourées d'un réseau de fibres organisées [1]. A partir de ces observations, nous proposons un modèle 2D où les cellules sont représentées par des sphères qui ne peuvent pas se recouvrir, et les fibres sont modélisées par des segments de longueur fixe qui ont la possibilité de se lier quand ils se croisent. Nous supposons que les forces mécaniques agissant sur les cellules et les fibres sont de deux types: (i) une force de répulsion entre cellules et fibres $W_{pot}$ et (ii) une force d'alignement entre les fibres liées, générant un couple à la jonction des fibres. L'action de ce couple est modélisé par une énergie $W_{align}$. Nous incorporons les phénomènes biologiques suivants : (a) La différenciation des cellules souches est modélisée par l'apparition de nouvelles cellules dans le domaine par un processus stochastique en temps, (b) la croissance cellulaire est supposée être un phénomène régulier, (c) la plasticité du réseau de fibres est modélisée en donnant la possibilité aux fibres se croisant de se lier ou aux fibres liées de se décrocher. Ces processus sont supposés être des processus stochastiques dont les fréquences temporelles sont des paramètres du modèle. Nous supposons ensuite qu'à chaque temps d'observation, le système est à l'équilibre mécanique, c'est à dire que les agents se déplacent vers la configuration de potentiel minimal, où le potentiel est défini comme la somme les forces agissant entre chacune des entités. Selon ce principe physique, nous sommes amenés à résoudre, entre deux pas de temps, un problème de minimisation d'un potentiel, sous contraintes de non recouvrement des cellules et de maintien des liens de fibres:

$$(X, Y, \theta) = \underset{X_1 \; | \Phi(X_1) \leq 0, (Y_1, \theta_1) \; | \; \Psi(Y_1, \theta_1) = 0}{\text{argmin}} W(X_1, Y_1, \theta_1) \quad , \tag{6.1}$$

où $(X, Y, \theta)$ est l'ensemble des vecteurs position $X = \{X_i \in \mathbb{R}^2 \;\; 1 \leq i \leq N\}$ des $N$ cellules, les vecteurs de position $Y = \{Y_f \in \mathbb{R}^2 \;\; 1 \leq f \leq N_f\}$ des $N_f$ centres de fibres, et les angles des vecteurs orientation $\theta = \{\theta_f \in [-\frac{\pi}{2}, \frac{\pi}{2}) \;\; 1 \leq f \leq N_f\}$ des $N_f$ fibres. L'énergie libre totale du système $W(X, Y, \theta)$ inclue les fonctionnelles d'énergie des phénomènes (i) et (ii):

$$W(X, Y, \theta) = W_{pot}(X, Y, \theta) + W_{align}(Y, \theta). \tag{6.2}$$

Finalement, $\Phi(X)$ et $\Psi(Y, \theta)$ sont les fonctionnelles pour le non recouvrement des cellules (contraintes d'inégalité) et pour le maintien des liens de fibres (contraintes d'égalité) respectivement: $\Phi(X) = \{\Phi_{ij}(X) \;,\; 1 \leq i < j \leq N\}$, où $\Phi_{ij}$ est une fonctionnelle telle que $\Phi_{ij}(X) > 0$ si les cellules $i$ et $j$ se recouvrent. Pour les liens de fibres, $\Psi(Y, \theta) = \{\vec{V}_{i(k)j(k)}(Y, \theta) \;,\; 1 \leq k \leq K\}$, où $K$ est le nombre total de liens de fibres et $\vec{V}_{i(k)j(k)}$ est le vecteur joignant les positions des points d'attache sur chaque paire de fibres $(i(k), j(k))$ liées par le lien $k$ (le maintien des liens de fibres correspondant au cas où ce vecteur est nul, comme représenté en Fig. 4).

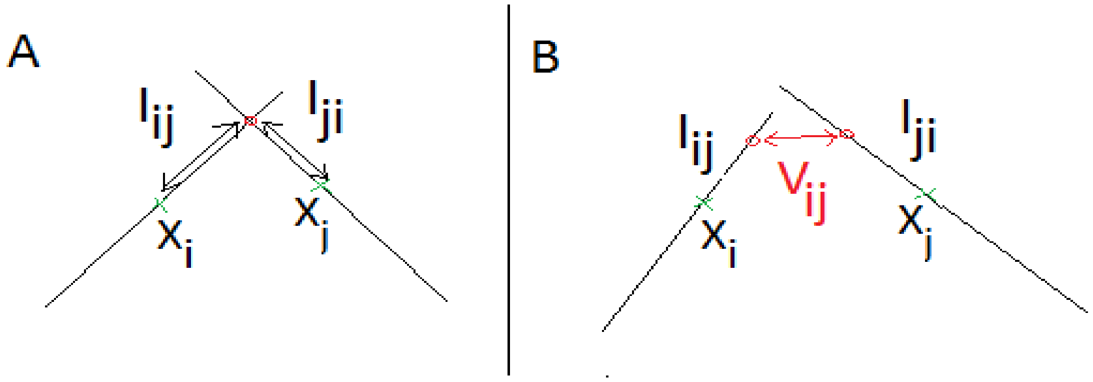

Figure 4: Liens de fibres s'intersectant. A. Situation au moment du lien. B. Potentiel $V_{ij}$ apres mouvement des fibres liées.

Le Lagrangien du système $\mathcal{L}(X, Y, \theta, \lambda, \mu)$ dépend de la position des cellules et des fibres, ainsi que de l'angle d'orientation des fibres $\theta$, et des multiplicateurs de Lagrange $\lambda$ et $\mu$ associés aux contraintes d'inégalités pour le non recouvrement des cellules et aux contraintes d'égalité de maintien des liens respectivement. Son expression est donnée par:

$$\mathcal{L}(X, Y, \theta, \lambda, \mu) = W(X, Y, \theta) + < \lambda, \Phi > + < \mu, \Psi >,$$

où $< . >$ désignant le produit scalaire. Le problème de minimisation (6.1) est ensuite résolu à chaque temps discret par un algorithme d'Uzawa.

L'évolution du système entre les temps discrets $t^n$ et $t^{n+1} = t^n + \Delta t$ est donnée par:

1. Croissance cellulaire:$\forall i \in [1, N]$:

   $R_i^3(t^{n+1/2}) = R_i^3(t^n) + K_g(1 + \eta\rho_g)$

où $\eta$ est un nombre aléatoire et $K_g, \rho_g$ deux paramètres du modèle.

2. Creation de nouvelles cellules: processus de Poisson de fréquence temporelle $\nu_e$.

   Probabilité d'ensemencer au point $X$:

   $\mathcal{P}(X, R) = \chi^\alpha$,

   où $\chi$ désigne la densité locale de cellules, $\alpha$ un paramètre du modèle
3. Attachement/détachement des liens: creation et suppression des liens

   selon des processus de Poisson de fréquences $\nu_f$ et $\nu_d$
4. Mouvement des cellules et fibres:

   Pour une configuration initiale $(X^{n+1/2}, Y^{n+1/2}, \theta^{n+1/2})$

   trouver $(X^{n+1}, Y^{n+1}, \theta^{n+1})$ tel que

   $$(X^{n+1}, Y^{n+1}, \theta^{n+1}) = \underset{X_1 \,|\Phi(X_1)\leq 0, (Y_1,\theta_1)\,|\,\Psi(Y_1,\theta_1)=0}{\text{argmin}} W(X_1, Y_1, \theta_1) \quad .$$

Nous définissons ensuite un ensemble de quantificateurs statistiques pour décrire les structures cellulaires et fibreuses à l'équilibre. Dans ce but, un groupement de cellules est défini comme un ensemble de sphères presque en contact, et nous avons accès au nombre total de groupements, ainsi qu'à leur élongation moyenne et l'écart-type de la distribution de leur anisotropie de forme. Les groupements de fibres sont définis comme les ensembles de fibres voisines presque alignées, et nous mesurons le nombre de groupements de fibres, leur élongation moyenne et l'alignement moyen de leurs constituants. Nous effectuons ensuite une analyse statistique en moyennant les valeurs de ces quantificateurs sur un grand nombre de simulations afin de les représenter en fonction des paramètres du modèle.

Afin de comparer les simulations numériques avec les données expérimentales, nous développons une méthode de traitement d'images pour (a) la détection des cellules et (b) la détection des groupements cellulaires. Comme seuls les adipocytes et lobules sont accessibles à partir des images biologiques, les quantificateurs pour les structures cellulaires uniquement peuvent être utilisés dans cette comparaison.

## 6.2 Chap. II: Modèle macroscopique pour un réseau complexe de fibres.

Dans ce chapitre, nous étudions la limite à grande échelle du modèle du chapitre I. Afin de simplifier le modèle, nous supposons que la présence de cellules est modélisée par un potentiel extérieur $W_{ext}(Y,\theta)$ dépendant des positions des centres de fibres et de leur angle d'orientation, et nous nous concentrons sur le réseau de fibres. Nous cherchons donc à étudier les propriétés d'un réseau de fibres composé de segments de longueur fixe qui se fixent et se détachent, et sujets à des interactions mécaniques. Pour modéliser les mouvements du tissu biologique, nous considérons aussi un bruit aléatoire en position et orientation à l'aide d'un terme d'entropie $W_{noise}(Y,\theta)$. Il est à noter que la dérivation d'un modèle macroscopique nécessite une description continue du modèle discret, et que la procédure de minimisation (6.1) est discrète en temps pour le modèle microscopique. Ainsi, le problème de minimisation est modifié en une descente de gradient pour une pénalisation quadratique de l'équation (6.1). Dans ce but, la fonctionnelle $\Psi(Y,\theta)$ pour les contraintes d'égalité de maintien des liens de fibres est incorporée dans l'énergie libre totale du système tel que :

$$W(Y,\theta) = W_{ext}(Y,\theta) + W_{align}(Y,\theta) + W_{noise}(Y,\theta) + \frac{\kappa}{2}|\Psi(Y,\theta)|^2,$$

où $\kappa$ est le facteur de pénalisation. Le mouvement et la rotation des fibres sont supposés suivre la direction de descente du gradient de cette énergie:

$$\frac{dY}{dt} = -\mu\nabla_X\Big(W_{ext} + W_{align} + W_{links} + W_{noise}\Big) \tag{6.3}$$

$$\frac{d\theta}{dt} = -\lambda\partial_\theta\Big(W_{ext} + W_{align} + W_{links} + W_{noise}\Big). \tag{6.4}$$

où $\mu$ et $\lambda$ sont des coefficients de mobilité.

Afin de dériver un modèle macroscopique à partir des équations (6.3)-(6.4), nous utilisons l'équation cinétique associée à cette dynamique particulaire. Dans ce but, nous définissons la fonction de distribution à une particule $f(x,\theta)$ décrivant les $N$ fibres individuelles, et la fonction de distribution à deux particules $g(x_1,\theta_1,\ell_1,x_2,\theta_2,\ell_2)$ décrivant les $K$ liens de fibres:

$$\begin{aligned} f^N(x,\theta,t) =& \frac{1}{N}\sum_{i=1}^N \delta_{(X_i(t),\theta_i(t))}(x,\theta), \\ g^K(x_1,\theta_1,\ell_1,x_2,\theta_2,\ell_2,t) =& \frac{1}{2K}\sum_{k=1}^K \delta_{(X_{i(k)},\theta_{i(k)},\ell^k_{i(k)},X_{j(k)},\theta_{j(k)},\ell^k_{j(k)})}(x_1,\theta_1,\ell_1,x_2,\theta_2,\ell_2) \\ &+ \delta_{(X_{j(k)},\theta_{j(k)},\ell^k_{j(k)},X_{i(k)},\theta_{i(k)},\ell^k_{i(k)})}(x_1,\theta_1,\ell_1,x_2,\theta_2,\ell_2), \end{aligned}$$

où $\delta_x(y)$ désigne la fonction de Dirac en $x$, i.e la distribution agissant sur les fonctions test $\phi(y)$ tel que $< \delta_x(y), \phi(y) >= \phi(x)$. Par une simple relation de fermeture, nous parvenons à obtenir la limite formelle d'un grand nombre d'individus et de liens et obtenons le théorème suivant:

**Theorem 6.1.** *La limite formelle des Equations* (6.3), (6.4) *pour* $K, N \to \infty$, $\frac{K}{N} \to \xi$, *où* $\xi > 0$ *est un paramètre fixé est donnée par:*

$$\frac{df}{dt} - \mu\Big(\nabla_x.((\nabla_x U)f) + \xi\nabla_x.F_1 + d\Delta_x f\Big) - \lambda\Big(\partial_\theta((\partial_\theta U)f) + \xi\partial_\theta F_2 + d\partial_\theta^2 f\Big) = 0, \tag{6.5}$$

*et*

$$\begin{aligned}\frac{dg}{dt} - \mu\Bigg[&\nabla_{x_1}.\Big(g\nabla_x U(x_1,\theta_1) + \xi\frac{g}{f(x_1,\theta_1)}F_1(x_1,\theta_1) + d\frac{g}{f(x_1,\theta_1)}\nabla_x f(x_1,\theta_1)\Big)\\ &+ \nabla_{x_2}.\Big(g\nabla_x U(x_2,\theta_2) + \xi\frac{g}{f(x_2,\theta_2)}F_1(x_2,\theta_2) + d\frac{g}{f(x_2,\theta_2)}\nabla_x f(x_2,\theta_2))\Big)\Bigg]\\ -\lambda\Bigg[&\partial_{\theta_1}\Big(g\partial_\theta U(x_1,\theta_1) + \xi\frac{g}{f(x_1,\theta_1)}F_2(x_1,\theta_1) + d\frac{g}{f(x_1,\theta_1)}\partial_\theta f(x_1,\theta_1)\Big)\\ &+ \partial_{\theta_2}\Big(g\partial_\theta U(x_2,\theta_2) + \xi\frac{g}{f(x_2,\theta_2)}F_2(x_2,\theta_2) + d\frac{g}{f(x_2,\theta_2)}\partial_\theta f(x_2,\theta_2)\Big)\Bigg] = S(g),\end{aligned} \tag{6.6}$$

*où*

$$\begin{aligned}F_1(x_1,\theta_1) &= \int (g\nabla_{x_1}V)(x_1,\theta_1,\ell_1,x_2,\theta_2,\ell_2)d\ell_1 d\ell_2\frac{d\theta_2}{\pi}dx_2,\\ F_2(x_1,\theta_1) &= \int \Big(g(\partial_{\theta_1}V + \partial_{\theta_1}b)\Big)(x_1,\theta_1,\ell_1,x_2,\theta_2,\ell_2)d\ell_1 d\ell_2\frac{d\theta_2}{\pi}dx_2.\end{aligned} \tag{6.7}$$

*Içi, le terme* $S(g)$ *décrit la dynamique de création/suppression de liens de fibres et son expression est donnée par :*

$$S(g) = \nu_f f(x_1,\theta_1)f(x_2,\theta_2)\delta_{\bar\ell(x_1,\theta_1,x_2,\theta_2)}(\ell_1)\delta_{\bar\ell(x_2,\theta_2,x_1,\theta_1)}(\ell_2) - \nu_d g, \tag{6.8}$$

La nouveauté de cette équation cinétique réside dans le fait qu'elle est un moyen simple de suivre les interactions à deux particules. Ces paires d'interactions peuvent être vues comme un graphique aléatoire des liens de fibres. En effet, comme les points d'attache sont localisés sur les fibres, ils sont transportés et suivent l'évolution des fibres individuelles. En même temps, ils contraignent le mouvement des fibres en forçant les fibres attachées à évoluer ensemble. Le potentiel de renforcement généré par les liens de fibres, $V$, est exprimé au niveau cinétique par des forces non locales $F_1$ et $F_2$ dans les équations Eqs. (6.5),(6.6). Les deuxième et troisième termes décrivent le transport en espace physique et en orientation dû au potentiel extérieur $U$, tandis que les quatrième et cinquième termes expriment la diffusion d'amplitude $\lambda d$ ou $\mu d$ et représentent le mouvement individuel des fibres. Le potentiel d'alignement entre fibres liées, $b$, s'exprime au niveau cinétique en une force $F_2$ et agit seulement sur les orientations des fibres. La partie gauche de l'équation $S(g)$ décrit le processus de Poisson de création/destruction des liens de fréquences respectives $\nu_f$ et $\nu_d$. La transition entre la dynamique particulaire et l'équation cinétique est seulement formelle.

Une fois que nous avons le modèle cinétique Eqs. (6.5)-(6.6), nous utilisons un changement d'échelle pour dériver le modèle macroscopique. Plus précisément, nous introduisons les variables macroscopiques :

$$\tilde{t} = \varepsilon t \quad , \quad \tilde{x} = \sqrt{\varepsilon} x,$$

et montrons que dans un régime d'attachement/détachement très rapide des liens, la fonction de distribution à deux particules $g^\varepsilon$ peut être écrite comme le produit de deux fonctions de distribution à une particule $f^\varepsilon$:

$$g^\varepsilon(x_1, \theta_1, \ell_1, x_2, \theta_2, \ell_2) = \frac{\nu_f}{\nu_d} f^\varepsilon(x_1, \theta_1) f^\varepsilon(x_2, \theta_2) \delta_{\bar{\ell}(x_1,\theta_1,x_2,\theta_2)}(\ell_1) \delta_{\bar{\ell}(x_2,\theta_2,x_1,\theta_1)}(\ell_2) + O(\varepsilon^2).$$

Cette relation de fermeture nous permet alors de simplifier le système (6.5) et nous pouvons alors passer à la limite grande échelle $\varepsilon \to 0$. Nous montrons que les solutions d'équilibre de l'équation cinétique sont de la forme :

$$f(x, \theta) = \rho(x) M_{\theta_0(x)}(\theta), \quad M_{\theta_0(x)}(\theta) = \frac{1}{Z} e^{-r \cos 2(\theta - \theta_0(x))}$$

où $r$ est un paramètre du modèle, $Z$ une fonction de normalisation telle que $f$ est une densité de probabilité, $\rho(x)$ est la densité locale des fibres et $\theta_0(x)$ leur angle d'orientation. En utilisant le nouveau concept d'invariants collisionnels généralisés ([23]), nous obtenons la limite macroscopique de l'équation cinétique. Quand $\varepsilon$ tend vers 0, nous obtenons un système à deux équations : une pour la densité $\rho$:

$$\partial_t \rho - \nabla_x . (\nabla_x U^0 \rho) - d \Delta_x \rho = 0, \tag{6.9}$$

où l'on a supposé : $U(x, \theta) = U^0(x) + U^1(\theta)$, avec $U^0$ le potentiel extérieur agissant sur les positions des fibres et $U^1$ agissant sur l'orientation des fibres. La deuxième équation décrit l'évolution de l'orientation moyenne locale des fibres $\theta_0(x)$:

$$\begin{aligned} &\rho \partial_t \theta_0 - \rho \nabla_x U^0 . \nabla_x \theta_0 - 2\alpha_2 \nabla_x \rho . \nabla_x \theta_0 - \alpha_2 \rho \Delta_x \theta_0 \\ &\quad + \alpha_3 (\rho \nabla_x^2 \theta_0 + \nabla_x \theta_0 \otimes \nabla_x \rho + \nabla_x \rho \otimes \nabla_x \theta_0) \ : [\omega_0 \otimes \omega_0 - \omega_0^\perp \otimes \omega_0^\perp] \\ &\qquad + \Big( 2\rho \alpha_3 \nabla_x \theta_0 \otimes \nabla_x \theta_0 - \alpha_4 \nabla_x^2 \rho \Big) : [\omega_0 \otimes \omega_0^\perp + \omega_0^\perp \otimes \omega_0] + \alpha_5 \rho < \partial_\theta U^1 >= 0, \end{aligned} \tag{6.10}$$

où $\omega_0 = (\cos\theta_0, \sin\theta_0)$ désigne le vecteur directionnel 2D de norme 1 associé à l'angle $\theta_0$, $\omega_0^\perp$ désigne son orthogonal et $< h >= \int_{-\pi/2}^{\pi/2} h(\theta) M_{\theta_0}(\theta) \frac{d\theta}{\pi}$ pour toute fonction $h$ de $\theta \in [-\frac{\pi}{2}, \frac{\pi}{2})$. Les coefficients $\alpha_1, \alpha_2, \alpha_3, \alpha_4, \alpha_5$ sont entièrement déterminés par les paramètres du modèle.

## 6.3 Chap III: Modèle macroscopique pour des fibres liées avec interactions d'alignement: théorie d'existence et simulations numériques

Dans ce chapitre, nous cherchons à valider numériquement le modèle macrocopique en le comparant à son IBM. Nous montrons d'abord la bonne correspondance entre les modèles IBM du chapitre I et II dans un régime de paramètres. Afin de comparer la dynamique microscopique au modèle macroscopique, nous avons besoin de mieux comprendre le modèle macroscopique. Pour ce faire, nous considérons dans un premier temps que la distribution de fibres est homogène, i.e $\rho(x) = \rho_0$ avec $\rho_0 > 0$ une constante, et nous intéressons aux solutions stationnaires. Nous montrons que dans ce cas, l'orientation locale moyenne des fibres $\theta_0(x)$ résoud une équation elliptique quasi linéaire qui est résolvable sous une condition structurelle pour le potentiel extérieur.

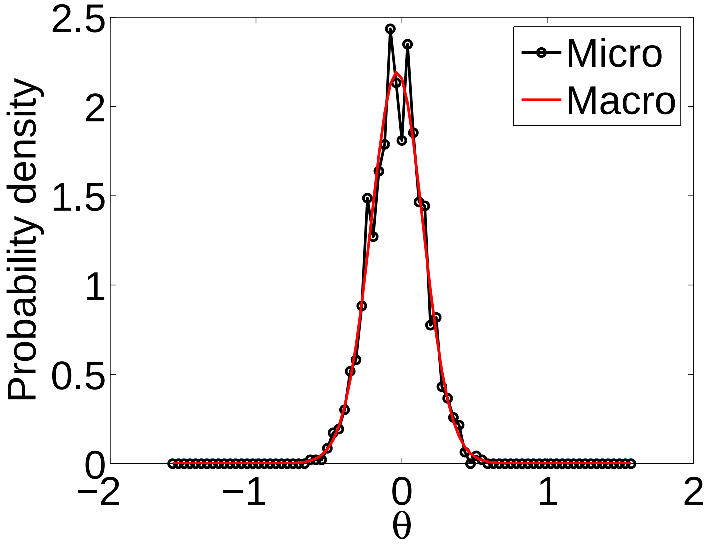

Figure 5: Distribution des angles de fibres dont le centre est proche du centre du domaine, moyennée sur 20 simulations (courbe noire), comparée à sa distribution théorique (courbe rouge).

Les simulations numériques du modèle macroscopique montrent un phénomène de flambement en fonction des paramètres du modèle ainsi que de la force du potentiel extérieur, ce qui nous permet de déduire des propriétés physiques à notre réseau macroscopique de fibres. Ensuite, nous comparons numériquement les solutions du modèle macroscopique à son IBM correspondant. Nous montrons que la distribution des orientations locales de fibres du modèle microscopique correspond à celle prédite par le modèle macrocopique, et nous sommes en mesure de calculer un paramètre d'ordre pour le modèle IBM (voir Fig. 5). Le coût de calcul du modèle IBM ne nous permet pas d'être dans la limite cinétique, ce qui amène à des solutions différentes dans certains régimes de paramètres. Cependant, nous montrons que pour un ensemble de paramètres les structures obtenues par le modèle IBM sont en concordance avec les prédictions du modèle macroscopique. Ce travail est donc une première étape dans la validation du modèle macroscopique par comparaison à son IBM.

## 6.4 Chap IV. Modèle de croissance tumorale

Dans ce chapitre, nous cherchons à comprendre le rôle des contraintes de densité sur les propriétés de propagation d'une masse croissante de cellules. Les cellules sont modélisées comme des sphères 2D de centre $X_i \in \mathbb{R}^2$ et de rayon $R > 0$. Afin de modéliser les interactions de courte portée, nous introduisons une fonction d'interaction $\phi \geq 0$ et considérons la dynamique suivante :

$$\frac{dx_i}{dt} = -\sum_{j=1}^{N} \phi_{ij}(x_i - x_j), \qquad \text{with } \phi_{ij} = \phi(\frac{x_i - x_j}{2R}), \tag{6.11}$$

où $i$ et $j$ sont les indices des cellules, et :

$$\phi(r) = \begin{cases} |1 - r^\alpha|, & \text{if } 0 \leq r \leq 1 \\ 0 & \text{otherwise,} \end{cases}$$

pour $\alpha = 1$ ou $-1$. Il est à noter que la répulsion est active seulement quand deux particules sont à une distance inférieure à $2R$.

En utilisant des arguments classiques de la théorie cinétique, nous obtenons le modèle cinétique associé à (6.11) :

$$\partial_t \rho + \nabla_x \cdot (G[\rho]\rho) = 0, \tag{6.12}$$

avec

$$G[\rho](x) = -\int_{y \in \mathbb{R}^2} \phi\left(\left|\frac{x-y}{2R}\right|^2\right)(y - x)\rho(y)\,\mathrm{d}y. \tag{6.13}$$

Dans la limite asymptotique $R \to 0$, nous montrons que le modèle consiste en une équation en milieu poreux :

$$\partial_t \rho = \alpha_R \nabla_x \cdot \Big(\rho \nabla_x \rho\Big), \tag{6.14}$$

avec

$$\alpha_R = \pi (2R)^4 \int_{r \geq 0} \phi(|r|^2) r^3 \mathrm{d}r. \tag{6.15}$$

Les simulations numériques montrent que les solutions de ce modèle se répandent en espace, tandis que la dynamique microscopique prédit des solutions à support compact fixe à l'état stationnaire. Nous montrons numériquement que la différence entre les deux modèles peut être expliquée par le fait que les masses de Dirac ne sont pas stables pour l'équation macroscopique.

Afin d'obtenir une meilleure correspondance entre les deux échelles, nous proposons de modifier le noyau d'intéraction du modèle cinétique, afin de prendre en compte le fait que la répulsion n'agit que lorsque la densité de particules dépasse le seuil $\rho_{\max}$. Dans ce but, nous définissons la fonction $W[\rho]$:

$$W[\rho] = -2 \int_{|x-y|<2R} (\rho - \rho_{\max})^+ (y - x) dy.$$

L'équation d'évolution pour la densité de particules $\rho$ s'écrit alors :

$$\partial_t \rho + \nabla_x . (W[\rho] \rho) = 0.$$

Par ce moyen, la diffusion n'est active que dans un disque où la densité est supérieure à ce seuil $\rho_{\max}$. Nous montrons que dans la limite $R \to 0$, nous obtenons l'équation continue suivante :

$$\partial_t \rho = \beta(R) \nabla_x . (\mathbf{1}_{\rho(x) \geq \rho_{\max}} \rho \nabla_x \rho),$$

où $\beta(R)$ est un coefficient dépendant de la taille des particules et $\mathbf{1}_{\rho(x) \geq \rho_{\max}}$ une fonction égale à 1 si $\rho \leq \rho_{\max}$, 0 sinon. Ainsi, nous obtenons une équation de diffusion non linéaire, où la diffusion n'est active que lorsque la densité locale est supérieure à un seuil. Les simulations numériques montrent un bon accord entre le modèle ainsi obtenu et l'IBM. En ajoutant un terme source, nous montrons que nous obtenons des ondes progressives prédites par les deux modèles.

## 6.5 Chap V. Extensions des travaux

Dans ce chapitre, nous présentons les extensions de nos travaux. Nous proposons deux modèles (en cours) construits sur les mêmes principes que ceux développés pour notre modèle IBM du chapitre I. Le premier est un modèle pour la vasculogénèse, le deuxième pour l'agrégation balistique.

### 6.5.1 Un modèle pour la vasculogénèse

Dans cette section, nous présentons les points principaux du modèle développé avec B. Aymard et P. Degond pour la vasculogénèse. Dans ce modèle, quatre acteurs sont considérés : les capillaires, le flux sanguin, l'oxygène et le tissu. Les $K$ capillaires sont modélisés comme des tubes de longueur fixe décrits par un vecteur position $X_k = (x_k, y_k) \in \mathbb{R}^2$ de leur centre et un vecteur orientation $\omega_k = (\cos\theta_k, \sin\theta_k) \in \mathbb{S}^1$ d'angle $\theta_k$ défini modulo $\pi$ pour modéliser l'isotropie du flux sanguin. Chaque unité élémentaire de capillaire est supposée générer une matrice de porosité élémentaire et une matrice de diffusion élémentaire, qui participent à la porosité et diffusivité globale du milieu. Afin de modéliser l'apparence et la destruction de capillaires selon les besoins du tissu, les unités de capillaire sont créées et supprimées selon des processus de Poisson de fréquence $\nu_c$ et $\nu_r$ dépendant du gradient d'oxygène.

La matrice de porosité globale du milieu $\mathbf{K}(X)$ mesurée au point $X = (x, y) \in \mathbb{R}^2$ (respectivement la matrice de diffusion $\mathbf{D}(X)$) est ensuite définie comme la somme de toutes les matrices élémentaires de porosité (respectivement matrices élémentaires de diffusion) générées par le réseau capillaire et de la matrice de porosité d'un milieu homogène :

$$\begin{cases} \mathbf{K}(\mathbf{X}) = k_h \mathbf{I}_2 + \displaystyle\sum_{k\, s.t. ||\mathbf{X}_k - \mathbf{X}|| \leq R} \kappa\, (\boldsymbol{\omega}_k \otimes \boldsymbol{\omega}_k), \\ \mathbf{D}(\mathbf{X}) = d_h \mathbf{I}_2 + \displaystyle\sum_{k\, s.t. ||\mathbf{X}_k - \mathbf{X}|| \leq R} d\, (\boldsymbol{\omega}_k \otimes \boldsymbol{\omega}_k), \end{cases}$$

où $k_h$, $d_h$, $\kappa$, $d$ et $R$ sont des constantes positives réelles et $\mathbf{I}_2$ la matrice identité de taille 2.
Le flux sanguin $\mathbf{u}$ est ensuite supposé suivre la loi de Darcy :

$$\begin{cases} \mathbf{u} = -\mathbf{K} \nabla p \\ -\text{div}(\mathbf{K} \nabla p) = 0 \end{cases} \tag{6.16}$$

où $\nabla p$ désigne le gradient de pression du flux sanguin. L'oxygène est modélisé par sa densité $\rho$. Le mouvement de l'oxygène est supposé être déterminé par deux éléments : (i) transport par le sang et (ii) diffusion à travers le tissu. De plus, l'oxygène est consommé par le tissu. Dans ce premier travail, nous supposons que la consommation d'oxygène est homogène. Ces trois hypothèses amènent à une équation de transport diffusion avec terme source :

$$\partial_t \rho + \nabla.(\rho \mathbf{u}) - \nabla.(\rho \mathbf{D} \nabla \rho) = -\beta \rho, \tag{6.17}$$

où $\beta$ est un réel positif modélisant la consommation d'oxygène et $\mathbf{D}$ est la matrice de diffusion du système. Le système complet s'écrit :

1. Flux sanguin

$$\begin{cases}\mathbf{u} = -\mathbf{K}\nabla p \\ \mathrm{div}(\mathbf{u}) = 0\end{cases}$$

2. Oxygène: transport diffusion avec terme source

$$\begin{cases}\partial_t \rho + \nabla.(\rho \mathbf{u}) - \nabla.(\rho \mathbf{D} \nabla \rho) = -\beta \rho\end{cases}$$

3. Réseau de capillaires : création et destruction par processus de Poisson de fréquences $\nu_c$ et $\nu_r$
4. Tissu (matrice de porosité et de diffusion)

$$\begin{cases}\mathbf{K}(\mathbf{X}) = k_h \mathbf{I}_2 + \sum\limits_{k\, s.t. ||\mathbf{X}_k - \mathbf{X}|| \leq R} \kappa \left(\boldsymbol{\omega}_k \otimes \boldsymbol{\omega}_k\right) \\ \mathbf{D}(\mathbf{X}) = d_h \mathbf{I}_2 + \sum\limits_{k\, s.t. ||\mathbf{X}_k - \mathbf{X}|| \leq R} d \left(\boldsymbol{\omega}_k \otimes \boldsymbol{\omega}_k\right)\end{cases}$$

Les premières simulations numériques du modèle seront montrées dans cette section.

### 6.5.2 Un modèle d'agrégation balistique

Dans cette section, nous présentons les travaux en cours avec P. Degond et M. Ferreira sur la modélisation de l'agrégation balistique. Le but final de ce modèle est de parvenir à comprendre la formation du tissu épithélial. Les cellules épithéliales sont groupées ensemble en bandes de tissu, et maintenues ensemble par l'action de plusieurs interactions : jonction étanche, adhérents, desmosomes, jonction lacunaire... Différents types d'épithélium sont présents dans les systèmes réels, et sont distingués par la forme de leurs cellules. Par exemple, si les cellules squameuses sont fines et plates, d'autres sont allongées et prennent la forme de colonnes. Le but de ce projet est de construire un modèle mathématique permettant de prendre en compte plusieurs géométries de cellules. L'idée est de modéliser les cellules de géométrie complexe comme un ensemble d'unités élémentaires de géométrie simple connectées, comme des sphères 2D par exemple.

Comme point de départ, un modèle de cellules auto-propulsées s'attachant lorsqu'elles s'entre-choquent est proposé. Dans ce modèle, les cellules sont auto-propulsées à vitesse constante (dans une direction fixe aléatoire) tant qu'elles ne s'entrechoquent pas. Quand deux cellules entrent en collision, elles se lient et restent attachées tout au long du mouvement, avec une même vitesse et dans la même direction. Afin d'éviter le recouvrement de cellules, une méthode de minimisation est proposée pendant chaque collision. Le système complet s'écrit :

- 1. Mouvement :

$$\forall i = 1 \ldots N, \quad \hat{X}_i^n = X_i^{n-1} + \delta_t V_i^{n-1}.$$

- Réajustement par minimisation :
  Pour $(X_i, X_j) \in A \times A$,

  $$\phi(X_i, X_j) = (R_i + R_j + \varepsilon \min\{R_i, R_j\})^2 - d(X_i, X_j)^2$$

  où $S$ est l'ensemble de sphère presque en contact :

  $$S = \{(i, j) \in \{1 \ldots N\} \mid \phi(X_i, X_j) \geq 0\}.$$

  Nous considérons le potentiel suivant :

  $$W(X_1, ..., X_N) = \frac{1}{2} \sum_{(i,j) \in S_0} d(X_i, X_j)^2;$$

  l'ajustement consiste en la minimisation suivante :

  $$(X_1^n, ..., X_N^n) = \operatorname*{argmin}_{\phi_0(X_i, X_j) < 0,\ i,j=1,...,N} W(X_1, ..., X_N),$$

  avec comme condition initiale $(\hat{X}_1^n, ..., \hat{X}_N^n)$.

- Actualisation des vitesses :

  $$\forall k = 1, ..., M_n,\ \forall i \in C_k^n, \quad V_i^n = \frac{\sum_{j \in C_k^n} V_j^{n-1}}{\operatorname{card}(C_k^n)},$$

  où $C_1^n, ..., C_{M_n}^n$ désigne les groupements de cellules.

# Introduction(english version)

## 7 Motivations

In this Thesis, we study the mechanisms involved in the self-organization of biological systems. These complex systems are composed of numerous agents interacting at different scales and self-organizing to form and maintain complex functional structures (for instance organs). We aim at understanding which mechanisms and agents primarily drive tissue morphogenesis and homeostasis and which are secondary to this organization. The self-organization in biological systems has given rise to a large variety of studies, but is still largely unknown [2]. It is very difficult to understand which individual mechanisms lead to the appearance of organized and stable structures at the level of the tissue. This difficulty comes from the fact that the interactions are of several types (chemical, mechanical, molecular, genomics), and imply several agents and interactions at different scales. To gain insight into such problems, a natural approach is to use mathematical modeling. Indeed, the building of a biologically-relevant model enables to test several hypothesis on the emergence and/or maintain of functional structures and to explore different scenarios. A further key advantage of mathematical models is that they are developed in a general framework, therefore the same models are not specific to the system considered but can be used to study further physical or biological problems. A model will validate an hypothesis on the interactions if the structures obtained are in good agreement with the structures of real tissues. However, it is noteworthy that a mathematical model does not aim at faithfully reproduce the reality but it helps the understanding of an observed phenomenon. Moreover, the biological reality may be difficult to access/measure, making the model difficult to compare with biological data. Therefore, the building of mathematical models often requires further biological experiments, segmentation and image processing methods, analysis of the experimental data etc. The confrontation between the model and the experimental results is delicate because of two main reasons. First, the experimental results may vary from one experience to another and therefore measurements are subject to random fluctuations. Secondly, we have a limited number of experiments while a model requires many parameters.

In our study, we consider the biological tissue as a spatially organized ecological system engaging a reduced number of agents and interactions. We take the example of the adipose tissue which is the principal energy store of the organism and plays a key role in energy and weight regulation.

# 8 The Adipose Tissue

There exist two types of Adipose Tissues which play distinct and complementary roles: the white (WAT) and brown (BAT). The WAT is principally composed of white adipocytes which store the extra energy of the organism. It represents the largest energy store of the organisms. On the contrary, the BAT is made of brown adipocytes because of a denser irrigation compared to the WAT. It is specialized into adaptive thermogenesis: its main function is to transfer energy from food into heat. In our study, we investigate the WAT. It is composed of mature adipocytes (lipid droplets), preadipocytes (their precursors), and a stroma vascular fraction containing blood cells, endothelial cells and macrophages. Figure 6 shows a part of a sub cutaneous mature adipose tissue extracted from a healthy mouse (experiments in the StromaLab). Then, the whole mouse inguinal adipose tissue is fixed, embeded in agarose and cut into slices. The slices are treated by a CD34-BODIPY lipophilic bright red fluorescent dye (work of specialists from ITAV). In Fig. 6, adipocytes appear in red, stem cells in green and the extra cellular matrix (ECM) in blue. This image shows that the mature state of adipose tissues consist of adipocytes grouped into clusters of specific forms, referred to as lobules, surrounded by an aligned and organized fiber network.

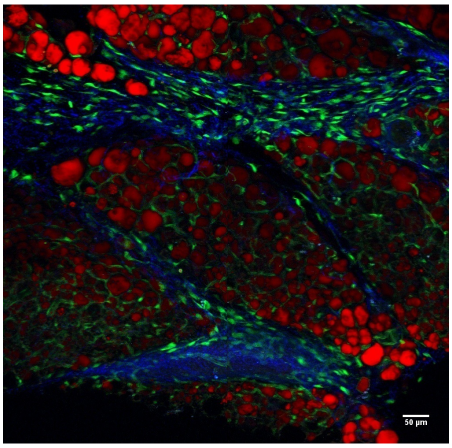

Figure 6: 2D Image of a subcutaneous mature adipose tissue extracted from a healthy mouse. CD34-Bodipy-Second harmonics / visualization IMARIS.

The metabolism is an important factor in adipogenesis by determining and influencing the physiological status and the fates of precursor cells. In this context, vascularization supplies nutrients and oxygen. Innervation controls immature cells and regeneration processes. By draining metabolites such as $CO_2$, blood supply also participates into the formation of niches, gradients, and cell activity. On the other hand, the ECM and ECM regenerating cells (myofibroblasts) play a key role in tissue homeostasis: they create mechanical constraints, serve as attachment points for cells and contribute to cell migration by giving directionality to cell motion. Another key determinant in adipose tissues are the stem cells (or undifferentiated cells), which have the ability to become functional entities of the tisse (adipocytes).

All together, these chemical, biological and mechanical phenomena play different combined roles in the emergence of functional structures and in the homeostasis of the tissue. Taking all of them into account would lead to models with overall complexity and difficult to interpret. Our work here provides, in the case of adipose tissue, simplified models engaging a reduced number of agents and interactions.

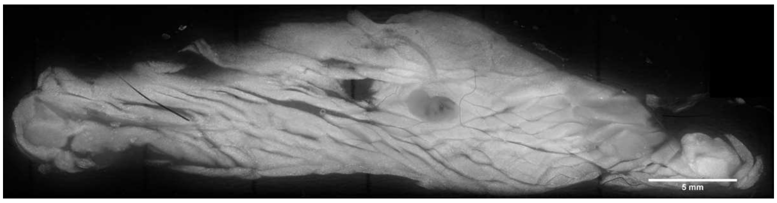

Figure 7: 2D Image of a whole mouse inguinal adipose tissue.

Finally, as shown by Fig. 7 (large portion of adipose tissue), it is noteworthy that the organizational level into lobules varies from high to low according to the position in the adipose tissue. It reveals well-organized lobular structures in its upper part and more disordered structures in its lower part. We are thus led to develop models at different scales: (i) a microscopic scale where we want to understand the organization of cells within an extra cellular matrix, and (ii) a larger scale to adress the question of the organization of the whole tissue.

# 9 Models

As previously explained, we need to consider the biological tissue at different scales: at the scale of the agents and at the scale of the whole tissue. To study the system at the scale of the agents, we developed an Individual Based model which enabled us to describe each agent and interaction. To obtain a description at a larger scale and describe more global structures, we then needed to develop a macroscopic model.

## 9.1 Individual Based Model

Most of the models used to adress a biological question are Individual Based Models (IBM), or 'microscopic models'. The main advantage of such models lies in the fact that they enable the description of each agent and interaction through the use of variables such as their positions, speed, form... These models allow to precisely describe the different interactions thanks to functionals defined from heuristic rules deduced from the real system. They indeed describe the time evolution of these variables, either at continuous or discrete times. In dynamical systems, the agents can either be self-propelled or be subjected to external forces driving their motion. In this second case, equation of motions can be deducted from physical laws such as the principle of dynamics or the minimization of an energy for instance.

Several IBM have been proposed to understand the self-organization of biological systems. Here, we give an overview of the models that can be found in the literature.

The study of biological systems that involve emergence of both cell and fiber structures has given rise to a wild variety of models. In such systems, interactions can be of three types : (i) cell/cell, (ii) cell/fiber and (iii) fiber/fiber. Models focusing on interactions of type (i) such as [4] are developed to understand the emergence of cell structures such as tumors. They often suppose that cell motion is free from cell/Extra Cellular Matrix (ECM) interactions, or consider the action of the ECM on cell motion via external forces. Recently, it has been biologically demonstrated in [5] that cell motion is highly dependent on the medium and can involve complex chemical processes. Thus, many authors have developed models incorporating interactions of type (ii). The mathematical literature on this subject can be partitioned into three main viewpoints: (a) mechanical models like in [8], where cells exert a tension on the ECM (and inversely), (b) chemotaxis-type models ( [7, 9] ), where cell motion is driven by chemical gradients or (c) transport models ([9, 10, 12, 13]) where the ECM gives directional information for cell motion (contact guidance [13]).

Recently, authors like in [14, 15] have been focusing on the properties of biological fibrous networks, i.e interactions of type (iii) mainly driven by fiber/fiber interactions. Different approaches are usually employed to model fiber structures: the first idea is to create a time discrete model for fibers and cross links (see for instance [16, 18, 19]). Models like [20] treat the fiber network as a viscoelastic material while others consider it as a porous medium [21], a two-phase viscous fluid [12], or an active gel [22]. In [14], the authors present a particle-interaction model for biological networks where fibers are seen as particles and the cross-links as means of interactions.

## 9.2 Macroscopic models

Because IBM's describe the motion of each agent and interaction, they quickly become computationally challenging. For systems involving several million of individuals, it is more efficient to look for continuum models, and model the mass of agents as a whole. Macroscopic models describe the evolution of this mass and keep a computational cost independent of the size of the system [31, 28]. Macroscopic models also have the advantage to be theoretically analysed. A mathematical framework is available in which we can predict and demonstrate the behaviour of solutions to the model. For IBM's, few theoretical results are available and a majority of the works are empirical. However, macroscopic models lose information at the individual scale. In order to keep at best the description at the microscopic scale, it is important to rigourously link both models, i.e derive a macroscopic model from an IBM. The passage from one to the other is performed through a change of scale in space and time [33]. The macroscopic model then describes the dynamics of the microscopic model on large time and space distances. If the macroscopic model is derived from a microscopic one, it is then closely linked to a microscopic dynamics that can be experimentally measured. Rigorously establishing macroscopic models from their microscopic counterpart is the central task of kinetic theory [32, 32, 34, 35]. However, some of the classical techniques fail due to the specific nature of the agent's interactions in complex systems, specifically: (i) the lack of conservation relations, (ii) the appearance of multiple equilibria and symmetry-breaking phase transitions, (iii) the breakdown of propagation of chaos due to the appearance of correlations. A theory of Generalized Collision Invariants (GCI) have been recently developed [29, 30, 23, 37] which enables to obtain a macroscopic limit even for systems with a reduced number of conservation properties.

# 10 Overview of the project

In this thesis, we wanted to understand the main mechanisms involved in the self-organization of adipose tissues. To this aim, we followed the methodology represented in the diagram of Figure 8. In close collaboration with a team of biologists and of image specialists, we first built an individual based model thanks to heuristic rules coming from the biological reality (chap I). The goal of this model was to show that the self-organization of cells and fibers into lobule-like structures of cells in an organized fiber network was mainly driven by mechanical rules and could be reproduced by a simple model engaging few agents and interactions.

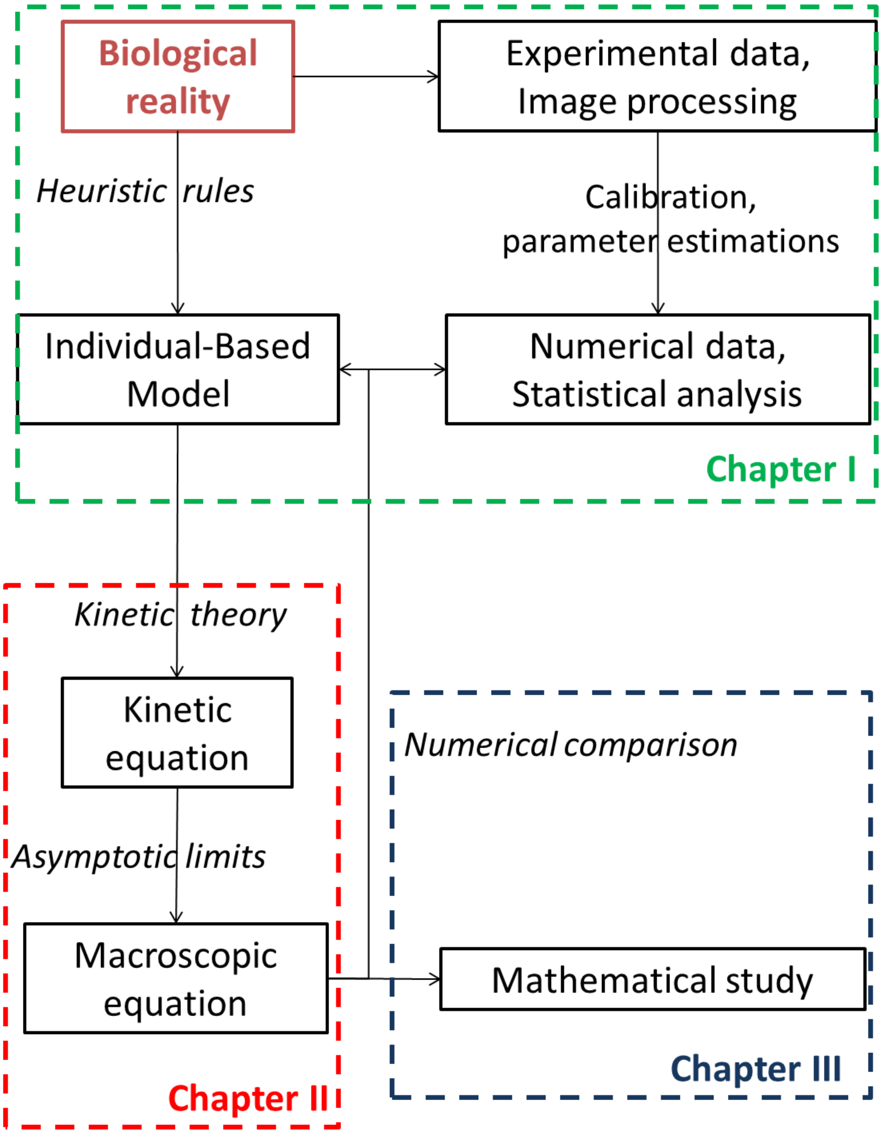

Figure 8: A diagram of the use of mathematical modeling to answer a biological question. Based on heuristic rules coming from the biology, an individual based model is developed. A statistical analysis of the numerical structures obtained with the microscopic model together with a treatment of the experimental data allow a calibration and estimation of the model parameters for the microscopic model. A first validation of the IBM appears from the comparison model/experimental data. By the use of kinetic theory, a kinetic model linked to the microscopic dynamics is developed, and its asymptotic limit leads to the derivation of a macroscopic equation, which can be analysed theoretically and numerically compared to its microscopic corresponding model.

The individual based model we proposed for adipose tissue morphogenesis was qualitatively and quantitatively compared to experimental data as a validation, and showed good agreement with the observations of real tissues. The confrontation of the model results to the experiments was in the frame of an interdisciplinary network with biologists, image processing specialists and computer scientists.

In order to model the tissue at a larger scale, we aimed to derive meso and macroscopic models from the IBM of chapter I using techniques of kinetic theory. We first concentrate on the fibrous network and aim at obtaining a macroscopic model for fiber elements having the ability to cross-link or unlink each other and to align with each other at the cross links. In order to capture the correct effects of the microscopic dynamics on the large-scale structures, we aimed at linking the macroscopic model to its microscopic version as rigorously as possible. This is the aim of Chapter II, where we first derive a kinetic model from the underlying IBM and secondly, we perform a diffusion approximation of the latter to obtain the continuum model. The kinetic model provides a statistical mechanics description of the underlying IBM by investigating how the probability distribution of fibers in position and orientation space evolves in time. We obtain a close system of two equations describing the evolution of two distribution functions: the fiber distribution function and the cross-link distribution function. We then consider the fast linking/unlinking regime in which the model can be reduced to the fiber distribution function only and investigate its diffusion limit.

As the derivation of the macroscopic model is only formal, the correspondence between the obtained model and the underlying IBM needs to be confirmed by numerical simulations and mathematical proofs. This is the aim of Chapter III, where we perform a first study of the macroscopic model. In this chapter, we first show existence of stationary solutions to the macroscopic equation for fiber mean orientation, in the case of a homogeneous fiber density. We then numerically study the properties of the solutions, and show that the macroscopic model features a buckling phenomenon depending on the external force applied to the fibrous network and in a range of model parameters. This observation highlights physical properties of the fiber network featured by the macroscopic equation. As a first validation of the macroscopic model, we then compare numerically its solutions to the ones of its underlying IBM. In a range of parameters, we are able to show a good correspondence between the two models.

Chapter IV and V are beyond the scope of adipose tissues. Chapter IV is the result of a collaborative work with S. Motsch, where we are interested in understanding how density constraints impact the propagation properties of a growing mass of cells. Cell-cell non overlapping constraints are ubiquitous in models for collective behaviors and, of particular interest, in modeling of tumor growth. It consists of considering that only a finite number of individuals/agents can occupy a given space. This can be used for modeling incompressible fluids for instance. We first propose an agent-based model for cells -represented as 2D spheres- randomly moving and interacting through non overlapping interactions. The introduction of cell division and cell apoptosis in this model leads to special solutions such as propagation waves at the microscopic level. We then derive a macroscopic model from the underlying IBM, and show that if the particle dynamics features compact supported solutions, the macroscopic density keeps spreading. We therefore propose a modified version of teh macroscopic model that we are able to link to the microscopic dynamics. We finally show that the two models are in good agreement.

Finally, chapter V is devoted to the extensions of our works. In a first part, we present the works (in progress) of B. Aymar and P. Degond for modeling the vasculogenesis. In the proposed model, four actors are considered: the capillaries, the blood flow, the oxygen and the tissue. In this model, we aim to build a hybrid model, in which the blood flow and oxygen are described by macroscopic variables (flow and density respectively), and the capillary network as a set of discrete elementary capillaries. The connection with our works lies in the way of modeling the capillaries, which bear analogies with the modeling of the fiber network in the model of chapter I. The second model is a work in progress with M. Ferreira, S. Motsch and P. Degond and aims at modeling ballistic aggregation. The underlying idea of this work, common with our works on adipose tissue, consists in saying that complex geometrical structures can be modeled by means of connected elementary units of simple geometry: 2D spheres for instance. As a starting point of this work, we aim to develop a model for self-propelled 2D spheres that connect and remain together when they collide. We then study the type of geometrical structures that can be obtained at equilibrium with such a recruitment process.

# 11 Contributions of the work

## 11.1 On the microscopic model for Adipose Tissue

The model we developed on adipose tissue morphogenesis is the fruit of a close collaboration with a team of biologists from the StromaLab and a team of image specialists from the Institute of Advanced Technologies of Toulouse. We first built a biologically relevant individual based model describing the self-organization of cells and extra cellular matrix fiber elements. The originality of our work lies in the hypothesis that this self-organization can be reproduced by only considering simple mechanical interactions between a reduced number of agents. We conducted an in-depth quantitative analysis of the experimental and numerical data to test several hypothesis on the emergence of lobule-like structures of cells in the adipose tissue. Thanks to an image processing method we developed for the biological images and appropriate quantitative descriptors of the fiber and cell structures, we show a good correspondence between the biological and numerical structures. This model shows that the self-organization of agents of adipose tissues can be the result of simple mechanical interactions involving a reduced number of agents and biological phenomena.

On a biological viewpoint, this work is the first attempt to understand the emergence of the lobular structure of the adipose tissue by interfacing a mathematical model and experimental results. It suggested that, surprisingly, the appearance of lobule-like structures of cells could be anterior to vasculogenesis in adipose tissue morphogenesis.

On a mathematical viewpoint, this work shows that complex geometrical structures such as fiber networks can be modeled as sets of connected elementary units, which connections are seen as constraints through the use of functionals. This novelty has been used to build other types of models, such as (i) a model for epithelial tissue formation, in which the complex geometry of epithelial cells is described by a set of connected spheres (work in progress), and (ii) a model for self-organization of vascularization from a porous media flow, where the vascular network is modeled as a set of elementary connected segments (work in progress). These works are presented in Chap V.

## 11.2 On the derivation of a macroscopic model for a complex fiber network

The second part of this work consists in the derivation of a continuous model from the IBM proposed in the first part. The challenge is to obtain a macroscopic description of a complex fiber network composed of a huge number of individual fibers which can link/unlink together and interact through local interactions. We successfully derive a system of two kinetic equations: one for the evolution of the individual fiber distribution function (which is linked to the probability of finding a fiber around a given point of the domain) and the second for the two particle distribution function (linked to the probability of finding a pair of fibers linked in a given configuration). Without any supplementary hypothesis, we obtained a closed problem for these two distribution functions. Thanks to newly developed generalized collision invariant technique because of the lack of conservation equation (see [23]), we were able to formally obtain the large scale limit in space and time in a regime of fast linking/unlinking of fibers. Under this regime, we obtain a system of two equations: a classical continuity equation for the fiber density and a non linear equation for the fiber mean orientation. For the obtained macroscopic model, analytical studies remain open. We thus focus on the numerical simulation of the macroscopic model and we show a good correspondence between the simulations of the macroscopic model and the microscopic one.

## 11.3 Macroscopic model for linked fibers with alignment interactions: existence theory and numerical simulations

In this chapter, we aimed to provide a first theoretical and numerical study of the macroscopic model of chapter II. We first performed an analytic and numerical study of the macroscopic equation in the case of a homogeneous fiber density. Under some regularity assumptions for the external fiber rotation potential, we were able to prove existence of solutions to the equation for the fiber mean local orientations. Numerical simulations of the macroscopic model had interesting features such as the appearance of a buckling phenomenon which highlights the physical properties of the macroscopic fiber network.

We then performed a first numerical comparison between the macroscopic model and the underlying IBM. We showed that the distribution of fiber mean local orientation of the microscopic model were in good agreement with the predictions of the macroscopic model. In particular, we were able to estimate numerically the order parameter in the individual based model. However, because of the computational cost of the particle simulations, the simulations of the microscopic model were still far from the kinetic regime with the numerical parameters of the microscopic model. This led to a poor quantitative correspondence between the microscopic and macroscopic values of the order parameter. However, we showed that an adapted regime of the macroscopic model enabled the comparison between the profiles of the solutions.

### 11.4 On the study of the influence of density constraints in a model for tumor growth

In order to understand the role of cell-cell non overlapping interactions in the propagation properties of a growing mass of cells, we introduced the cell dynamics used to build the model of Chap I in a model for tumor growth (Chap. IV). The microscopic dynamics showed interesting features such as traveling wave solutions that were not predicted by the derived macroscopic model. This was due to the fact Dirac masses are unstable for the macroscopic equation. We proposed a modified version of the macroscopic model which took into account congestion features for the cell density and we were able to show a good correspondence between the macroscopic model and the individual based model.

## 12 Results

### 12.1 Chap. I: Individual Based model for adipose tissues

In this chapter, we introduce a model for adipose tissue morphogenesis. The experiments show that at homeostasis, adipose tissues are composed of adipocytes grouped into lobule-like structures surrounded by an aligned fiber network [1]. We build an IBM starting from these observations. We consider that the principal agents involved in this self-organization are the adipocytes - reprensented as 2D spheres that cannot overlap- and the fibers - modeled as sets of interconnected segments of fixed length-. We introduce the following set of heuristic rules: (i) cells and fibers are supposed to interact through a mechanical repulsion potential $W_{pot}$. (ii) linked fibers are supposed to be subjected to a potential torque at their junction which forces them to align. The action of the torque is modeled as an energy $W_{align}$. We introduce the following biological features: (a) The connections between fiber pairs are supposed to be dynamical in time, i.e the linking and unlinking of fibers are supposed to follow Poisson processes of chosen frequencies. (b) Stem cell differentiation is modeled through the appearance of new cells in the domain, either random in space or biased by the local density of existing cells. This process is supposed to be random in time. (c) Cell apoptosis is neglected and we only consider fat storage by a regular volumic growth of cells.

The underlying physical principle in our model consists in considering that at each time, the system is at mechanical equilibrium, *i.e* cell and fiber positions and fiber orientation angles solve:

$$(X, Y, \theta) = \underset{X_1 \, |\Phi(X_1)\leq 0, (Y_1,\theta_1) \, | \, \Psi(Y_1,\theta_1)=0}{\operatorname{argmin}} W(X_1, Y_1, \theta_1) \quad , \tag{12.18}$$

where $(X, Y, \theta)$ is the set of the position vectors $X = \{X_i \in \mathbb{R}^2 \;\; 1 \leq i \leq N\}$ of the

$N$ cells, the position vectors $Y = \{Y_f \in \mathbb{R}^2 \;\; 1 \leq f \leq N_f\}$ of the $N_f$ fiber centers, and the fiber orientation angles $\theta = \{\theta_f \in [-\frac{\pi}{2}, \frac{\pi}{2}) \;\; 1 \leq f \leq N_f\}$ of the $N_f$ fibers. The total free energy $W(X, Y, \theta)$ of the system includes both mechanical energy functions associated to (i) and (ii) and reads:

$$W(X, Y, \theta) = W_{pot}(X, Y, \theta) + W_{align}(Y, \theta). \tag{12.19}$$

Finally, $\Phi(X)$ and $\Psi(Y, \theta)$ are the vectors of the cell-cell non overlapping inequality constraints and equality constraint for the maintain of fiber links respectively: $\Phi(X) = \{\Phi_{ij}(X) \;,\; 1 \leq i < j \leq N\}$, where $\Phi_{ij}$ a functional such that $\Phi_{ij}(X) > 0$ if cells $i$ and $j$ are overlapping. For fiber links, $\Psi(Y, \theta) = \{\vec{V}_{i(k)j(k)}(Y, \theta) \;,\; 1 \leq k \leq K\}$, where $K$ is the total number of fiber links and $\vec{V}_{i(k)j(k)}$ is the vector joining the joint positions on fibers of the linked pair $(i(k), j(k))$ associated to link $k$ (note that this vector must remain 0 to model the maintain of fiber links, see Fig. 9).

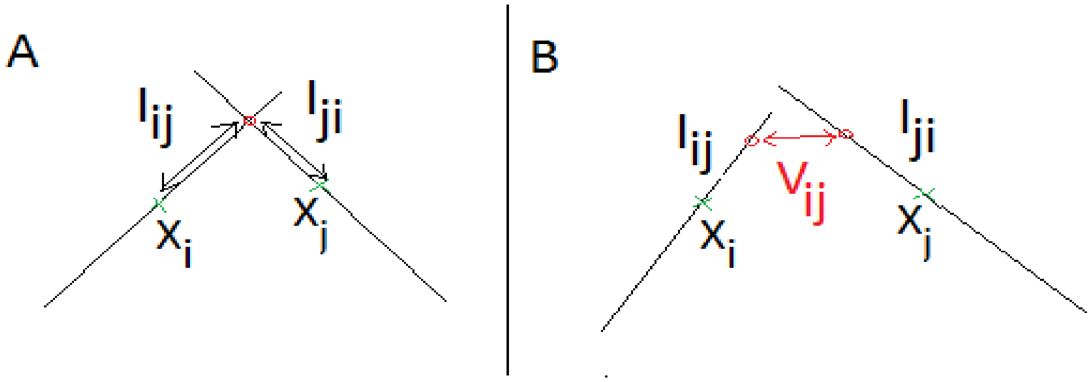

Figure 9: Intersecting linked fibers. A. Situation at linking time. B. Restoring potential $V_{ij}$ after motion of the fibers.

The Lagrangian $\mathcal{L}(X, Y, \theta, \lambda, \mu)$ of the system depends upon cell and fiber positions, fiber orientation angles $\theta$ and Lagrangian multipliers $\lambda$ and $\mu$ associated to the inequality constraints of cell-cell no overlapping and to the equality constraints of maintain of fiber links respectively. Its expression then reads:

$$\mathcal{L}(X, Y, \theta, \lambda, \mu) = W(X, Y, \theta) + <\lambda, \Phi> + <\mu, \Psi>,$$

where $< . >$ denotes the scalar product. The minimization problem (12.18) is then solved at each discrete time using an Uzawa algorithm.

The evolution of the system between discrete times $t^n$ and $t^{n+1} = t^n + \Delta t$ reads:

1. Cell growth: for all $i \in [1, N]$:
   $R_i^3(t^{n+1/2}) = R_i^3(t^n) + K_g(1 + \eta\rho_g)$
   where $\eta$ a random number and $K_g, \rho_g$ two model parameters.
2. Creation of new cells: Poisson process of frequency $\nu_e$ in time.
   Probability of inseminating at point $X$:
   $\mathcal{P}(X, R) = \chi^\alpha$,
   where $\chi$ is the local cell density, $\alpha$ a model parameter
3. Fiber linking/unlinking: creation and removal of fiber cross-links
   with Poisson processes of frequencies $\nu_f$ and $\nu_d$
4. Cell and fiber motion:
   For initial configuration $(X^{n+1/2}, Y^{n+1/2}, \theta^{n+1/2})$
   find $(X^{n+1}, Y^{n+1}, \theta^{n+1})$ such that
   $$(X^{n+1}, Y^{n+1}, \theta^{n+1}) = \underset{X_1 \,|\Phi(X_1)\leq 0, (Y_1,\theta_1)\,|\,\Psi(Y_1,\theta_1)=0}{\operatorname{argmin}} W(X_1, Y_1, \theta_1) \quad .$$

We then define a set of statistical quantifiers to describe the cell and fiber structures obtained at equilibrium. To this aim, a cell cluster is defined as a set of cells almost in contact and we compute the total number of cell clusters, their averaged elongation and the standard deviation of their shape anisotropy direction. Fiber clusters are defined as sets of neighboring quasi-aligned fibers, and we measure the number of fiber clusters, their elongation and their mean alignment. We then perform a statistical analysis by averaging the values of these quantifiers over numerous simulations and represent them as functions of the model parameters.

In order to compare the numerical simulations with the experimental data, we developed segmentation techniques on the biological images for (a) cell detection and (b) cell cluster detection. Adipocytes and lobules only were visualized in biological images at hand, therefore the statistical quantifiers for the cell structures only were accessible from biological images.

## 12.2 Chap. II: Macroscopic model for fibers interacting through alignment interactions

In this chapter, we are interested in the large-scale dynamics of one part of the microscopic model of chapter I. To simplify the model, we focus on the modeling of the fiber network only. The presence of the cells in the medium is reduced to an external potential $W_{ext}(Y,\theta)$ which depends on fiber positions and orientation angles. We are thus interested in the properties of a fiber network composed of fiber elements of fixed length which have the ability to connect together, disconnect, and are subjected to mechanical interactions. We also incorporate random fiber motion which may occur in association with the movements of the tissue through the use of an entropy term $W_{noise}(Y,\theta)$. Note that the derivation of macroscopic equations needs a continuous description of the agent's motion and that the minimization procedure (12.18) is discrete in time in the microscopic model. Therefore, we consider a gradient descent for a quadratic penalization of the minimization problem (12.18). To this aim, the functional $\Psi(Y,\theta)$ for the equality constraints of maintain of fiber links is incorporated in the total free-energy of the system such that:

$$W(Y,\theta) = W_{ext}(Y,\theta) + W_{align}(Y,\theta) + W_{noise}(Y,\theta) + \frac{\kappa}{2}|\Psi(Y,\theta)|^2,$$

where $\kappa$ is the penalization factor. Fiber motion and rotation is then supposed to be in the steepest descent of the gradient of this energy:

$$\frac{dY}{dt} = -\mu\nabla_X\Big(W_{ext} + W_{align} + W_{links} + W_{noise}\Big) \tag{12.20}$$

$$\frac{d\theta}{dt} = -\lambda\partial_\theta\Big(W_{ext} + W_{align} + W_{links} + W_{noise}\Big). \tag{12.21}$$

where $\mu$ and $\lambda$ are mobility coefficients.

To derive a macroscopic model from this microscopic model, we use the kinetic equation associated with this particle dynamics. To this aim, we define the one-particle distribution function $f(x,\theta)$ describing the $N$ individual fibers, and the two particle distribution function $g(x_1,\theta_1,\ell_1,x_2,\theta_2,\ell_2)$ describing the $K$ fiber links:

$$\begin{aligned} f^N(x,\theta,t) =& \frac{1}{N}\sum_{i=1}^{N}\delta_{(X_i(t),\theta_i(t))}(x,\theta), \\ g^K(x_1,\theta_1,\ell_1,x_2,\theta_2,\ell_2,t) =& \frac{1}{2K}\sum_{k=1}^{K}\delta_{(X_{i(k)},\theta_{i(k)},\ell^k_{i(k)},X_{j(k)},\theta_{j(k)},\ell^k_{j(k)})}(x_1,\theta_1,\ell_1,x_2,\theta_2,\ell_2) \\ &+ \delta_{(X_{j(k)},\theta_{j(k)},\ell^k_{j(k)},X_{i(k)},\theta_{i(k)},\ell^k_{i(k)})}(x_1,\theta_1,\ell_1,x_2,\theta_2,\ell_2), \end{aligned}$$

where $\delta_x(y)$ denotes the dirac function at $x$, i.e the distribution acting on test functions $\phi(y)$ such that $<\delta_x(y),\phi(y)>=\phi(x)$. By a simple closure relation, we successfully obtain the formal limit of a large number of individual fibers and links and prove the following theorem:

**Theorem 12.1.** *The formal limit of Eqs.* (12.20), (12.21) *for* $K, N \to \infty$, $\frac{K}{N} \to \xi$, *where* $\xi > 0$ *is a fixed parameter reads:*

$$\frac{df}{dt} - \mu\Big(\nabla_x.((\nabla_x U)f) + \xi\nabla_x.F_1 + d\Delta_x f\Big) - \lambda\Big(\partial_\theta((\partial_\theta U)f) + \xi\partial_\theta F_2 + d\partial_\theta^2 f\Big) = 0, \tag{12.22}$$

*and*

$$\begin{aligned}\frac{dg}{dt} - \mu\Bigg[&\nabla_{x_1}.\Big(g\nabla_x U(x_1,\theta_1) + \xi\frac{g}{f(x_1,\theta_1)}F_1(x_1,\theta_1) + d\frac{g}{f(x_1,\theta_1)}\nabla_x f(x_1,\theta_1)\Big)\\ &+ \nabla_{x_2}.\Big(g\nabla_x U(x_2,\theta_2) + \xi\frac{g}{f(x_2,\theta_2)}F_1(x_2,\theta_2) + d\frac{g}{f(x_2,\theta_2)}\nabla_x f(x_2,\theta_2))\Big)\Bigg]\\ -\lambda\Bigg[&\partial_{\theta_1}\Big(g\partial_\theta U(x_1,\theta_1) + \xi\frac{g}{f(x_1,\theta_1)}F_2(x_1,\theta_1) + d\frac{g}{f(x_1,\theta_1)}\partial_\theta f(x_1,\theta_1)\Big)\\ &+ \partial_{\theta_2}\Big(g\partial_\theta U(x_2,\theta_2) + \xi\frac{g}{f(x_2,\theta_2)}F_2(x_2,\theta_2) + d\frac{g}{f(x_2,\theta_2)}\partial_\theta f(x_2,\theta_2)\Big)\Bigg] = S(g),\end{aligned} \tag{12.23}$$

*where*

$$\begin{aligned}F_1(x_1,\theta_1) &= \int (g\nabla_{x_1}V)(x_1,\theta_1,\ell_1,x_2,\theta_2,\ell_2)d\ell_1 d\ell_2\frac{d\theta_2}{\pi}dx_2,\\ F_2(x_1,\theta_1) &= \int \Big(g(\partial_{\theta_1}V + \partial_{\theta_1}b)\Big)(x_1,\theta_1,\ell_1,x_2,\theta_2,\ell_2)d\ell_1 d\ell_2\frac{d\theta_2}{\pi}dx_2.\end{aligned} \tag{12.24}$$

*Here,* $S(g)$ *describes the dynamics of creation/deletion of fiber links and reads:*

$$S(g) = \nu_f f(x_1,\theta_1)f(x_2,\theta_2)\delta_{\bar\ell(x_1,\theta_1,x_2,\theta_2)}(\ell_1)\delta_{\bar\ell(x_2,\theta_2,x_1,\theta_1)}(\ell_2) - \nu_d g, \tag{12.25}$$

The main novelty of this kinetic equation is that it is a simple way of keeping track of the two-particle interactions. These pair of interactions can be seen as a way of describing a random graph of the links of the fibers. Indeed, as the links are located on the fibers, they are convected and follow the motion of the fibers. At the same time, they constrain the linked fibers to move together, so they directly impact their motion. The restoring potential generated by the maintain of the links, $V$, is expressed as non local forces $F_1$ and $F_2$ in Eqs. (12.22),(12.23). The second and fifth terms describe transport in physical and orientational spaces due to the external potential $U$, while the fourth and seventh terms are diffusion terms of amplitude $\lambda d$ or $\mu d$ which represent the random motion of the fibers. The kinetic counterpart of the alignment force between linked fibers $b$ is comprised in the force $F_2$ and only acts on the orientation of the fibers. The right hand side $S(g)$ of equation describes the Poisson processes of linking/unlinking at frequencies $\nu_f$

and $\nu_d$, respectively. The transition between the particle dynamics to the kinetic equation is only formal.

Once we have the kinetic equation Eqs. (12.22)-(12.23), we use an hydrodynamics scaling in order to derive a macroscopic model. More precisely, we introduce the new macroscopic variables:

$$\tilde{t} = \varepsilon t \quad , \quad \tilde{x} = \sqrt{\varepsilon} x,$$

and show that in a regime of fast linking/unlinking, the two-particle distribution function $g^\varepsilon$ can be written as a product of two one particle distributions $f^\varepsilon$:

$$g^\varepsilon(x_1,\theta_1,\ell_1,x_2,\theta_2,\ell_2) = \frac{\nu_f}{\nu_d} f^\varepsilon(x_1,\theta_1) f^\varepsilon(x_2,\theta_2)\delta_{\bar{\ell}(x_1,\theta_1,x_2,\theta_2)}(\ell_1)\delta_{\bar{\ell}(x_2,\theta_2,x_1,\theta_1)}(\ell_2)+O(\varepsilon^2).$$

This closure relation simplifies system (12.22) and we are able to obtain the large scale limit $\varepsilon \to 0$. We show that the equilibrium solutions of the kinetic equation obtained are of form

$$f(x,\theta) = \rho(x) M_{\theta_0(x)}(\theta), \quad M_{\theta_0(x)}(\theta) = \frac{1}{Z} e^{-r\cos 2(\theta-\theta_0(x))}$$

where $r$ is a model parameter, $Z$ a normalization function such that $f$ is a density distribution, $\rho(x)$ is the local density of fibers and $\theta_0(x)$ their local orientation angle. By the use of the concept of generalized collision invariant ([23]), we obtain the macroscopic limit of our kinetic equation. When $\varepsilon$ goes to 0, we obtain a system of two equations, one for the fiber density $\rho$:

$$\partial_t\rho - \nabla_x.(\nabla_x U^0 \rho) - d\Delta_x\rho = 0, \tag{12.26}$$

where we have supposed $U(x,\theta) = U^0(x)+U^1(\theta)$, where $U^0$ is the external potential acting on the fiber positions and $U^1(\theta)$ acting on fiber orientations. The evolution equation for the fiber mean direction angle $\theta_0(x)$ reads:

$$\begin{aligned}\rho\partial_t\theta_0 - \rho\nabla_x U^0.\nabla_x\theta_0 - 2\alpha_2\nabla_x\rho.\nabla_x\theta_0 - \alpha_2\rho\Delta_x\theta_0 \\ +\alpha_3(\rho\nabla_x^2\theta_0 + \nabla_x\theta_0\otimes\nabla_x\rho + \nabla_x\rho\otimes\nabla_x\theta_0) : [\omega_0\otimes\omega_0 - \omega_0^\perp\otimes\omega_0^\perp] \\ + \Big(2\rho\alpha_3\nabla_x\theta_0\otimes\nabla_x\theta_0 - \alpha_4\nabla_x^2\rho\Big) : [\omega_0\otimes\omega_0^\perp + \omega_0^\perp\otimes\omega_0] + \alpha_5\rho < \partial_\theta U^1 >= 0,\end{aligned} \tag{12.27}$$

where $\omega_0 = (\cos\theta_0, \sin\theta_0)$ denotes the 2D directional vector of norm 1 associated to the angle $\theta_0$, $\omega_0^\perp$ denotes its orthogonal vector and $< h >= \int_{-\pi/2}^{\pi/2} h(\theta) M_{\theta_0}(\theta)\frac{d\theta}{\pi}$ for any function $h$ of $\theta \in [-\frac{\pi}{2}, \frac{\pi}{2})$. The coefficients $\alpha_1, \alpha_2, \alpha_3, \alpha_4, \alpha_5$ are fully determined by the model parameters.

## 12.3 Chap III: Macroscopic model for linked fibers with alignment interactions: existence theory and numerical simulations

In this chapter, we aim at validating numerically the macroscopic model developed in the previous chapter by comparing its solutions to the ones obtained with the microscopic model. We first aim at comparing the IBM of chap I to its modified version which serves as starting point of Chap II. We show the correspondence between the two formulations in a well chosen regime. To perform the comparison between the particle dynamics and the macroscopic model, we must better understand the macroscopic model. To simplify its analysis, we study the case of a homogeneous fiber distribution $\rho(x) = \rho_0$ for $\rho_0 > 0$ a constant, and take an interest in the stationary solutions. We show that in this case, the stationary mean local orientation of fibers $\theta_0(x)$ solves a quasi linear elliptic equation that is solvable under a structural condition for the external potential.

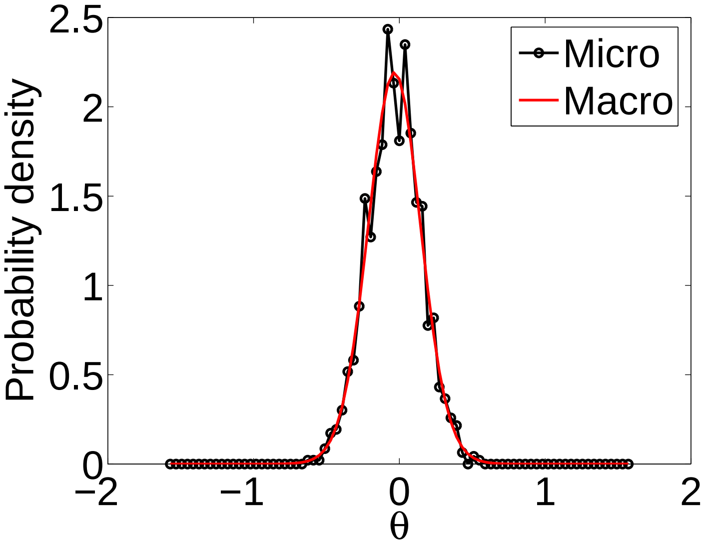

Figure 10: The distribution of fiber local mean orientation angles near the center of the domain in $x$ averaged over 20 simulations (black line), compared with its theoretical distribution (red line).

The numerical simulations of the macroscopic model show a buckling phenomenon which enables first conclusions on the physical properties of the macroscopic fiber network. Then, we aim to compare numerically the macroscopic model to the underlying IBM. We show that the distribution of fiber mean local orientation of the microscopic model are in good agreement with the predictions of the macroscopic model and we are able to compute the order parameter of the microscopic model (see Fig. 10). The computational cost of the IBM does not allow us to perform simulations of the microscopic model under the kinetic regime, which leads to different solutions for the microscopic and macroscopic models for the same set of parameters. However, we show that for each set of parameters for the microscopic model, there exist a regime in which the macroscopic model has the same features as its microscopic version.

## 12.4 Chap IV. Tumor growth model

In this chapter, we aim at understanding the role of density constraints in the propagation properties of a growing mass of cells. Cells are modeled as 2D spheres of center $X_i \in \mathbb{R}^2$ and of radius $R > 0$. In order to model short-range interactions among particles, we introduce an interaction function $\phi \geq 0$ and consider the following dynamics:

$$\frac{dx_i}{dt} = -\sum_{j=1}^{N} \phi_{ij}(x_i - x_j), \qquad \text{with } \phi_{ij} = \phi(\frac{x_i - x_j}{2R}), \tag{12.28}$$

where $i$ and $j$ are the indexes of the cells, and:

$$\phi(r) = \begin{cases} |1 - r^\alpha|, & \text{if } 0 \leq r \leq 1 \\ 0 & \text{otherwise,} \end{cases}$$

for $\alpha = 1$ or $-1$. Note that repulsion is only active when two particles are at distance smaller than $2R$.

Using classical arguments of kinetic theory, we then obtain the following kinetic model related to (12.28):

$$\partial_t \rho + \nabla_x \cdot (G[\rho]\rho) = 0, \tag{12.29}$$

with

$$G[\rho](x) = -\int_{y\in\mathbb{R}^2} \phi\left(\left|\frac{x-y}{2R}\right|^2\right)(y - x)\rho(y)\,\mathrm{d}y. \tag{12.30}$$

In the asymptotic limit $R \to 0$, we show that the model reduces to the porous media equation:

$$\partial_t \rho = \alpha_R \nabla_x \cdot \Big(\rho \nabla_x \rho\Big), \tag{12.31}$$

with

$$\alpha_R = \pi(2R)^4 \int_{r\geq 0} \phi(|r|^2) r^3 \mathrm{d}r. \tag{12.32}$$

The numerical simulations show a spreading of the particles, whereas the microscopic dynamics predicts compact-supported stationary solutions. We numerically show that the difference between the two solutions can be explained by the fact that Dirac mass are unstable solutions of the macroscopic model.

In order to obtain a better description of the microscopic model at a macroscopic scale, we propose a modified version of the interaction kernel of the kinetic model. For this purpose, we consider that the repulsion is active only when the density of particles is above a threshold $\rho_{\max}$ and we introduce the function $W[\rho]$:

$$W[\rho] = -2 \int_{|x-y|<2R} (\rho - \rho_{\max})^{+}(y-x)dy.$$

The evolution equation for the particle density $\rho$ then reads:

$$\partial_t \rho + \nabla_x \cdot (W[\rho]\rho) = 0.$$

By this mean, repulsion is only active in a disc where the density is above the threshold $\rho_{\max}$. We show that in the limit $R \to 0$, we obtain the following macroscopic equation:

$$\partial_t \rho = \beta(R) \nabla_x \cdot (\mathbf{1}_{\rho(x) \geq \rho_{\max}} \rho \nabla_x \rho),$$

where $\beta(R)$ is a coefficient depending on the size of the particles and $\mathbf{1}_{\rho(x)\geq\rho_{\max}}$ the function equals to 1 if $\rho \leq \rho_{\max}$, 0 otherwise. By this mean, we obtain a non linear diffusion equation the diffusion being active only where the cell density exceeds a given threshold. The numerical simulations show the good agreement with the solutions of this modified macroscopic model with the IBM. When adding a source term, we show analogous wave solutions featured by both models.

## 12.5 Chap V. Extensions of the works

This chapter is devoted to the extensions of our work. We present two models that are built using the concepts we developed for our individual based model presented in Chap I. These two models are preliminary works. The first one aims at modeling the self-organization of vascularization, the second one is a model for ballistic aggregation.

### 12.5.1 A model for vasculogenesis

In this section, we present the main features of a model developed with B. Amard and P. Degond for vasculogenesis. In this model, four major actors are considered: the capillaries, the blood flow, the oxygen and the tissue. The $K$ capillaries are modeled as tubes of fixed length and are described by a (two-dimensional) position vector $X_k = (x_k, y_k) \in \mathbb{R}^2$ of their center and a two-dimensional orientation vector $\omega_k = (\cos\theta_k, \sin\theta_k) \in \mathbb{S}^1$, with an orientation angle $\theta_k$ defined modulo $\pi$ to model the isotropy of the blood flow. Each capillary unit is supposed to generate an elementary porosity matrix and an elementary diffusion matrix which participate into the global porosity and diffusion properties of the medium. In order to model appearance and destruction of capillaries according to the needs of the tissue, capillary units are created and deleted with (random) Poisson processes of frequencies $\nu_c$ and $\nu_r$ depending on the gradients of the oxygen concentration.

The global porosity matrix $\mathbf{K}(X)$ of the medium computed at point $X = (x, y) \in \mathbb{R}^2$ (resp. diffusion matrix $\mathbf{D}(X)$) is then defined as the sum of all the elementary porosity matrices (resp. elementary diffusion matrices) generated by the capillary network and a porosity matrix of a homogeneous medium:

$$\begin{cases} \mathbf{K}(\mathbf{X}) = k_h \mathbf{I}_2 + \displaystyle\sum_{k\, s.t. ||\mathbf{X}_k - \mathbf{X}|| \leq R} \kappa\, (\boldsymbol{\omega}_k \otimes \boldsymbol{\omega}_k), \\ \mathbf{D}(\mathbf{X}) = d_h \mathbf{I}_2 + \displaystyle\sum_{k\, s.t. ||\mathbf{X}_k - \mathbf{X}|| \leq R} d\, (\boldsymbol{\omega}_k \otimes \boldsymbol{\omega}_k), \end{cases}$$

with $k_h$, $d_h$, $\kappa$, $d$ and $R$ real positive constants and $\mathbf{I}_2$ the identity matrix of size 2. The blood flow $\mathbf{u}$ is then supposed to be described by Darcy's law:

$$\begin{cases} \mathbf{u} = -\mathbf{K} \nabla p \\ -\mathrm{div}(\mathbf{K} \nabla p) = 0 \end{cases} \tag{12.33}$$

where $\nabla p$ denotes the blood pressure gradient vector. The oxygen is modeled by its density $\rho$. Oxygen motion is supposed to be driven by two different phenomena: (i) convection by the blood, or (ii) diffusion through the tissue. Moreover, oxygen is supposed to be consumed by the tissue. In this first work, the consumption does not depend on time neither space. These three hypothesis lead to a convection-diffusion equation with a source term:

$$\partial_t \rho + \nabla.(\rho \mathbf{u}) - \nabla.(\rho \mathbf{D} \nabla \rho) = -\beta \rho, \tag{12.34}$$

where $\beta$ is a real positive parameter modeling oxygen consumption and $\mathbf{D}$ is the diffusion matrix of the medium. The full system writes:

1. Blood flow
$$\begin{cases}\mathbf{u} = -\mathbf{K}\nabla p \\ \mathrm{div}(\mathbf{u}) = 0\end{cases}$$
2. Oxygen convection/diffusion/consumption
$$\begin{cases}\partial_t \rho + \nabla.(\rho \mathbf{u}) - \nabla.(\rho \mathbf{D} \nabla \rho) = -\beta\rho\end{cases}$$
3. Capillary network: creation and removal with Poisson 's processes of frequencies $\nu_c$ and $\nu_r$
4. Tissue (porosity matrix and diffusion matrix)
$$\begin{cases}\mathbf{K}(\mathbf{X}) = k_h \mathbf{I}_2 + \displaystyle\sum_{k\, s.t. ||\mathbf{X}_k - \mathbf{X}|| \leq R} \kappa\, (\boldsymbol{\omega}_k \otimes \boldsymbol{\omega}_k) \\ \mathbf{D}(\mathbf{X}) = d_h \mathbf{I}_2 + \displaystyle\sum_{k\, s.t. ||\mathbf{X}_k - \mathbf{X}|| \leq R} d\, (\boldsymbol{\omega}_k \otimes \boldsymbol{\omega}_k)\end{cases}$$

First numerical simulations of this model will be shown.

### 12.5.2 A model for ballistic aggregation

In this chapter, we present the works in progress with P. Degond and M. Ferreira on the modeling of epithelial tissue formation. Epithelial cells are bound together in sheets of tissue called epithelia. These sheets are held together through several types of interactions, including tight junctions, adherens, desmosomes, and gap junctions. Several types of epithelia can be found in real systems. They are defined by the shape and function of its cells. For instance, squamous cells (belonging to the squamous epithelium) have the appearance of thin, flat plates while columnar epithelial cells are elongated and column-shaped. The goal of the project is to build a mathematical model which can take into account different geometries for the cells. The idea is to model a cell as a set of connected elementary units of simple geometry such as 2D spheres.

As a starting point, a model for self-propelled particle which attach together throughout motion is being developed. In this model, cells move with a constant velocity in a given direction as long as they don't collide. When two cells collide, they link together and remain attached during motion afterwards: they keep moving together with the same velocity and in the same direction. In order to avoid cell overlapping, a minimization method is used during each collision. By this mean, the colliding cells will rearrange to be in a non overlapping configuration which minimizes their distance. The full system can be written:

- First step: free motion.
$$\forall i = 1 \dots N, \quad \hat{X}_i^n = X_i^{n-1} + \delta_t V_i^{n-1}.$$

- Second step: Readjustment by minimization
  Define, for $(X_i, X_j) \in A \times A$,

  $$\phi(X_i, X_j) = (R_i + R_j + \varepsilon \min\{R_i, R_j\})^2 - d(X_i, X_j)^2$$

  and $S$ the set of the pairs of quasi-touching spheres :

  $$S = \{(i,j) \in \{1 \dots N\} \mid \phi(X_i, X_j) \geq 0\}\,.$$

  Consider the following potential :

  $$W(X_1, ..., X_N) = \frac{1}{2} \sum_{(i,j) \in S_0} d(X_i, X_j)^2;$$

  the adjustment is then made by solving locally the minimization problem

  $$(X_1^n, ..., X_N^n) = \operatorname*{argmin}_{\phi_0(X_i, X_j) < 0,\ i,j=1,...,N} W(X_1, ..., X_N),$$

  starting with $(\hat{X}_1^n, ..., \hat{X}_N^n)$.

- Third step: Actualization of the velocity;

  $$\forall k = 1, ..., M_n,\ \forall i \in C_k^n, \quad V_i^n = \frac{\sum_{j \in C_k^n} V_j^{n-1}}{\mathrm{card}(C_k^n)},$$

  where $C_1^n, ..., C_{M_n}^n$ denote the different cell clusters.

# Bibliography

[1] Wasserman F (2011) *The development of adipose tissue.* Compr physiol Supplement 15: Handbook of Physiology, Adipose Tissue:87-100 First published in print 1965. doi:101002/cphycp050110.

[2] S. Camazine, J-L Deneubourg, N.R. Francks, J. Sneyd, G. Theraulaz, E. Bonabeau (2001) *Self-organization in Biological Systems*, Princeton University Press,Princeton, NJ

[3] P. Degond, C. Appert-Rolland, M. Moussaid, J. Pettre, G. Theraulaz (2013) *A hierarchy of heuristic-based models of crowd dynamics*, Mathematical Physics, 52:1033-1068

[4] D. Drasdo, S. Holmet, (2005) *A single cell based-model of tumor growth in-vitro: monolayers, spheroids*, Phys Biol. 2(3):133-47

[5] Friedl,P., Hegerfeldt,Y., Tusch, M.,(2004) *Collective cell migration in morphogenesis, cancer*, Int. J. Dev. Biol.,48:441-449

[6] D. Manoussaki, S. R. Lubkin, R. B. Vemon, J. D. Murray, (1996) *A mechanical model for the formation of vascular networks in vitro*, Acta Biotheoretica, 44(3-4):271-282

[7] M. Lushnikov, N. Chen,, M. Alber, (2008) *Macroscopic dynamics of biological cells interacting via chemotaxis, direct contact*, Physical Review E 78, 061904

[8] A. Tosin, D. Ambrosi, L. Preziosi (2006),*Mechanics, chemotaxis in the morphogenesis of vascular networks*, Bull. Math. Biol., 68:1819-1836

[9] , Hillen, T.,(2006)*Mesoscopic, macroscopic models for mesenchymal motion*, J. Math. Biol., 53(4):585-616

[10] A. Chauviere, T. Hillen, L. Preziosi, (2007) *Continuum model for mesenchymal motion in a fibrous network*, Networks, Heterogeneous Media, 2:333-357

[11] W. Alt, M. Dembo, (1999)*Cytoplasm dynamics, cell motion: two phase flow models*,Mathematical Biosciences, 156(1):207-228

[12] R.B. Dickinson,(2000) *A generalized transport model for biased cell migration in an anisotropic environment*,J. Math. Biol., 40:97-135

[13] S. Guido, RT Tranquillo, (1993)*Amethodology for the systematic, quantitative study of cell contact guidance in oriented collagen gels. Correlation of fibroblast orientation, gel birefringence.*, J. Cell. Sci., 105:317-331

[14] R. Alonso, J. Young, Y. Cheng, (2014) *A particle interaction model for the simulation of biological, cross-linked fibers inspired from flocking theory*, Cell. mol. bioeng., 7(1):58-72

[15] C.P. Broedersz et al,(2010)*Cross-link governed dynamics of biopolymer networks*, PRL 105, 238101

[16] J.A Astrom, P.B.S Kumar, I. Vattulaine, M. Karttunen (2005)*Strain hardening in dense actin networks*, Phy. Rev. E. 71:050901

[17] G.A. Buxton, N. Clarke, P.J. Hussey (2009)*Actin dynamics, the elasticity of cytoskeletal networks*, Express Polymer Letters, 3(9):579-587.

[18] D.A Head, A.J. Levine, F.C MacKintosh,(2003) *Distinct regimes of elastic response, deformation modes of cross-linked cytoskeletal, semiflexible polymer networks*, Phys. Rev. E. 68:061907

[19] H. Krasher, J. Lammerding, H. Huang, R.T. Lee, R.D. Kamm (2003) *A three-dimensional viscoelastic model for cell deformation with experimental verification*, Biophys. J. ,85(5):3336-49

[20] L.A. Tabler, Y. Shi, L. Yang, P.V. Bayly (2011)*A poroelastic model for cell crawling including mechanical coupling between cytoskeletal contraction, actin polymerization*, J. Mech. Mat. Struct., 6:569-589

[21] J.F. Joanny, F. Jlicher, K. Kruse, J. Prost (2007)*Hydrodynamic Theory for Multi-Component Active Polar Gels*, New J. Phys. 9 442

[22] N. Bellomo, J. Soler, (2012)*On the mathematical theory of the dynamics of swarms viewed as complex systems*, Math. Models Meth. Appl. Sci. ,22(supp 1):1140006

[23] E. Bertin, M. Droz, G. Gregoire, (2009)*Hydrodynamic equations for self-propelled particles: microscopic derivation, stability analysis*, J. Phys A: Math. Theor. 42, 445001

[24] S-Y Ha, E. Tadmor (2008) *From particle to kinetic, hydrodynamic descriptions of flocking*, Kinetic, Related Models, 1:415-435

[25] P. Degond, S. Motsch, (2008) *Continuum limit of self-driven particles with orientation interaction*, Math. Mod. Meth. App. S. 18:1193-1215

[26] P. Friedl, E.B.Brocker, (2000) *The biology of cell locomotion within three dimensional extracellular matrix*, Cell Mol. Life Sci, 51:595-615.

[27] Y. Sone, (2002) *Kinetic Theory, Fluid Dynamics*, Birkhausser,

[28] N. Bellomo. (2007) Modeling complex living systems: a kinetic theory and stochastic game approach.

[29] P. Degond, G Dimarco, T. B. N. Mac and N. Wang, *Macroscopic models of collective motion with repulsion*, Commun. Math. Sci., to appear, arxiv preprint 1404.4886.

[30] P. Degond, J-G. Liu, S. Motsch and V. Panferov, (2013)*Hydrodynamic models of self-organized dynamics: derivation and existence theory*, Methods Appl. Anal. 20 089-114.

[31] J.D. Murray. (2003) Mathematical biology.

[32] L. Edelstein-Keshet. (2005) Mathematical models in biology.

[33] P. Degond. (2004) *Macroscopic limits of the Boltzmann equation: a review.* Modeling and computational methods for kinetic equations, P. Degond, G. Russo, L. Pareschi (eds), Birkhauser

[34] F. Filbet, P. LaurenÃ§ot, and B. Perthame. (2005) *Derivation of hyperbolic models for chemosensitive movement.* Journal of Mathematical Biology, 50(2):189-207

[35] B. Perthame. (2007) Transport equations in biology.

[36] P. Degond and S. Motsch,(2008)*Continuum limit of self-driven particles with orientation interaction*, Math. Models Methods Appl. Sci. 18 Suppl. 1193-1215.

[37] A. Frouvelle, (2012)*A continuum model for alignment of self-propelled particles with anisotropy and density-dependent parameters*, Math. Models Methods Appl. Sci. 22 1250011

# Chapter 1

# Simple mechanical cues could explain adipose tissue morphology

This chapter has been written in collaboration with F. Delebecque, P. Degond, A. Lorsignol, C. Barreau, J. Rouquettes, X. Descombes and L. Casteilla. It has been submitted to the journal PloS computational Biology.

**Abstract:** The mechanisms by which organs acquire their functional structure and realize its maintenance (or homeostasis) over time are still largely unknown. In this paper, we investigate this question on adipose tissue. Adipose tissue can represent 20 to 50% of the body weight. Its investigation is key to overcome a large array of metabolic disorders that heavily strike populations worldwide. Adipose tissue consists of lobular clusters of adipocytes surrounded by an organized collagen fiber network. By supplying substrates needed for adipogenesis, vasculature was believed to induce the regroupment of adipocytes near capillary extremities. This paper shows that the emergence of these structures could be explained by simple mechanical interactions between the adipocytes and the collagen fibers. Our assumption is that the fiber network resists the pressure induced by the growing adipocytes and forces them to regroup into clusters. Reciprocally, cell clusters force the fibers to merge into a well-organized network. We validate this hypothesis by means of a two-dimensional Individual Based Model (IBM) of interacting adipocytes and extra-cellular-matrix fiber elements. The model produces structures that compare quantitatively well to the experimental observations. Our model seems to indicate that cell clusters could spontaneously emerge as a result of simple mechanical interactions between cells and fibers and surprisingly, vasculature is not directly needed for these structures to emerge.

**Acknowledgments** DP gratefully acknowledges the hospitality of Imperial College London, where part of this research was conducted. This work was partially supported by the CNRS under PEPS MATH (Modelling Adipose Tissue Homeostasis) and by the "Région Midi Pyrénées", under grant APRTCN 2013. PD acknowledges support from the British "Engineering and Physical Research Council" under grant ref: EP/M006883/1, support from the Royal Society and the Wolfson foundation through a Royal Society Wolfson Research Merit Award and from NSF by NSF Grant RNMS11-07444 (KI-Net). DP wishes to thank J. Fehrenbach (IMT, Toulouse) for enlighting discussions on image processing.

## Sommaire

**1 Significance statement . . . . . . . . . . . . . . . . . . . . 59**
**2 Introduction . . . . . . . . . . . . . . . . . . . . . . . . . 59**
**3 Results . . . . . . . . . . . . . . . . . . . . . . . . . . . . 61**
**4 Discussion . . . . . . . . . . . . . . . . . . . . . . . . . . 69**
**5 Materials . . . . . . . . . . . . . . . . . . . . . . . . . . . 71**
**6 Supporting Information . . . . . . . . . . . . . . . . . . . . 73**

# 1 Significance statement

Because of the key role of adipose tissue in the energy homeostasis and associated diseases, there is a great deal of interest in understanding the biology of this tissue. Very few is known about the key to understanding its structuration as lobules. We postulate that lobule emergence is the result of a self-organization process driven by bidirectional mechanical interactions between adipocytes and fibers. We test this hypothesis by means of a 2D individual based model of interacting adipocytes and fiber elements. Indeed, our model produces structures that compare quantitatively well to the experimental observations. This clearly shows that cell clusters of adipose tissue could spontaneously emerge as a result of simple mechanical interactions, with no direct involvement of vasculature.

# 2 Introduction

White adipose tissue (WAT) is the main energy store of the organism. It is interconnected with all physiological functions via its endocrine functions. It plays a key role in the energy homeostasis and weight of the organism. It is a highly plastic tissue composed of differentiated adipocytes that are able to store and release fatty acids as well as to secrete numerous cytokines and hormones [1]. Mature adipocytes represent only 40 to 60% of the whole cell population. The other cells form a heterogeneous population named stroma-vascular fraction (SVF). Adipocyte progenitors are present in the SVF throughout adult life [2]. They can proliferate and/or be recruited according to physiological or pathological situations, participate to the turnover of adipocytes and are also believed to be supporting cells. Because of their important role and due to the explosive worldwide development of obesity, the molecular pathways driving adipocyte differentiation are now well investigated and described [3]. In contrast, the global organization at the tissue scale is poorly understood. Since Wassermann's work in 1960 [4], very few investigations have been performed at this scale. These seminal investigations revealed that adipose tissue is constituted of distinct lobules containing clusters of adipocytes. Moreover, observing its development, Wassermann described the emergence of mature WAT from primitive structures constituted of an unstructured fiber network containing endothelial cells and fibroblast-like cells. The latter are believed to be preadipocytes. In adult adipose tissue, lobules housing adipocytes are separated from each other by well-structured separations (or septa) composed of extracellular matrix (ECM) [5]. Thereafter the number of lobular unit seems to remain approximately constant. In excessive development of adipose tissue occurring during obesity, increased fibrosis (formation of excess fibrous tissue) is observed and many reports associate these changes with adipocyte dysfunctions [6, 7]. This suggests that a proper maintenance of adipose tissue architecture is critical for its normal functionality.

Because the global architecture of adipose tissue and its organization into lobules are robust throughout adult life and seem fundamental elements of adipose tissue homeostasis, modeling the process of lobule emergence will greatly improve our understanding of adipose tissue biology and plasticity in physiological or pathological conditions. Numerous models of tissue morphogenesis can be found in the literature, describing the emergence of self-organization of cells and fibers. Due to their simplicity and flexibility, the most widely used models are Individual Based Models (IBM) (see [8], [9] and references therein). They describe the behavior of each agent (e.g. a cell or a fiber element) and its interactions with the surrounding agents over time. Due to the high computational cost of IBM, mean-field kinetic or continuous models, which are more efficient to describe the large scales, are often preferred. All these models include one or several of the following interactions: (i) cell/cell, (ii) cell-fiber and (iii) fiber-fiber interactions. Models of interacting cells moving in ECM-free media such as [10] focus on interactions of type (i). Based on the mechanisms reviewed in [34], a wide variety of models incorporating interactions of type (ii) have been proposed such as: (a) mechanical models [12], (b) chemotaxis-type models ([13, 14] and references therein), where cell motion is driven by chemical gradients or (c) models of contact guidance [15] (see

[16, 17, 18]) where the ECM gives directional information for cell motion. However, how the processes are coordinated to produce directed motion is not well understood. Fiber-fiber interactions have been explored in [19], where a model of a fibrous network composed of cross-linked fiber elements is proposed. Other authors treat the fibrous network as a continuum, such as a porous medium [20] or an active gel [21] for instance. However, the literature so far provides little clues on the mechanisms underlying contact guidance or fiber self-organization. In the present paper, we demonstrate that directionally organized cell and fiber structures can emerge without appealing to contact guidance or fiber directional interactions, as a result of simple mechanical interactions between the cells and the fiber network. Our model is of more microscopic nature than previously proposed mechanical models [12, 22] and aims at describing the emergence of the lobular structures observed in adipose tissue.

The scenario is that, due to the fiber resisting the pressure induced by the growing adipocytes, the latter are forced to regroup into clusters. Adipocyte clusters in turn force the fibers to merge into a well-organized network. To validate this scenario, we developed a two-dimensional IBM modelling adipocytes interacting with ECM fiber elements. The model and experiment data showed strikingly similar lobule-like structures and revealed that vasculature was not needed for lobular self-organization to emerge.

# 3 Results

**Experiments and image processing**. Fig. 1.11 shows part of a sub-cutaneous adipose tissue from an adult mouse. The adipocytes were visualized by immunostaining of perilipin, a protein that surrounds the unilocular lipid droplets. In Fig. 1.11A, the ECM fiber network appears in black as a background. This picture clearly reveals the organization of the adipose tissue in lobules. We implemented classical image processing methods to extract the centers and radii of the cells (Fig. 1.11B) and the different lobules (Fig. 1.11C) (see SI for details). The quality of the cell and lobule segmentation methods were carefully checked.

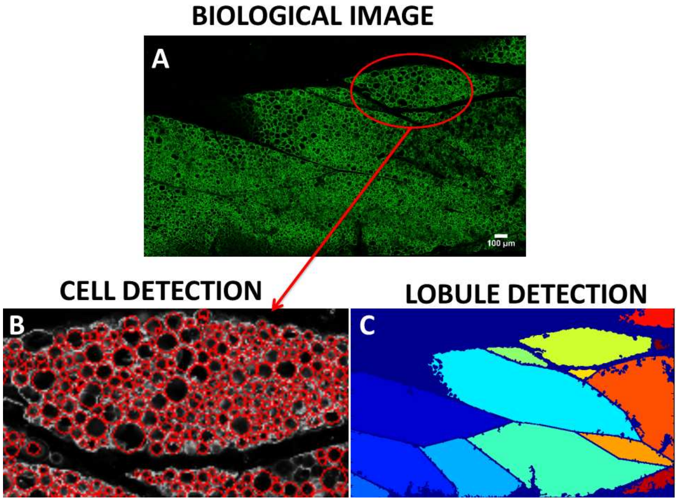

Figure 1.11: (A) 2D Image of a part of mouse sub-cutaneous adipose tissue. Lipid droplets were immunostained for perilipin (green). ECM between adipocyte clusters appears in black. (B) Magnification of the part enclosed by the red line on image (A), showing the result of cell detection. Cells appear as red circles. (C) Image (A) after lobule detection. Detected lobules have been distinguished by different colors.

**Description of the model**. We postulated that, in WAT, the agents contributing the most to mechanical balance were the fibers and the adipocytes. The fibers were modelled as straight segments of fixed and uniform length described by their centers and their directional unit vectors. The cells were represented as 2D spheres described by their centers and radii. At any given time, the two sets of agents were supposed to realize the minimum of the mechanical energy of the system (described below). We incorporated the following biological features : *(i) Pre-adipocyte differentiation:* Immature cells are much smaller than adipocytes. So, we supposed that they had negligible impact on the mechanical equilibrium and we did not incorporate them in the model. The transformation of an immature cell into an adipocyte was modelled as the creation (or “insemination”) of a new adipocyte. All new adipocytes were inseminated with the same small radius. New adipocytes were inseminated at random times following a Poisson process. The location of the insemination was also random with either uniform probability in the domain or with a bias resulting in a higher insemination probability at locations where existing adipocytes were already present. In this last case, the existing cell density in a disk of radius $R$ around the randomly chosen insemination point $X$ was computed and normalized by the maximal possible density (corresponding to adipocytes in contact with each other), resulting in a dimensionless parameter $\chi$ comprised between 0 and 1. Then, the insemination probability at $X$ was taken proportional to $\chi^{\alpha}$, with biasing parameter $\alpha > 0$. This modelled a quorum-sensing process where a pre-adipocyte sensed the adipocyte density $\chi$ up to a sensing distance $R$ and made a decision whether to differentiate into an adipocyte according to the value of the quorum-sensing parameter $\chi^{\alpha}$ (the larger $\alpha$, the larger the local adipocyte density needed to be to trigger differentiation). *(ii) Adipocyte growth:* The ability to store and release energy according to the needs of the organism was modelled through the regular growth of the cells. Therefore, thanks to (i) and (ii), we incorporated both hyperplasia (cell number increase) and hypertrophy (cell size increase). As the turnover of adipocytes is small and not related to adipose tissue morphology [23], we neglected the apoptosis of adipose cells. We assumed that the volume of each adipocyte reached a maximal value beyond which it stayed constant. *(iii) Adipocyte incompressibility and non-overlapping:* Adipocytes are reservoirs of fat, which is an incompressible liquid, and they cannot overlap. Therefore, we assumed that the radius of each disk was unaffected by whatever mechanical efforts were exerted onto it and that two neighboring disks could not overlap. *(iv) Fiber resistance to adipocyte pressure:* To model adipocyte confinement by fiber elements, we supposed that fibers and adipocytes repelled each other. For the sake of simplicity we assumed that the fiber-cell repulsion potential iso-lines were ellipses with focii at the two ends of the fiber segment and that the potential vanished beyond a certain distance from the fiber. These features modelled the anisotropy of the fiber confinement force and the fact that it is a contact force. *(v) Fiber growth and elongation:* Fiber elongation [24] was modelled by giving the possibility for fibers to attach to each other. Pairs of unlinked intersecting fibers could link to each other at random times following a Poisson process. Similarly, pairs of linked fibers could unlink at random times following a Poisson process in order to model fiber breakage due to ECM remodelling processes. The linking and unlinking frequencies were referred to as $\nu_f$ and $\nu_d$ respectively, and the parameter $\chi_\ell = \frac{\nu_f}{\nu_f + \nu_d}$, where $\chi_\ell \in [0, 1]$ represented a measure of the fraction of linked fibers among the pairs of intersecting fibers. *(vi) Fiber alignment and resistance to bending:* To model fiber resistance to bending, linked fibers were subjected to a potential torque at their junction. This torque vanished when the fibers were aligned, and consequently acted as a linked-fiber alignment mechanism. This torque was characterized by a stiffness parameter $c_1 > 0$ playing the role of a flexural modulus. The larger the $c_1$ the more rigid the fiber assembly was.

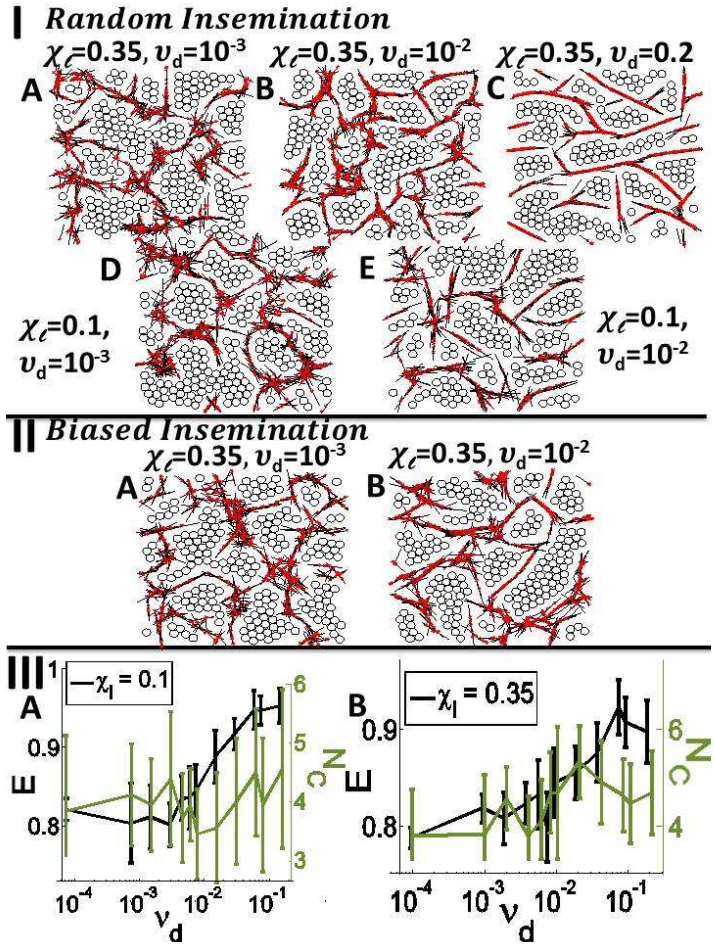

Figure 1.12: (I): Model results with random insemination and flexural modulus $c_1 = 1$. First line (Figs. (I A), (I B), (I C)): for linked fiber fraction $\chi_\ell = 0.35$. Second line (Figs. (I D), (I E)): for $\chi_\ell = 0.1$. On each line, the unlinking frequency $\nu_d$ is increasing from left to right (Figs (1 A), (1 D): $\nu_d = 10^{-3}$), (Figs (1 B), (1 E): $\nu_d = 10^{-2}$), (Figs (1 C) $\nu_d = 0.2$). As the unlinking frequency $\nu_d$ increases, cell cluster morphology changes from compactly shaped in (I A), (I B) and (I D) to elongatedly shaped in (I C), (I E), while fiber cluster morphology changes from disordered in (I A) or (I D) to long and aligned in (I C). (II): Model results with biased insemination for $\alpha = 10^{-3}$ for $\chi_\ell = 0.35$, $c_1 = 1$ and increasing values of the unlinking frequency $\nu_d$ from left to right (Fig. (II A): $\nu_d = 10^{-3}$ ; Fig. (II B): $\nu_d = 10^{-2}$). Biased insemination does not significantly lead to different morphologies compared with random insemination. (III): cell cluster number $N_C$ (in green) and mean cell cluster elongation $E$ (in black), averaged over 10 simulations and plotted as functions of the unlinking frequency $\nu_d$ for linked fiber fraction $\chi_\ell = 0.1$ (Fig. (III A)) and $\chi_\ell = 0.35$ (Fig. (III B)).The mean cell cluster elongation $E$ increases with $\nu_d$, with two plateaus for $\nu_d \leq 10^{-2}$ and $\nu_d \geq 10^{-1}$ whatever $\chi_\ell$ is. For $\chi_\ell = 0.1$, the cell cluster number $N_C$ is almost independent of $\nu_d$ while for $\chi_\ell = 0.35$, $N_C$ increases after $\nu_d \approx 10^{-3}$ and then reaches a constant value around $\nu_d \approx 0.05$.

The mechanical energy of the system included the cell-fiber interaction potentials (iv) and the linked fiber-fiber alignment potential (vi). At each time step, a minimum of this mechanical energy subject to the nonoverlapping constraint between cells (iii) and to the linkeage constraint between linked fibers (v) was sought. At the beginning of the next time step, new adipocytes were inseminated (i), adipocyte radii were increased (ii) and pairs of fibers were linked/unlinked (v). These phenomena induced disruption of the mechanical equilibrium and a minimum of this new energy was again sought, and so on. The model was implemented on a 2D square domain and boundary conditions were assumed periodic (i.e. each agent was assumed periodically repeated beyond the boundary of the square domain). The numerical simulations were initialized with a randomly distributed fiber network (according to a uniform distribution over all possible direction angles or over a sub-interval of directions angles centered about a given angle $\theta_1$ and of width $2\theta_2$). New cells were inseminated at a constant rate until reaching a cell volume fraction of 50%, a number consistent with the experimental observations.

**Influence of the model parameters**. Fig. 1.12 (I) was obtained using random adipocytes insemination. It illustrates that the linking-unlinking dynamics strongly influenced the morphology of the final structures. The first line of figures (Fig. 1.12 (I A) to (I C)) corresponds to a large fraction of linked fibers $\chi_\ell = 0.35$ and, from left to right, to an increasing unlinking frequency $\nu_d$. Larger values of $\nu_d$ allow for faster remodeling of the fiber network topology. We observed that the cell cluster morphology changed from compactly shaped (Fig. 1.12 (I A) or (I B)) to elongatedly shaped (Fig. 1.12 (I C)), while the fiber cluster morphology changed from disordered (Fig. 1.12 (I A)) to aligned (Fig. 1.12 (I B)). Finally the fibers self-organize into rigid long fiber threads (Fig. 1.12 (I C)). For a slow linking-unlinking process (Fig. 1.12 (I A)), the fiber network topology was almost frozen and this generated rigidly connected fiber structures that were too stiff to self-organize. A faster linking-unlinking process (Fig. 1.12 (I B)) allowed for the remodeling of the network topology and for the local alignment of the fibers thanks to the alignment torque generated at the links. However, for a very fast linking-unlinking dynamics (Fig. 1.12 (I C)), the aligned fiber threads were reinforced by the fast creation of links, increasing the rigidity of the network. A preferred fiber direction locally emerged and favored the growth of cell clusters in that particular direction, thereby generating elongated cell clusters. The second line of figures (Fig. 1.12 (I D) and (I E)) corresponds to a smaller fraction of linked fibers $\chi_\ell = 0.1$. In this case, the fiber network was less rigid compared to the previous case. Fiber clusters were consequently smaller, and failed to surround the cell structures, generating bigger cell clusters. Fig. 1.12 (II) was obtained using biased insemination with $\alpha = 0.001$ and the larger fraction of linked fibers $\chi_\ell = 0.35$. Again, the unlinking frequency $\nu_d$ increases from left to right. It shows that biased insemination did not have a significant influence on the final cell and fiber structures (see Supplementary Information for more details). For a well calibrated fiber linking-unlinking dynamics, the model was able to produce lobule-like structures without the need of biased insemination (see 1.12 (I)).

**Quantitative analysis**. In order to quantify cell and ECM fiber structures, we defined a set of statistical descriptors (SQ). A cell cluster was defined as a group of at least 5 adipocytes in contact with each other, and $N_C$ was the number of cell clusters per 100 adipocytes. Parameter $E$ measured the average elongation of cell clusters. It was comprised between 0 (for disk-like cell clusters) and 1 (for cord-like clusters). We verified that our conclusions did not depend on the chosen minimal size (here 5) of the cell clusters. The SQ $\Theta$ measured the standard deviation of the shape anisotropy direction of cell clusters. For this purpose, each cell cluster was best-matched to an ellipse and the cluster shape anisotropy direction was defined as the angle of the ellipse semi-major axis with a reference direction. Small values of $\Theta$ indicated a preferred shape anisotropy direction of cell-clusters. We also defined fiber cluster SQ (see SI for details)).

**Identification of different morphologies** For each set of model parameters, we computed the SQ on the obtained final structures and averaged them over 10 realizations. In Fig. 1.12 (III), we plotted the mean cluster number $N_C$ (in green) and the mean cell cluster elongation $E$ (in black) as functions of the fiber unlinking frequency $\nu_d$ for two values of the linked fiber fraction $\chi_\ell = 0.1$ (Fig. 1.12 (III A)) and $\chi_\ell = 0.35$ (Fig. 1.12 (III B)). These plots revealed an increase of the cell cluster elongation $E$ as the unlinking frequency $\nu_d$ increases, whatever value the linked fiber fraction $\chi_\ell$ took. We identified two plateaus of values of $E$: $E \approx 0.8$ for $\nu_d \leq 10^{-2}$ and $E \approx 0.95$ for $\nu_d \geq 10^{-1}$. The corresponding cell structures were compactly shaped (Fig. 1.12 (I A) (I B), (I D) or (I E)) or elongatedly shaped (Fig. 1.12 (I C)) respectively. For a value of the linked fiber fraction $\chi_\ell = 0.1$, no significant change in the mean cluster number $N_C$ arose as the unlinking frequency $\nu_d$ increased (Fig. 1.12 (III A)). By contrast, for a value of the linked fiber fraction $\chi_\ell = 0.35$, the mean cluster number $N_C$ increased with increasing unlinking frequency $\nu_d$ in the range $[10^{-3}, 0.05]$ and then stayed constant for larger values of $\nu_d$ (Fig. 1.12 (III B)). The most biologically relevant structures, composed of well-separated lobule-like cell clusters in an organized fiber network, were characterized by a low value of the mean elongation $E$ and a large value of the mean cluster number $N_C$. From Fig. 1.12 III, we realized that the best combination of parameters was a linked fiber fraction of $\chi_\ell = 0.35$ and an unlinking frequency $\nu_d \in [10^{-2}, 10^{-1}]$. For these parameters, the model produced biologically relevant cell and fiber structures (Fig. 1.12 (I B)), without the need for biased insemination. We refer to the SI for a discussion of the influence of the biasing parameter $\alpha$ and of the role of the alignment force $c_1$.

**Comparisons with experimental data**. The image processing enabled the computation of the SQ $N_C$, $E$ and $\Theta$ on the biological images, thus allowing for a quantitative comparison between the model and the experimental results. To compare the biological and numerical SQ, we non-dimensionalized the mean cluster number $N_C$ and the mean elongation of cell clusters $E$ by reference values referred to as $N_{ref}$ and $E_{ref}$ respectively. The numerical (respectively biological) reference values $N_{ref}$, $E_{ref}$ were defined as the mean value of $N_C$ or $E$ over all the numerical (respectively biological) experiments. As biological images suggest that parts of adipose tissue exhibit a preferred direction, we ran simulations for different initial fiber configurations such that the initial fiber angles $\theta_{init}$ were uniformly chosen in the range $[\theta_1 \pm \theta_2]$. Parameter $\theta_1$ measured the mean initial fiber direction and $\theta_2$ was related to its standard deviation. The larger $\theta_2$, the more disordered the initial network was (with $\theta_2 = \pi$ as the extreme case where the fiber initial distribution was fully isotropic). We also considered the case where the mean fiber direction could depend on the position in the form $\theta_1(x_1, x_2) = \theta_1^+$ if $x_1 > 0$ and $\theta_1(x_1, x_2) = \theta_1^-$ if $x_1 < 0$ where $(x_1, x_2)$ are the coordinates of a point in the computational domain and $x_1 = 0$ corresponds to the vertical middle line. This corresponded to the case where the initial fiber mean direction changed abruptly from $\theta_1^-$ to $\theta_1^+$ across the vertical middle line. We realized a database containing, for each set of model parameters $(\nu_d, \theta_1, \theta_2)$ (or in the case of position-dependent initial mean fiber direction, $(\nu_d, \theta_1^-, \theta_1^+, \theta_2)$), the SQ $N_C$, $E$ and $\Theta$ for 10 different simulations. The simulations were performed with random insemination and the other parameters were chosen to the value $\chi_\ell = 0.35$ and $c_1 = 1$, according to the previous analysis. For each biological image, we first searched the database of numerical simulations to find the combination of parameters which minimized the quadratic difference between the experimental SQ and the mean of the model SQ. Then, within the 10 simulations generated for this set of parameters, we selected the one minimizing the quadratic difference between the experimental and model SQ.

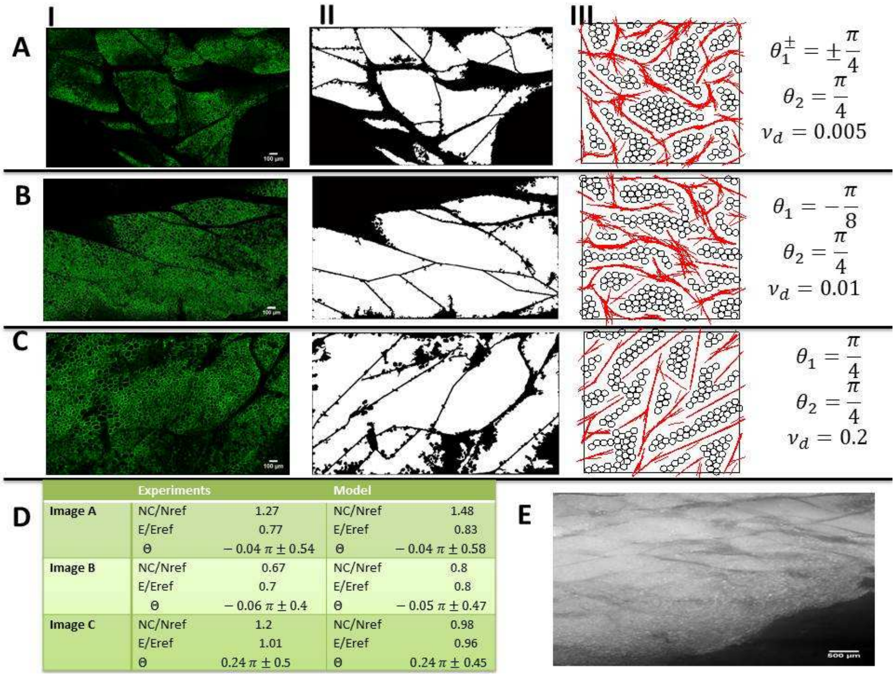

| | Experiments | | Model | |
|---|---|---|---|---|
| Image A | NC/Nref | 1.27 | NC/Nref | 1.48 |
| | E/Eref | 0.77 | E/Eref | 0.83 |
| | Θ | $-0.04\,\pi \pm 0.54$ | Θ | $-0.04\,\pi \pm 0.58$ |
| Image B | NC/Nref | 0.67 | NC/Nref | 0.8 |
| | E/Eref | 0.7 | E/Eref | 0.8 |
| | Θ | $-0.06\,\pi \pm 0.4$ | Θ | $-0.05\,\pi \pm 0.47$ |
| Image C | NC/Nref | 1.2 | NC/Nref | 0.98 |
| | E/Eref | 1.01 | E/Eref | 0.96 |
| | Θ | $0.24\,\pi \pm 0.5$ | Θ | $0.24\,\pi \pm 0.45$ |

Figure 1.13: (A) to (C) : (I) Biological images of perilipin immunostained adipose tissue. The white scale bar at the bottom right is for $100\mu m$. (II) Biological images after lobule detection. (III) Numerical simulation with parameter values offering the best correspondence with biological images. The parameter values for each simulation are indicated on the right. (D) Table showing the SQ computed on the biological data and numerical simulations. The model reproduces the observed structures qualitatively and quantitatively well. (E): image of a large portion of adipose tissue. The white scale bar at the bottom right is for $500\mu m$ : we notice the coexistence of similar structures as in images (A), (B) and (C) at different locations in the tissue.

Fig. 1.13 (A) to (C) show three biological images before (I) and after (II) lobule detection, as well as the corresponding best simulation (III) applying the previously detailed method and the associated set of parameters $\nu_d$, $\theta_1$ (or $\theta_1^{\pm}$) and $\theta_2$. Table (D) provides the SQ corresponding to images (A) to (C) for both the experimental data and numerical simulations. Finally, in Fig. 1.13 (E), a larger portion of the adipose tissue is shown (the white scale bar at the bottom right indicates $500\,\mu m$ for (E) and $100\,\mu m$ for (A) to (C)).

The lobule segmentation (column (II)) revealed that the elongation of the lobular structures increased from (A) to (C). We notice that the value of the unlinking frequency $\nu_d$ corresponding to the best numerical fit increases as well, confirming the analysis made above. In these three cases, the lobule-like cell structures of the numerical simulations are similar to the ones observed in the corresponding biological images (compare columns (II) and (III) of Fig. 1.13), and the values of the SQ given by the model are very close to the experimental ones (see Table (D)). These results show that the model is able to reproduce the data in a fairly wide range of situations by simply modifying the model parameters. In real tissues the organizational level varies from high to low according to the position in the tissue. In Fig 1.13 (E), a large portion of adipose tissue is shown. It reveals well-organized lobular structures in its upper part and more disordered structures in its lower part. Simulation of the entire tissue using the model would be possible (although computationally intensive) by simply varying the parameters of the model to match the variation of the organizational level of the tissue.

# 4 Discussion

To our knowledge, this work is the first attempt to understand the emergence of the lobular structure of the adipose tissue by interfacing a mathematical model and experimental results. The originality of our work lies in the assumption that adipose tissue architecture results from a self-organization process principally driven by mechanical interactions between adipocytes and the ECM. This corresponds to a co-organization where the cell clusters and the fiber structures evolve simultaneously. Our mathematical model is able to reproduce the clustering of adipocytes into lobular units surrounded by the ECM fiber network. Simply varying a few parameters allowed us to span a large variety of morphologies. Our results suggest that adipose tissue organization could be principally driven by mechanical cues, in addition to a limited number of biologically-controlled phenomena such as fiber-fiber chemical linking.

The structures that emerged from the mathematical model can be classified into three types: (a) middle-sized compact cell clusters surrounded by a disorganized fiber network, (b) middle-sized compact cell clusters surrounded by a well-organized network of thick fiber threads, or (c) elongated clusters surrounded by a network of thin and rigid fiber threads. Each type of structure corresponded to a range of model parameters of the fiber linking-unlinking dynamics.

Structures of type (a) were obtained for a slow fiber linking-unlinking dynamics. The rigidly connected fiber structures could not self-organize, leading to a disordered fiber network. However, the system was able to produce middle sized cell clusters of lobular shape as a result of cell-fiber repulsion. This reflected the ability for a connected fiber network to exert a pressure on the cell structures and confine them into separated zones. For a faster fiber linking-unlinking dynamics, the remodeling of fiber structures was enabled, and fibers could arrange more easily into organized patterns, thanks to the torque acting on linked fibers. For a well chosen range of the unlinking frequency $\nu_d$ and of the flexural modulus $c_1$ (see discussion of $c_1$ in SI), the model produced biologically relevant cell and fiber structures of type (b). Finally, structures of type (c) were observed for fast fiber linking-unlinking dynamics. In this case, fibers easily aligned with each other and fiber stiffness was reinforced by the links and associated torque acting on linked fibers. This imposed local directional constraints to cell cluster growth, favoring cell cluster elongation. Moreover, due to increased fiber rigidity, the fibers failed to surround the cell structures. The model matched experimental results qualitatively well with the most simple insemination rule, namely random cell insemination. This result is of major importance since it suggests that no preferred location for differentiation of immature cells into adipocytes is required.

It is noteworthy that the global organization of the tissue can be obtained without any direct involvement of vasculature. This is what is suggested by the minor influence of biased insemination on the morphology of the obtained cell structures. Therefore, our results suggest that the global architecture of adipose tissue would not be primarily driven by vasculature as suggested by Wassermann's pictures [4] and several papers describing the key role of angiogenesis in adipogenesis [27]. However by correlating the appearance of new adipocytes to a larger concentration of existing adipocytes, biased insemination provides an indirect way to account for vasculature. Indeed, blood supplies the substrates required for adipogenesis and favors the appearance of new adipocytes at the extremities of capillaries where existing adipocytes are already present.

Other phenomena have been explored, such as random cell motion or random fiber motion (which may occur in association with the movements of the tissue), fiber local alignment (to model ECM reorganization by stem cells) and the suppression of isolated cells (to model isolated cell apoptosis). These additional phenomena led to a broad range of tissue structures. Although not necessarily relevant for adipose tissue, these structures could account for other organs (such as muscles, liver, etc.) or pathological adipose tissues (such as fibrotic ones). More quantitative work is needed and these questions will be developed in future works.

Further improvements of the model could be made. Vasculature formation could be explicitly introduced in the model and would provide more hints about its role on adipogenesis. Incorporating immature cells could help investigating their role in the reconstruction of the ECM [28]. Similarly, coupling cell apoptosis with spontaneous ECM reconstruction [29] would improve the treatment of the latter. The adipocyte growth law could be made dependent on the local stress as in [30, 31]. Macroscopically, introducing a disruption of the equilibrium by suppressing a part of the tissue would open up new applications of the model, such as the investigation of the spatial reorganization of the tissue in the process of wound healing. From a mathematical viewpoint, the development of a macroscopic model from the present IBM would allow us to perform simulations on larger domains and address the question of the organization of the whole tissue.

# 5 Materials

**Model.** Numerical simulations were performed on a 2D square grid with periodic boundary conditions. Each of the $N_a$ cells was modelled as a 2D sphere described by its center and its radius. Two adjacent spheres could not overlap. The $N_f$ fiber elements were represented as straight segments of fixed and uniform length and described by their center and their directional angle. We started the simulations with $N_f$ fibers randomly distributed in the domain and no cell. The interactions between the agents were of 3 types: (i) fiber-cell interactions, (ii) cell-cell interactions and (iii) fiber-fiber interaction. (i) was modelled by a repulsive potential between fiber elements and cells. (ii) was modelled as a non-overlapping constraint between adjacent adipocytes and (iii) contained (a) the constraint relating two linked fibers at their common joint (the position of the joint within each fiber was supposed fixed) and (b) the torque forcing two linked fibers to align, which modelled fiber resistance to bending. At each time, a minimum of the mechanical energy expressing (i) and (iii b) was sought under the cell non-overlapping constraint (ii) and the linked fiber constraint (iii a). The potentials modelling (i) and (iii b) were supposed to be sums of elementary binary potential elements computed between two agents (cells and fibers for (i), two fibers for (iii a)). The cell-fiber potential iso-lines were ellipses with the two ends of the fiber as focii. The potential vanished beyond a certain distance from the fiber. The linked fiber-fiber potential was proportional to the square of the sine of the angle between the two fibers. The cell-cell non-overlapping condition was ensured by inequality constraints of the form $\Phi_{ij} \geq 0$ expressing that cells numbered $i$ and $j$ could not overlap. Specifically, $\Phi_{ij}$ was the square of the distance of the cell centers minus the square of the sum of the radii. The constraints relating two linked fibers numbered $\ell$ and $m$ at their joint was defined by a vector equality constraint of the form $\Psi_{\ell,m} = 0$ where $\Psi_{\ell,m}$ is the vector joining the joint position on fiber $\ell$ and that on fiber $m$. The constraints were taken into account by a min-max approach. With this aim, a Lagrangian was formed by combining the mechanical potential with the constraints, the coefficients of this combination being the Lagrange multpliers. The min-max problem was solved by means of a classical Uzawa algorithm. A precise expression of the Lagrangian and details about the Uzawa algorithm can be found in the SI. At each time step, the mechanical equilibrium was disturbed by the biological phenomena, namely (i) new adipocyte insemination, (ii) adipocyte growth and (iii) the formation of new fiber links and the removal of some existing links. After disturbance by these biological phenomena, a new constrained minimization of the mechanical energy was realized in order to restore the mechanical equilibrium. Then, time was incremented and the process started again until final time. The computation was stopped when a cell volume fraction of about 50% is reached. Cell growth was modelled as a linear-in-time volumic growth with rate $\nu_g$. The time-dynamics of the creation/deletion of fiber links and the insemination of new cells were supposed to follow Poisson processes. Each frequency associated to a Poisson process was a parameter of the model. The selection of these parameters is detailed in the SI. When biased insemination was activated, the location of new inseminated cells was biased by the biasing parameters $\alpha$ and sensing distance $R$. For this purpose, we let the probability of inseminating a new cell at a randomly chosen point $X$ be a function of the local density of existing adipocytes. More precisely, we computed the number of existing cells contained in the ball of radius $R$ centered in $X$. This number was normalized by the total number of maximal radius cells that could be contained in such a ball, giving rise to a normalized density $\chi$. The probability of inseminating at point $X$ was then set equal to $\chi^\alpha$.

**Immunohistochemistry and confocal microscopy.** Whole mouse inguinal adipose tissue (AT) were fixed, embeded in agarose and cut into 300$\mu$m slices. Slices were permeabilized in PBS/2% Normal Horse serum 0.2% triton 4h at, room temperature (RT), and then incubated in anti-perilipin antibody (1/250, P1873 Sigma, 24h RT). After washing, slices were incubated in alexa488-conjugated goat anti-rabbit IgG (1/250, A11008 Molecular Probes). Imaging was performed using a Confocal Laser Scanning microscope (LSM510 NLO - Carl Zeiss, Jena, Germany) with an objective lens LCI "Plan- Neofluar" 25x/0,8 and excited using a 488 nm argon laser. Images were obtained by the stitching of 45 acquired images with 10% overlapping with Fiji defined by image metadata Grid/collection stitching plugins [32]. Automatic image segmentation techniques were developed for (i) cell segmentation and (ii) lobule segmentation. A fully-automatic method for (i) based on a marker-controlled watershed technique [33] was implemented. The watershed function was defined as the gradient of the image intensity after gaussian filtering. Foreground markers (cell centers) were localized by inferior tresholding and research of local maxima of the image intensity and background markers (fiber network) by superior tresholding. (ii) was performed with a semi-automatic method, by (a) thresholding and morphological opening-by-reconstruction of the binary image (automatic) and (b) manual separation of the lobular structures by straight lines (visually determined) when (a) was not efficient enough. More information on the image processing can be found in the SI.

# 6 Supporting Information

## 6.1 Introduction

The outline of this Supporting information is the following: the first section is devoted to the mathematical modeling: section 6.2.1 describes the mechanical interactions in the model. The computation of the constraints is detailed in section 6.2.2. Sections 6.2.3 details the modeling of the biological phenomena. The minimization algorithm is given in section 6.2.4. Sections 6.2.5 and 6.2.6 are dedicated to the fitting of the numerical parameters and to computing considerations respectively. In section 6.3, statistical quantifiers are defined to allow the comparison between numerical simulations and biological images. Section 6.4 is devoted to image processing. Finally, the results are presented in section 6.5: in section 6.5.1 additional results supporting the conclusions of the main text are given. Section 6.5.2 is dedicated to the analysis of the influence of the flexural modulus $c_1$. Section 6.5.3 gives a more detailed analysis of the biased insemination process. Finally, section 6.5.4 presents the study of an initial anisotropic fiber network.

## 6.2 Mathematical model

We refer to section **Description of the model** of the main text for an overview of the model. Let us recall the main features and introduce some notations. The two-dimensional Individual Based Model (IBM) consists of $N_a$ adipocytes, which are modeled as 2D growing spheres of center $X_i$ and radius $R_i$ for $i$ in $[1, N_a]$, and $N_f$ extra-cellular-matrix fiber elements which are represented by straight lines of fixed length $L_f$, of center $Y_k$ and orientational angle $\theta_k$ for $k \in [1, N_f]$. Adipocytes are prevented to overlap to model volume exclusion between cells. Fiber elements have the ability to link to or unlink from each other to model fiber elongation or rupture. The resistance of fibers to growing adipocytes is modeled by a repulsion potential $W_{pot}$ between cells and fibers. Additionally, fibers offer resistance to bending through an alignment potential $W_{al}$ acting between two linked fiber elements. Cells and fibers seek to minimize their mechanical interaction energy resulting from these two potentials, subject to the non-overlapping constraint between cells and to the linkeage constraint between linked fibers. In the course of the simulation, adipocytes grow, new adipocytes appear as a result of stem-cell differentiation, new fiber links can appear and existing links can disappear. These phenomena disrupt the mechanical equilibrium and force the cells and fibers to move in order to restore the equilibrium.

### 6.2.1 Mechanical interaction potential

Given a configuration at a fixed time, let $C$ be the set of cell center positions and radii: $C = \{(X_i, R_i)\ ,\ i \in [1, N_a]\}$ and $F$ the set of fiber center positions and fiber directional angles: $F = \{(Y_k, \theta_k)\ ,\ k \in [1, N_f]\}$. The global mechanical energy of the system reads:

$$\mathcal{W}(C, F) = W_{pot}(C, F) + W_{al}(F). \tag{6.1}$$

where $W_{pot}$ and $W_{al}$ read:

$$W_{pot}(C, F) = \sum_{1\le i\le N_a} \sum_{1\le k\le N_f} W_{i,k}(X_i, Y_k, \theta_k) \tag{6.2}$$

$$W_{al}(F) = c_1 \sum_{(k,m)\in[1,N_f]} p^t_{km} \sin^2(\theta_k - \theta_m). \tag{6.3}$$

Here, $p^t_{km}$ are time-dependent coefficients that are equal to 1 if fibers $k$ and $m$ are linked and are equal to 0 otherwise. Their time-evolution is given section I.3. The alignment potential $W_{al}$ is supposed to be of intensity $c_1$ and consists of the sum of elementary alignment potentials between fibers of a linked pair. This potential tends to align two linked fibers together. The repulsion potential $W_{pot}$ is supposed to be the sum of two-particle potential elements, $W_{i,k}$, modeling the mechanical interaction between cell $i$ and fiber $k$. For two given vectors $X$ and $Y$ of $\mathbb{R}^2$ and an angle $\theta \in [-\pi, \pi]$, $W_{i,k}(X, Y, \theta)$ reads:

$$W_{i,k}(X, Y, \theta) = \begin{cases} \frac{\tilde{W}(\lambda_k^+)}{d_{0,i}}(d_{0,i} - d(X, Y, \theta)) & \text{if } d(X, Y, \theta) \le d_{0,i} \\ 0 & \text{otherwise} \end{cases} \tag{6.4}$$

where:

$$d(X, Y, \theta) = |X - Y + \frac{L_f}{2}\omega(\theta)| + |X - Y - \frac{L_f}{2}\omega(\theta)| - L_f, \tag{6.5}$$

and $\omega(\theta) = \begin{pmatrix} \cos\theta \\ \sin\theta \end{pmatrix}$ is the unit vector associated to the fiber angle $\theta$. The fiber-cell repulsion potential iso-lines are ellipses with focii located at the two ends of the fiber segment. The potential vanishes beyond distance $d_{0,i}$ to the fiber center (see Fig. 1.14). Parameter $d_{0,i}$ is set such that the length of the ellipse semi-minor axis is $\tau R_i$ (see Fig. 1.14), with $\tau$ a parameter set equal to 3 in the simulations. In this case, a fiber repels cell $i$ up to a distance $\tau R_i$ in its orthogonal direction. A direct computation gives:

$$d_{0,i} = -L_f + 2\sqrt{\Delta_i},\ \Delta_i = (\frac{L_f}{2})^2 + (\tau R_i)^2.$$

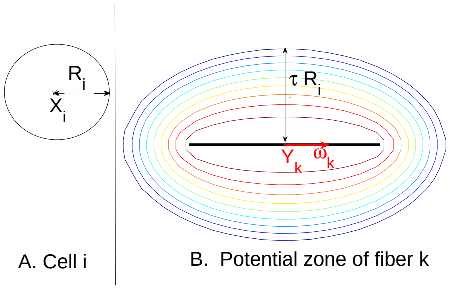

A. Cell i

B. Potential zone of fiber k

Figure 1.14: A: Cell $i$ of radius $R_i$. B: Isolines of a potential generated by an horizontal fiber $k$ with $\tau = 2$. Maximal repulsion distance $\tau R_i$ in the orthogonal direction of the fiber.

Table 1.1: Model parameters

| Name | Value | Description |
|---|---|---|
| **Domain** | | |
| $N_s$ | 100 | Total number of numerical boxes |
| $L_s$ | 3 | Length side of a numerical box |
| $x_{\max} - x_{\min}$ | 30 | Length side of the square domain |
| **Agents** | | |
| $N_a$ | 180 | Number of adipocytes |
| $N_f$ | 800 | Number of fibers |
| $R_{\max}$ | 0.66 | Maximal radius of cells |
| $L_f$ | 3 | Fiber length |
| **Mechanical cell-fiber repulsion potential** | | |
| $W_0$ | 5 | Minimal potential force |
| $W_1$ | 15 | Maximal potential force |
| $\tau R_{\max}$ | $3R_{\max}$ | Fiber-cell repulsion distance |

Finally, the factor $\tilde{W}(\lambda_k^+)$ in (6.4) measures the strength of each repulsion potential element. In order to model the fact that a fiber network is stiffer when the fibers are aligned [34], $\tilde{W}(\lambda_k^+)$ is assumed to be a linear increasing function of the fiber local alignment $\lambda_k^+$. The local alignment of fibers around fiber $k$ is computed in a neighborhood $B(Y_k, R_{al})$, where $R_{al}$ is the sensing distance up to which fiber $k$ senses the direction of its neighbors. Let $P_k$ denote the mean of the projection matrices on the direction vectors of the fibers in $B(Y_k, R_{al})$:

$$P_k = \frac{1}{n_k} \sum_{m | Y_m \in B(Y_k, R_{al})} \omega_m \otimes \omega_m, \tag{6.6}$$

where $n_k$ denotes the number of fibers contained in $B(Y_k, R_{al})$, and $\omega_m$ is the directional vector of fiber $m$. The maximal eigenvalue $\lambda_k^+$ of $P_k$ measures the mean alignment of the fibers in $B(Y_k, R_{al})$. Its corresponding normalized eigenvector gives the mean direction of the fibers in $B(Y_k, R_{al})$. A direct computation leads to:

$$\lambda_k^+ = \frac{1+\sqrt{\Delta}}{2}$$

where

$$\Delta = 1 + \frac{4}{n_k^2}\Bigg[\bigg(\sum_{m|Y_m\in B(Y_k,R_{al})} \cos\theta_m \sin\theta_m\bigg)^2 \\ - \sum_{m|Y_m\in B(Y_k,R_{al})} (\cos\theta_m)^2 \sum_{m|Y_m\in B(Y_k,R_{al})} (\sin\theta_m)^2\Bigg]$$

Note that $\lambda_k^+ = 1$ when all the fibers in $B(Y_k, R_{al})$ have the same direction and $\lambda_k^+ = 0$ when the fiber directions are fully random. The intensity of the potential element is then set to:

$$\tilde{W}(\lambda_k^+) = (W_1 - W_0)\lambda_k^+ + W_0,$$

where $W_0$ and $W_1$ are the intensities of the repulsion potential between fiber $k$ and cell $i$, when the local alignment around fiber $k$ is weak or strong respectively.

### 6.2.2 Constraints

In order to model adipocyte incompressibility and non overlapping, we assume that the radius of each disk is unaffected whatever mechanical efforts are exerted onto it. The non overlapping constraint between cells $i$ and $j$ is written as an inequality constraint on the following function $\Phi_{ij}$:

$$\Phi_{ij}(X_i, X_j) = (R_i + R_j)^2 - |X_i - X_j|^2. \tag{6.7}$$

One immediately notes that cells $i$ and $j$ do not overlap if and only if $\Phi_{ij}(X_i, X_j) \leq 0$.

To model fiber growth and elongation or conversely rupture, unlinked (resp. linked) intersecting fibers have the possibility to link (resp. unlink) at random times. As long as a pair of linked fibers remains linked, the attachment sites of the two linked fibres are kept at the same point. The maintain of the link between fibers $k$ and $m$ is modeled as equality constraints $\vec{\Psi}_{km} = 0$ with:

$$\vec{\Psi}_{km}(Y_k, Y_m, \theta_k, \theta_m) = Y_k + \ell_{km}\omega(\theta_k) - Y_m - \ell_{mk}\omega(\theta_m), \tag{6.8}$$

where $\ell_{km}$ is the distance of the center of fiber $k$ to its attachment site with fiber $m$ (see Fig. 1.15) at the moment when the link is created. We use, if $\sin(\theta_m - \theta_k) \neq 0$:

$$\ell_{km} = \frac{(x_m^0 - x_k^0)\sin\theta_m^0 - (y_m^0 - y_k^0)\cos\theta_m^0}{\sin(\theta_m^0 - \theta_k^0)} \tag{6.9}$$

where $Y_k^0 = (x_k^0, y_k^0)$ are the 2D coordinates of the center of fiber $k$ when the link is created (and similarly for fiber $m$, see Fig. 1.15).

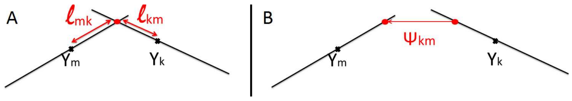

Figure 1.15: A. Creation of a link between intersecting fibers $Y_m$ and $Y_k$. Link lengths $\ell_{mk}$ and $\ell_{km}$. B. Constraint vector $\vec{\Psi}_{km}$ (see Eq. (6.8)) after fiber motion.

Finally, cell radii are assumed to be kept fixed during the minimization of the global energy. This amounts to excluding cell radii from the variables of the minimization problem. At each time step, the minimization of the global mechanical energy under the above detailed constraints is written:

$$(C, F) = \underset{\Phi(\tilde{C})\leq 0,\ \Psi(\tilde{F})=0}{\operatorname{argmin}} \mathcal{W}(\tilde{C}, \tilde{F}), \tag{6.10}$$

where:

$$\Phi(C) = \Big(\Phi_{ij}(X_i, X_j)\Big)_{(i,j)\in[1,N_a]^2},$$
$$\Psi(F) = \Big(\vec{\Psi}_{km}(Y_k, Y_m, \theta_k, \theta_m)\Big)_{(k,m)\in\mathcal{N}_f},$$

where $\mathcal{N}_f$ denotes the set of linked fiber pairs: $\mathcal{N}_f = \{(k,m) \in [1, N_f]^2,\ k < m,\ p_{km}^t = 1\}$.

### 6.2.3 Modeling of the main biological phenomena

*Pre-adipocyte differentiation:* New adipocytes of minimal radius $R_e$ are inseminated at random times following a Poisson process of frequency $\nu_e$. The location of the insemination is random with either uniform probability in the domain or with a bias resulting in a higher insemination probability at locations where existing adipocytes are already present. In this last case, the probability of inseminating at a random point $X$, $\mathcal{P}(X, R)$ is a function of the cell density computed in the ball of center $X$ and of radius $R$ and normalized by the maximal possible density in this ball. This models a quorum-sensing process around point $X$ where a preadipocyte senses the adipocyte density $\chi(X,R)$, up to a sensing distance $R$. This normalized density reads:

$$\chi(X,R) = \frac{\sum\limits_{i|X_i\in B(X,R)} \pi R_i^2}{\pi R_{\max}^2 N_R},$$

where $N_R$ is the maximal number of cells of radius $R_{\max}$ contained in $B(X,R)$ (for instance $N_R = 7$ for $R = 2R_{\max}$). Note that $\chi \in [0,1]$. Then, the probability of inseminating at $X$, $\mathcal{P}(X,R)$, reads:

$$\mathcal{P}(X,R) = \chi^\alpha,$$

where $\alpha > 0$ is the biasing parameter. We define the characteristic time of the insemination process, $t_e$, as the mean time needed to inseminate $N_{\max}$ cells:

$$t_e = \frac{N_{\max}}{\nu_e}.$$

*Adipocyte growth* The volumes of the cells are supposed to grow linearly with time. Given a cell $i$ at time $t$, the radius of cell $i$ at time $t+\Delta t$ reads:

$$R_i^3(t+\Delta t) = R_i^3(t) + K_g(1+\eta\rho_g)$$

where $\eta$ is a random number chosen uniformly in $[0,1]$ and $K_g$, $\rho_g$ are two parameters such that $\frac{K_g}{\Delta t}$ is the mean volumic cell growth per unit of time and $\frac{K_g\rho_g}{\Delta t}$ is related to the standard deviation of the volumic cell growth per unit of time. The characteristic time of cell growth $t_g$ is defined as the mean time needed for a cell to reach its maximal radius $R_{\max}$ and reads:

$$t_g = \frac{R_{\max}^3 \Delta t}{K_g}.$$

*Fiber growth or rupture:* Fiber elongation is modeled by giving fibers the ability to attach to each other. Pairs of unlinked intersecting fibers link together at random times following a Poisson process of frequency $\nu_\ell$. To model fiber rupture, two linked fibers unlink following a Poisson process of frequency $\nu_d$. Let $(k,m) \in [1,N_f]^2$ and define $p_{km}^t$ such that $p_{km}^t = 1$ if fibers $k$ and $m$ are linked, 0 otherwise. The time evolution of $p_{km}^t$ is given by:

$$\begin{aligned}
\mathbb{P}(p_{km}^{t+\Delta t} = 1 | p_{km}^t = 0) &= 1 - e^{-\nu_\ell \Delta t} \text{ if } \max(\ell_{km}, \ell_{mk}) \le \frac{L_f}{2} \\
&= 0 \qquad\qquad \text{otherwise} \\
\mathbb{P}(p_{km}^{t+\Delta t} = 0 | p_{km}^t = 1) &= 1 - e^{-\nu_d^{km} \Delta t},
\end{aligned}$$

where $\ell_{km}$ and $\ell_{mk}$ are given by Eq. (6.9). $\mathbb{P}(p_{km}^{t+\Delta t} = 1 | p_{km}^t = 0)$ describes the transition probability for a transition of $p_{km}^t$ from 0 to 1 during the time interval $[t, t+\Delta t]$ while $\mathbb{P}(p_{km}^{t+\Delta t} = 0 | p_{km}^t = 1)$ refers to the transition probability for the reverse process. We define $t_\ell$ and $t_d$ as the characteristic times of the linking and unlinking of fibers: respectively:

$$t_\ell = \frac{1}{\nu_\ell},\ t_d = \frac{1}{\nu_d}.$$

In order to analyse the fiber linking/unlinking process, we define the ratio $\chi_\ell$:

$$\chi_\ell = \frac{\nu_f}{\nu_f + \nu_d}$$

Note that $\chi_\ell$ is directly correlated to the fraction of linked fibers (among pairs of intersecting fibers) at equilibrium if the linking-unlinking process was acting alone and will be referred to as the 'linked fiber fraction' for short. For each unlinking frequency $\nu_d$ and each linked fibers fraction $\chi_\ell$, the linking frequency is set to $\nu_f = \frac{\chi_\ell}{1-\chi_\ell}\nu_d$.

### 6.2.4 Uzawa algorithm

The constrained minimization problem (6.10) is solved with an Arrow-Hurwicz-Uzawa type algorithm [35]. To perform the minimization, we introduce a Lagrangian:

$$\begin{aligned} \mathcal{L}(C, F, \lambda, \vec{\mu}) &= \mathcal{W}(C, F) + \Phi_\lambda(C) + \Psi_{\vec{\mu}}(F), \\ \Phi_\lambda(C) &= \sum_{1 \le i,j \le N_a} \lambda_{ij} \Phi_{ij}(C) \\ \Psi_{\vec{\mu}}(F) &= \sum_{(k,m) \in \mathcal{N}_f} \vec{\mu}_{km} . \vec{\psi}_{km}(F), \end{aligned} \tag{6.11}$$

where $\lambda = \left(\lambda_{ij}\right)_{(i,j) \in [1,N_a]^2}$, $\lambda_{ij} > 0$ and $\vec{\mu} = \left(\vec{\mu}_{km}\right)_{(k,m) \in \mathcal{N}_f}$, $\vec{\mu}_{km} \in \mathbb{R}^2$ are the sets of Lagrange multipliers of the constraints.

Given a configuration $(C(t_n), F(t_n))$ at time $t_n = n\Delta t$ the configuration $(C(t_{n+1}), F(t_{n+1}))$ at time $t_{n+1} = (n+1)\Delta t$ is defined as the limit as $p \to \infty$ of the iterative sequence $(C^p, F^p)$ where $(C^p, F^p, \lambda^p, \vec{\mu}^p)$ is defined for all $(i,j) \in [1, N_a]^2$ and all $(k,m) \in \mathcal{N}_f$ by:

$$\begin{aligned} X_i^{p+1} &= X_i^p - \alpha_a^i \nabla_{X_i} \mathcal{L}(C^p, F^p, \lambda^p, \vec{\mu}^p) \\ Y_k^{p+1} &= Y_k^p - \alpha_f^k \nabla_{Y_k} \mathcal{L}(C^p, F^p, \lambda^p, \vec{\mu}^p) \\ \theta_k^{p+1} &= \theta_k^p - \alpha_\theta^k \partial_{\theta_k} \mathcal{L}(\mathcal{C}^p, \mathcal{F}^p, \lambda^p, \vec{\mu}^p) \\ \lambda_{ij}^{p+1} &= \max(0, \lambda_{ij}^p + \lambda_1 \Phi_{ij}(C^{p+1})), \\ \vec{\mu}_{km}^{p+1} &= \vec{\mu}_{km}^p + \mu_2 \vec{\Psi}_{km}(F^{p+1})). \end{aligned} \tag{6.12}$$

with initial condition $(C^0, F^0, \lambda^0, \vec{\mu}^0) = (C(t_n), F(t_n), \lambda^0, \vec{\mu}^0)$ and $\lambda^0_{ij} = 0$, $\vec{\mu}^0_{km} = 0$, for all $(i, j) \in [1, N_a]^2$ and all $(k, m) \in \mathcal{N}_f$. The parameters $\lambda_1$ and $\mu_2$ control the actualization of the constraints and their choice is detailed in the next section. The minimization steps $\alpha^i_a$, $\alpha^k_f$ and $\alpha^k_\theta$ control the elementary motion of cell $i$ and fiber $k$ and the elementary rotation of fiber $k$ respectively. Their computation is detailed in the next section. The convergence test of the algorithm reads:

$$|\frac{\mathcal{L}^{p+1} - \mathcal{L}^p}{\mathcal{L}^p}| \leq \epsilon_r, \tag{6.13}$$

for a chosen $\epsilon_r > 0$. Here, $\mathcal{L}^p$ is the value of the Lagrangian at iteration $p$. Because of the non convexity of the minimization problem, the uniqueness of the solution to (6.10) is not ensured and a configuration at each time step corresponds to a local minimum of the minimization problem.

### 6.2.5 Choice of the numerical parameters

In this section, the numerical parameters $\alpha^i_a, \alpha^k_f$ and $\alpha^k_\theta$ of (6.12) are chosen such that the amplitude of the change of each variable remains controlled. Given three bounds $\delta_a$, $\delta_f$ and $\delta_\theta$, the goal is to ensure $|X^{p+1}_i - X^p_i| \leq \delta_a$, $|Y^{p+1}_k - Y^p_k| \leq \delta_f$ and $|\theta^{p+1}_k - \theta^p_k| \leq \delta_\theta$, for each cell $i$ and fiber $k$. Using (6.11) and (6.12), the following expressions hold:

$$\begin{aligned}
|X^{p+1}_i - X^p_i| &= \alpha^i_a |\nabla_{X_i} \mathcal{W} + \nabla_{X_i} \Phi_\lambda| \\
|Y^{p+1}_k - Y^p_k| &= \alpha^k_f |\nabla_{Y_k} \mathcal{W} + \nabla_{Y_k} \Psi_{\vec{\mu}}| \\
|\theta^{p+1}_k - \theta^p_k| &= \alpha^k_\theta |\partial_{\theta_k} \mathcal{W} + \partial_{\theta_k} \Psi_{\vec{\mu}}|.
\end{aligned}$$

The parameters $\alpha^i_a$, $\alpha^k_f$ and $\alpha^k_\theta$ are consequently set such that:

$$\begin{aligned}
\alpha^i_a &= \frac{\delta_a}{2} \min(\frac{1}{|\nabla_{X_i} \mathcal{W}|}, \frac{1}{|\nabla_{X_i} \Phi_\lambda|}) \\
\alpha^k_f &= \frac{\delta_f}{2} \min(\frac{1}{|\nabla_{Y_k} \mathcal{W}|}, \frac{1}{|\nabla_{Y_k} \Psi_\mu|}) \\
\alpha^k_\theta &= \frac{\delta_\theta}{2} \min(\frac{1}{|\partial_{\theta_k} \mathcal{W}|}, \frac{1}{|\partial_{\theta_k} \Psi_\mu|}.
\end{aligned} \tag{6.14}$$

The gradients of the potential $\mathcal{W}$ have the following upper bounds for all $i \in [1, N_a]$ and $k \in [1, N_f]$ (see (6.1)-(6.5)):

$$\begin{aligned}
|\nabla_{X_i}\mathcal{W}| &\leq \sum_{1\leq k\leq N_f} \frac{W_1}{d_{0,i}} \sim \frac{W_1 n_i^f}{d_0} \\
|\nabla_{Y_k}\mathcal{W}| &\leq \sum_{1\leq i\leq N_a} \frac{W_1}{d_{0,i}} \sim \frac{W_1 n_k^a}{d_0} \\
|\partial_{\theta_k}\mathcal{W}| &\leq \sum_{1\leq i\leq N_a} \frac{L_f W_1}{2d_{0,i}} + 2 \sum_{m\ |\ (k,m)\in\mathcal{N}_f} c_1 \sim \frac{L_f W_1 n_k^a}{d_0} + 2\ell_k^f c_1,
\end{aligned}$$

where $n_i^f$, $n_k^a$ and $\ell_k^f$ denote the number of fibers interacting with cell $i$, the number of cells interacting with fiber $k$ and the number of fibers linked to fiber $k$ respectively. Here, $d_0$ is the value of $d_{0,i}$ evaluated with $R_i = R_{\max}$. The following upper bounds for the gradients of the constraint functions (see Eqs. (6.7)-(6.9)) are chosen:

$$\begin{aligned}
|\nabla_{X_i}\Phi_\lambda| &\leq 4R_i \sum_{j\neq i} |\lambda_{ij}|, \\
|\nabla_{Y_k}\Psi_\mu| &\leq \sum_{m\ |\ (k,m)\in\mathcal{N}_f} |\vec{\mu}_{km}|, \\
|\partial_{\theta_k}\Psi_\mu| &\leq \frac{L_f}{2} \sum_{m\ |\ (k,m)\in\mathcal{N}_f} |\vec{\mu}_{km}|.
\end{aligned}$$

These three gradient bounds are estimated at each iteration of the minimization algorithm and are included into Eqs. (6.14) to compute the values of the numerical steps. We now turn towards the determination of $\lambda_1$ and $\mu_2$ of Eqs. (6.12). Dimensionnally, the following estimations can be set from the expression of the Lagrangian Eq. (6.11) (for all pairs $(i,j)$ and $(k,m)$):

$$\lambda_{ij} = O(\frac{W_0}{R_{\max}^2}),\ |\vec{\mu}_{km}| = O(\frac{W_0}{L_f}).$$

From the actualization of the constraints given by iterations of Eqs. (6.12), we set:

$$\lambda_{ij} \sim \lambda_1 R_{\max}^2,\ \vec{\mu}_{km} \sim \mu_2 L_f$$

Then, parameters $\lambda_1$ and $\mu_2$ are set equal to:

$$\lambda_1 = \frac{W_0}{R_{\max}^4},\ \mu_2 = \frac{W_0}{L_f^2}$$

The values of the parameters $\delta_a$, $\delta_f$ and $\delta_\theta$ are taken of the order of $10^{-3}$ and the convergence test tolerance to $\epsilon_r = 10^{-5}$ (the complete set of the numerical parameters can be found in Table 1.3).

Table 1.2: Model parameters for pre-adipocyte differentiation (Poisson process) and adipocyte growth (regular process). Associated time frequencies.

| Phenomenon | Parameters | Frequencies |
|---|---|---|
| Pre-adipocyte differentiation | $R = 1.32$, $R_e = 0.001$ | $\nu_e = 10$ |
| Adipocyte growth | $K_g = 0.0016$, $\rho_g = 0.2$ | $\nu_g = 10$ |

Table 1.3: Numerical parameters

| Name | Value | Phenomenon |
|---|---|---|
| $\Delta t$ | 0.1 | Time step |
| $\delta_a$ | $10^{-3}$ | Adipocyte maximal displacement |
| $\lambda_1$ | 30 | Lagrange multiplier actualization |
| $\delta_f$ | $10^{-3}$ | Fiber maximal displacement |
| $\delta_\theta$ | $10^{-2}$ | Fiber maximal angular change |
| $\vec{\mu}_2$ | 30 | Lagrange multiplier actualization |
| $i_{\max}$ | 2500 | Iteration number |
| $\epsilon_r$ | $10^{-5}$ | Convergence test tolerance |

### 6.2.6 Decreasing the computational time

The simulations are performed on a 2D-domain $\Omega = [x_{\min}, x_{\max}] \times [y_{\min}, y_{\max}]$. In order to reduce the computational time, the domain is divided into sub-squares whose side length $L_s$ is a measure of the maximal distance of the agent interactions. The goal is to compute each interaction potential element with the agents located in neighboring sub-squares of the domain only. The procedure is classical and details are omitted. Periodic boundary conditions are set by creating ghost numerical boxes of length $L_s$ at each boundary of the domain.

## 6.3 Statistical quantifiers

This section is devoted to the computation of statistical quantifiers used to describe cell and fiber structures in both numerical simulations and biological images. A cell cluster is defined as a set of cells almost in contact. Let $\sim_a$ be the reflexive and symmetric relation:

$$j \sim_a i \ \Leftrightarrow j \in \mathcal{N}_i,$$

where $\mathcal{N}_i$ is the set of cell $i$ neighbors:

$$\mathcal{N}_i = \{j \in [1, N_a]\ , j \neq i, \mid |X_i - X_j| \leq (R_i + R_j + \epsilon_a)^2\}, \tag{6.15}$$

where $\epsilon_a$ is the maximal allowed distance up to which two cells not in contact are defined as neighbors and is set to 50% $\max(R_i, R_j)$. The equivalence relation $\sim_A$ then reads:

$$\begin{aligned} j \sim_A i \Leftrightarrow & \exists n \in \mathbb{N}^*, \exists (a_1..a_n) \\ & \text{such that } j \sim_a a_1 \sim_a ... \sim_a a_n \sim_a i. \end{aligned}$$

Cells $i$ and $j$ belong to the same cluster if and only if $i \sim_A j$. Fig. 1.16 shows an example of cell cluster separation.

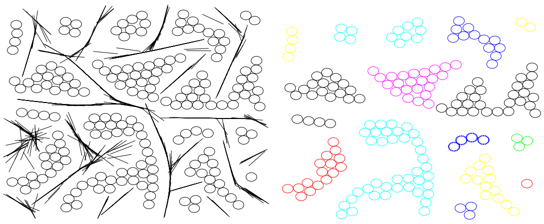

Figure 1.16: Example of cell cluster detection. Left: original numerical simulation. Cells are represented as 2D black spheres, fibers as black segments. Right: After cell cluster detection. Cells which belong to the same cluster are indicated with the same color.

The statistical quantifier $N_C$ is defined as the total number of cell clusters which have more than 5 adipocytes per 100 adipocytes.

The statistical quantifier $E$ measures the mean elongation of the cell clusters, and is defined as the number of cells at the boundary of the clusters normalized by the total number of cells in the clusters. As the parameter $E$ is irrelevant for clusters with less than 5 cells, its computation is restricted for clusters $c$ such that $n_c > 5$ and reads:

$$E = \frac{\sum_{c=1}^{N_C} \mathrm{Card}(\mathcal{R} \cap \mathcal{C}_c)}{\sum_{c=1}^{N_C} n_c}.$$

Here, $\mathcal{C}_c$ is the set of indices of the cells belonging to cluster $c$, $n_c$ is the number of cells in cluster $c$ and $\mathcal{R}$ is the set of indices of all cells with less than 5 neighbors:

$$\mathcal{R} = \{i \in [1, N_a],\ \mathrm{Card}(\mathcal{N}_i) \leq 5\},$$

where $\mathcal{N}_i$ is defined by Eq. (6.15).

Finally, in order to determine if the cell clusters have anisotropic shape with a preferred direction, we define the SQ $\Theta^c$ as the angle of cluster $c$ shape anisotropy direction. For this purpose, let $X^c$ be the center-of-mass of cluster $c$, i.e:

$$X^c = \frac{1}{n_c} \sum_{i \in \mathcal{C}_c} X_i.$$

Then, we define $P^c$ as the mean of the projection matrices on the vectors $X_i - X^c$, for all $i$ in cluster $c$:

$$P^c = \frac{1}{n_c} \sum_{i \in \mathcal{C}_c} (X_i - X^c) \otimes (X_i - X^c).$$

The maximal eigenvalue $\lambda_c^+$ of $P^c$ gives a measure of the shape anisotropy of cell cluster $c$ and its associated eigenvector $u^c = (u_1^c, u_2^c)$ gives the shape anisotropy direction. Then, $\Theta^c$ is defined as:

$$\Theta^c = \arctan(\frac{u_2^c}{u_1^c}).$$

Note that $\Theta^c \in [-\frac{\pi}{2}, \frac{\pi}{2}]$. The SQ $\Theta$ is then defined as the circular standard deviation of all the angles $\Theta^c$ for all clusters:

$$\Theta = \sqrt{-2\ln(\bar{R})},$$

where $\bar{R}$ reads:

$$\bar{R} = \frac{\sqrt{\left( \sum_{c=1}^{N_C} \cos\Theta^c \right)^2 + \left( \sum_{c=1}^{N_C} \sin\Theta^c \right)^2}}{N_C}.$$

Finally, the mean $\bar{\Theta}$ of $\Theta^c$ over all the cell clusters reads:

$$\bar{\Theta} = \frac{1}{2} \arg\Big( \sum_{c=1}^{N_C} e^{2i\Theta^c} \Big),$$

which ensures that $\bar{\Theta} \in [-\frac{\pi}{2}, \frac{\pi}{2}]$. Note that large $\Theta$ corresponds to fully isotropic cell cluster organization, while small $\Theta$ indicates that cell clusters have a preferential direction.

In order to describe the fiber structures, we define a fiber cluster as a set of neighboring quasi-aligned fiber elements and $\Lambda$ as an estimate of the average curvilinear length of such fiber clusters. Finally, $A$ measures the mean alignment of the fibers of a cluster. For this purpose, let us define $\mathcal{M}_k$ as the set of neighbors of fiber $k$, quasi-aligned with fiber $k$. Then:

$$\begin{aligned}\mathcal{M}_k = \{m \in [1, N_f]\,, m \neq k, \\ \min(d_f(Y_k, Y_m), d_f(Y_m, Y_k)) \leq 0 \\ \text{and } |\sin(\theta_k - \theta_m)| < \sin(\frac{\pi}{4})\},\end{aligned}$$

where $d_f(Y_k, Y_m)$ reads:

$$d_f(Y_k, Y_m) = d(Y_k, Y_m^-) + d(Y_k, Y_m^+) - 2\sqrt{(\frac{L_f}{2})^2 + (\tau_f L_f)^2}.$$

Here, $Y_m^{\pm} = Y_m \pm \frac{L_f}{2}\omega_m$ and $d(X, Y)$ is the distance of point $X$ to point $Y$. Note that $d_f(Y_k, Y_m) \leq 0$ (resp. $d_f(Y_m, Y_k) \leq 0$) if the center of fiber $k$ (resp. $m$) is contained in the ellipse of focii $Y_m^{\pm}$ (resp. $Y_k^{\pm}$) with semi minor axis of length $\tau_f L_f$ and semi major axis of length $\sqrt{(\frac{L_f}{2})^2 + (\tau_f L_f)^2}$. We chose $\tau_f = \frac{1}{3}$, which means that a fiber detects a neighboring fiber up to a distance $\frac{L_f}{3}$ in its orthogonal direction. This allows us to define fiber clusters as sets of quasi-aligned neighboring fibers. Let us define the reflexive and symmetric relation $\sim_f$ by:

$$k \sim_f m \;\Leftrightarrow m \in \mathcal{M}_k.$$

Define the equivalence relation $\sim_F$ such that:

$$\begin{aligned}k \sim_F m \Leftrightarrow \exists n \in \mathbb{N}^*, \exists (a_1..a_n) \\ \text{such that } k \sim_f a_1 \sim_f ... \sim_f a_n \sim_f m.\end{aligned}$$

Then, we say that fibers $k$ and $m$ belong to the same cluster if and only if $m \sim_F k$. Fig. 1.17 shows the results of fiber cluster detection from the numerical simulation displayed on Fig. 1.16.

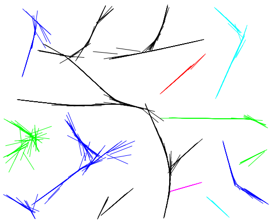

Figure 1.17: Example of fiber cluster detection, corresponding to simulation of Fig. 1.16. Fibers which belong to the same cluster are indicated with the same color.

The mean elongation of fiber clusters is estimated by $\Lambda$. Given a fiber cluster $c_f$ and a division of the simulation domain into squares of side length $L_f$, the length of $c_f$ is estimated by $L_f \Lambda_F^{c_f}$, where $\Lambda_F^{c_f}$ is the number of squares which contain the centers of at least one fiber of $c_f$. Then, the dimensionless mean fiber cluster elongation $\Lambda$ is defined as the mean of $L_s \Lambda_F^{c_f}$ over all the fiber clusters, normalized by the maximal cell diameter:

$$\Lambda = \frac{L_f}{2R_{\max} N_{T_f}} \sum_{1 \leq c_f \leq N_{T_f}} \Lambda_F^{c_f},$$

where $N_{T_f}$ is the total number of fiber clusters. The longer the fiber clusters, the larger the $\Lambda$.

Finally, we define the SQ $A$ to quantify the mean alignment of the fibers of a cluster. Given a fiber cluster $c_f$, the mean alignment of its fibers is defined as the maximal eigenvalue $\lambda_{c_f}^+$ of the mean projection matrix defined by Eq. (6.6), where the set $B(V_k, R_{al})$ is replaced by the set of all fibers of cluster $c_f$. Then, $A$ is defined as the mean of the fiber cluster alignment, weighted by the number of fibers in the cluster:

$$A = \frac{1}{N_F} \sum_{1 \leq c_f \leq N_{T_f}} \lambda_{c_f}^+ n_{c_f},$$

where $n_{c_f}$ is the number of fibers in cluster $c_f$.

## 6.4 Image processing

This section is devoted to the algorithms and results of the image processing. The goal is to develop segmentation techniques for (a) cell detection and (b) cell cluster detection, in order to compute the SQs on biological images and compare them to those of numerical simulations. It is noteworthy that adipocytes and lobules only are visualized in biological images at hand, therefore SQs $E$, $N_C$ and $\Theta$ only are accessible from biological images.

*(a) Detection/separation of cells* First, a fully-automatic method for cell detection based on marker-controlled watershed segmentation has been realized.We use Marker-controlled watershed segmentation, according to the following procedure:

(i) The biological image is first filtered by a local median filter which associates to each pixel its median value in its local neighborhood

(ii) The segmentation is performed on the gradient of the transformed image. The gradient is high at the borders of the objects and low inside the objects.

(iii) Compute foreground markers. These are connected blobs of pixels within each of the objects. The morphological techniques 'opening-by-reconstruction' and 'closing-by-reconstruction' are used to clean up the image. These operations create flat maxima inside each object that can be located using the intrinsic Matlab function imregionalmax.

(iv) Compute background markers. These are pixels that are not part of any object. We perform a simple thresholding of the intensity image: each pixel whose intensity is lower than the mean intensity of the image is set to 0.

(v) Modify the gradient map so that it only has minima at the foreground and background marker locations.

(vi) Compute the watershed transform of the modified gradient map.

Object boundaries are located where $W = 0$, where $W$ is the watershed transform of the marked image gradient. This method enables the separation of multiple objects. Each object is characterized by a center (center of mass of the detected region) and a radius $R$ (radius of a circle which has the same area $a$ as the object): $R$ is thus computed as $\sqrt{a/\pi}$.

*(b)Detection/separation of lobule-like clusters.* For cell cluster detection, a semi-automatic method has been developed. Each sub-images (squares occupying 0.1% of the image area) is filtered by median filtering with the intrinsic function medfilt2 of Matlab. Each output pixel contains the median value in the 3-by-3 neighborhood around the corresponding pixel in the input image. A thresholding of the intensity image fixed at 40% of the mean intensity of the subimage is then applied. This threshold appeared to be robust and was used for each studied biological image. The connected objects with 8-connectivity are computed using the Matlab intrinsic function bwlabel. Finally, objects containing less than 2000 pixels (noise objects) are suppressed with the intrinsic Matlab function bwareaopen. If neighboring cell clusters are still visually connected at a point, a line is plotted by hand to separate the two clusters. The process of cell cluster detection is semi-automatic in this sense, but this procedure is sufficient for the purpose of this work, given the low number of biological images to be treated.

## 6.5 Results and their analysis

### 6.5.1 Simulations of the main text

Here, supplementary results on the simulations of the main text are given. Fig. 1.18 shows the values of the Statistical Quantifiers $\Lambda$ and $A$ corresponding to the simulations of the main text, with random insemination and flexural modulus $c_1 = 1$ (see Fig. 3 (I) of Main Text). The values of the SQ are averaged over 10 simulations and plotted as functions of the fiber unlinking frequency $\nu_d$ for two different linked fiber fraction $\chi_\ell = 0.1$ (black curve) and $\chi_\ell = 0.35$ (blue curve). We refer the reader to section 'Results' of Main Text for the analysis of the cell structures, and we focus here on the fiber network.

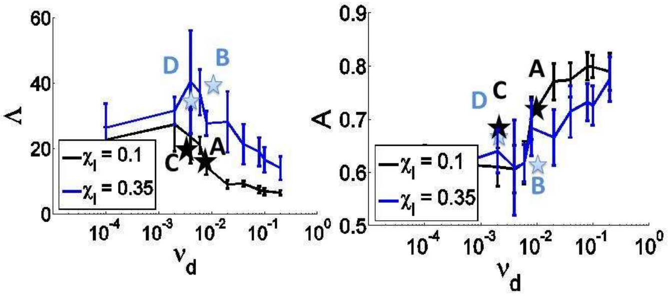

Figure 1.18: Statistical Quantifiers $\Lambda$ and $A$ of the simulations of Main Text (see Fig. 3 (I) of Main Text), with random insemination, flexural modulus $c_1 = 1$, as functions of the fiber unlinking frequency $\nu_d$ for two different linked fiber fraction $\chi_\ell = 0.1$ (black curve) and $\chi_\ell = 0.35$ (blue curve). The mean fiber cluster elongation $\Lambda$ is a non monotonous function of the unlinking frequency $\nu_d$, that first increases and then decreases with $\nu_d \in [10^{-3}, 0.1]$. The mean alignment of the fiber clusters $A$ increases with $\nu_d$, with two plateau values for $\nu_d \leq 10^{-3}$ and $\nu_d \geq 10^{-1}$. Values corresponding to the simulations of Main Text with biased insemination with biasing parameter $\alpha = 10^{-3}$ are indicated as blue stars for $\chi_\ell = 0.35$ and black ones for $\chi_\ell = 0.1$. The values of $A$ and $\Lambda$ for random and biased inseminations are similar in the range of $\nu_d \in [10^{-3}, 10^{-2}]$.

Fig.1.18 first reveals that the fiber SQ have plateau values for $\nu_d \leq 10^{-3}$. For a slow fiber linking-unlinking process ($\nu_d \leq 10^{-3}$), the fibers in the clusters are poorly aligned (low value of $A$) and the mean fiber cluster elongation $\Lambda$ is fairly large, meaning that the fibers keep their initial entanglement. As $\nu_d$ increases, the mean fiber cluster elongation $\Lambda$ increases until reaching a maximal value for $\nu_d \approx 0.005$. Then, $\Lambda$ loses 50% of its value when $\nu_d$ increases in the range $[0.005, 0.1]$. The mean elongation $A$ increases with $\nu_d$ from the value $A \approx 0.6$ to $A \approx 0.8$ as $\nu_d$ increases in the same range. This tends to show that the fiber linking-unlinking dynamics strongly influences the final structures. For a slow fiber linking-unlinking dynamics, due to fiber interconnections the fiber network is extremely ridig. In this case, fibers fail to align because of the high connectivity of the network which prevents any configurational change. As $\nu_d$ increases, the lifetime of each link decreases, allowing the remodeling of the fiber network. Consequently, fiber structures are more flexible and more aligned. However, if the linking-unlinking process is too fast, the fiber structures easily align, forming long fiber threads. These fiber threads are then reinforced by the fast creation of links, increasing the rigidity of the fiber patterns. Preferred directions locally emerge in the fiber network and favor the growth of cell clusters in these directions. The cell clusters are consequently elongated. In Fig. 1.18, blue and black stars show the values of $\Lambda$ and $A$ with biased insemination for $\alpha = 10^{-3}$, for two different values of $\nu_d = 0.005$ and $\nu_d = 10^{-2}$. Blue stars correspond to $\chi_\ell = 0.35$, black ones for $\chi_\ell = 0.1$. These plots reveal that biased insemination does not influence the fiber structures in the range of $\nu_d \in [10^{-3}10^{-2}]$. We refer to section IV.3 for more details on the role of biased insemination.

Three different morphologies (which will be referred to as "phases") are obtained according to the values of the parameters: (A) Lobule-like cell clusters surrounded by a disorganized (unaligned) fiber network, (B) lobule-like cell structures in an aligned fiber network, and (C) elongated cell structures in a network composed of long and rigid fiber threads. Each type of structure is obtained in a specific range of the parameters $\nu_d$ and $\chi_\ell$ of the fiber linking-unlinking dynamics and can described by a convenient set of SQs. In order to quantify the passage from one morphology to another, we choose the following SQ: the mean fiber cluster alignment $A$ and the mean cell cluster elongation $E$. We identify the threshold values $A^* = 0.68$ for $A$ and $E^* = 0.89$ for $E$. Structures of type (A) correspond to $A < A^*$ and $E < E^*$. Type (B) is described by $A > A^*$ and $E < E^*$ and finally type (C) by $A > A^*$ and $E > E^*$. Fig. 1.19 shows a phase diagram representing the various obtained morphologies in the $(E, A)$ plane. Each point in this phase diagram has been obtained by averaging the SQ over 10 simulations. The separatrix between phases (A) and (B) (i.e. the line $A = A^*$) is shown in red and the separatrix between phases (B) and (C) (i.e. the line $E = E^*$) is shown in blue. For each region, we show simulation results in the corresponding range of the parameters $\nu_d$ and $\chi_\ell$ for the sake of illustration.

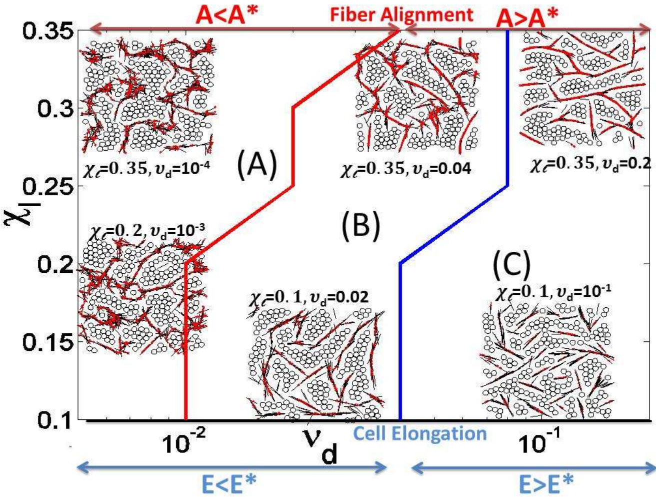

Figure 1.19: Phase diagram representing the separation lines between the three morphologies (A), (B) and (C) (Phase (A): $A < A^*$ and $E < E^*$ ; Phase (B): $A > A^*$ and $E < E^*$ ; Phase (C): $A > A^*$ and $E > E^*$), as function of the unlinking frequency $\nu_d$ and of the linked fiber fraction $\chi_\ell$. The separatrix $A = A^*$ between Phases (A) and (B) is plotted in red, while the separatrix $E = E^*$ between Phases (B) and (C) is plotted in blue. For each phase, two simulations in the corresponding range of parameters $\nu_d$ and $\chi_\ell$ are shown.

Fig. 1.19 first shows that the SQ describe the final cell and fiber structures fairly well. The simulations corresponding to morphology of type (B) are obtained for $\nu_d \in [10^{-2}, 10^{-1}]$ in the case of random insemination and $c_1 = 1$. Moreover, if we take also into account the other SQs (see main text for the values of $N_C$), the more biologically relevant structures are obtained in this range of $\nu_d$ and for $\chi_\ell > 0.2$.

### 6.5.2 Influence of the flexural modulus $c_1$

Here, we perform a statistical analysis of the influence of the fiber flexural modulus $c_1$. Fig. 1.20 (I) shows simulations with random insemination and two different flexural moduli $c_1 = 0.01$ (first row) and $c_1 = 10$ (second row), for $\chi_\ell = 0.35$ and three different unlinking frequencies $\nu_d = 10^{-3}$ (Fig. 1.20 (I A) and (I D)), $\nu_d = 10^{-2}$ (Fig. 1.20 (I B) and (I E)) and $\nu_d = 0.2$ (Fig. 1.20 (I C) and (I F)). Fig. 1.20 (II) shows the values of the fiber SQ $A$ (Fig. 1.20 (II a)), $\Lambda$ (Fig. 1.20 (II b)), $E$ (Fig. 1.20 (II c)) and $N_C$ (Fig. 1.20 (II d)), averaged over 10 simulations and plotted as functions of the unlinking frequency $\nu_d$ for two different values $c_1 = 0.01$ (black curve) and $c_1 = 10$ (blue curve) of the flexural modulus.

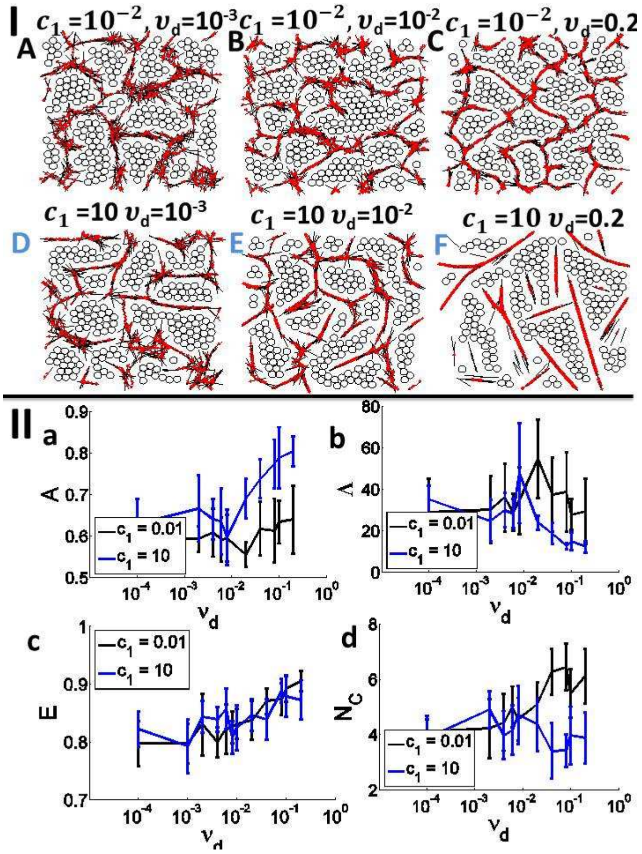

Figure 1.20: (I) Simulations with random insemination and two different flexural moduli $c_1 = 0.01$ (first row) and $c_1 = 10$ (second row), for linked fiber fraction $\chi_\ell = 0.35$ and three different unlinking frequencies $\nu_d = 10^{-3}$ (Figs. (I A) and (I D)), $\nu_d = 10^{-2}$ (Figs. (I B) and (I E)) and $\nu_d = 0.2$ (Figs. (I C) and (I F)). For a small flexural modulus $c_1 = 0.01$, fiber structures change slowly from disorganized clusters (Figs. (I A) and (I B)) to more aligned fiber patterns (Fig. (I C)) as $\nu_d$ increases. A larger value of $c_1 = 10$ leads to more aligned fiber clusters. The morphology changes from well-organized fiber clusters surrounding separated cell clusters (Figs. (I D) and (I E)) to long and rigid fiber threads that fail to surround cell structures (Fig. (I F) as $\nu_d$ increases. (II) Fiber cluster mean alignment $A$ (Fig. (II a)), fiber cluster mean elongation $\Lambda$ (Fig. (II b)), cell cluster mean elongation $E$ (Fig. (II c)) and mean cell cluster number $N_C$ (Fig. (II d)) as functions of the unlinking frequency $\nu_d$ for two different values $c_1 = 0.01$ (black curve) and $c_1 = 10$ (blue curve) of the flexural modulus.

The first row of Figs. 1.20 (I) (Fig. 1.20 (I A), (I B) and (I C)) shows that for a small flexural modulus $c_1 = 0.01$, the cell structures change from well-separated lobule-like cell clusters (Fig. 1.20 (I A)) to slightly more elongated clusters (Fig. 1.20 (I C)) and the fiber structures change from a disorganized fiber network (Fig. 1.20 (I A) or (I B)) to more aligned fiber clusters (Fig. 1.20 (I C)), as $\nu_d$ increases. For a large flexural modulus $c_1 = 10$ (second row of Fig. 1.20 I, i.e. Fig. 1.20 (I D), (I E) and (I F)), the fiber structures are more aligned: the model generates organized fiber clusters able to bend around the cell structures (Fig. 1.20 (I D) and (I E)). For a fast linking-unlinking (Fig. 1.20 (I F)), a rigid fiber network composed of long fiber threads which fail to surround the cell clusters is observed.

These observations are confirmed by the values of the Statistical Quantifiers $A$ and $\Lambda$ (for fiber clusters) and $E$ and $N_C$ (for cell clusters) shown in Figs. 1.20 (II) as functions of the unlinking frequency $\nu_d$, for $c_1 = 0.01$ (black curves) and $c_1 = 10$ (blue curves). Figs. 1.20 (II a) shows that the mean alignment of the fiber clusters increases with $c_1$ (compare the black and blue curves), and the difference between the values of $A$ for $c_1 = 0.01$ and for $c_1 = 10$ increases with the fiber unlinking frequency $\nu_d$. This is because the fibers are more rigidly maintained with a slow linking-unlinking dynamics than with a fast one (see previous section), and are thus less sensitive to alignment. Fig. 1.20 (II b) shows that the mean fiber cluster elongation $\Lambda$ is a non monotonous function of $\nu_d$ for $c_1 = 0.01$ (black curve) and a monotonically decreasing function for $c_1 = 10$ (blue curve). For $c_1 = 0.01$, $\Lambda$ first increases to reach a maximal value at $\nu_d \approx 0.05$ and then decreases. This reflects the ability that the fibers have to surround the cell clusters when the flexural modulus is small and the unlinking frequency $\nu_d$ is moderate, as already seen in the previous section. This ability is lost with a larger flexural modulus and $\Lambda$ becomes just a decreasing function of $\nu_d$.

Fig. 1.20 (II c) shows that the flexural modulus $c_1$ does not seem to significantly change the mean cell cluster elongation. Finally, Fig. 1.20 (II d) reveals that the number of cell clusters $N_C$ is significantly lower for $c_1 = 10$ than for $c_1 = 0.01$ for $\nu_d > 10^{-3}$. For $c_1 = 10$ and $\nu_d \in [10^{-3}, 0.1]$, this is because ECM rigidity is too large and the fibers fail to separate cell structures, compared to the case $c_1 = 1$ (see Main Text). For $\nu_d > 0.1$, we recover the previously described case of a fast fiber linking-unlinking dynamics. As fibers fastly self-organize into long and directed rigid threads, they force the cells to group into chord-like unseparated structures.

To sum up, large flexural modulus favors fiber alignment and ECM rigidity compared to small $c_1$. Moreover, the choice of the flexural modulus has to be carrefully linked to the fiber linking-unlinking dynamics, which also triggers fiber network alignment and rigidity. For a well calibrated fiber linking-unlinking process and increasing values of $c_1$, the structures change from (a) compact middle sized cell clusters in a disorganized fiber network ($c_1 = 0.01$), (b) compact middle sized cell clusters in an organized fiber network ($c_1 = 1$) and (c) elongated cell clusters in fewer quantities inside an organized network ($c_1 = 10$). For $c_1 < 1$, ECM alignment is small and the fiber network cannot easily organize. By contrast, when $c_1 = 1$, ECM alignment is moderate and the fibers that are not too constrained can align. However for $c_1 > 1$, ECM rigidity is too large and this results in elongated cell clusters. Experimentally, it is observed that the lobules are more elongated at the periphery of the tissue than inside. Thus, our results suggest that fibers could be more stretched at the periphery. To support this hypothesis, it would be interesting to develop an experimental quantification method to estimate a local stress tensor similar to what has previously been done for adipocyte stiffness [36]. This analysis suggests that the different morphologies observed in adipose tissues of healthy mice according to the location of fat (central or peripheral)can be due to ECM stiffness. Varying its value is sufficient to break the architecture of the tissue.

### 6.5.3 Influence of the biased insemination

Figs. 1.21 (I) shows simulation results obtained with random insemination (Figs. 1.21 (I A), (I B), (I C)) and with biased insemination for $\alpha = 10^{-3}$ (Figs. 1.21 (I D), (I E), (I F)), for three values of the unlinking frequency $\nu_d$ (from left to right, $\nu_d = 10^{-4}$, $\nu_d = 10^{-2}$ and $\nu_d = 0.2$). Fig. 1.21 (II) shows the values of the SQ $A$ (Fig. 1.21 (II a)), $\Lambda$ (Fig. 1.21 (II b)), $E$ (Fig. 1.21 (II c)) and $N_C$ (Fig. 1.21 (II d)), averaged over 10 simulations, as functions of the unlinking frequency $\nu_d$, for random insemination (in black) and for biased insemination with $\alpha = 10^{-3}$ (in blue). In these simulations, the flexural modulus between linked fibers is $c_1 = 1$ and the linked fiber fraction $\chi_\ell = 0.35$. The numerical and model parameters can be found in Table 1.2.

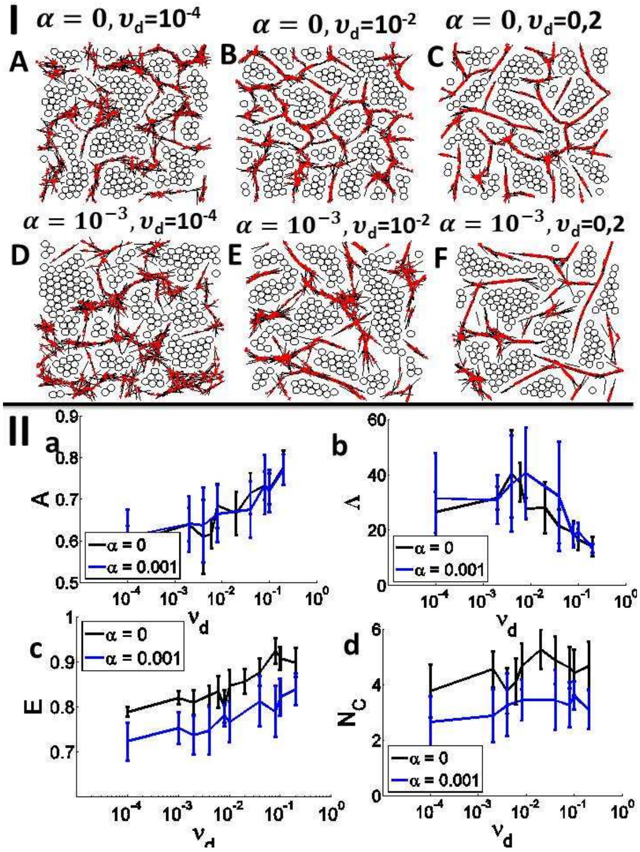

Figure 1.21: (I) Simulations with random insemination (Figs. (I A), (I B), (I C)) and with biased insemination with $\alpha = 10^{-3}$ (Figs. (I D), (I E), (I F)), for three values of the unlinking frequency $\nu_d$ (from left to right, $\nu_d = 10^{-4}$, $\nu_d = 10^{-2}$ and $\nu_d = 0.2$). Values of the flexural modulus $c_1 = 1$ and linked fiber fraction $\chi_\ell = 0.35$ have been used. (II) Fiber cluster mean alignment $A$ (Fig. (II a)), fiber cluster mean elongation $\Lambda$ (Fig. (II b)), cell cluster mean elongation $E$ (Fig. (II c)) and mean cell cluster number $N_C$ (Fig. (II d)) averaged over 10 simulations as functions of the unlinking frequency $\nu_d$ with random insemination (in black) or with biased insemination with $\alpha = 10^{-3}$ (in blue).

Figs. 1.21 (I D), (I E), (I F) show that biased insemination leads to the creation of a smaller number of bigger cell clusters than random insemination (compare with Figs. 1.21 (I A), (I B), (I C)). This is because biased insemination favors insemination of new adipocytes at locations where cell clusters pre-exist. The regroupment of cells into clusters leaves regions devoid of cells (see Figs. 1.21 (I E)). Figs. 1.21 (II a) and (II b) show that biased insemination does not have a significant influence on the fiber cluster alignment $A$, but seems to slightly reduce the fiber elongation. For cell clusters, Fig. 1.21 (II c) shows that biased insemination seems to reduce cell cluster elongation. This can be explained by the fact that cell clusters are larger with biased insemination than with random insemination, which results in a decrease of $E$. In this case, the statistical quantifier $E$ does not allow us to conclude on the form of the cell clusters. Finally, Fig. 1.21 (II d) shows that biased insemination leads to cell clusters in fewer number than random insemination. Indeed, biased insemination favors the recruitement of new cells by existing clusters, leading to larger clusters in fewer number.

Altogether, this analysis demonstrates that biased insemination with small $\alpha$ does not have a significant impact on the cell and fiber structures for a properly chosen fiber linking/unlinking dynamics. This suggests that, in a sufficiently rigid fiber network, cell clusterization is mainly driven by cell-fiber interactions. Cells and fibers self-organize into middle-sized well-separated cell clusters and aligned fiber structures whatever the type of insemination (random or biased with small $\alpha$) is.

### 6.5.4 Anisotropic initial fiber network

As discussed in Main Text, parts of the adipose tissue reveal an anisotropic cell and fiber organization. In order to obtain oriented cell clusters, we studied the properties of the model starting from an initially anisotropic fiber network. For this purpose, we let the initial fiber directional angles $\theta_f^0$ be randomly chosen according to a uniform distribution in the interval $[\theta_1 - \theta_2, \theta_1 + \theta_2]$, where $\theta_2$ is related to the standard deviation of the distribution. Note that the smaller $\theta_2$, the more aligned the fibers initially are. By contrast, the simulations shown so far correspond to a fully isotropic initial network, i.e. to the case $\theta_2 = \pi/2$. The initial number of fiber links was carefully adjusted to be independent of the initial value of $\theta_2$ throughout the forthcoming simulations. Indeed, the probability that pairs of fibers intersect is much smaller in an aligned network than in a fully isotropic one. Simulations of Fig. 1.22 have been obtained with random insemination, flexural modulus $c_1 = 1$ and linked fiber fraction $\chi_\ell = 0.35$, for different unlinking frequencies $\nu_d$ and different values of $\theta_2$. Three types of structures have obtained according to the values of $\nu_d$ and $\theta_2$: (a) lobule-like non oriented cell clusters, (b) lobule-like oriented cell clusters, and (c) elongated and oriented cell clusters. In order to quantify the passage from one morphology to another one, we use the following SQ: the mean cell cluster elongation $E$ and the standard deviation of cell cluster shape anisotropy $\Theta$. We identify the threshold values $E^* = 0.89$ for $E$ (the same value as in section IV-1) and $\Theta^* = 0.7$ for $\Theta$. Structures of type (a) correspond to $\Theta > \Theta^*$ and $E < E^*$. Type (b) is described by $\Theta < \Theta^*$ and $E < E^*$ and finally type (c) by $\Theta < \Theta^*$ and $E > E^*$. Fig. 1.22 shows a phase diagram in the $(E, \Theta)$ plane. Each point in this phase diagram correspond to statistical quantifiers $(E, \Theta)$ averaged over 10 simulations. The red and blue lines correspond to the separatrix between phases (a) and (b) (of equation $\Theta = \Theta^*$) and between phases (b) and (c) (of equation $E = E^*$) respectively. Fig. 1.22 also shows a typical simulation result for each phase, and its position on the phase diagram according to the values of $E$ and $\Theta$.

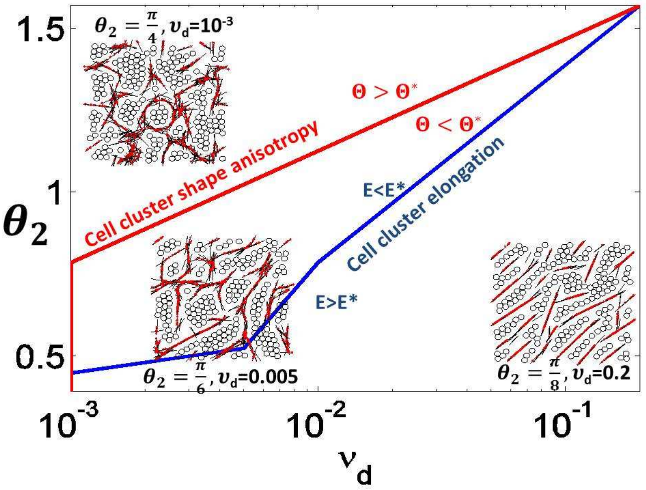

Figure 1.22: Simulation results for an anisotropic initial fiber network. According to the values of the model parameters $\nu_d$ and $\theta_2$, three phases have been obtained and classified by means of the mean cell cluster elongation $E$ and the standard deviation of cell cluster shape anisotropy $\Theta$: Phase (a): for $\Theta > \Theta^*$ and $E < E^*$. Phase (b) for $\Theta < \Theta^*$ and $E < E^*$. Phase (c) for $\Theta < \Theta^*$ and $E > E^*$. This figure displays the phase diagram in the $(E, \Theta)$ plane. Each point in this phase diagram correspond to statistical quantifiers $(E, \Theta)$ averaged over 10 simulations. The red and blue lines correspond to the separatrix between phases (a) and (b) (of equation $\Theta = \Theta^*$) and between phases (b) and (c) (of equation $E = E^*$) respectively. The figure also displays a typical simulation result for each phase, and its position on the phase diagram according to the values of $E$ and $\Theta$. The simulations were performed with random insemination, linked fiber fraction $\chi_\ell = 0.35$, fiber flexural modulus $c_1 = 1$.

Fig. 1.22 shows that, when the initial fiber network is anisotropic, the emergence of a shape anisotropy of the cell clusters depends on the fiber linking-unlinking dynamics. For a slow linking-unlinking dynamics ($\nu_d = 10^{-3}$) the initial orientation of the fibers must be strongly biased to obtain directionality in the cell and fiber final structures. Otherwise (for $\theta_2 > \frac{\pi}{5}$), the initial orientation of the network is lost, and cell structures without preferential direction are obtained (see Fig. 1.22 A). This suggests that for this slow linking-unlinking frequency, cells disturb the initial organization of the fiber network so much that this initial organization is lost. For a fast fiber linking-unlinking dynamics ($\nu_d = 0.2$ see Fig. 1.22 C), cell structures are elongated due to the rigidity of the fiber network induced by the fast linking frequency and the action of the alignment torque at the created links. In this case, the fiber network imposes its preferred direction to cell cluster growth and we recover elongated cell clusters as in the case of an initially isotropic fiber network (see section IV.1). Fig. 1.22 (B) shows that there exist a range of values of $\nu_d$ and $\theta_2$ for which the model is able to generate lobule-like cell clusters having anisotropic shapes and a preferred shape anisotropy direction. These configurations are obtained for $\nu_d \in ]10^{-3}, 10^{-2}[$ and for $\theta_b \in [\frac{\pi}{8}, \frac{\pi}{4}]$.

# Bibliography

[1] Ouchi N, Parker J-L, Lugus J-J and Walsh K (2011), Adipokines in inflammation and metabolic disease. Nat Rev Immunol, 11:85-97.

[2] Sepe A, Tchkonia T, Thomou T, Zamboni M, Kirkland J-L (2011) Aging and regional differences in fat cell progenitors - a mini-review. Gerontology 57(1):66-75.

[3] Cristancho A-G, Lazar M-A (2011) Forming functional fat: a growing understanding of adipocyte differentiation. Nat Rev Mol Cell Biol 11:722-34.

[4] Wasserman F (2011) The development of adipose tissue. Compr physiol Supplement 15: Handbook of Physiology, Adipose Tissue:87-100 First published in print 1965. doi:101002/cphycp050110.

[5] Napolitano L (1963) The differentiation of white adipose cells an electron microscope study. J Cell Biol 18:663-679.

[6] Divoux A, Clement K (2011) Architecture and the extracellular matrix: the still unappreciated components of the adipose tissue. Obes Rev 12:494-503.

[7] Sun K, Tordjman J, Clement K, Scherer PE (2013) Fibrosis and adipose tissue dysfunction. Cell Metab 18(4):470-477.

[8] Drasdo D (2003) On selected individual-based approaches to the dynamics in multicellular systems. Multiscale Modelling and Numerical Simulations, eds W. Alt, M. Chaplain, M. Griebel, J. Lenz (Birkhäuser, Basel, Switzerland), pp 109-203.

[9] Hwang M, Garbey M, Berceli S-A, Tran-Son-Tay R (2009) Rule-Based Simulation of Multi-Cellular Biological Systems-A Review of Modeling Techniques, Cell Mol Bioeng 2(3):285-294.

[10] Drasdo D, Höhme S (2005) A single cell based-model of tumor growth in-vitro: monolayers and spheroids. Phys Biol 2(3):133-47.

[11] Friedl P, Bröcker E-B (2000) The biology of cell locomotion within three dimensional extracellular matrix. Cell Mol Life Sci 57(1):41-64

[12] Murray J-D, Oster G-F, Harris A-K (1983) A mechanical model for mesenchymal morphogenesis. J Math Biol 17:125-129.

[13] Lushnikov P-M, Chen N, , Alber M (2008) Macroscopic dynamics of biological cells interacting via chemotaxis and direct contact. Physic Rev E 78:061904

[14] Ambrosi D, Bussolino F, Preziosi L (2005) A review of vasculogenesis models. Journal of Theoretical Medecine 6(1):1-19.

[15] Guido S, Tranquillo R-T (1993) A methodology for the systematic and quantitative study of cell contact guidance in oriented collagen gels correlation of fibroblast orientation and gel birefringence. J Cell Sci 105:317-331.

[16] Dickinson R-B (2000) A generalized transport model for biased cell migration in an anisotropic environment. J Math Biol 40:97-135.

[17] Hillen T (2006) Mesoscopic and macroscopic models for mesenchymal motion. J Math Biol 53(4):585-616.

[18] Hillen T, Hinow P, Wang Z-A (2010) Mathematical analysis of a kinetic model for cell movement in network tissues. Discrete and Continuous Dynamical Systems 14(3):1055- 1080.

[19] Alonso R, Young J, Cheng Y (2014) A particle interaction model for the simulation of biological and cross-linked fibres inspired from flocking theory. Cellular and molecular bioengenering 7(1):58-72.

[20] Taber L-A, Shi Y, Yang L, Bayly P-V (2011) A poroelastic model for cell crawling including mechanical coupling between cytoskeletal contraction and actin polymerization. J Mech Mat Struct 6(1-4):569-589.

[21] Joanny J-F, Jülicher F, Kruse K, Prost J (2007) Hydrodynamic theory for multicomponent active polar gels. New J Phys 9(442):422.

[22] Shraiman B-I (2005) Mechanical feedback as a possible regulator of tissue growth. PNAS 102(9):3318-3323.

[23] Arner E, et al. (2010) Adipocyte turnover: relevance to human adipose tissue morphology. Diabetes 59(1):105-109.

[24] Ciarletta P, Ben Amar M (2009) A finite dissipative theory of temporary interfillar bridges in the extra-cellular matrix of ligaments and tendons. Interface 6(39):909-924.

[25] Ailhaud G (1999) Cross talk between adipocytes and their precursors: relationships with adipose tissue development and blood pressure. Annals of the New York Academy of Sciences 892:127-133.

[26] Hemmingsen M, et al. (2013) The role of paracrine and autocrine signaling in the early phase of adipogenic differentiation of adipose-derived stem cells. PloS One 8(5):e63638.

[27] Corvera S, Gealekman O (2014) Adipose tissue angiogenesis: impact on obesity and type-2 diabetes. Biochim Biophys Acta 1842(3):463-72.

[28] Friedl P, Hegerfeldt Y, Tusch M (2004) Collective cell migration in morphogenesis and cancer. Int J Dev Biol 48:441-449.

[29] Galle J, Hoffmann M, Aust G (2009) From single cells to tissue architecture : a bottom-up approach to modelling the spatio-temporal organization of complex multicellular systems. J Math Biol 58(1-2):261-83.

[30] Chen C-Y, Byrne H-M, King J-R (2001) The influence of growth induced stress from the surrounding medium on the development of multicell spheroids. J Math Biol 43:191-220.

[31] Rodriguez E-K, Hoger A, McCulloch A-D (1994) Stress-dependent finite growth in soft elastic tissues. J Biomech 27(4):455-467.

[32] Preibisch S, Saalfeld S, Tomancak P (2009) Globally optimal stitching of tiled 3d microscopic image acquisitions. Bioinformatics 25(11):1463-1465.

[33] Vincent L, Soille P (1991) Watersheds in digital spaces: An efficient algorithm based on immersion simulations. IEEE Trans Pattern Anal Mach Intell 13(16):583-598.

[34] Friedl P, Bröcker E-B (2000) The biology of cell locomotion within three dimensional extracellular matrix. *Cell Mol Life Sci* 57(1):41-64.

[35] Arrow KJ, Hurwicz L, Uzawa H (1958) Studies in linear and nonlinear programming, Stanford University Press

[36] Shoham N, et al. (2014) Adipocyte stiffness increases with accumulation of lipid droplets. *Biophys J* 106(6):1421-31.

# Chapter 2

# Macroscopic model for linked fibers with alignment interactions

This chapter have been written in collaboration with P. Degond and F. Delebecque and has given rise to an article to be submitted.

---

**Abstract:** We introduce an individual-based model for fiber elements having the ability to cross-link or unlink each other and to align with each other at the cross links. We first formally derive a kinetic model for the fiber and cross-links distribution functions. We then consider the fast linking/unlinking regime in which the model can be reduced to the fiber distribution function only and investigate its diffusion limit. The resulting macroscopic model consists of a system of nonlinear diffusion equations for the fiber density and mean orientation. In the case of a homogeneous fiber density, we show that the model is elliptic.

---

**Acknowledgements:** This work was supported by the "Région Midi Pyrénées", under grant APRTCN 2013. PD acknowledges support from the British "Engineering and Physical Research Council" under grant ref: EP/M006883/1, from the Royal Society and the Wolfson foundation through a Royal Society Wolfson Research Merit Award and from NSF by NSF Grant RNMS11-07444 (KI-Net). PD is on leave from CNRS, Institut de Mathématiques de Toulouse, France. DP gratefully acknowledges the hospitality of Imperial College London, where part of this research was conducted.

**Key words:** fibers, cross-links, allignment, kinetic equation, diffusion approximation, von Mises Fisher distribution, generalized collision invariant, ellipticity

**AMS Subject classification:** 82C31, 82C40, 82C70, 92C10, 92C17,

## Sommaire

1 **Introduction** . . . . . . . . . . . . . . . . . . . . . . . . . . 102

2 **Individual Based Model** . . . . . . . . . . . . . . . . . . . 106

3 **Derivation of a kinetic model** . . . . . . . . . . . . . . . 111

4 **Scaling** . . . . . . . . . . . . . . . . . . . . . . . . . . . . . 114

5 **Large scale limit** . . . . . . . . . . . . . . . . . . . . . . 123

6 **Homogeneous fiber distribution** . . . . . . . . . . . . . 133

7 **Conclusion** . . . . . . . . . . . . . . . . . . . . . . . . . . 138

8 **Appendix A** . . . . . . . . . . . . . . . . . . . . . . . . . . 142

9 **Appendix B** . . . . . . . . . . . . . . . . . . . . . . . . . . 150

# 1 Introduction

The topic of complex systems is attracting an increasingly abundant literature, due to its paramount importance in life and social sciences. Complex systems consist of a large number of agents interacting through local interactions only and yet able to self-organize into large-scale coherent structures and collective motion [36]. Among examples of interactions leading to collective motion, the alignment interaction has been the subject of many studies since the seminal work of Vicsek and co-authors [35]. In Vicsek's model, self-propelled point particles tend to align with their neighbors up to some noise. Vicsek's particles are polar: they carry a definite direction and orientation defined by the unit vector of their propulsion velocity. Their alignment interaction is also polar in the sense that a particle moving in an opposite direction to its neighbors will eventually reverse its direction of motion. However, other alignment rules have been studied as well. Polar particles can be subjected to nematic alignment. In this case, a particle moving in an opposite direction to its neighbors will not reverse its direction of motion, as opposed to the polar alignment case. Nematic alignment has been used as a model for the volume exclusion interaction [5, 20, 29]. Particles can also be apolar, for instance if they randomly reverse their direction of motion. Apolar particles interacting through nematic alignment have been proposed as a model for vibrating rods [6] or fiber networks [1]. In the related field of nematic liquid crystals, volume exclusion interactions between rod-like particles are also modelled as an alignment force [18, 24, 28]. But additionally, the molecules are convected by the background solvent and are subjected to rotation by the fluid shear. Additionally, they contribute to the fluid dynamics of the liquid solvent through an additional extra-stress tensor. Usually, the polymer chains are supposed of fixed length, although lately, models of polymer chains of variables lengths have appeared [12].

In the present work, we are interested in a system consisting of fibers (or polymer chains) of variable lengths. This model aims to describe the network of collagen fibers in a fibrous tissue. We model fiber length variation (through polymerization / depolymerization) as well as the ability for the fibers to establish cross-links between them by the same basic rules described as follows. We assume the existence of a fiber unit element (or monomer) modeled as a line segment of fixed length $L$. We suppose that two fiber elements that cross each-other may form a link, thereby creating a longer fiber. There is no limit to the number of cross-links a given fiber can make. Therefore, the fibers have the ability to branch off and to achieve complex network topologies. We include fiber resistance to bending by assuming the existence of torque which, in the absence of any other force, makes the two linked fiber elements align with each other. Fibers are also subject to random positional and orientational noise and to external positional and orientational potential forces. Finally, cross-links may also be removed to model possible fiber breakage or depolymerization.

Our model features apolar fiber particles (since they are not self-propelled), interacting through nematic alignment with the other fibers they are linked to. Thus, the model bears analogies with previous models of apolar particles interacting through nematic alignment [6, 1]. However, the interaction network topology (which keeps track of which fiber pairs are cross-linked) is different, as ours is determined by the distribution of cross-links. The fact that this network topology changes with time through dynamic cross-linking or unlinking processes is one specific feature of the present work. In the absence of cross-link remodeling, i.e. when the cross-links lifetime is infinite and no new cross-links is created, each connected component of the fiber network can be seen as an unstretchable elastic string since all connected fiber elements will spontaneously align with each other. However, cross-link removal or creation events (supposed to occur at Poisson distributed random times) introduce a fluid-like component to the rheology of the fibers, thereby confering some visco-elastic character to the medium. Cross-link-governed statics and dynamics of fiber networks have been intensely studied in the literature [3, 8, 9, 21, 27]. However, most models consider passive cross-links which only act on the fibers by a spring-like attractive force. Here, our description introduces active links which tend to align the two fibers with each other. By doing so, we are also able to take into account fiber breakage, elongation and branching just in addition to and in the same way as fiber linking/unlinking because cross-linked fiber elements can be seen as two parts of the same fiber. Another difference from previous literature is that fibers in our model are subject to noise making the system more akin to a fluid or a gas than to a solid. By contrast to classical polymeric fluid studies, we do not assume that the fibers are transported by a fluid and modify its rheological properties but this feature could be added in future work.

This model was first introduced in [30] where it was coupled with the dynamics of spherical particles modelling cells. This model has been built to describe the self-organization of the adipose tissue, where spheres represent adipocytes and fibers, the surrounding collagen fibers. In this work, we demonstrated that the interaction between cells and fibers led to the spontaneous formation of cell clusters of ovoid shape akin to the adipose lobules that form the functional subunits of the adipose tissue. In [30], only a discrete Individual-Based Model (IBM) was considered. The present work focuses on the fibrous medium only and aims to derive meso and macroscopic models from the background IBM using techniques of kinetic theory. Indeed, the computational cost of an IBM scales polynomially with the number of agents, which makes them practically untractable for large systems. Continuum models allow to break this curse of scaling but they suppose that a suitable coarse-graining procedure which averages out the fine-scale structure has been applied to the IBM. In order to capture the correct effects of the fine-scale dynamics on the large-scale structures, it is of paramount importance to perform this coarse-graining as rigorously as possible. This is the aim of the present work.

The derivation of a continuum model from the fiber dynamics is done in two steps. We first derive a kinetic model from the underlying IBM and secondly, we perform a diffusion approximation of the latter to obtain the continuum model. The kinetic model provides a statistical mechanics description of the underlying IBM by investigating how the probability distribution of fibers in position and orientation space evolves in time. Here, we will show that the mere distribution of fibers is not sufficient to close the system and that the cross-link probability distribution needs to be introduced. The cross-links provide correlations between the fibers and consequently their distribution can be viewed as similar to the two-particle fiber distribution. We will formally show that the knowledge of the one- and two-particle distributions is enough to provide a valid kinetic description of the system. Of course, this fact needs to be confirmed by numerical simulations and mathematical proofs. But if it proves correct, this model provides a unique example, to our knowledge, of a kinetic model which is closed at the level of the two-particle distribution function. Indeed, the question whether or not kinetic descriptions must include higher order distribution functions has been actively discussed in the recent years [10, 11, 25, 26]. We also note that the introduction of the cross-link distribution functions provides an economic and efficient way of statistically tracking the fiber network topology. This methodology could prove interesting for other situations of dynamically evolving networks.

The second step consists of a diffusion approximation of the previously derived kinetic model. It starts with changing the time and space units to macroscopic ones. The macroscopic space unit is large compared to the typical spatial scale of the fibers, e.g. their length and the macroscopic time unit is large to the typical time scale of the fibers, e.g. the time needed for two linked fibers to align with each other. A diffusive rescaling relates the time and space rescaling in such a way that the ratio of the microscopic to macroscopic time units is the square of that of the spatial units. This choice is made necessary by the absence of any polarization in the medium which makes diffusive behavior dominate. A key assumption that we make here is to assume that the linking/unlinking frequencies are very large: the typical linking/unlinking time measured in the macroscopic time unit scales like the square of the typical fiber alignment time (also measured in macroscopic unit), which is very small. This allows us to deduce an algebraic relation between the cross-link distribution function and the fiber distribution function, and to realize a closure of the kinetic equation at the level of the fiber distribution function alone. This assumption is questionable given the biological applications we have in mind, but it provides a first step towards a more complete theory involving finite linking/unlinking times.

From these assumptions, we derive a singular perturbation problem for the fiber kinetic distribution function that has the form of a classical diffusion approximation problem [4, 16, 31], whose leading order collision operator comes from the nematic alignment of the fibers due to the alignment torque at the cross-links. This operator has equilibria in the form of generalized von Mises distributions of the fiber directions. The von Mises distribution extends Gaussian distributions to probabilities defined on the unit circle. It is peaked around a mean fiber direction angle $\theta_0$. The continuum model describes how the local fiber density $\rho$ and the local fiber direction $\theta_0$ vary as functions of position $x$ and time $t$. To obtain these evolution equations, we must integrate the kinetic equation against suitably chosen collision invariants. This operation cancels the singularly perturbed term. Here, the difficulty it that there exists only one such collision invariant in the classical sense, which allows us to find an equation for the density $\rho$ only. To find an equation for the mean fiber direction $\theta_0$, we use the recently developed theory of Generalized Collision Invariants (GCI) [14, 15, 17, 19]. The resulting system is a nonlinear coupled system of diffusion equations for $\rho$ and $\theta_0$. In the case of a homogeneous fiber distribution, when the density is uniform in space and constant in time, we show that the resulting nonlinear diffusion model for $\theta_0$ is parabolic. In future work, it will be shown that this system is well-posed. Numerical simulations will demonstrate that the continuum model provides a consistent approximation of the underlying IBM for the fiber dynamics. Numerous macroscopic models for fibrous media have been previously considered in the literature but very few of them have been derived from an underlying IBM. Most of them are heuristically derived from continuum theories such as mechano-chemical principles [2, 33], thermodynamics [22] or viscous fluid mechanics [23].

The outline of this paper is as follows. In Section 2, we start with the description of the IBM. Section 3 is devoted to the derivation of the kinetic model. The scaling assumptions and the scaled kinetic equations are derived in Section 4. In Section 5, we perform the large scale limit of the so-obtained equations. Finally, Section 6 is devoted to the analysis of the model in the case of a homogeneous fiber density. Conclusions and perspectives are drawn in Section 7. Some technical computations are detailed in Appendices.

## 2 Individual Based Model for fibers interacting through alignment interactions

We intend to model a medium consisting of interconnected fibers. To simplify the geometric description of fibers, we decompose them into fiber elements of uniform fixed length and consider that a fiber consists of several connected fiber elements. The link between two connected fibers can be positionned at any point along the fibers (not only the extremities) and a given fiber can be connected to any number of other fibers, thereby allowing to model the branching off of a fiber into several branches. The links are not permanent. The topology of the fiber network is constantly remodelled through link creation/deletion processes. To model fiber resistance to bending, we suppose that pairs of linked fibrs are subject to a torque that tends to align the two fibers with respect to each other. Finally, the fibers are subject to random positional and orientational noises to model the movements of the tissue and to positional and orientational potential forces to model the action of external elements. In the case of a fibrous tissue, these external elements may consist of cells or other tissues.

In this paper, we restrict ourselves to a two-dimensional model. We consider a set of $N$ fiber elements modelled as small line segments of uniform and fixed length $L$, described by their center $X_i \in \mathbb{R}^2$ and their angle $\theta_i$ with respect to a fixed reference direction. As the fiber elements are assumed apolar, $\theta_i$ is an angle of lines, i.e. $\theta_i \in [-\frac{\pi}{2}, \frac{\pi}{2})$ modulo $\pi$. We define energies related to each of the phenomena described above namely an energy for the maintenance of the links $W_{\text{links}}$, an energy for the alignment torque $W_{\text{align}}$, an energy for the action of the external elements $W_{\text{ext}}$, an energy for the noise contribution $W_{\text{noise}}$ and a total energy made of the sum of all these energies:

$$W_{\text{tot}} = W_{\text{links}} + W_{\text{ext}} + W_{\text{align}} + W_{\text{noise}}, \tag{2.1}$$

All these energies are functions of the $N$ fiber positions $(X_i)_{i=1}^N$ and orientations $(\theta_i)_{i=1}^N$. Note that $W_{\text{noise}}$ is rather an entropy than an energy, so that $W_{\text{tot}}$ is indeed the total free energy of the system. Fiber motion and rotation during a time interval between two fiber linking-unlinking events is supposed to occur in the steepest descent direction to this free energy, namely according to:

$$\frac{dX_i}{dt} = -\mu \, \nabla_{X_i} W_{\text{tot}}, \quad \forall i \in \{1, \ldots, N\}, \tag{2.2}$$

$$\frac{d\theta_i}{dt} = -\lambda \, \partial_{\theta_i} W_{\text{tot}}, \quad \forall i \in \{1, \ldots, N\}, . \tag{2.3}$$

Eqs. (2.2) and (2.3) express the motion and rotation of the individuals in an overdamped regime in which the forces due to friction are very large compared to the inertial forces. Fiber velocity and angular speed are proportional to the force exerted on the fiber through two mobility coefficients $\mu$ and $\lambda$ which are considered given. We now detail the expressions of the four energies involved in the expression (2.1) of the total free energy of the system, as well as how Eqs. (2.2) and (2.3) are supplemented by Poisson jump processes when a linking/unlinking event occurs.

To define the expression of $W_{\text{links}}$, we consider a time at which no linking/unlinking process occurs. Then, the set of links is well-defined and supposed to have $K$ elements. Let $k \in \{1, \ldots, K\}$ be a given link and denote by $(i(k), j(k))$ the pair of indices corresponding to the two fibers connected by this link. To make the labeling of the pair unique, we assume without loss of generality that the first element of the linked pair is always the one with lowest index, i.e. $i(k) < j(k)$. The link is supposed to connect two points $X_{i(k)}^k$ and $X_{j(k)}^k$ on fibers $i(k)$ and $j(k)$ respectively. These points are determined by the algebraic distances $\ell_{i(k)}^k$ and $\ell_{j(k)}^k$ to the centers $X_{i(k)}$ and $X_{j(k)}$ of the two fibers respectively; We thus have the relation:

$$X_{i(k)}^k = X_{i(k)} + \ell_{i(k)}^k \omega_{i(k)}, \quad X_{j(k)}^k = X_{j(k)} + \ell_{j(k)}^k \omega_{j(k)},$$

where $\ell_{i(k)}^k$, $\ell_{j(k)}^k \in [-L/2, L/2]$ and where, for any fiber $i$, we let $\omega_i = (\cos\theta_i, \sin\theta_i)$ be the unit vector in the direction of the fiber. All along the link lifetime, the link places a spring-like restoring force that attracts $X_{i(k)}$ back to $X_{j(k)}$ (and vice-versa) as soon as their are displaced one with respect to each other. This restoring force gives rise to a potential energy $V(X_{i(k)}, \theta_{i(k)}, \ell_{i(k)}^k, X_{j(k)}, \theta_{j(k)}, \ell_{j(k)}^k)$, with

$$V(X_1, \theta_1, \ell_1, X_2, \theta_2, \ell_2) = \frac{\kappa}{2} |X_1 + \ell_1 \omega(\theta_1) - (X_2 + \ell_2 \omega(\theta_2))|^2, \tag{2.4}$$

where $\kappa$ is the intensity of the restoring force. Obviously, the larger $\kappa$, the better the maintainance of the link is ensured. The potential $W_{\text{links}}$ is then assumed to be the sum of all the linked fiber spring forces:

$$W_{\text{links}} = \frac{1}{2}\sum_{k=1}^{K} V(X_{i(k)}, \theta_{i(k)}, \ell^k_{i(k)}, X_{j(k)}, \theta_{j(k)}, \ell^k_{j(k)}). \tag{2.5}$$

We stress the fact that the quantities $\ell^k_{i(k)}$ and $\ell^k_{j(k)}$ remain constant throughout the link lifetime. They are determined at the time of the creation of the link (see below and Fig. 2.23).

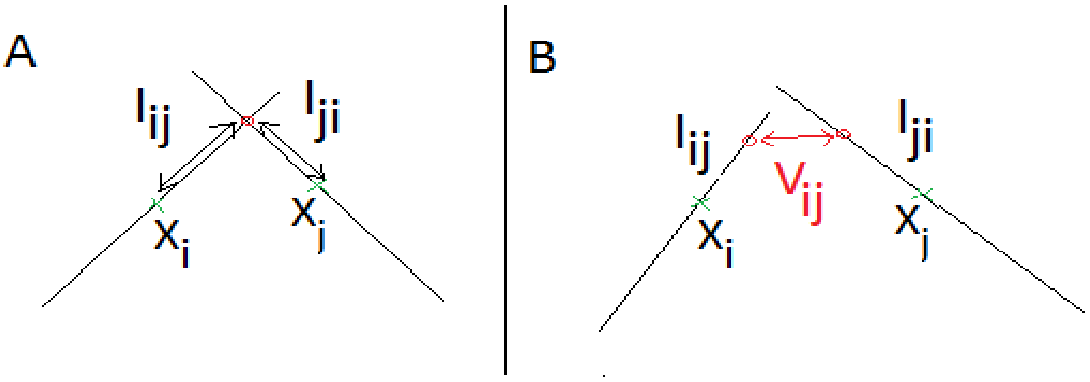

Figure 2.23: Intersecting linked fibers. $l_{ij}$ and $l_{ji}$ refer to $\bar{\ell}(X_i, \theta_i, X_j, \theta_j)$ and $\bar{\ell}(X_j, \theta_j, X_i, \theta_i)$ (2.12). A. Situation at linking time. B. Restoring potential $V_{ij}$ (2.4) after motion of the fibers.

The external potential $W_{\text{ext}}$ associated with the external forces is supposed to be the sum of potential forces $U(X_i, \theta_i)$ acting on each of the $N$ fibers:

$$W_{\text{ext}} = \sum_{i=1}^{N} U(X_i, \theta_i). \tag{2.6}$$

Here, $U(x, \theta)$ is a given, possibly time-dependent smooth function. In the case where the system describes the collagen fibers in a tissue, $U$ aims to model the presence of cells or other organs.

Linked fibers are subjected to an alignment force at their junction to model fiber resistance to bending. This force tends to align linked fibers $i(k)$ and $j(k)$ and derives from the potential $b(\theta_{i(k)}, \theta_{j(k)})$ which reads:

$$b(\theta_1, \theta_2) = \alpha |\sin(\theta_1 - \theta_2)|^{\beta}, \tag{2.7}$$

where $\alpha$ plays the role of a flexural modulus and $\beta$ is a modeling parameter. The binary alignment potential only depends on the angles $\theta_1$ and $\theta_2$, and the total alignment energy $W_{\text{align}}$ is supposed to be the sum of all the binary alignment interactions:

$$W_{\text{align}} = \frac{1}{2} \sum_{k=1}^{K} b(\theta_{i(k)}, \theta_{j(k)}). \tag{2.8}$$

We include random positional and orientational motion of the fiber elements which, in the context of tissue dynamics, originate from the random movements of the subject. With this aim, we introduce an entropy term:

$$W_{\text{noise}} = d \sum_{i=1}^{N} \log(\tilde{f})(X_i, \theta_i), \tag{2.9}$$

where $\tilde{f}$ is a 'regularized density':

$$\tilde{f}(x, \theta) = \frac{1}{N} \sum_{i=1}^{N} \xi^N(x - X_i)\, \eta^N(\theta - \theta_i).$$

Here, $\xi^N$ and $\eta^N$ are regularization functions which allow to define the logarithm of $\tilde{f}$ and have the following properties:

$$\begin{aligned}
&\xi^N \in C^\infty(\mathbb{R}^2), \quad \eta^N \in C^\infty_{per}([-\frac{\pi}{2}, \frac{\pi}{2}]), \quad \xi^N \geq 0, \quad \eta^N \geq 0, \\
&\int \xi^N(x) dx = 1, \quad \int_{-\pi}^{\pi} \eta^N(\theta) \frac{d\theta}{2\pi} = 1, \\
&\text{Supp}(\xi^N) \subset B(0, R^N), \quad \text{Supp}(\eta^N) \subset [-M^N, M^N],
\end{aligned}$$

where $C^\infty(\mathbb{R}^2)$ is the set of infinitely differentiable functions on $\mathbb{R}^2$, $C^\infty_{per}([-\frac{\pi}{2}, \frac{\pi}{2}])$ the set of periodic $C^\infty$ functions of $[-\frac{\pi}{2}, \frac{\pi}{2}]$ and Supp stands for the support of a function. Here, $R^N$ and $M^N$ are chosen such that $\sqrt{N} R^N$ and $N M^N \to \infty$ as $N \to \infty$. The mean interparticle distance in $x$ and $\theta$ are respectively of order $\frac{1}{\sqrt{N}}$ and $\frac{1}{N}$. This condition is equivalent to $\frac{1}{\sqrt{N} R^N} \to 0$ and $\frac{1}{N M^N} \to 0$, which means that as $N \to \infty$, the number of particles inside the support of a regularizing kernel tends to infinity. This way of modeling the influence of the noise is customary in polymer dynamics [7]. In the next section, we show that such an entropy term gives rise to diffusion terms at the level of the mean-field kinetic model.

By inserting (2.5), (2.6), (2.8) and (2.9) into (2.2), (2.3), we find the fiber equation of motion, during any time interval between two linking/unlinking events:

$$\begin{aligned}
\frac{dX_i}{dt} =& -\mu\Bigg[\frac{1}{2}\sum_{k=1,i(k)=i}^{K} \nabla_{x_1} V(X_{i(k)},\theta_{i(k)},\ell^k_{i(k)},X_{j(k)},\theta_{j(k)},\ell^k_{j(k)}) \\
&+\frac{1}{2}\sum_{k=1,j(k)=i}^{K} \nabla_{x_2} V(X_{i(k)},\theta_{i(k)},\ell^k_{i(k)},X_{j(k)},\theta_{j(k)},\ell^k_{j(k)}) + \nabla_x(U+\log \tilde{f}^N)(X_i,\theta_i)\Bigg], \\
\frac{d\theta_i}{dt} =& -\lambda\Bigg[\frac{1}{2}\sum_{k=1,i(k)=i}^{K} \partial_{\theta_1} V(X_{i(k)},\theta_{i(k)},\ell^k_{i(k)},X_{j(k)},\theta_{j(k)},\ell^k_{j(k)}) \\
&+\frac{1}{2}\sum_{k=1,j(k)=i}^{K} \partial_{\theta_2} V(X_{i(k)},\theta_{i(k)},\ell^k_{i(k)},X_{j(k)},\theta_{j(k)},\ell^k_{j(k)}) + \partial_\theta(U+\log \tilde{f}^N)(X_i,\theta_i) \\
&+\frac{1}{2}\sum_{k=1,i(k)=i}^{K} \partial_{\theta_1} b(\theta_{i(k)},\theta_{j(k)}) + \frac{1}{2}\sum_{k=1,j(k)=i}^{K} \partial_{\theta_2} b(\theta_{i(k)},\theta_{j(k)})\Bigg],
\end{aligned}$$

which we can write:

$$\begin{aligned}
\frac{dX_i}{dt} =& -\mu\Bigg[\Bigg(\frac{1}{2}\sum_{k=1}^{K}\delta_{i(k)}(i)\nabla_{x_1}V + \frac{1}{2}\sum_{k=1}^{K}\delta_{j(k)}(i)\nabla_{x_2}V\Bigg)(C^k_{i(k),j(k)}) \\
&+\nabla_x(U+\log\tilde{f}^N)(X_i,\theta_i)\Bigg],
\end{aligned} \tag{2.10}$$

$$\begin{aligned}
\frac{d\theta_i}{dt} =& -\lambda\Bigg[\Bigg(\frac{1}{2}\sum_{k=1}^{K}\delta_{i(k)}(i)\partial_{\theta_1}V + \frac{1}{2}\sum_{k=1}^{K}\delta_{j(k)}(i)\partial_{\theta_2}V\Bigg)(C^k_{i(k),j(k)}) + \partial_\theta(U+\log\tilde{f}^N)(X_i,\theta_i) \\
&+\Bigg(\frac{1}{2}\sum_{k=1}^{K}\delta_{i(k)}(i)\partial_{\theta_1}b + \frac{1}{2}\sum_{k=1}^{K}\delta_{j(k)}(i)\partial_{\theta_2}b\Bigg)(\theta_{i(k)},\theta_{j(k)})\Bigg],
\end{aligned} \tag{2.11}$$

with $C^k_{i(k),j(k)} = (X_{i(k)},\theta_{i(k)},\ell^k_{i(k)},X_{j(k)},\theta_{j(k)},\ell^k_{j(k)})$ and $\delta_{i(k)}(i)$ is the Kronecker symbol, i.e. $\delta_{i(k)}(i) = 1$ if $i(k) = i$ and $\delta_{i(k)}(i) = 0$ otherwise.

When two fibers $i$ and $j$ intersect each other, because of the continuity of their motion, they are going to intersect each other during a time interval $[t_*, t^*]$. We assume that, during this time span, the linking probability follows a Poisson process of parameter $\nu_f$, i.e. the probability that a link is formed during the interval $[t_*, t]$ with $t < t^*$ is $1 - e^{-\nu_f(t-t_*)}$. Only one link can be formed between the two fibers of the same fiber pair. Supposing that a link, indexed by $k$ is formed between the fibers $i$ and $j$ (such that $i = i(k)$ and $j = j(k)$ if $i < j$) at a time $t_k \in [t_*, t^*]$, we denote by $X_k$ the attachment site of the link. The distance $\bar{\ell}(X_{i(k)},\theta_{i(k)},X_{j(k)},\theta_{j(k)})$ between the center $X_{i(k)}$ of fiber $i(k)$ to the $k$-th link attachment site $X^k$ with fiber

$j(k)$ (see Figure 2.23.B) can be directly computed by:

$$\bar{\ell}(X_{i(k)},\theta_{i(k)},X_{j(k)},\theta_{j(k)}) = \frac{(x_{j(k)}-x_{i(k)})\sin\theta_{j(k)} - (y_{j(k)}-y_{i(k)})\cos\theta_{j(k)}}{\sin(\theta_{j(k)}-\theta_{i(k)})}, \quad (2.12)$$

where $X_{i(k)} = (x_{i(k)}, y_{i(k)})$ are the coordinates of the center of fiber $i(k)$. For $X=(x,y)$ and $\omega=(\alpha,\beta)$, we denote by $X\times\omega = x\beta - y\alpha$.

Then, $\bar{\ell}(X_{i(k)},\theta_{i(k)},X_{j(k)},\theta_{j(k)})$ can be written:

$$\bar{\ell}(X_{i(k)},\theta_{i(k)},X_{j(k)},\theta_{j(k)}) = \frac{|(X_{j(k)}-X_{i(k)})\times\omega(\theta_{j(k)}|}{|\omega(\theta_{i(k)})\times\omega(\theta_{j(k)})|},$$

where again, $\omega(\theta)=(\cos\theta,\sin\theta)$ is the directional vector associated to angle $\theta$. The fact that the two fibers are intersecting each other at time $t_k$ is written:

$$|\bar{\ell}(X_{i(k)},\theta_{i(k)},X_{j(k)},\theta_{j(k)})| \le \frac{L}{2}, \quad \text{and} \quad |\bar{\ell}(X_{j(k)},\theta_{j(k)},X_{i(k)},\theta_{i(k)})| \le \frac{L}{2},$$

where $L$ is the fiber length and where all positions and angles are evaluated at time $t_k$. The quantities $\bar{\ell}(X_{i(k)},\theta_{i(k)},X_{j(k)},\theta_{j(k)})$ and $\bar{\ell}(X_{j(k)},\theta_{j(k)},X_{i(k)},\theta_{i(k)})$ at the time $t_k$ of the formation of the link set the positions of the attachment sites $X^k_{i(k)}$ and $X^k_{j(k)}$ of the link on fibers $i$ and $j$. Therefore, $\ell^k_{i(k)}$ and $\ell^k_{j(k)}$ remain constant throughout the link lifetime and equal to their value at the time $t_k$. So, we have

$$\frac{d}{dt}\ell^k_{i(k)} = \frac{d}{dt}\ell^k_{j(k)} = 0,$$

throughout the lifetime of the link.

We also assume that existing links can disappear according to a Poisson random process of parameter $\nu_d$, i.e. the probability that the link disappears in the time interval $[t_k,t]$ is $1-e^{-\nu_d(t-t^k)}$.

The next section is devoted to the asymptotic limit $N,K\to\infty$ of this model.

# 3 Derivation of a kinetic model

Here, the derivation of a kinetic model from the Individual Based Model of section 2 is performed. The empirical measure $f^N(x,\theta,t)$ of the fibers is introduced:

$$f^N(x,\theta,t) = \frac{1}{N}\sum_{i=1}^{N}\delta_{(X_i(t),\theta_i(t))}(x,\theta),$$

where $\delta_{(X_i(t),\theta_i(t))}(x,\theta)$ denotes the Dirac delta located at $(X_i(t),\theta_i(t)$. It gives the probability to find a fiber at point $x$ and orientational angle $\theta$ at time $t$. The empirical measure $g^K(x_1,\theta_1,\ell_1,x_2,\theta_2,\ell_2,t)$ of the fiber links is given by:

$$\begin{aligned} g^K(x_1,\theta_1,\ell_1,x_2,\theta_2,\ell_2,t) = & \frac{1}{2K}\sum_{k=1}^{K} \delta_{(X_{i(k)},\theta_{i(k)},\ell^k_{i(k)},X_{j(k)},\theta_{j(k)},\ell^k_{j(k)})}(x_1,\theta_1,\ell_1,x_2,\theta_2,\ell_2) \\ & + \delta_{(X_{j(k)},\theta_{j(k)},\ell^k_{j(k)},X_{i(k)},\theta_{i(k)},\ell^k_{i(k)})}(x_1,\theta_1,\ell_1,x_2,\theta_2,\ell_2), \end{aligned}$$

with a similar definition of the Dirac deltas. It gives the probability of finding a link with associated lengths within a volume $d\ell_1 d\ell_2$ about $\ell_1$ and $\ell_2$, this link connecting a fiber located within a volume $dx_1\frac{d\theta_1}{\pi}$ about $(x_1,\theta_1)$ with a fiber located within a volume $dx_2\frac{d\theta_2}{\pi}$ about $(x_2,\theta_2)$. One notes that $(\ell_1,\ell_2)$ is defined in $[-\frac{L}{2},\frac{L}{2}]^2$. Then, at the limit $N,K\to\infty$, $\frac{K}{N}\to\xi$, where $\xi>0$ is a fixed parameter, $f^N\to f$, $g^K\to g$ where $f$ and $g$ satisfy equations given in the following theorem:

**Theorem 3.1.** *The formal limit of Eqs.* (2.2), (2.3) *for* $K,N\to\infty$, $\frac{K}{N}\to\xi$, *where* $\xi>0$ *is a fixed parameter reads:*

$$\frac{df}{dt} - \mu\Big(\nabla_x\cdot((\nabla_x U)f) + \xi\nabla_x\cdot F_1 + d\Delta_x f\Big) - \lambda\Big(\partial_\theta((\partial_\theta U)f) + \xi\partial_\theta F_2 + d\partial^2_\theta f\Big) = 0, \tag{3.1}$$

*and*

$$\begin{aligned} \frac{dg}{dt} - \mu\Bigg[&\nabla_{x_1}\cdot\Big(g\nabla_x U(x_1,\theta_1) + \xi\frac{g}{f(x_1,\theta_1)}F_1(x_1,\theta_1) + d\frac{g}{f(x_1,\theta_1)}\nabla_x f(x_1,\theta_1)\Big) \\ &+ \nabla_{x_2}\cdot\Big(g\nabla_x U(x_2,\theta_2) + \xi\frac{g}{f(x_2,\theta_2)}F_1(x_2,\theta_2) + d\frac{g}{f(x_2,\theta_2)}\nabla_x f(x_2,\theta_2))\Big)\Bigg] \\ -\lambda\Bigg[&\partial_{\theta_1}\Big(g\partial_\theta U(x_1,\theta_1) + \xi\frac{g}{f(x_1,\theta_1)}F_2(x_1,\theta_1) + d\frac{g}{f(x_1,\theta_1)}\partial_\theta f(x_1,\theta_1)\Big) \\ &+ \partial_{\theta_2}\Big(g\partial_\theta U(x_2,\theta_2) + \xi\frac{g}{f(x_2,\theta_2)}F_2(x_2,\theta_2) + d\frac{g}{f(x_2,\theta_2)}\partial_\theta f(x_2,\theta_2)\Big)\Bigg] = S(g), \end{aligned} \tag{3.2}$$

*where*

$$\begin{aligned} F_1(x_1,\theta_1) &= \int (g\nabla_{x_1}V)(x_1,\theta_1,\ell_1,x_2,\theta_2,\ell_2)d\ell_1 d\ell_2\frac{d\theta_2}{\pi}dx_2, \\ F_2(x_1,\theta_1) &= \int \Big(g(\partial_{\theta_1}V + \partial_{\theta_1}b)\Big)(x_1,\theta_1,\ell_1,x_2,\theta_2,\ell_2)d\ell_1 d\ell_2\frac{d\theta_2}{\pi}dx_2, \end{aligned} \tag{3.3}$$

*and* $S(g)$ *is given by:*

$$S(g) = \nu_f f(x_1,\theta_1)f(x_2,\theta_2)\delta_{\bar\ell(x_1,\theta_1,x_2,\theta_2)}(\ell_1)\delta_{\bar\ell(x_2,\theta_2,x_1,\theta_1)}(\ell_2) - \nu_d g, \tag{3.4}$$

*where* $\delta_{\bar\ell}(\ell_1)$ *denotes the Dirac delta at* $\bar\ell$, *i.e. the distribution acting on test functions* $\phi(\ell_1)$ *such that* $\langle\delta_{\bar\ell}(\ell_1),\phi(\ell_1)\rangle = \phi(\bar\ell)$

This kinetic model consists of two evolution equations. The first one (Eq. (3.1)) is an equation for the individual fibers and describes the evolution of the one-particle distribution function $f$. Eq. (3.2) is an equation for the links between fiber pairs. The distribution function $g$ describes the correlations between fiber pairs brought by the presence of links. It can be viewed as a kind of two-particle fiber distribution function. This model is, to our knowledge, a unique explicit example of a kinetic model written in terms of the one and two particle ditributions and closed at this level. Also, the distribution function $g$ can be seen as a way of describing the random graph of the fiber links, namely the graph where the nodes are the fibers and the edges are the links. This statistical description of a random graph could be useful to describe other kinds of random networks, notably in social sciences. As the links are tightly tied to the fibers, they are convected by them and follow their motion. Simultaneously, they constrain the linked fibers to move together, so they directly influence their motion. The action of the links on the individual fiber motion is contained in the third and sixth force terms $F_1$ and $F_2$ of Eq. (3.1) and are the kinetic counterparts of (2.4). The second and fith terms describe transport in physical and orientational spaces due to the external potential and are the kinetic counterparts of (2.6). The fourth and seventh terms are diffusion terms of amplitude $\lambda d$ and $\mu d$ respectively. They represent the random motion of the fibers and originate from the interactions described by Eq. (2.9). The individual motion of the fibers is thus related to the motion of its linked neighbors. The left-hand side of Equation (3.2) describes the evolution of the links between fibers. Indeed, it is composed of the convective terms generated by the external potential and by the diffusion terms. The forces induced by the restoring potential generated by the links again gives rise to the non local terms $F_1$ and the first term of $F_2$. The kinetic counterpart of the alignment force between linked fibers (see Eq. (2.8)) is encompassed in the second term of the force $F_2$ and only acts on the orientation of the fibers. The right hand side $S(g)$ of equation (3.2) describes the Poisson processes of linking/unlinking at frequencies $\nu_f$ and $\nu_d$, respectively. The first term describes the formation of the link and the Dirac deltas indicate that, at the link creation time, the link lengths $\ell_1$ and $\ell_2$ are set by the geometric configuration of the fibers at the attachment time. Also, because $\ell_1$ and $\ell_2$ are restricted to lie in the interval $[-L/2, L/2]$, we see that the link creation term is non-zero only when two fiber elements are intersecting each other. The second term just describes a decay of the link distribution at the rate set by the Poisson process, i.e. $\nu_d$.

The formal proof of this result is inspired from [32], and the detailed computations can be found in appendix 8. The rigorous proof of this result is an open question and is left for future work.

# 4 Scaling

## 4.1 Dimensionless Equations

We express the problem in dimensionless variables. For this purpose, let $t_0$ be the unit of time and $x_0$, $f_0 = \frac{1}{x_0^2}$, $g_0 = \frac{1}{x_0^6}$ and $U_0 = \frac{x_0^2}{t_0^2}$ the units of space, distribution function and energy. The scaling of $f(x, \theta)$ and $g(x_1, \theta_1, \ell_1, x_2, \theta_2, \ell_2)$ comes from the fact that they are probability distribution functions on a 2D domain. The following dimensionless variables are defined:

$$\bar{x} = \frac{x}{x_0},\ \bar{\ell} = \frac{\ell}{x_0},\ \bar{f} = \frac{f}{f_0} = f x_0^2,\ \bar{g} = \frac{g}{g_0} = g x_0^6,\ \bar{U} = \frac{t_0^2 U}{x_0^2}.$$

and the following dimensionless parameters are introduced:

$$\mu' = \frac{\mu}{t_0},\ \lambda' = \frac{\lambda x_0^2}{t_0},\ \nu_f' = t_0 \nu_f,\ \nu_d' = t_0 \nu_d, L' = \frac{L}{x_0},\ d' = \frac{d t_0^2}{x_0^2}, \alpha' = \frac{\alpha t_0^2}{x_0^2},\ \kappa' = \kappa t_0^2.$$

First of all, from the expression of $V$ (see Eq. (2.4)), we get:

$$\begin{aligned} V(x_1, \theta_1, \ell_1, x_2, \theta_2, \ell_2) &= \frac{\kappa'}{2t_0^2}(x_1 + \ell_1 \omega(\theta_1) - x_2 - \ell_2 \omega(\theta_2))^2 \\ &= \frac{x_0^2}{t_0^2} \bar{V}(\bar{x}_1, \theta_1, \bar{\ell}_1, \bar{x}_2, \theta_2, \bar{\ell}_2), \end{aligned}$$

with

$$\bar{V}(\bar{x}_1, \theta_1, \bar{\ell}_1, \bar{x}_2, \theta_2, \bar{\ell}_2) = \frac{\kappa'}{2}(\bar{x}_1 + \bar{\ell}_1 \omega(\theta_1) - \bar{x}_2 - \bar{\ell}_2 \omega(\theta_2))^2.$$

Now, from Eq. (3.3), one notes that:

$$F_1(x_1, \theta_1) = \frac{1}{x_0 t_0^2} \bar{F}_1(\bar{x}_1, \theta_1),$$

where

$$\bar{F}_1(\bar{x}_1, \theta_1) = \int\limits_{\mathbb{R}^2} \int\limits_{-\frac{\pi}{2}}^{\frac{\pi}{2}} \int\limits_{-L'/2}^{L'/2} \int\limits_{-L'/2}^{L'/2} \nabla_{\bar{x}_1} \bar{V}(\bar{x}_1, \theta_1, \bar{\ell}_1, \bar{x}_2, \theta_2, \bar{\ell}_2) \bar{g}(\bar{x}_1, \theta_1, \bar{\ell}_1, \bar{x}_2, \theta_2, \bar{\ell}_2) d\bar{\ell}_1 d\bar{\ell}_2 \frac{d\theta_2}{\pi} d\bar{x}_2.$$

Similarly, $F_2(x_1, \theta_1) = \frac{1}{t_0^2} \bar{F}_2(\bar{x}_1, \theta_1)$, where:

$$\begin{aligned} \bar{F}_2(\bar{x}_1, \theta_1) &= \bar{F}_{al}(\bar{x}_1, \theta_1) + \bar{F}_{link}(\bar{x}_1, \theta_1), \\ \bar{F}_{link}(\bar{x}_1, \theta_1) &= \int\limits_{\mathbb{R}^2} \int\limits_{-\frac{\pi}{2}}^{\frac{\pi}{2}} \int\limits_{-L'/2}^{L'/2} \int\limits_{-L'/2}^{L'/2} \Big(\bar{g} \partial_{\theta_1} V\Big)(\bar{x}_1, \theta_1, \bar{\ell}_1, \bar{x}_2, \theta_2, \bar{\ell}_2) d\bar{\ell}_1 d\bar{\ell}_2 \frac{d\theta_2}{\pi} d\bar{x}_2, \\ \bar{F}_{al}(\bar{x}_1, \theta_1) &= \int\limits_{\mathbb{R}^2} \int\limits_{-\frac{\pi}{2}}^{\frac{\pi}{2}} \int\limits_{-L'/2}^{L'/2} \int\limits_{-L'/2}^{L'/2} \Big(\bar{g} \partial_{\theta_1} \bar{b}\Big)(\bar{x}_1, \theta_1, \bar{\ell}_1, \bar{x}_2, \theta_2, \bar{\ell}_2) d\bar{\ell}_1 d\bar{\ell}_2 \frac{d\theta_2}{\pi} d\bar{x}_2, \end{aligned}$$

where $\bar b(\theta_1,\theta_2) = \alpha'\sin(\theta_1-\theta_2)^\beta$. In this new set of variables, Eqs. (3.1)-(3.2) become:

$$\partial_{t'}\bar f - \chi\lambda'\nabla_{\bar x}\cdot(\nabla_{\bar x}\bar U\bar f) - \lambda'\partial_\theta(\partial_\theta\bar U\bar f) - \xi\lambda'\partial_\theta\bar F_2 - \chi\xi\lambda'\nabla_{\bar x}\cdot\bar F_1 - d'\lambda'\partial_\theta^2\bar f - d'\chi\lambda'\Delta_x\bar f = 0,$$

and

$$\begin{aligned}
&\partial_{t'}\bar g - \chi\lambda'\nabla_{\bar x_1}\cdot(\bar g\nabla_{\bar x}U(\bar x_1,\theta_1) + \xi\frac{\bar g}{\bar f(\bar x_1,\theta_1)}\bar F_1(\bar x_1,\theta_1))\\
&\quad -\lambda'\partial_{\theta_1}(\bar g\partial_\theta U(\bar x_1,\theta_1) + \xi\frac{\bar g}{\bar f(\bar x_1,\theta_1)}\bar F_2(\bar x_1,\theta_1))\\
&\quad\quad -\chi\lambda'\nabla_{\bar x_2}\cdot(\bar g\nabla_{\bar x}U(\bar x_2,\theta_2) + \xi\frac{\bar g}{\bar f(\bar x_2,\theta_2)}\bar F_1(\bar x_2,\theta_2))\\
&\quad\quad\quad -\lambda'\partial_{\theta_2}(\bar g\partial_\theta U(\bar x_2,\theta_2) + \xi\frac{\bar g}{\bar f(\bar x_2,\theta_2)}\bar F_2(\bar x_2,\theta_2))\\
&\quad\quad\quad\quad -d'\chi\lambda'\nabla_{\bar x_1}\cdot(\frac{\bar g}{\bar f(\bar x_1,\theta_1)}\nabla_{\bar x}\bar f(\bar x_1,\theta_1))\\
&\quad\quad\quad\quad\quad -d'\chi\lambda'\nabla_{\bar x_2}\cdot(\frac{\bar g}{\bar f(\bar x_2,\theta_2)}\nabla_{\bar x}\bar f(\bar x_2,\theta_2))\\
&\quad\quad\quad\quad\quad\quad -d'\lambda'\partial_{\theta_1}(\frac{\bar g}{\bar f(\bar x_1,\theta_1)}\partial_\theta\bar f(\bar x_1,\theta_1))\\
&\quad\quad\quad\quad\quad\quad\quad -d'\lambda'\partial_{\theta_2}(\frac{\bar g}{\bar f(\bar x',\theta_2)}\partial_\theta\bar f(\bar x_2,\theta_2)) = \bar S(\bar g),
\end{aligned}$$

where $\chi = \frac{\mu'}{\lambda'}$ and:

$$\begin{aligned}
\bar S(\bar g)(\bar x_1,\theta_1,\bar\ell_1,\bar x_2,\theta_2,\bar\ell_2) =& \nu_f'\bar f(\bar x_1,\theta_1)\bar f(\bar x_2,\theta_2)\delta_{\bar\ell(\bar x_1,\theta_1,\bar x_2,\theta_2)}(\bar\ell_1)\delta_{\bar\ell(\bar x_2,\theta_2,\bar x_1,\theta_1)}(\bar\ell_2)\\
&- \nu_d'\bar g(\bar x_1,\theta_1,\bar\ell_1,\bar x_2,\theta_2,\bar\ell_2).
\end{aligned}$$

Finally, if the space and time scales $x_0$, $t_0$ are chosen such that $\lambda' = \chi = 1$, i.e:

$$x_0^2 = \frac{\mu}{\lambda}, \quad t_0 = \mu,$$

the dimensionless equations for $\bar f$ and $\bar g$ read (dropping the primes and tildes for the sake of clarity):

$$
\begin{aligned}
&\partial_t f - \nabla_x \cdot (\nabla_x U f) - \partial_\theta(\partial_\theta U f) - \xi \partial_\theta F_2 - \xi \nabla_x \cdot F_1 - d\partial_\theta^2 f - d\Delta_x f = 0,\\
&\partial_t g - \nabla_{x_1} \cdot (g \nabla_{x_1} U(x_1,\theta_1) + \xi \frac{g}{f(x_1,\theta_1)} F_1(x_1,\theta_1)) - \partial_{\theta_1}(g \partial_\theta U(x_1,\theta_1) + \xi \frac{g}{f(x_1,\theta_1)} F_2(x_1,\theta_1))\\
&\quad -\nabla_{x_2} \cdot (g \nabla_x U(x_2,\theta_2) + \xi \frac{g}{f(x_2,\theta_2)} F_1(x_2,\theta_2)) - \partial_{\theta_2}(g \partial_\theta U(x_2,\theta_2) + \xi \frac{g}{f(x_2,\theta_2)} F_2(x_2,\theta_2))\\
&\qquad -d\nabla_{x_1} \cdot (\frac{g}{f(x_1,\theta_1)} \nabla_{x_1} f(x_1,\theta_1)) - d\nabla_{x_2} \cdot (\frac{g}{f(x_2,\theta_2)} \nabla_x f(x_2,\theta_2))\\
&\qquad - d\partial_{\theta_1}(\frac{g}{f(x_1,\theta_1)} \partial_\theta f(x_1,\theta_1)) - d\partial_{\theta_2}(\frac{g}{f(x_2,\theta_2)} \partial_\theta f(x_2,\theta_2)) = S(g)(x_1,\theta_1,\ell_1,x_2,\theta_2,\ell_2),
\end{aligned}
\tag{4.1}
$$

with

$$
\begin{aligned}
F_1(x_1,\theta_1) &= \int_{\mathbb{R}^2} \int_{-\frac{\pi}{2}}^{\frac{\pi}{2}} \int_{-L/2}^{L/2} \int_{-L/2}^{L/2} \nabla_{x_1} V(x_1,\theta_1,\ell_1,x_2,\theta_2,\ell_2) g(x_1,\theta_1,\ell_1,x_2,\theta_2,\ell_2) d\ell_1 d\ell_2 \frac{d\theta_2}{\pi} dx_2,\\
F_2(x_1,\theta_1) &= F_{al}(x_1,\theta_1) + F_{link}(x_1,\theta_1),\\
F_{link}(x_1,\theta_1) &= \int_{\mathbb{R}^2} \int_{-\frac{\pi}{2}}^{\frac{\pi}{2}} \int_{-L/2}^{L/2} \int_{-L/2}^{L/2} \Big(g \partial_{\theta_1} V\Big)(x_1,\theta_1,\ell_1,x_2,\theta_2,\ell_2) d\ell_1 d\ell_2 \frac{d\theta_2}{\pi} dx_2,\\
F_{al}(x_1,\theta_1) &= \int_{\mathbb{R}^2} \int_{-\frac{\pi}{2}}^{\frac{\pi}{2}} \int_{-L/2}^{L/2} \int_{-L/2}^{L/2} \Big(g \partial_{\theta_1} \bar{b}\Big)(x_1,\theta_1,\ell_1,x_2,\theta_2,\ell_2) d\ell_1 d\ell_2 \frac{d\theta_2}{\pi} dx_2,
\end{aligned}
$$

and

$$
\begin{aligned}
S(g)(x_1,\theta_1,\ell_1,x_2,\theta_2,\ell_2) = &\nu_f f(x_1,\theta_1) f(x_2,\theta_2) \delta_{\ell(x_1,\theta_1,x_2,\theta_2)}(\ell_1) \delta_{\ell(x_2,\theta_2,x_1,\theta_1)}(\ell_2)\\
&- \nu_d g(x_1,\theta_1,\ell_1,x_2,\theta_2,\ell_2).
\end{aligned}
$$

## 4.2 Scaled equations

So far, the chosen time and space scales are microscopic ones, and describe the system at the scale of the agent interactions. In order to describe the system at a macroscopic scale, a small parameter $\varepsilon \ll 1$ is introduced and the space and time units are set to $\tilde{x_0} = \varepsilon^{-1/2} x_0$, $\tilde{t_0} = \varepsilon^{-1} t_0$. The fiber length measured at scale $x_0$ is supposed to stay of order 1 as $\varepsilon \to 0$, i.e. $L = O(1)$. The variables $x$, $t$, $\ell$ and unknowns $f$ and $g$ are then correspondingly changed to $\tilde{x} = \sqrt{\varepsilon} x$, $\tilde{t} = \varepsilon t$, $\tilde{\ell} = \sqrt{\varepsilon} \ell$, $\tilde{f}(\bar{x},\theta) = \varepsilon^{-1} f(x,\theta)$ and $\tilde{g}(\tilde{x}_1,\theta_1,\tilde{\ell}_1,\tilde{x}_2,\theta_2,\tilde{\ell}_2) = \varepsilon^{-3} g(x_1,\theta_1,\ell_1,x_2,\theta_2,\ell_2)$. We suppose that the external potential $U(x,\theta)$ is decomposed into $U(x,\theta) = U^0(x) + U^1(\theta)$, where $U^0$ is acting on the space variable only and $U^1$ is a $\pi$-periodic potential acting on fiber orientation angles only. The external potential acting on the space variables is supposed to be one order of magnitude stronger than the one acting on the fiber rotations: $U^0 = O(1)$, $U^1 = O(\varepsilon)$, i.e. $\tilde{U}^1 = \varepsilon^{-1}U^1$ with $\tilde{U}^1 = O(1)$. The strength of the alignment potential is supposed to be large $\alpha = O(\varepsilon^{-1})$, i.e. $\tilde{\alpha} = \varepsilon\alpha$ with $\tilde{\alpha} = O(1)$, and we choose the exposant $\beta = 1$. The intensity of the alignment potential between linked fibers is supposed to be small $\kappa = O(\varepsilon)$, i.e. $\tilde{\kappa} = \varepsilon^{-1}\kappa$ with $\tilde{\kappa} = O(1)$ and the diffusion coefficient and parameter $\xi$ are supposed to stay of order 1: $d, \xi = O(1)$. In order to simplify the analysis of the system, the process of linking/unlinking is supposed to occur at a very fast time scale, i.e. $\tilde{\nu}_f = \varepsilon^2\nu_f$ and $\tilde{\nu}_d = \varepsilon^2\nu_d$, with $\tilde{\nu}_f$, $\tilde{\nu}_d = O(1)$. The macroscopic restoring potential $\tilde{V}$ is defined such that:

$$\tilde{V}(\tilde{x}_1, \theta_1, \tilde{\ell}_1, \tilde{x}_2, \theta_2, \tilde{\ell}_2) = \frac{\tilde{\kappa}}{2}|\tilde{x}_1 + \tilde{\ell}_1\omega(\theta_1) - \tilde{x}_2 - \tilde{\ell}_2\omega(\theta_2)|^2,$$

Then,

$$\begin{aligned} V(x_1, \theta_1, \ell_1, x_2, \theta_2, \ell_2) &= \tilde{V}(\tilde{x}_1, \theta_1, \tilde{\ell}_1, \tilde{x}_2, \theta_2, \tilde{\ell}_2), \\ \partial_\theta V(x_1, \theta_1, \ell_1, x_2, \theta_2, \ell_2) &= \partial_\theta \tilde{V}(\tilde{x}_1, \theta_1, \tilde{\ell}_1, \tilde{x}_2, \theta_2, \tilde{\ell}_2), \\ \nabla_x V(x_1, \theta_1, \ell_1, x_2, \theta_2, \ell_2) &= \sqrt{\varepsilon}\nabla_{\tilde{x}} \tilde{V}(\tilde{x}_1, \theta_1, \tilde{\ell}_1, \tilde{x}_2, \theta_2, \tilde{\ell}_2). \end{aligned}$$

Similarly, we have

$$b(\theta_1, \theta_2) = \alpha|\sin(\theta_1 - \theta_2)| = \frac{\tilde{\alpha}}{\varepsilon}|\sin(\theta_1 - \theta_2)| = \frac{1}{\varepsilon}\tilde{b}(\theta_1, \theta_2),$$

and consequently,

$$\partial_{\theta_1} b(\theta_1, \theta_2) = \frac{1}{\varepsilon}\partial_{\theta_1}\tilde{b}(\theta_1, \theta_2).$$

Then we have:

$$\begin{aligned} \nabla_{x_1} F_1 &= \sqrt{\varepsilon}\nabla_{\tilde{x}_1}\left( \int_{L^\varepsilon} \sqrt{\varepsilon}\nabla_{\tilde{x}_1}\tilde{V}(\tilde{x}_1, \theta_1, \tilde{\ell}_1, \tilde{x}_2, \theta_2, \tilde{\ell}_2)\varepsilon^3\tilde{g}(\tilde{x}_1, \theta_1, \tilde{\ell}_1, \tilde{x}_2, \theta_2, \tilde{\ell}_2)\frac{d\tilde{x}_2\frac{d\theta_2}{\pi}d\tilde{\ell}_1 d\tilde{\ell}_2}{\varepsilon^2}\right) \\ &= \varepsilon^2\nabla_{\tilde{x}_1}\tilde{F}_1, \\ F_{link}(x_1, \theta_1) &= \int_{L^\varepsilon} \partial_{\theta_1}\tilde{V}(\tilde{x}_1, \theta_1, \tilde{\ell}_1, \tilde{x}_2, \theta_2, \tilde{\ell}_2)\varepsilon^3\tilde{g}(\tilde{x}_1, \theta_1, \tilde{\ell}_1, \tilde{x}_2, \theta_2, \tilde{\ell}_2)\frac{d\tilde{x}_2\frac{d\theta_2}{\pi}d\tilde{\ell}_1 d\tilde{\ell}_2}{\varepsilon^2} \\ &= \varepsilon\tilde{F}_{link}, \\ F_{al}(x_1, \theta_1) &= \int_{L^\varepsilon} \frac{1}{\varepsilon}\partial_{\theta_1}\tilde{b}(\theta_1, \theta_2)\varepsilon^3\tilde{g}(\tilde{x}_1, \theta_1, \tilde{\ell}_1, \tilde{x}_2, \theta_2, \tilde{\ell}_2)\frac{d\tilde{x}_2\frac{d\theta_2}{\pi}d\tilde{\ell}_1 d\tilde{\ell}_2}{\varepsilon^2} = \tilde{F}_{al}, \end{aligned}$$

where $L^\varepsilon = \mathbb{R}^2 \times [-\frac{\pi}{2}, \frac{\pi}{2}] \times [-\frac{\sqrt{\varepsilon}L}{2}, \frac{\sqrt{\varepsilon}L}{2}]^2$. Finally, we define $X_1$ and $X_2$ such that:

$$\begin{aligned} X_1(x_1, \theta_1) &= \sqrt{\varepsilon}\nabla_{\tilde{x}}\tilde{U}^0(\tilde{x}_1) + \xi\varepsilon^{\frac{3}{2}}\frac{\tilde{F}_1}{\varepsilon\tilde{f}}(\tilde{x}_1, \theta_1) = \sqrt{\varepsilon}\tilde{X}_1(\tilde{x}_1, \theta_1), \\ X_2(x_1, \theta_1) &= \frac{\varepsilon d\partial_{\theta_1}\tilde{f} + \xi\varepsilon\tilde{F}_{link}}{\varepsilon\tilde{f}} = \tilde{X}_2(\tilde{x}_1, \theta_1), \end{aligned}$$

with $\tilde{X}_1(\tilde{x}_1,\theta_1)$ and $\tilde{X}_2(\tilde{x}_1,\theta_1)$ defined by

$$\begin{aligned}\tilde{X}_1(\tilde{x}_1,\theta_1) &= \nabla_{\tilde{x}}\tilde{U}^0(\tilde{x}_1) + \xi\frac{\tilde{F}_1}{\tilde{f}}(\tilde{x}_1,\theta_1),\\ \tilde{X}_2(\tilde{x}_1,\theta_1) &= \frac{d\partial_{\theta_1}\tilde{f} + \xi\tilde{F}_{link}}{\tilde{f}}.\end{aligned}$$

The macroscopic fiber linking/unlinking operator $S(\tilde{g})$ is similar to the one defined Eq. (3.4). Indeed, from Eq. (2.12): $\bar{\ell}(x_1,\theta_1,x_2,\theta_2) = \varepsilon^{-1/2}\bar{\ell}(\tilde{x}_1,\theta_1,\tilde{x}_2,\theta_2)$ and thus:

$$S(\tilde{g}) = \tilde{\nu_f}\tilde{f}(\tilde{x}_1,\theta_1)\tilde{f}(\tilde{x}_2,\theta_2)\delta_{\bar{\ell}(\tilde{x}_1,\theta_1,\tilde{x}_2,\theta_2)}(\tilde{\ell})\delta_{\bar{\ell}(\tilde{x}_1,\theta_1,\tilde{x}_2,\theta_2)}(\tilde{\ell}_2) - \tilde{\nu}_d\tilde{g}.$$

Altogether, the macroscopic version of Eqs. (4.1) reads (dropping the tildes for the sake of clarity):

$$\begin{aligned}&-\xi\partial_{\theta_1}F_{al} - \varepsilon\Big(\xi\partial_\theta F_{link} + d\partial_\theta^2 f\Big)\\ &\qquad + \varepsilon^2\Big(\partial_t f - \nabla_x\cdot(\nabla_x U f) - \partial_\theta(\partial_\theta U f) - \xi\nabla_x\cdot F_1 - d\Delta_x f\Big) = 0,\end{aligned} \tag{4.2}$$

and

$$\begin{aligned}&-S(g) - \varepsilon\xi\Big(\partial_{\theta_1}\big(gF_{al}(x_1,\theta_1)\big) + \partial_{\theta_2}\big(gF_{al}(x_2,\theta_2)\big)\Big) - \varepsilon^2\Big(\partial_{\theta_1}\big(gX_2(x_1,\theta_1)\big) + \partial_{\theta_2}\big(gX_2(x_2,\theta_2)\big)\Big)\\ &+\varepsilon^3\Big(\partial_t g - \nabla_{x_1}\cdot(gX_1(x_1,\theta_1)) - \nabla_{x_2}\cdot(gX_1(x_2,\theta_2)) - \partial_{\theta_1}\big(g\partial_\theta U^1(\theta_1)\big) - \partial_{\theta_2}(g\partial_\theta U^1(\theta_2)\big)\\ &\qquad - d\nabla_{x_1}\cdot(g\frac{\nabla_x f}{f}(x_1,\theta_1)) - d\nabla_{x_2}\cdot(g\frac{\nabla_x f}{f}(x_2,\theta_2))\Big) = 0.\end{aligned} \tag{4.3}$$

From now on, we note $f^\varepsilon = \tilde{f}$ and $g^\varepsilon = \tilde{g}$. The following proposition holds:

**Proposition 4.1.** *Assuming $f^\varepsilon$ and $g^\varepsilon$ exist, then, formally, they satisfy:*

$$\begin{aligned}&-\xi\partial_\theta\Big(\partial_\theta\Phi[f^\varepsilon](x,\theta)f^\varepsilon\Big) - d\partial_\theta^2 f^\varepsilon\\ &\qquad + \varepsilon\Big[\partial_t f^\varepsilon - \nabla_x\cdot(\nabla_x U^0 f^\varepsilon) - \partial_\theta\Big(\Big[\partial_\theta U^1 + \xi G[f^\varepsilon](x,\theta)\Big]f^\varepsilon\Big) - d\Delta_x f^\varepsilon\Big] = O(\varepsilon^2),\end{aligned} \tag{4.4}$$

*and*

$$g^\varepsilon(x_1,\theta_1,\ell_1,x_2,\theta_2,\ell_2) = \frac{\nu_f}{\nu_d}f^\varepsilon(x_1,\theta_1)f^\varepsilon(x_2,\theta_2)\delta_{\bar{\ell}(x_1,\theta_1,x_2,\theta_2)}(\ell_1)\delta_{\bar{\ell}(x_2,\theta_2,x_1,\theta_1)}(\ell_2) + O(\varepsilon^2), \tag{4.5}$$

*with*

$$\Phi[f^\varepsilon](x_1,\theta_1) = C_1 \int_{-\frac{\pi}{2}}^{\frac{\pi}{2}} \sin^2(\theta-\theta_2) f^\varepsilon(x_1,\theta_2)\frac{d\theta_2}{\pi} \tag{4.6}$$

$$G[f^\varepsilon](x_1,\theta_1) = C_2 \sum_{i,j=1}^{2} \frac{\partial^2}{\partial x_i \partial x_j} \int_{-\frac{\pi}{2}}^{\frac{\pi}{2}} f^\varepsilon(x_1,\theta_2) B_{ij}(\theta_1,\theta_2)\frac{d\theta_2}{\pi}, \tag{4.7}$$

$$C_1 = \frac{\alpha L^2 \nu_f}{2\nu_d}\ ,\ C_2 = \frac{\alpha L^4 \nu_f}{48\nu_d}, \tag{4.8}$$

*and*

$$B(\theta_1,\theta_2) = \sin 2(\theta_1-\theta_2)[\omega(\theta_1)\otimes\omega(\theta_1)+\omega(\theta_2)\otimes\omega(\theta_2)] = \Big(B_{ij}(\theta_1,\theta_2)\Big)_{i,j=1,2}. \tag{4.9}$$

**Remark 4.1.** *In the proof of proposition 4.1, we will show that*

$$\begin{aligned} F_1^\varepsilon(x_1,\theta_1) &= O(\varepsilon^3), \\ F_{link}^\varepsilon(x_1,\theta_1) &= O(\varepsilon^3), \\ F_{al}^\varepsilon(x_1,\theta_1) &= \varepsilon\partial_{\theta_1}\Phi[f^\varepsilon](x_1,\theta_1) + \varepsilon^2 G[f^\varepsilon](x_1,\theta_1) + O(\varepsilon^3). \end{aligned} \tag{4.10}$$

The proof of this proposition is given in section 4.3. From these equations, one notes that the hypothesis of dominant creation/deletion of links makes the reaction forces $F_1$ and $F_{link}$ of order $O(\varepsilon^3)$. In this case, the process of linking/unlinking is so fast that the constraint is satisfied at all times. Moreover, under this assumption, the first contribution of the alignment force acting on a fiber is the sum of elementary alignment forces generated by its intersecting fibers, weighted by $\frac{\nu_f}{\nu_d}$. One also notes that the alignment force $F_{al}$ is local in space.

Under these scaling assumptions, the leading order of the left-hand side of Eq. (4.4) takes the form of a collision operator of kinetic theory. It acts on the orientation vector $\theta$ only and it expresses that the alignment potential (2.8) is counter-balanced by the diffusion term which tends to spread the particles isotropically on the sphere. The other terms act at lower order $\varepsilon$.

As the large scale limit involves an expansion of the solution around a local equilibrium, the study of the local equilibria of the collision operator are of key importance. Therefore, section 5 will be dedicated to the study of the properties of the left-hand side of (4.4).

## 4.3 Proof of proposition 4.1

*Proof.* From Eq. (4.3), one notes that the source term $S(g^\varepsilon)$ is of order $O(\varepsilon)$. Thus:

$$g^\varepsilon(x_1,\theta_1,\ell_1,x_2,\theta_2,\ell_2) = \frac{\nu_f}{\nu_d} f^\varepsilon(x_1,\theta_1) f^\varepsilon(x_2,\theta_2)\delta_{\bar\ell(x_1,\theta_1,x_2,\theta_2)}(\ell_1)\delta_{\bar\ell(x_2,\theta_2,x_1,\theta_1)}(\ell_2) + O(\varepsilon). \tag{4.11}$$

Inserting this expression into the relations for $F_1^\varepsilon$ and $F_{link}^\varepsilon$ and $F_{al}^\varepsilon$ (see Eqs. (3.3)), one obtains (dropping the tildes for the new variables, and denoting $\tilde V = \tilde V(x_1,\theta_1,\ell_1,x_2,\theta_2,\ell_2)$ and $b^\varepsilon = b^\varepsilon(\theta_1,\theta_2)$):

$$\begin{aligned}
F_1^\varepsilon =& \frac{\nu_f f^\varepsilon(x_1,\theta_1)}{\nu_d}\int_{L^\varepsilon}\Big(\nabla_{x_1}\tilde V f^\varepsilon(x_2,\theta_2)\delta_{\bar\ell(x_1,\theta_1,x_2,\theta_2)}(\ell_1)\delta_{\bar\ell(x_2,\theta_2,x_1,\theta_1)}(\ell_2) + O(\varepsilon)\Big)dx_2\frac{d\theta_2}{\pi}d\ell_1 d\ell_2,\\
F_{link}^\varepsilon =& \frac{\nu_f f^\varepsilon(x_1,\theta_1)}{\nu_d}\int_{L^\varepsilon}\Big(\partial_{\theta_1}\tilde V f^\varepsilon(x_2,\theta_2)\delta_{\bar\ell(x_1,\theta_1,x_2,\theta_2)}(\ell_1)\delta_{\bar\ell(x_2,\theta_2,x_1,\theta_1)}(\ell_2) + O(\varepsilon)\Big)dx_2\frac{d\theta_2}{\pi}d\ell_1 d\ell_2,\\
F_{al}^\varepsilon =& \frac{\nu_f f^\varepsilon(x_1,\theta_1)}{\nu_d}\int_{L^\varepsilon}\Big(\partial_{\theta_1} b^\varepsilon f^\varepsilon(x_2,\theta_2)\delta_{\bar\ell(x_1,\theta_1,x_2,\theta_2)}(\ell_1)\delta_{\bar\ell(x_2,\theta_2,x_1,\theta_1)}(\ell_2) + O(\varepsilon)\Big)dx_2\frac{d\theta_2}{\pi}d\ell_1 d\ell_2.
\end{aligned} \tag{4.12}$$

We note that if $\phi(x_1,\theta_1,\ell_1,x_2,\theta_2,\ell_2) \in L^\infty(L^\varepsilon)$ with sufficient decay at infinity, then

$$\int_{L^\varepsilon}\nabla_{x_1}\tilde V\,\phi\,dx_2\,\frac{d\theta_2}{\pi}d\ell_1 d\ell_2 \le \varepsilon C,$$

since the measure of $L^\varepsilon$ intersected with any compact set of $\mathbb{R}^2\times[-\pi/2,\pi/2]\times\mathbb{R}^2$ is of order $\varepsilon$. Indeed, the domain of integration with respect to $\ell_1$ or $\ell_2$ has a measure of order $\varepsilon$. Thus, assuming that the $O(\varepsilon)$ remainder in (4.11) is an $L^\infty$ function, which is legitimate in view of the diffusive character of (4.3), we get:

$$\begin{aligned}
F_1^\varepsilon =& \frac{\nu_f f^\varepsilon(x_1,\theta_1)}{\nu_d}\int\limits_{K^\varepsilon(x_1,\theta_1)}\nabla_{x_1}\tilde V(x_1,\theta_1,\bar\ell(x_1,\theta_1,x_2,\theta_2),x_2,\theta_2,\bar\ell(x_2,\theta_2,x_1,\theta_1))f^\varepsilon(x_2,\theta_2))dx_2\frac{d\theta_2}{\pi}\\
&+O(\varepsilon^2),\\
F_{link}^\varepsilon =& \frac{\nu_f f^\varepsilon(x_1,\theta_1)}{\nu_d}\int\limits_{K^\varepsilon(x_1,\theta_1)}\partial_{\theta_1}\tilde V(x_1,\theta_1,\bar\ell(x_1,\theta_1,x_2,\theta_2),x_2,\theta_2,\bar\ell(x_2,\theta_2,x_1,\theta_1))f^\varepsilon(x_2,\theta_2)dx_2\frac{d\theta_2}{\pi}\\
&+O(\varepsilon^2),\\
F_{al}^\varepsilon =& \frac{\nu_f f^\varepsilon(x_1,\theta_1)}{\nu_d}\int\limits_{K^\varepsilon(x_1,\theta_1)}\partial_{\theta_1} b(\theta_1,\theta_2)f^\varepsilon(x_2,\theta_2)dx_2\frac{d\theta_2}{\pi}+O(\varepsilon^2),
\end{aligned} \tag{4.13}$$

where $K^\varepsilon(x_1,\theta_1)$ is the set of fibers intersecting fiber in $(x,\theta)$, given by:

$$K^\varepsilon(x_1,\theta_1)=\{(x_2,\theta_2)\mid |\bar\ell(x_1,\theta_1,x_2,\theta_2)|\le\sqrt{\varepsilon}L/2\ ,|\bar\ell(x_2,\theta_2,x_1,\theta_1)|\le\sqrt{\varepsilon}L/2\}. \tag{4.14}$$

From the fact that $\tilde V$ is a quadratic function of $x_1+\ell_1\omega(\theta_1)-x_2-\ell_2\omega(\theta_2)$ and the fact that setting $\ell_1=\bar\ell(x_1,\theta_1,x_2,\theta_2)$ and $\ell_2=\bar\ell(x_2,\theta_2,x_1,\theta_1)$ just cancels this expression, one immediately notes that:

$$\nabla_{x_1}\tilde V(x_1,\theta_1,\bar\ell(x_1,\theta_1,x_2,\theta_2),x_2,\theta_2,\bar\ell(x_2,\theta_2,x_1,\theta_1))=0,$$
$$\partial_{\theta_1}\tilde V(x_1,\theta_1,\bar\ell(x_1,\theta_1,x_2,\theta_2),x_2,\theta_2,\bar\ell(x_2,\theta_2,x_1,\theta_1))=0.$$

So, finally:

$$F_1^\varepsilon=O(\varepsilon^2),\quad F_{links,2}^\varepsilon=O(\varepsilon^2). \tag{4.15}$$

We are left with:

$$F_{al}^\varepsilon=\frac{\nu_f}{\nu_d}f^\varepsilon(x_1,\theta_1)\int\limits_{K^\varepsilon(x_1,\theta_1)}\partial_{\theta_1}b(\theta_1,\theta_2)f^\varepsilon(x_2,\theta_2)dx_2\frac{d\theta_2}{\pi}+O(\varepsilon^2). \tag{4.16}$$

From now on, we write $\omega_1=\omega(\theta_1)$ and $\omega_2=\omega(\theta_2)$. By the change of variables $x_2\mapsto(s_1,s_2)$ defined by

$$x_2=x_1+\frac{\sqrt{\varepsilon}L}{2}s_1\omega_1-\frac{\sqrt{\varepsilon}L}{2}s_2\omega_2,$$

with associated Jacobian

$$J_{x_2}=\frac{L\sqrt{\varepsilon}}{2}\begin{pmatrix}\cos\theta_1 & -\cos\theta_2\\ \sin\theta_1 & -\sin\theta_2\end{pmatrix},$$

and $|\det(J_{x_2})|=\frac{L^2\varepsilon}{4}|\sin(\theta_1-\theta_2)|$, we have:

$$F_{al}^\varepsilon(x_1,\theta_1)=\varepsilon C(x_1,\theta_1)\int\limits_{-\frac{\pi}{2}}^{\frac{\pi}{2}}\int\limits_{|s_1|,|s_2|\le1}|\sin(\theta_1-\theta_2)|\partial_{\theta_1}b(\theta_1,\theta_2)f^\varepsilon(x_1+\frac{\sqrt{\varepsilon}L}{2}s_1\omega_1-\frac{\sqrt{\varepsilon}L}{2}s_2\omega_2,\theta_2)$$
$$ds_1ds_2\frac{d\theta_2}{\pi}+O(\varepsilon^2),$$

where $C(x_1,\theta_1)=\frac{L^2\nu_f f^\varepsilon(x_1,\theta_1)}{4\nu_d}$. Thanks to (2.7) with $\beta=1$, one notes that $\partial_{\theta_1}b(\theta_1,\theta_2)=\alpha\partial_{\theta_1}|\sin(\theta_1-\theta_2)|$, and then, $|\sin(\theta_1-\theta_2)|\partial_{\theta_1}b(\theta_1,\theta_2)=\frac{\alpha}{2}\partial_{\theta_1}\sin^2(\theta_1-\theta_2)$. Then,

$$F_{al}^\varepsilon(x_1,\theta_1)=\frac{\varepsilon\alpha}{2}C(x_1,\theta_1)\int\limits_{-\frac{\pi}{2}}^{\frac{\pi}{2}}\int\limits_{|s_1|,|s_2|\le1}\partial_{\theta_1}\sin^2(\theta_1-\theta_2)\ f^\varepsilon(x_1+\frac{\sqrt{\varepsilon}L}{2}s_1\omega_1-\frac{\sqrt{\varepsilon}L}{2}s_2\omega_2,\theta_2)$$
$$ds_1ds_2\frac{d\theta_2}{\pi}+O(\varepsilon^2). \tag{4.17}$$

By Taylor expansion, we have:

$$\begin{aligned}
f^\varepsilon(x_1+\frac{\sqrt{\varepsilon}L}{2}s_1\omega_1-\frac{\sqrt{\varepsilon}L}{2}s_2\omega_2,\theta_2) = f^\varepsilon(x_1,\theta_2) &+ \frac{\sqrt{\varepsilon}L}{2}\nabla_x f^\varepsilon(x_1,\theta_2).(s_1\omega_1-s_2\omega_2)\\
&+\frac{\varepsilon L^2}{4}(s_1\omega_1-s_2\omega_2)^T\nabla_x^2 f^\varepsilon(x_1,\theta_2)(s_1\omega_1-s_2\omega_2)\\
&+O((\frac{\sqrt{\varepsilon}L}{2}|s_1\omega_1-s_2\omega_2|)^3),
\end{aligned}$$

where $\nabla_x^2 f^\varepsilon$ is the spatial-hessian matrix of $f^\varepsilon$ ($(\nabla_x^2 f)_{ij} = \frac{\partial^2 f}{\partial x_i \partial x_j}$), and for any vector $a$ of $\mathbb{R}^2$ and any $2\times 2$ matrix B : $a^T Ba = \sum_{(i,j)\in[1,2]^2} B_{ij}a_j a_i$. Integrating over $s_1, s_2 \in [-1,1]$, the odd terms with respect to either $s_1$ or $s_2$ vanish. Therefore:

$$\begin{aligned}
&\int_{-\frac{\pi}{2}}^{\frac{\pi}{2}}\int_{|s_1|,|s_2|\le 1}\partial_{\theta_1}\sin^2(\theta_1-\theta_2)f^\varepsilon(x_1+\frac{\sqrt{\varepsilon}L}{2}s_1\omega_1-\frac{\sqrt{\varepsilon}L}{2}s_2\omega_2,\theta_2)ds_1ds_2\frac{d\theta_2}{\pi}\\
&\quad = 4\int_{-\frac{\pi}{2}}^{\frac{\pi}{2}}\partial_{\theta_1}\sin^2(\theta_1-\theta_2)f^\varepsilon(x_1,\theta_2)\frac{d\theta_2}{\pi}\\
&\qquad\quad +\frac{\varepsilon L^2}{6}\int_{-\frac{\pi}{2}}^{\frac{\pi}{2}}\partial_{\theta_1}\sin^2(\theta_1-\theta_2)\nabla_x^2 f^\varepsilon(x_1,\theta_2):[\omega_1\otimes\omega_1+\omega_2\otimes\omega_2]\frac{d\theta_2}{\pi}+O(\varepsilon^2),
\end{aligned} \tag{4.18}$$

where $\forall A,B \in \mathbb{R}^2$ , $A : B = \sum_{i,j\in[1,2]} A_{ij}B_{ij}$ and for any vectors $\omega, \omega' \in \mathbb{R}^2$, we write $(\omega\otimes\omega')_{ij} = \omega_i\omega'_j$. Then:

$$\int_{-\frac{\pi}{2}}^{\frac{\pi}{2}}\partial_{\theta_1}\sin^2(\theta_1-\theta_2)\nabla_{x_1}^2 f^\varepsilon(x_1,\theta_2):[\omega_1\otimes\omega_1+\omega_2\otimes\omega_2]\frac{d\theta_2}{\pi} = \sum_{(i,j)=1}^{2}\frac{\partial^2}{\partial x_i x_j}\int_{-\frac{\pi}{2}}^{\frac{\pi}{2}} f^\varepsilon(x_1,\theta_2)B_{ij}(\theta_1,\theta_2)\frac{d\theta_2}{\pi}, \tag{4.19}$$

where:

$$B_{ij}(\theta_1,\theta_2) = [\omega_i(\theta_1)\omega_j(\theta_1)+\omega_i(\theta_2)\omega_j(\theta_2)]\sin(2(\theta_1-\theta_2)).$$

A first consequence of what precedes is that $F_{al}^\varepsilon = O(\varepsilon)$. Therefore, $S(g^\varepsilon) = O(\varepsilon^2)$ (instead of formally $O(\varepsilon)$ as seen from Eq. (4.3)). As a consequence, the remainder in (4.11) is $O(\varepsilon^2)$ instead of being $O(\varepsilon)$, and the same is true for the remainders in (4.12). Consequently, the remainders in (4.13) are $O(\varepsilon^3)$ instead of being $O(\varepsilon^2)$ as before. It follows that the remainders in (4.15)-(4.16) are $O(\varepsilon^3)$ as well. Then, inserting (4.18) and (4.19) into (4.16) (with remainder $O(\varepsilon^2)$), we get (4.5)-(4.4), which ends the proof. □

From now on, we focus on Eq. (4.4) in which we neglect the $O(\varepsilon^2)$ terms, namely

$$-\xi\partial_\theta\Big(\partial_\theta\Phi[f^\varepsilon](x,\theta)f^\varepsilon\Big) - d\partial_\theta^2 f^\varepsilon \\ + \varepsilon\Big[\partial_t f^\varepsilon - \nabla_x\cdot(\nabla_x U^0 f^\varepsilon) - \partial_\theta\Big(\Big[\partial_\theta U^1 + \xi G[f^\varepsilon](x,\theta)\Big]f^\varepsilon\Big) - d\Delta_x f^\varepsilon\Big] = 0, \tag{4.20}$$

where $\Phi$ and $G$ are given by (4.6)-(4.7) respectively, and we investigate the limit $\varepsilon \to 0$. This is the object of the next section.

# 5 Large scale limit

In this section, the limit $\varepsilon \to 0$ of the solution $f^\varepsilon$ to (4.20) is explored. For this purpose, Eq. (4.20) is rewritten

$$\partial_t f^\varepsilon - \nabla_x\cdot(\nabla_x U^0 f^\varepsilon) - \partial_\theta\Big((\partial_\theta U^1 + \xi G[f^\varepsilon])f^\varepsilon\Big) - d\Delta_x f^\varepsilon = \frac{1}{\varepsilon}Q(f^\varepsilon), \tag{5.1}$$

where the collision operator $Q(f^\varepsilon)$ is defined by

$$Q(f) = d\partial_\theta^2 f + \xi\partial_\theta(\partial_\theta\Phi[f])f), \tag{5.2}$$

$$\Phi[f] = C_1\int_{-\frac{\pi}{2}}^{\frac{\pi}{2}} \sin^2(\theta-\theta_2)f\frac{d\theta_2}{\pi}, \tag{5.3}$$

and where we recall that $C_1$ and $G[f]$ are defined by (4.7) and (4.8) respectively. The operator $Q$ is a non linear operator on $f$ which acts on $\theta$ only and leaves $x$ and $t$ as parameters. For each function $\Phi(\theta)$, we define $M_\Phi(\theta)$ by:

$$M_\Phi(\theta) = \frac{1}{Z}e^{-\xi\Phi(\theta)/d}, \tag{5.4}$$

where $Z$ is a normalization factor such that $Z = \int_{-\frac{\pi}{2}}^{\frac{\pi}{2}} e^{-\xi\Phi(\theta)/d}\frac{d\theta}{\pi}$. Thus, $M_\Phi(\theta)$ is a probability distribution of $\theta$. Such functions are called generalized Von Mises distributions (the Von Mises distribution being the case of $\Phi(\theta) = -\cos\theta$). The next section is devoted to the analysis of the properties of $Q(f)$ and follows closely [13].

## 5.1 Properties of $Q$

### 5.1.1 Equilibria

In this section, the equilibria of the operator $Q$ are studied, and the following proposition is proven:

**Proposition 5.1.** *Here, we restrict ourselves to functions of $\theta$ only.*
*(i) The operator $Q$ can be written:*

$$Q(f) = d\partial_\theta\Bigg(M_{\Phi[f]}\partial_\theta(\frac{f}{M_{\Phi[f]}})\Bigg). \tag{5.5}$$

*(ii) The equilibrium solutions of $Q$, i.e. the functions $f$ such that $Q(f) = 0$ are of the form $f(\theta) = \rho M_{\Phi[f]}$, where $M_{\Phi[f]}$ is defined by Eq. (5.4) and $\rho$ is a positive constant.*

This proposition shows that the equilibria of operator $Q$ are generalized Von Mises distributions of $\theta$, weighted by the particle density.

*Proof.* To prove (i), one can note that:

$$d\partial_\theta\Bigg(M_{\Phi[f]}\partial_\theta(\frac{f}{M_{\Phi[f]}})\Bigg) = d\partial_\theta\Bigg(\partial_\theta f - f\partial_\theta(\log(M_{\Phi[f]}))\Bigg) = \partial_\theta\Bigg(d\partial_\theta f + \xi\partial_\theta\Phi[f]f\Bigg) = Q(f).$$

To prove (ii), note that $f = \rho M_{\Phi[f]}$ is solution of (5.5). Conversely, suppose that $f$ is such that

$$d\partial_\theta\Bigg(M_{\Phi[f]}\partial_\theta(\frac{f}{M_{\Phi[f]}})\Bigg) = 0.$$

We define the sets $H_f$ and $V_f$ by:

$$H_f = \{\phi \text{ measurable on } [-\frac{\pi}{2}, \frac{\pi}{2}] \mid \int_{-\frac{\pi}{2}}^{\frac{\pi}{2}} \left|\frac{\phi}{M_{\Phi[f]}}\right|^2 M_{\Phi[f]}\frac{d\theta}{\pi} < +\infty\},$$

and

$$V_f = \{\phi \in H \mid \int_{-\frac{\pi}{2}}^{\frac{\pi}{2}} \left|\partial_\theta(\frac{\phi}{M_{\Phi[f]}})\right|^2 M_{\Phi[f]}\frac{d\theta}{\pi} < +\infty\}.$$

The norms $\|\cdot\|_{H_f}$, $\|\cdot\|_{V_f}$ on $H_f$ and $V_f$ are then defined such that:

$$\|\phi\|_{V_f}^2 = \|\phi\|_{H_f}^2 + |\phi|_{V_f}^2.$$

where

$$\|\phi\|_{H_f} = \int_{-\pi/2}^{\pi/2} \left|\frac{\phi}{M_{\Phi[f]}}\right|^2 M_{\Phi[f]}\frac{d\theta}{\pi},$$

and

$$|\phi|_{V_f} = \int_{-\pi/2}^{\pi/2} \left|\partial_\theta(\frac{\phi}{M_{\Phi[f]}})\right|^2 M_{\Phi[f]}\frac{d\theta}{\pi}.$$

For $f \in V_f$ using Green's formula, we get:

$$\int_{-\pi/2}^{\pi/2} d\partial_\theta\Bigg(M_{\Phi[f]}\partial_\theta(\frac{f}{M_{\Phi[f]}})\Bigg)\frac{f}{M_{\Phi[f]}}\frac{d\theta}{\pi} = -d\int_{-\pi/2}^{\pi/2} M_{\Phi[f]}\left|\partial_\theta(\frac{f}{M_{\Phi[f]}})\right|^2\frac{d\theta}{\pi} = 0,$$

and thus, $\partial_\theta(\frac{f}{M_{\Phi[f]}}) = 0$. Then, $f = \rho M_{\Phi[f]}$, with $\rho > 0$, which ends the proof. □

Now, the following lemma is proven:

**Lemma 5.2.** *For any function* $f(\theta)$*, the potential function* $\Phi[f](\theta)$ *of Eq.* (5.3) *can be written:*

$$\Phi[f](\theta) = C - \frac{C_1}{2}\eta_f \cos 2(\theta - \theta_f), \tag{5.6}$$

*where* $C_1$ *is given by* (4.8)*,* $C = \frac{C_1 \rho_f}{2}$*,* $\rho_f = \int_{-\pi/2}^{\pi/2} f \frac{d\theta}{\pi}$ *and* $(\eta_f, \theta_f) \in \mathbb{R}^+ \times [-\frac{\pi}{2}, \frac{\pi}{2})$ *are uniquely defined by:*

$$\eta_f \begin{pmatrix} \cos 2\theta_f \\ \sin 2\theta_f \end{pmatrix} = \int_{-\frac{\pi}{2}}^{\frac{\pi}{2}} \begin{pmatrix} \cos 2\theta' \\ \sin 2\theta' \end{pmatrix} f(\theta') \frac{d\theta'}{\pi},$$

*or equivalently by:*

$$\int_{-\frac{\pi}{2}}^{\frac{\pi}{2}} \cos 2(\theta' - \theta_f) f(\theta') \frac{d\theta'}{\pi} = \eta_f \ , \qquad \int_{-\frac{\pi}{2}}^{\frac{\pi}{2}} \sin 2(\theta' - \theta_f) f(\theta') \frac{d\theta'}{\pi} = 0. \tag{5.7}$$

*Remark that the second condition is equivalent to saying that*

$$\theta_f = \frac{1}{2} \tan^{-1} \Big( \frac{\int \sin 2\theta' f(\theta') d\theta'}{\int \cos 2\theta' f(\theta') d\theta'} \Big),$$

*and this defines* $\theta_f$ *uniquely modulo* $\pi$*.*

*Proof.* As $\sin^2(\theta - \theta') = \frac{1}{2}(1 - \cos 2\theta \cos 2\theta' - \sin 2\theta \sin 2\theta')$, $\Phi[f]$ can be decomposed into:

$$\begin{aligned}
\Phi[f](\theta) &= C_1 \int_{-\frac{\pi}{2}}^{\frac{\pi}{2}} \sin^2(\theta - \theta') f(\theta') \frac{d\theta'}{\pi} \\
&= \frac{C_1}{2} \left( \int_{-\frac{\pi}{2}}^{\frac{\pi}{2}} f(\theta') \frac{d\theta'}{\pi} - \cos 2\theta \int_{-\frac{\pi}{2}}^{\frac{\pi}{2}} \cos 2\theta' f(\theta') \frac{d\theta'}{\pi} - \sin 2\theta \int_{-\frac{\pi}{2}}^{\frac{\pi}{2}} \sin 2\theta' f(\theta') \frac{d\theta'}{\pi} \right) \\
&= \frac{C_1}{2} \Big( \rho - \eta_f \cos 2(\theta - \theta_f) \Big),
\end{aligned}$$

The result follows. ☐

Let us now suppose that $\frac{\nu_f}{\nu_d}$ depends on $\eta_f$:

**Hypothesis 5.1.** *The parameter* $\frac{\nu_f}{\nu_d}$ *is supposed to be inversely proportional to the local fiber density:* $\frac{\nu_f}{\nu_d} = \frac{\gamma}{\eta_f}$*, with* $\gamma$ *a constant.*

Note that, thanks to Hypothesis 5.1, we have

$$\frac{\xi C_1 \eta_f}{2d} = \alpha \frac{\xi L^2 \nu_f}{2\nu_d} \eta_f \frac{1}{2d} = \frac{\xi \alpha L^2 \gamma}{4d} = r, \tag{5.8}$$

where $r$ is a constant depending only on the data of the problem.

**Proposition 5.3.** *Here, we restrict ourselves to functions of $\theta$ only. Under Hypothesis 5.1, the equilibrium solutions of $Q$, i.e. the functions $f_{eq}$ such that $Q(f_{eq}) = 0$ are of the form:*

$$f_{eq}(\theta) = \rho M_{\theta_0}(\theta), \tag{5.9}$$

*for arbitrary $\rho \in [0, \infty)$ and $\theta_0 \in [-\frac{\pi}{2}, \frac{\pi}{2})$ and where:*

$$\begin{aligned} M_{\theta_0} &= \frac{e^{r \cos 2(\theta - \theta_0)}}{Z}, \\ Z = Z(r) &= \int_{-\frac{\pi}{2}}^{\frac{\pi}{2}} e^{r \cos 2(\theta-\theta_0)} \frac{d\theta}{\pi}, \end{aligned} \tag{5.10}$$

*with $r$ given by (5.8). We have $\eta_f = \rho c(r)$ with*

$$c(r) = \frac{\int_{-\frac{\pi}{2}}^{\frac{\pi}{2}} \cos 2\theta e^{r \cos 2\theta} \frac{d\theta}{\pi}}{\int_{-\frac{\pi}{2}}^{\frac{\pi}{2}} e^{r \cos 2\theta} \frac{d\theta}{\pi}}. \tag{5.11}$$

Proposition 5.3 gives a precise description of the equilibria of $Q$, in terms of classical von Mises-Fisher distributions.

*Proof of proposition 5.3.* From Proposition 5.1, the equilibria of the collision operator $Q(f)$ are of the form

$$f = \rho \frac{e^{-\xi \frac{\Phi[f](\theta)}{d}}}{\int_{-\frac{\pi}{2}}^{\frac{\pi}{2}} e^{-\xi \frac{\Phi[f](\theta)}{d}} \frac{d\theta}{\pi}}.$$

Thanks to Eq. (4.8), Lemma 5.2,Eqs. (5.8) and (5.11), we get:

$$f(\theta) = \rho \frac{e^{-\frac{\xi C}{d} + \frac{\xi C_1}{2d} \eta_f \cos 2(\theta - \theta_f)}}{\int_{-\frac{\pi}{2}}^{\frac{\pi}{2}} e^{-\frac{\xi C}{d} + \frac{\xi C_1}{2d} \eta_f \cos 2(\theta' - \theta_f)} \frac{d\theta'}{\pi}} = \rho(x) \frac{e^{r \cos 2(\theta - \theta_f)}}{\int_{-\frac{\pi}{2}}^{\frac{\pi}{2}} e^{r \cos 2(\theta' - \theta_f)} \frac{d\theta'}{\pi}}, \tag{5.12}$$

where $(\eta_f, \theta_f) \in \mathbb{R}^+ \times [-\frac{\pi}{2}, \frac{\pi}{2})$ satisfy Eq. (5.7). Therefore, $f$ is of the form (5.9) with $r = \frac{\xi C_1 \eta_f}{2d}$. By Hypothesis 5.1 and (4.8), $r = \frac{\xi \alpha L^2 \gamma}{4d}$. Conversely, let $f$ be given by (5.9). Then, by (5.6),and (5.8), $\phi[f] = C - r\frac{d}{\xi} \cos 2(\theta - \theta_f)$ with $\theta_f$ uniquely determined by $\int_{-\pi/2}^{\pi/2} \sin 2(\theta - \theta_f) f(\theta) \frac{d\theta}{\pi} = 0$. But $\int_{-\pi/2}^{\pi/2} \sin 2(\theta - \theta_0) f(\theta) \frac{d\theta}{\pi} = 0$ by symmetry, showing that $\theta_f = \theta_0 \bmod(\pi)$. Therefore, $M_{\phi[f]} = M_{\theta_0}$ and $f = \rho M_{\phi[f]}$ showing that $f$ is an equilibrium, which ends the proof. ☐

Thanks to Eq. (5.11), Hypothesis 5.1 amounts to supposing that the ratio $\frac{\nu_f}{\nu_d}$ is inversely proportional to the fiber density.

Since there is no obvious conservation relation other than the conservation of the local fiber density, the only collision invariants in this model are the constants.

The integration of equation (4.4) against these invariants does not allow us to find the evolution equation for the mean orientation. In order to obtain an equation on $\theta_0$, inspired from [17], the concept of Generalized Collision Invariants (GCI), i.e. of collision invariants when acting on a restricted subset of functions $f$, is introduced.

### 5.1.2 Collision invariant

A collision invariant is a function $\Psi$ such that for all function $f$ of $\theta$, $\int Q(f)\Psi d\theta = 0$. However, due to the lack of momentum conservation, the only collision invariants are the constants. This is not enough to determine both $\rho$ and $\theta_0$. To this aim, following [19] and [17], we introduce the notion of GCI. For any $\theta_0 \in [-\frac{\pi}{2}\frac{\pi}{2})$, we define $L_{\theta_0}$ as the following linear operator:

$$L_{\theta_0} f = d\partial_\theta \bigg( M_{\theta_0} \partial_\theta (\frac{f}{M_{\theta_0}}) \bigg).$$

Note that $Q(f) = L_{\theta_f} f$ where $\theta_f$ satisfies Eq. (5.7).

**Definition 5.4.** *For a given $\theta_0 \in [-\frac{\pi}{2}, \frac{\pi}{2})$ a GCI associated to $\theta_0$ is a function $\Psi$ such that:*

$$\int_{-\frac{\pi}{2}}^{\frac{\pi}{2}} L_{\theta_0} f \Psi \frac{d\theta}{\pi} = 0 \ \ \forall f \, \textit{such that} \, \theta_f = \theta_0 \ \textit{mod}(\pi). \tag{5.13}$$

*The set of the GCI associated to a given $\theta_0 \in [-\frac{\pi}{2}, \frac{\pi}{2})$ is a linear space denoted by $\mathcal{G}_{\theta_0}$.*

**Lemma 5.5.** $\Psi \in \mathcal{G}_{\theta_0}$ *if and only if* $\exists \beta \in \mathbb{R}$ *such that:*

$$L^*_{\theta_0} \Psi = \beta \sin 2(\theta - \theta_0), \tag{5.14}$$

*where $L^*_{\theta_0}$ is the $L^2$ formal adjoint of $L_{\theta_0}$, i.e.*

$$L^*_{\theta_0} \Psi = -\frac{d}{M_{\theta_0}} \partial_\theta \bigg( M_{\theta_0} \partial_\theta \Psi \bigg).$$

*Proof.* By (5.7), the condition $\theta_f = \theta_0$ mod$(\pi)$ is equivalent to the linear constraint:

$$\int_{-\frac{\pi}{2}}^{\frac{\pi}{2}} f \sin 2(\theta - \theta_0) \frac{d\theta}{\pi} = 0.$$

By a classical duality argument [17], we deduce that $\Psi \in \mathcal{G}_{\theta_0}$ if and only if:

$$\exists \beta \in \mathbb{R} \text{ such that } \int_{-\frac{\pi}{2}}^{\frac{\pi}{2}} L_{\theta_0} f \Psi \frac{d\theta}{\pi} = \beta \int_{-\frac{\pi}{2}}^{\frac{\pi}{2}} f \sin 2(\theta - \theta_0) \frac{d\theta}{\pi} \ \forall f.$$

Note that now, there are no more constraints on $f$. Therefore, we can eliminate $f$ and get (5.14). ☐

**Proposition 5.6.** *Any GCI $\Psi_{\theta_0}$ associated to $\theta_0$ can be written:*

$$\Psi_{\theta_0}(\theta) = C + \beta g(\theta - \theta_0), \tag{5.15}$$

*with arbitrary $C$, $\beta \in \mathbb{R}$ and with $g$ an odd $\pi$ periodic function belonging to $H^1_0(0, \frac{\pi}{2})$, whose expression is:*

$$g(\theta) = \frac{1}{2r}\left(\theta - \frac{\pi}{2}\frac{\int_0^{\theta} e^{-r\cos 2\theta'}\frac{d\theta'}{\pi}}{\int_0^{\frac{\pi}{2}} e^{-r\cos 2\theta'}\frac{d\theta'}{\pi}}\right). \tag{5.16}$$

*Proof.* Following [19], [17], using Lax-Milgram's theorem and Poincaré's inequality, it is easy to show that the problem $L^*_{\theta_0}(\Psi) = \frac{d}{\xi}\beta\sin 2(\theta - \theta_0)$ has a unique solution in the space $\dot{H}^1(-\frac{\pi}{2}, \frac{\pi}{2})$ of functions $H^1(-\frac{\pi}{2}, \frac{\pi}{2})$ with zero mean. Then, the change of variables $\theta' = \theta - \theta_0$ is performed, and functions of the form $\Psi(\theta) = \beta g(\theta)$ with $g$ odd are searched. Then, $\Psi \in \dot{H}^1([-\frac{\pi}{2}, \frac{\pi}{2}])$ if and only if g belongs to $H^1_0(0, \frac{\pi}{2})$. Straightforward computations show that $\Psi$ is a solution of (5.14) if and only if $g$ is a solution of

$$(M_0 g')' = -\sin 2\theta M_0. \tag{5.17}$$

As $M_0(\theta) = \frac{e^{r\cos 2\theta}}{Z}$ and as we search for $g \in H^1_0(0, \frac{\pi}{2})$, an analytic expression for $g$ can be found. Indeed, since $-\sin 2\theta M_0 = \frac{1}{2r}M_0$, integrating (5.17) with respect to $\theta$ once, we get:

$$g'(\theta) = \frac{1}{2r} + CZe^{-r\cos 2\theta},$$

for an appropriate constant $C$. Then, since $g \in H^1_0(0, \frac{\pi}{2})$,

$$g(\theta) = \frac{\theta}{2r} + CZ\int_0^{\theta} e^{-r\cos 2\theta'}d\theta'.$$

Finally, as $g \in H^1_0(0, \pi)$, $g(0) = g(\pi) = 0$ and $C$ can be determined:

$$C = -\frac{\pi}{4rZ\int_0^{\frac{\pi}{2}} e^{-r\cos 2\theta'}d\theta'} = -\frac{1}{2rZ\int_{-\pi/2}^{\pi/2} e^{-r\cos 2\theta'}d\theta'} = -\frac{1}{2rZ^2}.$$

Indeed, we have:

$$\int_{-\pi/2}^{\pi/2} e^{-r\cos 2\theta'}d\theta' = \int_{-\pi/2}^{\pi/2} e^{r\cos 2\theta'}d\theta',$$

by the change of variable $\theta \to \frac{\pi}{2} - \theta$ for $\theta > 0$ and $\theta \to \frac{-\pi}{2} - \theta$ for $\theta < 0$. This yields the result. For further usage, we note that

$$g'(\theta) = \frac{1}{2r}(1 - \frac{1}{M_0 Z^2}). \tag{5.18}$$

$\square$

## 5.2 Limit $\varepsilon \to 0$

In this section, the formal limit $\varepsilon \to 0$ of Eq. (4.4) is studied. We aim to prove the following theorem:

**Theorem 5.7.** *Under the scaling 4.2 and 5.1, the solution* $f^\varepsilon$ *of eq.* (5.1) *formally converges to* $f(x,\theta,t)$ *given by*

$$f(x,\theta,t) = \rho(x,t) M_{\theta_0(x,t)}(\theta), \tag{5.19}$$

*where* $M_{\theta_0}$ *is given by* (5.10) *and* $\rho(x,t)$ *and* $\theta_0(x,t)$ *satisfy the following system:*

$$\partial_t \rho - \nabla_x \cdot (\nabla_x U^0 \rho) - d\Delta_x \rho = 0, \tag{5.20}$$

*and*

$$\begin{aligned} &\rho\partial_t\theta_0 - \rho\nabla_x U^0 \cdot \nabla_x\theta_0 - 2\alpha_2\nabla_x\rho\cdot\nabla_x\theta_0 - \alpha_2\rho\Delta_x\theta_0 \\ &\quad +\alpha_3(\rho\nabla_x^2\theta_0 + \nabla_x\theta_0\otimes\nabla_x\rho + \nabla_x\rho\otimes\nabla_x\theta_0) : [\omega_0\otimes\omega_0 - \omega_0^\perp\otimes\omega_0^\perp] \\ &\qquad + \Big(2\rho\alpha_3\nabla_x\theta_0\otimes\nabla_x\theta_0 - \alpha_4\nabla_x^2\rho\Big) : [\omega_0\otimes\omega_0^\perp + \omega_0^\perp\otimes\omega_0] + \alpha_5\rho\langle\partial_\theta U^1\rangle = 0, \end{aligned} \tag{5.21}$$

*where* $\langle h\rangle = \int_{-\pi/2}^{\pi/2} h(\theta)M_{\theta_0}(\theta)\frac{d\theta}{\pi}$ *for any function* $h$ *of* $\theta \in [-\frac{\pi}{2},\frac{\pi}{2})$, *and where the coefficients* $\alpha_2,\alpha_3,\alpha_4,\alpha_5$ *are given by:*

$$\begin{aligned} \alpha_2 &= \frac{d}{\alpha_1}(\alpha_1 + \frac{\xi\alpha L^4\gamma c(r)}{24}), \\ \alpha_3 &= \frac{\xi\alpha L^4\gamma}{24\alpha_1}(\frac{1}{4Z^2} - 1 + \frac{6dc(r)}{\xi\alpha L^2\gamma}), \\ \alpha_4 &= \frac{\xi\alpha L^4\gamma}{192Z^2\alpha_1}, \\ \alpha_5 &= \frac{1}{\alpha_1}, \end{aligned} \tag{5.22}$$

*with* $\alpha_1$ *given by:*

$$\alpha_1 = 1 - \frac{1}{Z^2}. \tag{5.23}$$

*Proof.* Suppose that all the functions are as smooth as needed and that all convergences are as strong as needed. In the limit $\varepsilon \to 0$, let $f^\varepsilon \to f$. As $Q(f^\varepsilon) = O(\varepsilon)$, then $Q(f) = 0$. By proposition 5.6, we deduce that $f$ is given by (5.19) with $\rho \geq 0$ and $\theta_0 \in [-\frac{\pi}{2},\frac{\pi}{2})$ to be determined. In order to find the equations for $\rho$ and $\theta_0$, we use the set of GCI given by Prop. 5.3.

**Equation for $\rho$** The use of the constant GCI amounts to integrating Eq. (5.1) over $[-\frac{\pi}{2},\frac{\pi}{2})$. This gives:

$$\int_{-\frac{\pi}{2}}^{\frac{\pi}{2}}\left\{\partial_t f^\varepsilon-\nabla_x\cdot(\nabla_x U^0 f^\varepsilon)-\partial_\theta\left(\left[\partial_\theta U^1+\xi G[f^\varepsilon](\theta)\right]f^\varepsilon\right)-d\Delta_x f^\varepsilon\right\}\frac{d\theta}{\pi}=0,$$

which leads to the continuity equation for $\rho^\varepsilon$:

$$\partial_t\rho^\varepsilon-\nabla_x\cdot(\nabla_x U^0\rho^\varepsilon)-d\Delta_x\rho^\varepsilon=0.$$

In the limit $\varepsilon\to 0$, $\rho^\varepsilon\to\rho$ which leads to Eq. (5.20).

**Equation for $\theta_0$** We multiply Eq. (5.1) by the GCI $\Psi_{\theta_{f^\varepsilon}}$ associated with the direction $\theta_{f^\varepsilon}$ of $f^\varepsilon$, namely $\Psi_{\theta_{f^\varepsilon}}=g(\theta-\theta_{f^\varepsilon})$ where $g$ is the function defined in Prop. 5.6. We integrate with respect to $\theta$ and first note that:

$$\int_{-\frac{\pi}{2}}^{\frac{\pi}{2}}Q(f^\varepsilon)\Psi_{\theta_{f^\varepsilon}}d\theta=\int_{-\frac{\pi}{2}}^{\frac{\pi}{2}}L_{\theta_{f^\varepsilon}}f^\varepsilon\Psi_{\theta_{f^\varepsilon}}d\theta=0,$$

by (5.13). Since $f^\varepsilon\to\rho M_{\theta_0}$, we have $\theta_{f^\varepsilon}\to\theta_0$ and $\Psi_{\theta_{f^\varepsilon}}\to\Psi_{\theta_0}$. Therefore, in the limit $\varepsilon\to 0$, we get:

$$\int_{-\frac{\pi}{2}}^{\frac{\pi}{2}}\left(\partial_t(\rho M_{\theta_0})-\nabla_x\cdot(\nabla_x U^0\rho M_{\theta_0})-\partial_\theta\left(\left[\partial_\theta U^1+\xi G[\rho M_{\theta_0}](\theta)\right]\rho M_{\theta_0}\right)-d\Delta_x(\rho M_{\theta_0})\right)\Psi_{\theta_0}d\theta=0. \tag{5.24}$$

For simplicity, we denote $M_{\theta_0}=M$. We have:

$$\Delta_x(\rho M)=M\Delta_x\rho+\rho\Delta_x M+2\nabla_x\rho\cdot\nabla_x M,$$
$$\nabla_x\cdot(\nabla_x U^0\rho M)=M\nabla_x\cdot(\nabla_x U^0\rho)+\rho\nabla_x U^0\cdot\nabla_x M.$$

Using the continuity equation (5.20), we have:

$$\partial_t(\rho M)=\rho\partial_t M+M\partial_t\rho=\rho\partial_t M+(\nabla_x\cdot(\nabla_x U^1\rho)+d\Delta_x\rho)M.$$

So:

$$\partial_t(\rho M)-\nabla_x\cdot(\nabla_x U^0\rho M)-d\Delta_x(\rho M)=\rho\partial_t M-\rho\nabla_x U^0\cdot\nabla_x M-d\rho\Delta_x M-2d\nabla_x\rho\cdot\nabla_x M.$$

Therefore, Eq. (5.24) reads:

$$\rho\int_{-\frac{\pi}{2}}^{\frac{\pi}{2}}\partial_t M\Psi\frac{d\theta}{\pi}-X_1-X_2-X_3-X_4=0, \tag{5.25}$$

where:

$$X_1 = \int_{-\frac{\pi}{2}}^{\frac{\pi}{2}} \left(\rho(\nabla_x U^0 + 2d\frac{\nabla_x \rho}{\rho}) \cdot \nabla_x M\right) \Psi \frac{d\theta}{\pi}, \tag{5.26}$$

$$X_2 = \int_{-\frac{\pi}{2}}^{\frac{\pi}{2}} \partial_\theta \left(\partial_\theta U^1 \rho M\right) \Psi \frac{d\theta}{\pi}, \tag{5.27}$$

$$X_3 = \xi \int_{-\frac{\pi}{2}}^{\frac{\pi}{2}} \partial_\theta \left( G[\rho M](\theta) \rho M\right) \Psi \frac{d\theta}{\pi}, \tag{5.28}$$

$$X_4 = d\rho \int_{-\frac{\pi}{2}}^{\frac{\pi}{2}} \Delta_x M \Psi \frac{d\theta}{\pi}. \tag{5.29}$$

We now turn to the development of each term of Eq. (5.25). We have:

$$\nabla_x M = 2r \sin 2(\theta - \theta_0) M \nabla_x \theta_0. \tag{5.30}$$

Then,

$$(\nabla_x U^0 + 2d\frac{\nabla_x \rho}{\rho}) \cdot \nabla_x M = 2r \sin 2(\theta - \theta_0) M \left(\nabla_x U^0 + 2d\frac{\nabla_x \rho}{\rho}\right) \cdot \nabla_x \theta_0,$$

and thus, $X_1$ can be written:

$$X_1 = 2r\rho \left(\nabla_x U^0 \cdot \nabla_x \theta_0 + 2d\frac{\nabla_x \rho \cdot \nabla_x \theta_0}{\rho}\right) \langle \sin 2(\theta - \theta_0) \Psi \rangle.$$

From integration by parts, the following relations can be written:

$$\langle \sin 2(\theta - \theta_0) \Psi \rangle = \frac{1}{4r^2}(1 - \frac{1}{Z^2}) = \frac{1}{4r^2} \alpha_1. \tag{5.31}$$

Therefore, we have:

$$X_1 = \frac{\rho \alpha_1}{2r}(\nabla_x U^0 \cdot \nabla_x \theta_0 + 2d\frac{\nabla_x \rho \cdot \nabla_x \theta_0}{\rho}). \tag{5.32}$$

Since $X_2$ is the integral of a $\pi$-periodic function over a period, we can write

$$X_2 = \int_{\theta_0 - \pi/2}^{\theta_0 + \pi/2} \partial_\theta \left(\partial_\theta U^1 \rho M\right) \Psi \frac{d\theta}{\pi}.$$

Now, by construction, (see prop 5.6), $\Psi(\theta_0 - \frac{\pi}{2}) = \Psi(\theta_0) = \Psi(\theta_0 + \frac{\pi}{2}) = 0$. So, integrating by parts, we have

$$X_2 = -\int_{\theta_0 - \pi/2}^{\theta_0 + \frac{\pi}{2}} \rho M \, \partial_\theta U^1 \, \partial_\theta \Psi \frac{d\theta}{\pi}.$$

Now, by construction again (see (5.18)), we have

$$\partial_\theta \Psi = \frac{1}{2r}(1 - \frac{1}{MZ^2}). \tag{5.33}$$

Using again the $\pi$-periodicity of $U^1$, we obtain:

$$X_2 = -\frac{\rho}{2r}\langle \partial_\theta U^1 (1 - \frac{1}{MZ^2})\rangle = -\frac{\rho}{2r}\langle \partial_\theta U^1 \rangle. \tag{5.34}$$

Now, let us turn to $X_3$. The details of this computation are postponed to appendix 9. We find:

$$\begin{aligned} X_3 = -\frac{dL^2}{12}\Bigg[ & -c(r)(\rho \Delta_x \theta_0 + 2\nabla_x \theta_0 \cdot \nabla_x \rho) \\ & + \Big(2\rho\gamma_1 \nabla_x \theta_0 \otimes \nabla_x \theta_0 - \frac{1}{8Z^2}\nabla_x^2 \rho\Big) : [\omega_0 \otimes \omega_0^\perp + \omega_0^\perp \otimes \omega_0] \\ & + \gamma_1(\rho \nabla_x^2 \theta_0 + \nabla_x \theta_0 \otimes \nabla_x \rho + \nabla_x \rho \otimes \nabla_x \theta_0) : [\omega_0 \otimes \omega_0 - \omega_0^\perp \otimes \omega_0^\perp]\Bigg], \end{aligned} \tag{5.35}$$

where, using (5.8),

$$\gamma_1 = \frac{1}{4Z^2} - 1 + \frac{3c(r)}{2r} = \frac{1}{4Z^2} - 1 + \frac{6dc(r)}{\alpha L^2 \xi \gamma}.$$

We note that $\frac{\alpha L^4 \gamma}{48r}\gamma_1 = \frac{1}{2r}\alpha_3$. Finally, let us explicit the last term $X_4$. A direct computation gives:

$$\Delta_x M = M\Bigg[4r\Big[r\sin^2 2(\theta - \theta_0) - \cos 2(\theta - \theta_0)\Big]|\nabla_x \theta_0|^2 + 2r \sin 2(\theta - \theta_0)\Delta_x \theta_0\Bigg].$$

Then, we deduce that

$$\begin{aligned} X_4 = d\rho\Bigg[ & 2r\Delta_x \theta_0 \langle \sin 2(\theta - \theta_0)\Psi\rangle \\ & + |\nabla_x \theta_0|^2 4r[-\langle \cos 2(\theta - \theta_0)\Psi\rangle + r\langle \sin^2 2(\theta - \theta_0)\Psi\rangle]\Bigg]. \end{aligned}$$

By symmetry, we have:

$$\langle \sin^2 2(\theta - \theta_0)\Psi\rangle = \frac{1}{r}\langle \cos 2(\theta - \theta_0)\Psi\rangle.$$

Therefore, with (5.31), we get:

$$X_4 = \frac{d\rho}{2r}(1 - \frac{1}{Z^2})\Delta_x \theta_0 = \frac{d\rho}{2r}\alpha_1 \Delta_x \theta_0. \tag{5.36}$$

Now, $\partial_t M = 2r \sin 2(\theta - \theta_0) M \partial_t \theta_0$, and

$$\rho \int_{-\frac{\pi}{2}}^{\frac{\pi}{2}} \partial_t M \ \Psi = 2r\rho \langle \sin 2(\theta - \theta_0)\Psi \rangle \partial_t \theta_0 = \frac{\rho}{2r}(1 - \frac{1}{Z^2})\partial_t \theta_0 = \frac{\alpha_1 \rho}{2r}\partial_t \theta_0 \tag{5.37}$$

Collecting (5.32) to (5.36) and inserting them into (5.25) leads to (5.21). □

# 6 Case of a homogeneous fiber distribution: stationary solutions

In this section, we study the stationary solutions of (5.20)-(5.21) in the case of a spatially homogeneous fiber distribution and consequently no external spatial potential $U^0 = 0$. We make the following assumption:

**Hypothesis 6.1.** *The fiber spatial distribution is supposed to be homogeneous, i.e. there exists a constant $\rho_0 > 0$ such that $\rho(x,t) = \rho_0$ for all $(x,t) \in \mathbb{R}^2 \times [0, \infty)$. We also suppose that there are no external spatial forces, i.e. $U^0 = 0$.*

We first note that in the absence of external forces, a uniform and constant density $\rho_0$ is a solution of Eq. (5.20). Now, we are interested in the stationary solutions for the fiber orientation equation (5.21). Noting that the terms involving the spatial derivatives of $\rho$, we find that such stationary solutions satisfy the following equation:

$$\begin{aligned} \alpha_2 \Delta_x \theta_0 - &\alpha_3 [\omega_0 \otimes \omega_0 - \omega_0^\perp \otimes \omega_0^\perp] : \nabla_x^2 \theta_0 \\ &- 2\alpha_3 [\omega_0 \otimes \omega_0^\perp + \omega_0^\perp \otimes \omega_0] : \nabla_x \theta_0 \otimes \nabla_x \theta_0 = \alpha_5 \langle \partial_\theta U^1 \rangle. \end{aligned} \tag{6.1}$$

In this equation, the coefficients $r$, $\alpha_1$, $\alpha_2$ and $\alpha_3$ are constants thanks to (5.8). Moreover, using (5.22), they can be written as functions of $d$, $L^2$ and $r$ as follows:

$$\alpha_1(r) = 1 - \frac{1}{Z(r)^2}, \tag{6.2}$$

$$\alpha_2(d, r, L^2) = d\left(1 + \frac{L^2 r c(r)}{6\alpha_1(r)}\right), \tag{6.3}$$

$$\alpha_3(d, r, L^2) = \frac{dL^2 r}{6\alpha_1(r)}\mathcal{A}(r). \tag{6.4}$$

with

$$\mathcal{A}(r) = \frac{dL^2 r}{6\alpha_1(r)} \left( \frac{1}{4Z(r)^2} - 1 + \frac{3}{2} \frac{c(r)}{r} \right). \tag{6.5}$$

We now show that (6.1) is an elliptic equation. We first introduce some definitions.

Given a function $\mathbf{f}(x, E)$ smooth in its arguments $x \in \Omega$, $E \in \mathbb{R} \times \mathbb{R}^2 \times \mathcal{S}_2(\mathbb{R})$, where $\mathcal{S}_2(\mathbb{R})$ is the space of $2 \times 2$ symmetric matrices with real coefficients, we define the non linear differential operator $F : C^\infty(\mathbb{R}^2) \to C^\infty(\mathbb{R}^2)$ such that for any $x \in \mathbb{R}^2$ and any $u \in C^\infty(\mathbb{R}^2)$, we have

$$F(u(x)) = \mathbf{f}(x, D^2 u(x)),$$

where $D^2 u = \{D^\alpha u, \alpha \in \mathbb{N}^2, |\alpha| \leq 2\}$ and where, for a multi-index $\alpha = (\alpha_1, \alpha_2) \in \mathbb{N}^2$, $|\alpha| = \alpha_1 + \alpha_2$ and $D^\alpha u = \frac{\partial^{|\alpha|} u}{\partial_{x_1}^{\alpha_1} \partial_{x_2}^{\alpha_2}}$. The operator $F$ is said to be elliptic at $u_1 \in C^\infty(\mathbb{R}^2)$ (see [34]) if its linearization $DF(u_1)$ is an elliptic, linear differential operator. We state the following proposition:

**Proposition 6.1.** *Eq. (6.1) can be put in the form*

$$\mathbf{f}(x, D^2\theta_0(x)) = 0, \quad x \in \mathbb{R}^2, \tag{6.6}$$

*where $\mathbf{f}(x, D^2\theta_0)$ is the following operator, quasi linear in $\theta_0$:*

$$\mathbf{f}(x, D^2\theta_0) = \sum_{i,j=1}^{2} \partial_{x_i} \Big( a_{ij}(\theta_0) \partial_{x_j} \theta_0 \Big) - \alpha_5 h(\theta_0). \tag{6.7}$$

*Here, $h(\theta_0) = \langle \partial_\theta U^1 \rangle$ and $A(\theta_0) = (a_{ij}(\theta_0))_{i,j=1,2}$ is a $2 \times 2$ matrix such that:*

$$A(\theta_0) = \begin{pmatrix} \alpha_2 - \alpha_3 \cos 2\theta_0 & -\alpha_3 \sin 2\theta_0 \\ -\alpha_3 \sin 2\theta_0 & \alpha_2 + \alpha_3 \cos 2\theta_0 \end{pmatrix}. \tag{6.8}$$

*Moreover, if the following condition is satisfied for all $r \in \mathbb{R}^+$:*

$$\mathcal{A}(r) + c(r) \geq 0, \tag{6.9}$$

*where $\mathcal{A}(r)$ is given by (6.5), then $F(\theta) = \mathbf{f}(x, D^2\theta)$ is elliptic at $\theta_1$ for all $\theta_1 \in C^2(\mathbb{R}^2)$.*

*Proof.* For any $\theta \in [-\frac{\pi}{2}, \frac{\pi}{2})$, letting $\omega(\theta) = (\cos\theta, \sin\theta)$ and $\omega^\perp(\theta) = (-\sin\theta, \cos\theta)$, we have:

$$\frac{d}{d\theta}[\omega(\theta) \otimes \omega(\theta) - \omega^\perp(\theta) \otimes \omega^\perp(\theta)] = 2[\omega(\theta) \otimes \omega^\perp(\theta) + \omega^\perp(\theta) \otimes \omega(\theta)].$$

Let $F : C^\infty(\mathbb{R}^2) \to C^\infty(\mathbb{R}^2)$ be the non linear differential operator defined by:

$$F(\theta_0) = \mathbf{f}(x, D^2\theta_0),$$

for $\mathbf{f}$ defined by (6.7). Let $DF(\theta_1)$ denote its linearization at $\theta_1$. Then, $DF(\theta_1)$ is a linear map from $C^2(\mathbb{R}^2)$ to $C^0(\mathbb{R}^2)$ and reads, for $v \in C^2(\mathbb{R}^2)$:

$$DF(\theta_1)v = \left.\frac{\partial F(\theta_1 + sv)}{\partial s}\right|_{s=0} = \sum_{i,j=1}^{2} \Big( a_{ij}(\theta_1)\partial_{x_i}\partial_{x_j} v \Big) + Lv, \tag{6.10}$$

where $L$ is a linear differential operator of order 1 the coefficients of which depend on $D\theta_1$:

$$\begin{aligned} Lv = &\sum_{i,j=1}^{2} \Big( a'_{ij}(\theta_1)(\partial_{x_i}\theta_1 \partial_{x_j} v + \partial_{x_i} v \partial_{x_j}\theta_1) \Big) + \sum_{i=1}^{2} \partial_{x_i} U^0 \partial_{x_i} v \\ &+ \sum_{i,j=1}^{2} \Big( a''_{ij}(\theta_1)\partial_{x_i}\theta_1\partial_{x_j}\theta_1 + a'_{ij}(\theta_1)\partial_{x_i x_j}\theta_1 - \alpha_5 h'(\theta_1) \Big) v, \end{aligned}$$

where $a'_{ij}(\theta_1)$ and $a''_{ij}(\theta_1)$ are the first and second order derivatives of the coefficients of matrix $A$ which read:

$$\begin{aligned} (a'_{ij}(\theta_1))_{i,j=1,2} &= 2\alpha_3 \begin{pmatrix} \sin 2\theta_1 & -\cos 2\theta_1 \\ -\cos 2\theta_1 & -\sin 2\theta_1 \end{pmatrix}, \\ (a''_{ij}(\theta_1))_{i,j=1,2} &= 4\alpha_3 \begin{pmatrix} \cos 2\theta_1 & \sin 2\theta_1 \\ \sin 2\theta_1 & -\cos 2\theta_1 \end{pmatrix}. \end{aligned}$$

Therefore, the linearization of $F$ at $\theta_1$ is elliptic provided that the matrix $A(\theta_1) = \Big(a_{ij}(\theta_1)\Big)_{i,j=1,2}$ is positive-definite.

Note that the determinant of the matrix $A(\theta_1) = (a_{ij}(\theta_1))_{i,j=1,2}$ is given by $\det(A(\theta_1)) = \alpha_2^2 - \alpha_3^2$ and does not depend on $\theta_1$. Moreover, $\det(A(\theta_1)) > 0$ provided that $|\frac{\alpha_2}{\alpha_3}| > 1$. The eigenvalues of the matrix $A(\theta_1)$ solve

$$\det(A(\theta_1) - \lambda I) = \lambda^2 - 2\lambda\alpha_2 + \alpha_2^2 - \alpha_3^2 = 0$$

and the determinant $\Delta = 4\alpha_3^2$ is strictly positive as long as $\alpha_3 \neq 0$. In this case, the matrix $A(\theta_1)$ has two distinct real eigenvalues given by:

$$\lambda^\pm = (\alpha_2 \pm \alpha_3).$$

Therefore, the matrix $A(\theta_1)$ is positive definite if and only if $\alpha_2 > |\alpha_3|$.

We now analyse the sign of each coefficient $\alpha_1, \alpha_2, \alpha_3$. First of all (see Eq. (5.10)), the $p$-th derivative $Z^{(p)}$ of $Z$ with respect to $r$ reads:

$$Z^{(p)}(r) = \int_{-\pi/2}^{\pi/2} (\cos 2\theta)^p e^{r\cos 2\theta} \frac{d\theta}{\pi},$$

and we have $Z^{(2k)}(r) \geq 0$ for all $k \in \mathbb{N}^+$ and all $r \in \mathbb{R}^+$ as the functions $\theta \to (\cos 2\theta)^{2k} e^{r\cos 2\theta}$ are positive for any $r \in \mathbb{R}^+$. We deduce that $Z^{(2k+1)}(r)$ are increasing functions of $r$ for any $k \in \mathbb{N}^+$. Note that from the symmetry of the function $\cos 2\theta$, we have for any $k \in \mathbb{N}^+$:

$$\int_{-\pi/2}^{\pi/2} (\cos 2\theta)^{2k+1} \frac{d\theta}{\pi} = Z^{(2k+1)}(0) = 0.$$

Therefore, we also have that $Z^{(2k+1)}(r) \geq Z^{(2k+1)}(0) \geq 0$ for any $k \in \mathbb{N}$. We thus obtain that for any $p \in \mathbb{N}$ and any $r \in \mathbb{R}^+$:

$$Z^{(p)}(r) \geq Z^{(p)}(0) \geq 0,$$

and we note that $Z(r) \to \infty$ as $r \to \infty$. Moreover, as $Z(0) = 1$ we deduce $Z(r) \geq 1$ for any $r \in [0, +\infty)$. We also note that:

$$c(r) = \frac{Z^{(1)}(r)}{Z(r)} \geq \frac{Z^{(1)}(0)}{Z(r)} \geq 0,$$

and we have:

$$\alpha_1(r) \geq 0, \quad \alpha_2(d, r, L^2) \geq 0 \quad \forall (r, L, d) \in \mathbb{R}^+ \times \mathbb{R} \times \mathbb{R}^+.$$

Now, by integration by parts, we can write:

$$\begin{aligned}\frac{c(r)}{r} &= \frac{1}{rZ(r)} \int_{-\pi/2}^{\pi/2} \cos 2\theta e^{r\cos 2\theta} \frac{d\theta}{\pi} = \frac{1}{Z(r)}\Big(1 - \int_{-\pi/2}^{\pi/2} \cos^2 2\theta e^{r\cos 2\theta} \frac{d\theta}{\pi}\Big) \\ &= \frac{1}{Z(r)}(1 - Z^{(2)}(r)),\end{aligned} \tag{6.11}$$

and using the previous analysis, we have:

$$Z^{(2)}(r) \geq Z^{(2)}(0) = \frac{1}{2}.$$

Therefore, (since $Z(r) \geq 1$):

$$\frac{c(r)}{r} \leq \frac{1}{2},$$

for any $r \in \mathbb{R}^+$. This relation together with the fact that $1 - \frac{1}{4Z^2(r)} \geq \frac{3}{4}$ leads to:

$$\alpha_3(d, r, L^2) = \frac{dL^2 r}{6\alpha_1(r)}\left(\frac{3c(r)}{2r} - (1 - \frac{1}{4Z^2})\right) \leq 0.$$

Now, we can write:

$$|\frac{\alpha_2}{\alpha_3}| > 1 \;\Leftrightarrow \alpha_2 > -\alpha_3,$$

or equivalently, using Eqs. (6.3) and (6.4):

$$|\frac{\alpha_2}{\alpha_3}| > 1 \;\Leftrightarrow \frac{6\alpha_1(r)}{drL^2} > -(\mathcal{A}(r) + c(r)).$$

Therefore, if (6.9) holds, then $\alpha_2 > |\alpha_3|$ and the matrix $A(\theta_1)$ is positive definite for all $r \in [0, 1]$, $L \in \mathbb{R}^+$, $d \in \mathbb{R}$, independently of $\theta_1 \in C^2(\mathbb{R}^2)$. We conclude that $F$ is elliptic at $\theta_1$ for all $\theta_1 \in C^2(\mathbb{R}^2)$, provided (6.9) holds. ☐

**Remark 6.1.** *As shown by Fig. 2.24 , $\mathcal{A}(r) + c(r)$ is positive for any $r \in \mathbb{R}^+$. The rigorous proof of this fact will be the subject of future work.*

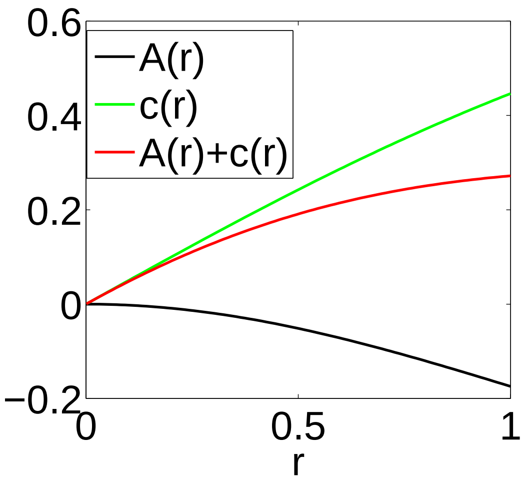

Figure 2.24: Functions $\mathcal{A}(r)$ (black), $c(r)$ (green) and $\mathcal{A}(r) + c(r)$ (red) as functions of $r \in [0, 100]$.

# 7 Conclusion

In this paper, we have formally derived a macroscopic model for temporarily linked fibers interacting through alignment at the links. We have shown that the corresponding kinetic model involves two distribution functions: the fiber distribution function and the cross-link distribution function. The latter can be seen as a joint two-particle fiber distribution function. This model provides a unique explicit example of a kinetic model closed at the level of the two particle distribution function. We then considered the regime of a fast fiber linking/unlinking process, where the link distribution function can be expressed simply in terms of the fiber distribution function. We studied the diffusive limit of the resulting equation and obtained a system of two coupled nonlinear diffusion equations for the fiber density and mean orientation. In the homogeneous fiber density case, we showed that the resulting quasilinear problem is elliptic. Future works will deeper investigate the mathematical properties of the models, such as rigorously proving the mean-field kinetic limit of the particle system or proving existence and uniqueness of smooth solutions for the macroscopic diffusion system. Numerical simulations will be performed to validate the macroscopic model by comparison with the individual based model. Further perspectives are the removal of the fast fiber linking/unlinking hypothesis, in order to understand how a finite lifetime of the cross-links affects the macroscopic dynamics.

# Bibliography

[1] R. Alonso, J. Young and Y. Cheng, A particle interaction model for the simulation of biological, cross-linked fibers inspired from flocking theory, *Cellular and molecular bioengineering* **7** (2014) 58-72.

[2] W. Alt and M. Dembo, Cytoplasm dynamics and cell motion: two phase flow models, *Math. Biosci.* **156** (1999) 207-228.

[3] J. A. Åström, P. B. S. Kumar, I. Vattulainen and M. Karttunen, Strain hardening, avalanches, and strain softening in dense cross-linked actin networks, *Phys. Rev. E* **77** (2008) 051913.

[4] C. Bardos, R. Santos and R. Sentis, Diffusion approximation and computation of the critical size, *Trans. Amer. Math. Soc.* **284** (1984) 617-649.

[5] A. Baskaran and M. C. Marchetti, Hydrodynamics of self-propelled hard rods, *Phys. Rev. E* **77** (2008) 011920.

[6] E. Bertin, H. Chaté, F. Ginelli, S. Mishra, A. Peshkov and S. Ramaswamy, Mesoscopic theory for fluctuating active nematics, *New J. Phys.* **15** (2013) 085032.

[7] R. Bird, C. Curtiss, R. Armstrong, and O. Hassager, Dynamics of Polymeric Liquids, Vol. 2, Kinetic Theory, John Wiley & Sons, New York, 1987.

[8] C. P. Broedersz, M. Depken, N. Y. Yao, M. R. Pollak, D. A. Weitz and F. C. MacKintosh, Cross-link-governed dynamics of biopolymer networks, *Phys. Rev. Lett.* **105** (2010) 238101.

[9] G.A. Buxton, N. Clarke and P. J. Hussey, Actin dynamics and the elasticity of cytoskeletal networks, *Express Polymer Letters* **3** (2009) 579-587.

[10] E. Carlen, R. Chatelin, P. Degond, and B Wennberg, Kinetic hierarchy and propagation of chaos in biological swarm models, Phys. D 260 (2013) 90-111.

[11] E. Carlen, P. Degond and B Wennberg, Kinetic limits for pair-interaction driven master equations and biological swarm models, *Math. Models Methods Appl. Sci.* **23** (2013)1339-1376.

[12] I. S. Ciuperca, E. Hingant, L. I. Palade and L. Pujo-Menjouet, Fragmentation and monomer lengthening of rod-like polymers, a relevant model for prion proliferation, *Discrete Contin. Dyn. Syst. Ser. B* **17** (2012) 775-799.

[13] P. Degond, C. Appert-Rolland, M. Moussaid, J. Pettré and G. Theraulaz, A hierarchy of heuristic-based models of crowd dynamics, *J. Stat. Phys.* **152** (2013) 1033-1068.

[14] P. Degond, G Dimarco, T. B. N. Mac and N. Wang, Macroscopic models of collective motion with repulsion, *Commun. Math. Sci.*, to appear, arxiv preprint # 1404.4886.

[15] P. Degond, J-G. Liu, S. Motsch and V. Panferov, Hydrodynamic models of self-organized dynamics: derivation and existence theory, *Methods Appl. Anal.* **20** (2013) 089-114.

[16] P. Degond and S. Mas-Gallic, Existence of solutions and diffusion approximation for a model Fokker-Planck equation, *Transport Theory and Statistical Physics* **16** (1987) 589-636.

[17] P. Degond and S. Motsch, Continuum limit of self-driven particles with orientation interaction, *Math. Models Methods Appl. Sci.* **18 Suppl.** (2008) 1193-1215.

[18] M. Doi and S. F. Edwards, The Theory of Polymer Dynamics, International Series of Monographs on Physics, Vol 73, Oxford University Press, Oxford, 1999.

[19] A. Frouvelle, A continuum model for alignment of self-propelled particles with anisotropy and density-dependent parameters, *Math. Models Methods Appl. Sci.* **22** (2012) 1250011.

[20] F. Ginelli, F. Peruani, M. Bär and H. Chaté, Large-scale collective properties of self-propelled rods, *Phys. Rev. Lett.* **104** (2010) 184502.

[21] D. A Head, A. J. Levine and F. C MacKintosh, Distinct regimes of elastic response and deformation modes of cross-linked cytoskeletal and semiflexible polymer networks, *Phys. Rev. E* **68** (2003) 061907.

[22] J. F. Joanny, F. Jülicher, K. Kruse and J. Prost, Hydrodynamic theory for multi-component active polar gels, *New J. Phys.* **9** (2007) 422.

[23] H. Karsher, J. Lammerding, H. Huang, R. T. Lee, R. D. Kamm and M. R. Kaazempur-Mofrad, A three-dimensional viscoelastic model for cell deformation with experimental verification, *Biophysical Journal* **85** (2003) 3336-3349.

[24] W. Maier and A. Saupe, Eine einfache molekulare Theorie des nematischen kristallinflüssigen Zustandes, *Z. Naturforsch.* **13** (1958) 564-566.

[25] S. Mischler and C. Mouhot, Kac's Program in Kinetic Theory, *Invent. Math.* **193** (2013) 1-147.

[26] S. Mischler, C. Mouhot and B. Wennberg, A new approach to quantitative propagation of chaos for drift, diffusion and jump processes, *Probab. Theory Related Fields* **161** (2015) 1-59.

[27] D. Oelz, C. Schmeiser and J. V. Small, Modeling of the actin-cytoskeleton in symmetric lamellipodial fragments, *Cell Adhesion and Migration* **2** (2008) 117-126.

[28] L. Onsager, The effects of shape on the interaction of colloidal particles, *Ann. New York Acad. Sci.* **51** (1949) 627-659.

[29] F. Peruani, A. Deutsch and M. Bär, Nonequilibrium clustering of self-propelled rods, *Phys. Rev. E* **74** (2006) 030904(R).

[30] D. Peurichard, F. Delebecque, A. Lorsignol, C. Barreau, J. Rouquette, X. Descombes, L. Casteilla and P. Degond, Simple mechanical cues could explain adipose tissue morphology, submitted.

[31] F. Poupaud, Diffusion approximation of the linear semiconductor Boltzmann equation: analysis of boundary layers, *Asymptot. Anal.* **4** (1991) 293-317.

[32] Y. Sone, Kinetic Theory and Fluid Dynamics, Birkhausser, 2002.

[33] L. A. Taber, Y. Shi, L. Yang and P. V. Bayly, A poroelastic model for cell crawling including mechanical coupling between cytoskeletal contraction and actin polymerization, *Journal of Mechanics of Materials and Structures* **6** (2011) 569-589.

[34] M.E. Taylor, Partial Differential Equations III: Nonlinear Equations, Applied Mathematical Sciences, vol 117, Springer, 1996.

[35] T. Vicsek, A. Czirók, E. Ben-Jacob, I. Cohen and O. Shochet, Novel type of phase transition in a system of self-driven particles, *Phys. Rev. Lett.* **75** (1995) 1226-1229.

[36] T. Vicsek and A. Zafeiris, Collective motion, *Phys. Rep.* **517** (2012) 71-140.

# 8 Proof of Theorem 3.1

## 8.1 Evolution equation for the fibers

For all observable functions $\Phi(x,\theta)$, we define:

$$\langle f^N, \Phi\rangle = \int \Phi(x,\theta) f^N(t,x,\theta)\,dx_1 d\theta = \frac{1}{N}\sum_{i=1}^{N} \Phi(X_i(t),\theta_i(t)).$$

Similarly, for all two-particle observable functions $\Psi(x_1,\theta_1,\ell_1,x_2,\theta_2,\ell_2)$, we define:

$$\begin{aligned}\langle\!\langle g^K, \Psi\rangle\!\rangle &= \int \Psi(x_1,\theta_1,\ell_1,x_2,\theta_2,\ell_2) g^K(x_1,\theta_1,\ell_1,x_2,\theta_2,\ell_2)\,dx_1 dx_2 \frac{d\theta_1}{\pi}\frac{d\theta_2}{\pi} d\ell_1 d\ell_2 \\ &= \frac{1}{2K}\sum_{k=1}^{K}\Big(\Psi(X_{i(k)},\theta_{i(k)},\ell^k_{i(k)},X_{j(k)},\theta_{j(k)},\ell^k_{j(k)}) + \Psi(X_{j(k)},\theta_{j(k)},\ell^k_{j(k)},X_{i(k)},\theta_{i(k)},\ell^k_{i(k)})\Big),\end{aligned}$$

where integrals over $x$ are carried over $\mathbb{R}^2$, in $\theta$ over $(-\frac{\pi}{2},\frac{\pi}{2})$ and in $\ell$ over $(-\frac{L}{2},\frac{L}{2})$. We recall the notations $C^k_{i(k),j(k)} = (X_{i(k)},\theta_{i(k)},\ell^k_{i(k)},X_{j(k)},\theta_{j(k)},\ell^k_{j(k)})$ (resp. $C^k_{j(k),i(k)} = (X_{j(k)},\theta_{j(k)},\ell^k_{j(k)},X_{i(k)},\theta_{i(k)},\ell^k_{i(k)})$). Then:

$$\frac{d}{dt}\langle f^N,\Phi\rangle = \frac{1}{N}\sum_{i=1}^{N}\Big(\nabla_x\Phi(X_i(t),\theta_i(t))\cdot\frac{dX_i(t)}{dt} + \partial_\theta\Phi(X_i(t),\theta_i(t))\frac{d\theta_i(t)}{dt}\Big).$$

Using (2.10) and (2.11), we obtain:

$$\begin{aligned}&\frac{d}{dt}\langle f^N,\Phi\rangle \\ &= -\frac{1}{N}\sum_{i=1}^{N}\Big[(\mu\nabla_x\Phi\cdot\nabla_x U + \lambda\partial_\theta\Phi\partial_\theta U)(X_i,\theta_i) + d(\mu\nabla_x\Phi\cdot\nabla_x\log(\tilde f^N) + \lambda\partial_\theta\Phi\partial_\theta\log(\tilde f^N))(X_i,\theta_i) \\ &\qquad + \mu\nabla_x\Phi(X_i,\theta_i)\cdot\frac{1}{2}\sum_{k=1}^{K}(\nabla_{x_1}V\delta_{i(k)}(i) + \nabla_{x_2}V\delta_{j(k)}(i))(C^k_{i(k),j(k)}) \\ &\qquad\quad + \lambda\partial_\theta\Phi(X_i,\theta_i)\frac{1}{2}\sum_{k=1}^{K}(\partial_{\theta_1}V\delta_{i(k)}(i) + \partial_{\theta_2}V\delta_{j(k)}(i))(C^k_{i(k),j(k)}) \\ &\qquad\qquad + \lambda\partial_\theta\Phi(X_i,\theta_i)\frac{1}{2}\sum_{k=1}^{K}(\partial_{\theta_1}b\;\delta_{i(k)}(i) + \partial_{\theta_2}b\;\delta_{j(k)}(i))(\theta_{i(k)},\theta_{j(k)})\Big].\end{aligned}$$

We get, using the definition of a distributional derivative:

$$
\begin{aligned}
\frac{d}{dt}\langle f^N, \Phi\rangle = \langle \mu\nabla_x\cdot\Big(f^N\nabla_x(U + d\log\tilde{f}^N)\Big) + \lambda\partial_\theta\Big(f^N\partial_\theta(U + d\log\tilde{f}^N)\Big), \Phi\rangle \\
-\frac{\mu}{2N}\sum_{i=1}^{N}\left(\nabla_x\Phi(X_i,\theta_i)\cdot\sum_{k=1}^{K}(\nabla_{x_1}V\delta_{i(k)}(i) + \nabla_{x_2}V\delta_{j(k)}(i))(C^k_{i(k),j(k)})\right) \\
-\frac{\lambda}{2N}\sum_{i=1}^{N}\left(\partial_\theta\Phi(X_i,\theta_i)\sum_{k=1}^{K}(\partial_{\theta_1}V\delta_{i(k)}(i) + \partial_{\theta_2}V\delta_{j(k)}(i))(C^k_{i(k),j(k)})\right) \\
-\frac{\lambda}{2N}\sum_{i=1}^{N}\left(\partial_\theta\Phi(X_i,\theta_i)\sum_{k=1}^{K}(\partial_{\theta_1}b\ \delta_{i(k)}(i) + \partial_{\theta_2}b\ \delta_{j(k)}(i))(\theta_{i(k)},\theta_{j(k)})\right).
\end{aligned}
$$

Now, exchanging the sums in $i$ and $k$ in the previous equation, one obtains:

$$
\begin{aligned}
\frac{d}{dt}\langle f^N, \Phi\rangle = \langle \mu\nabla_x\cdot\Big(f^N\nabla_x(U + d\log\tilde{f}^N)\Big) + \lambda\partial_\theta\Big(f^N\partial_\theta(U + d\log\tilde{f}^N)\Big), \Phi\rangle \\
-\frac{\mu}{2N}\sum_{k=1}^{K}\left(\nabla_{x_1}V(C^k_{i(k),j(k)})\cdot\nabla_x\Phi(X_{i(k)},\theta_{i(k)}) + \nabla_{x_2}V(C^k_{i(k),j(k)})\cdot\nabla_x\Phi(X_{j(k)},\theta_{j(k)}))\right) \\
-\frac{\lambda}{2N}\sum_{k=1}^{K}\left(\partial_{\theta_1}V(C^k_{i(k),j(k)})\partial_\theta\Phi(X_{i(k)},\theta_{i(k)}) + \partial_{\theta_2}V(C^k_{i(k),j(k)})\partial_\theta\Phi(X_{j(k)},\theta_{j(k)}))\right) \\
-\frac{\lambda}{2N}\sum_{k=1}^{K}\left(\partial_{\theta_1}b(\theta_{i(k)},\theta_{j(k)})\partial_\theta\Phi(X_{i(k)},\theta_{i(k)}) + \partial_{\theta_2}b(\theta_{i(k)},\theta_{j(k)})\partial_\theta\Phi(X_{j(k)},\theta_{j(k)})\right).
\end{aligned}
$$

From the symmetry of $V$ (see Eq. (2.4)), the following expressions hold:

$$
\nabla_{x_2}V(C^k_{i(k),j(k)}) = \nabla_{x_1}V(C^k_{j(k),i(k)}), \quad \partial_{\theta_2}V(C^k_{i(k),j(k)}) = \partial_{\theta_1}V(C^k_{j(k),i(k)}),
$$

and from the symmetry of $b$, we have:

$$
\partial_{\theta_2}b(\theta_{i(k)},\theta_{j(k)}) = \partial_{\theta_1}b(\theta_{j(k)},\theta_{i(k)}),
$$

leading to:

$$
\begin{aligned}
\frac{d}{dt}\langle f^N, \Phi\rangle = \langle \mu\nabla_x\cdot\Big(f^N\nabla_x(U + d\log\tilde{f}^N)\Big) + \lambda\partial_\theta\Big(f^N\partial_\theta(U + d\log\tilde{f}^N)\Big), \Phi\rangle \\
-\frac{\mu}{2N}\sum_{k=1}^{K}\left(\nabla_{x_1}V(C^k_{i(k),j(k)})\cdot\nabla_x\Phi(X_{i(k)},\theta_{i(k)}) + \nabla_{x_1}V(C^k_{j(k),i(k)})\cdot\nabla_x\Phi(X_{j(k)},\theta_{j(k)}))\right) \\
-\frac{\lambda}{2N}\sum_{k=1}^{K}\left(\partial_{\theta_1}V(C^k_{i(k),j(k)})\partial_\theta\Phi(X_{i(k)},\theta_{i(k)}) + \partial_{\theta_1}V(C^k_{j(k),i(k)})\partial_\theta\Phi(X_{j(k)},\theta_{j(k)}))\right) \\
-\frac{\lambda}{2N}\sum_{k=1}^{K}\left(\partial_{\theta_1}b(\theta_{i(k)},\theta_{j(k)})\partial_\theta\Phi(X_{i(k)},\theta_{i(k)}) + \partial_{\theta_1}b(\theta_{j(k)},\theta_{i(k)})\partial_\theta\Phi(X_{j(k)},\theta_{j(k)})\right),
\end{aligned}
$$

or again:

$$
\begin{aligned}
&\frac{d}{dt}\langle f^N,\Phi\rangle = \langle \mu\nabla_x\cdot\Big(f^N\nabla_x(U+d\log\tilde f^N)\Big)+\lambda\partial_\theta\Big(f^N\partial_\theta(U+d\log\tilde f^N)\Big),\Phi\rangle\\
&-\frac{K}{N}\langle\!\langle \frac{1}{2K}\sum_{k=1}^{K}\Big(\delta_{(C^k_{i(k),j(k)})}+\delta_{(C^k_{j(k),i(k)})}\Big)(x_1,\theta_1,\ell_1,x_2,\theta_2,\ell_2),\Big(\mu\nabla_{x_1}V(x_1,\theta_1,\ell_1,x_2,\theta_2,\ell_2)\cdot\nabla_x\Phi(x_1,\theta_1)\\
&\qquad\qquad +\lambda\partial_{\theta_1}V(x_1,\theta_1,\ell_1,x_2,\theta_2,\ell_2)\partial_{\theta_1}\Phi(x_1,\theta_1)+\lambda\partial_{\theta_1}b(\theta_1,\theta_2)\partial_{\theta_1}\Phi(x_1,\theta_1)\Big)\rangle\!\rangle.
\end{aligned}
$$

Therefore, we obtain:

$$
\begin{aligned}
\frac{d}{dt}\langle f^N,\Phi\rangle &= \langle \mu\nabla_x\cdot\Big(f^N\nabla_x(U+d\log\tilde f^N)\Big)+\lambda\partial_\theta\Big(f^N\partial_\theta(U+d\log\tilde f^N)\Big),\Phi\rangle\\
&\quad -\frac{K}{N}\langle\!\langle g^K,\mu\nabla_{x_1}V(x_1,\theta_1,\ell_1,x_2,\theta_2,\ell_2)\cdot\nabla_x\Phi(x_1,\theta_1)\rangle\!\rangle\\
&\qquad -\frac{K}{N}\langle\!\langle g^K,\lambda\Bigg(\partial_{\theta_1}V(x_1,\theta_1,\ell_1,x_2,\theta_2,\ell_2)+\partial_{\theta_1}b(\theta_1,\theta_2)\Bigg)\partial_\theta\Phi(x_1,\theta_1)\rangle\!\rangle.
\end{aligned}
$$

Finally, we get:

$$
\begin{aligned}
\frac{d}{dt}\langle f^N,\Phi\rangle =&\langle \mu\nabla_x\cdot\Big(f^N\nabla_x(U+d\log\tilde f^N)\Big)+\lambda\partial_\theta\Big(f^N\partial_\theta(U+d\log\tilde f^N)\Big),\Phi\rangle\\
&+\mu\frac{K}{N}\langle\!\langle\nabla_{x_1}\cdot\Big(g^K\nabla_{x_1}V\Big),\Phi(x_1,\theta_1)\rangle\!\rangle+\lambda\frac{K}{N}\langle\!\langle\partial_{\theta_1}\Big(g^K\partial_{\theta_1}V+\partial_{\theta_1}b\Big),\Phi(x_1,\theta_1)\rangle\!\rangle.\\
=&\langle \mu\nabla_x\cdot\Big(f^N\nabla_x(U+d\log\tilde f^N)\Big)+\lambda\partial_\theta\Big(f^N\partial_\theta(U+d\log\tilde f^N)\Big)\\
&+\frac{K}{N}[[\mu\nabla_{x_1}\cdot\Big(g^K\nabla_{x_1}V\Big)+\lambda\partial_{\theta_1}\Big(g^K(\partial_{\theta_1}V+\partial_{\theta_1}b)\Big)]](x_1,\theta_1),\Phi(x_1,\theta_1)\rangle,
\end{aligned}
\tag{8.1}
$$

where, for a distribution $T$ acting on functions of $(x_1,\theta_1,\ell_1,x_2,\theta_2,\ell_2)$, we denote by $[[T]](x_1,\theta_1)$ the distribution which to any function $\Phi(x_1,\theta_1)$ associates

$$\langle[[T]](x_1,\theta_1),\Phi(x_1,\theta_1)\rangle=\langle\!\langle T,\Phi\mathbf{1}\rangle\!\rangle,$$

and where $\mathbf{1}$ is the constant function of the variables $(x_1,\theta_1,\ell_1,x_2,\theta_2,\ell_2)$ equal to 1. In the formal limit $N\to\infty$, $\frac{K}{N}\to\xi$ and given the assumptions on the regularizing sequences $\xi^N$, $\eta^N$, we get that $f^N\to f$, $\tilde f^N\to f$. Then, $\nabla_x\cdot(f\nabla_x\log f)=\Delta_x f$ and $\partial_\theta(f\partial_\theta f)=\partial_\theta^2 f$ and we obtain:

$$\frac{df}{dt}-\mu\nabla_x\cdot((\nabla_xU)f)-\lambda\partial_\theta((\partial_\theta U)f)-\mu\xi\nabla_x\cdot F_1-\lambda\xi\partial_\theta F_2-d\mu\Delta_xf-d\lambda\partial_\theta^2f=0,\tag{8.2}$$

where,

$$
\begin{aligned}
F_1(x,\theta)&=\int(g\nabla_xV)(x_1,\theta_1,\ell_1,x_2,\theta_2,\ell_2)dx_2\frac{d\theta_2}{\pi}d\ell_1d\ell_2,\\
F_2(x,\theta)&=\int((g\partial_{\theta_1}V)(x_1,\theta_1,\ell_1,x_2,\theta_2,\ell_2)+g(x_1,\theta_1,\ell_1,x_2,\theta_2,\ell_2)\partial_{\theta_1}b(\theta_1,\theta_2))dx_2\frac{d\theta_2}{\pi}d\ell_1d\ell_2.
\end{aligned}
$$

## 8.2 Evolution equation for the fiber links

Following the same principle as for $f^N$ and given that the links are maintained over time, i.e. $\frac{d\ell^k_{i(k)}}{dt} = \frac{d\ell^k_{j(k)}}{dt} = 0$, $\forall\, k \in [1, K]$, one can write:

$$
\begin{aligned}
\frac{d}{dt}\langle\langle g^K, \Psi\rangle\rangle = \frac{1}{2K}\sum_{k=1}^{k}\Big[&\nabla_{x_1}\Psi(C^k_{i(k),j(k)})\cdot\frac{dX_{i(k)}}{dt} + \nabla_{x_1}\Psi(C^k_{j(k),i(k)})\cdot\frac{dX_{j(k)}}{dt} \\
&+ \nabla_{x_2}\Psi(C^k_{i(k),j(k)})\cdot\frac{dX_{j(k)}}{dt} + \nabla_{x_2}\Psi(C^k_{j(k),i(k)})\cdot\frac{dX_{i(k)}}{dt} \\
&+ \partial_{\theta_1}\Psi(C^k_{i(k),j(k)})\frac{d\theta_{i(k)}}{dt} + \partial_{\theta_1}\Psi(C^k_{j(k),i(k)})\frac{d\theta_{j(k)}}{dt} \\
&+ \partial_{\theta_2}\Psi(C^k_{i(k),j(k)})\frac{d\theta_{j(k)}}{dt} + \partial_{\theta_2}\Psi(C^k_{j(k),i(k)})\frac{d\theta_{i(k)}}{dt}\Big] \\
= E_1 + \ldots + E_4,&
\end{aligned}
\tag{8.3}
$$

where $E_k$ corresponds to the $k$-th line of (8.3). For the sake of simplicity, the computation of $E_1$ only is developed here. The computation of the other ones are similar and omitted. From Eqs. (2.2), (2.3), one obtains:

$$
\begin{aligned}
E_1 &= \frac{1}{2K}\sum_{K=1}^{k}\left[\nabla_{x_1}\Psi(C^k_{i(k),j(k)})\cdot\frac{dX_{i(k)}}{dt} + \nabla_{x_1}\Psi(C^k_{j(k),i(k)})\cdot\frac{dX_{j(k)}}{dt}\right] \\
&= -\frac{\mu}{2K}\sum_{k=1}^{K}\Bigg[\bigg(\nabla_{x_1}\Psi(C^k_{i(k),j(k)})\cdot\nabla_x\Big(U + d\log\tilde{f}^N\Big)(X_{i(k)},\theta_{i(k)}) \\
&\qquad + \nabla_{x_1}\Psi(C^k_{j(k),i(k)})\cdot\nabla_x\Big(U + d\log\tilde{f}^N\Big)(X_{j(k)},\theta_{j(k)}) \\
&\qquad + \frac{1}{2}\nabla_{x_1}\Psi(C^k_{i(k),j(k)})\cdot\sum_{k'=1}^{K}\bigg(\nabla_{x_1}V\delta_{(i(k'),i(k))} + \nabla_{x_2}V\delta_{(j(k'),i(k))}\bigg)(C^k_{i(k'),j(k')}) \\
&\qquad + \frac{1}{2}\nabla_{x_1}\Psi(C^k_{j(k),i(k)})\cdot\sum_{k'=1}^{K}\bigg(\nabla_{x_1}V\delta_{(i(k'),j(k))} + \nabla_{x_2}V\delta_{(j(k'),j(k))}\bigg)(C^k_{i(k'),j(k')})\Bigg],
\end{aligned}
$$

where we write $V = V(x_1, \theta_1, \ell_1, x_2, \theta_2, \ell_2)$. Now, exchanging the sums in $k$ and $k'$ and using the symmetry of $V$, one obtains:

$$
\begin{aligned}
E_1 = &-\mu\langle\langle g^K, \nabla_{x_1}\Psi(x_1,\theta_1,\ell_1,x_2,\theta_2,\ell_2)\cdot\Big(\nabla_x U + d\log\tilde{f}\Big)(x_1,\theta_1)\rangle\rangle \\
&- \frac{\mu}{4K}\sum_{k'=1}^{K}\bigg(\nabla_{x_1}V(C^k_{i(k'),j(k')})\cdot\sum_{k=1}^{K}\Big(\nabla_{x_1}\Psi(C^k_{i(k),j(k)})\delta_{(i(k),i(k'))} + \nabla_{x_1}\Psi(C^k_{j(k),i(k)})\delta_{(j(k),i(k'))}\Big)\bigg) \\
&- \frac{\mu}{4K}\sum_{k'=1}^{K}\bigg(\nabla_{x_1}V(C^k_{j(k'),i(k')})\cdot\sum_{k=1}^{K}\Big(\nabla_{x_1}\Psi(C^k_{i(k),j(k)})\delta_{(i(k),j(k'))} + \nabla_{x_1}\Psi(C^k_{j(k),i(k)})\delta_{(j(k),j(k'))}\Big)\bigg).
\end{aligned}
\tag{8.4}
$$

Because there is no restriction on the number of links per fiber, the sums over $k$ cannot be simplified in this case. In order to express the third and fourth terms, the number $C_i^{k'}$ (resp. $C_j^{k'}$) of fibers linked to fiber $i(k')$ (resp. $j(k')$) is introduced:

$$\begin{aligned} C_i^{k'} &= \mathrm{Card}(\{k \mid i(k) = i(k') \; or \; j(k) = i(k')\}, \\ C_j^{k'} &= \mathrm{Card}(\{k \mid i(k) = j(k') \; or \; j(k) = j(k')\}, \end{aligned}$$

where Card denote the cardinal of a set. Then, as $K \to \infty$, the following expression holds for any chosen fiber $k'$:

$$\frac{1}{2C_i^{k'}} \sum_{k=1}^{K} \Big( \Psi(C^k_{i(k),j(k)}) \delta_{i(k),i(k')} + \Psi(C^k_{j(k),i(k)}) \delta_{j(k),i(k')} ) \Big) \\ \underset{K\to\infty}{\to} \int (\Psi P)(X_{i(k')}, \theta_{i(k')}, \ell_1, x_2, \theta_2, \ell_2) dx_2 \frac{d\theta_2}{\pi} d\ell_1 d\ell_2,$$

where

$$P(X_{i(k')}, \theta_{i(k')}, \ell, x_2, \theta_2, \ell_2) = \frac{g(X_{i(k')}, \theta_{i(k')}, \ell, x_2, \theta_2, \ell_2)}{\int g(X_{i(k')}, \theta_{i(k')}, \ell_1, x_2, \theta_2, \ell_2) dx_2 \frac{d\theta_2}{\pi} d\ell_1 d\ell_2},$$

is the conditional probability of finding a link conditioned on the fact that one of the fibers of this link has the same location and orientation as $i(k')$. Then, as $N \to \infty, K \to \infty$ such that $\frac{K}{N} \to \xi > 0$ , $C_i^{k'}$ is the mean number of links per fiber. The mean number of links in the volume $dX_{i(k')} d\theta_{i(k')}$ is $K \int g(X_{i(k')}, \theta_{i(k')}, \ell, x_2, \theta_2, \ell_2) dx_2 \frac{d\theta_2}{\pi} d\ell_1 d\ell_2$ and the mean number of fibers in $dX_{i(k')} d\theta_{i(k')}$ is $N f(X_{i(k')}, \theta_{i(k')})$. Thus:

$$C_i^{k'} \underset{\substack{N\to\infty \\ K\to\infty \\ \frac{K}{N}\to\xi>0}}{\to} \xi \frac{\int g(X_{i(k')}, \theta_{i(k')}, \ell_1, x_2, \theta_2, \ell_2) dx_2 \frac{d\theta_2}{\pi} d\ell_1 d\ell_2}{f(X_{i(k')}, \theta_{i(k')})}.$$

So, we get:

$$\sum_{k=1}^{K} \Big( \Psi(C^k_{i(k),j(k)}) \delta_{i(k),i(k')} + \Psi(C^k_{j(k),i(k)}) \delta_{j(k),i(k')} \Big) \underset{\substack{N\to\infty \\ K\to\infty \\ \frac{K}{N}\to\xi>0}}{\to} \\ \frac{2\xi}{f(X_{i(k')}, \theta_{i(k')})} \int (\Psi g)(X_{i(k')}, \theta_{i(k')}, \ell_1, x_2, \theta_2, \ell_2) dx_2 \frac{d\theta_2}{\pi} d\ell_1 d\ell_2.$$

Inserting these expressions in Eq. (8.4), one obtains:

$$E_1 \underset{\substack{N\to\infty \\ K\to\infty \\ \frac{K}{N}\to\xi>0}}{\to} - \mu \langle\langle g, \nabla_{x_1} \Psi(x_1, \theta_1, \ell_1, x_2, \theta_2, \ell_2) \cdot \Big( \nabla_x U + d \log \tilde{f} \Big)(x_1, \theta_1) \rangle\rangle \\ - \mu \frac{\xi}{2K} \sum_{k'=1}^{K} \bigg( \nabla_{x_1} V(C^k_{i(k'),j(k')}) \cdot \psi_1(X_{i(k')}, \theta_{i(k')}) + \nabla_{x_1} V(C^k_{j(k'),i(k')}) \cdot \psi_1(X_{j(k')}, \theta_{j(k')}) \bigg),$$

where,

$$\psi_1(x_1,\theta_1) = \frac{1}{f(x_1,\theta_1)} \int \Big(g\nabla_{x_1}\Psi\Big)(x_1,\theta_1,\ell_1,x_2,\theta_2,\ell_2)dx_2\frac{d\theta_2}{\pi}d\ell_1 d\ell_2. \tag{8.5}$$

Finally, we find:

$$\begin{aligned} E_1 \underset{\substack{N\to\infty \\ K\to\infty \\ \frac{K}{N}\to\xi>0}}{\to} & -\mu\langle\!\langle g, \nabla_{x_1}\Psi(x_1,\theta_1,\ell_1,x_2,\theta_2,\ell_2)\cdot\Big(\nabla_x U + d\log\tilde{f}\Big)(x_1,\theta_1)\rangle\!\rangle \\ & -\xi\mu\langle\!\langle g, \nabla_{x_1}V(x_1,\theta_1,\ell_1,x_2,\theta_2,\ell_2)\cdot\psi_1(x_1,\theta_1)\rangle\!\rangle. \end{aligned}$$

After the same treatment for the four other terms of Eq. (8.3) and in the limit $K, N \to \infty, \frac{K}{N} \to \xi > 0$, one obtains the final equation for $g$ (writting $X$ for $(x_1,\theta_1,\ell_1,x_2,\theta_2,\ell_2)$):

$$\begin{aligned} & \frac{d}{dt}\langle\!\langle g(X), \Psi(X)\rangle\!\rangle \\ & = -\mu\langle\!\langle g(X), \nabla_{x_1}\Psi(X)\cdot\nabla_x U(x_1,\theta_1)\rangle\!\rangle - \mu\langle\!\langle g, \nabla_{x_2}\Psi(X)\cdot\nabla_x U(x_2,\theta_2)\rangle\!\rangle \\ & - \lambda\langle\!\langle g, \partial_{\theta_1}\Psi(X)\partial_\theta U(x_1,\theta_1)\rangle\!\rangle - \lambda\langle\!\langle g, \partial_{\theta_2}\Psi(X)\partial_\theta U(x_2,\theta_2)\rangle\!\rangle \\ & - d\mu\langle\!\langle g, \nabla_{x_1}\Psi(X)\cdot\nabla_x \log f(x_1,\theta_1)\rangle\!\rangle - d\mu\langle\!\langle g, \nabla_{x_2}\Psi(X)\cdot\nabla_x \log f(x_2,\theta_2)\rangle\!\rangle \\ & - d\lambda\langle\!\langle g, \partial_{\theta_1}\Psi(X)\partial_\theta \log f(x_1,\theta_1)\rangle\!\rangle - d\lambda\langle\!\langle g, \partial_{\theta_2}\Psi(X)\partial_\theta \log f(x_2,\theta_2)\rangle\!\rangle \\ & - \mu\xi\langle\!\langle g, \nabla_{x_1}V(X)\cdot\psi_1(x_1,\theta_1)\rangle\!\rangle - \mu\xi\langle\!\langle g, \nabla_{x_1}V(X)\cdot\psi_2(x_1,\theta_1)\rangle\!\rangle \\ & - \lambda\xi\langle\!\langle g, \Big(\partial_{\theta_1}V(X) + \partial_{\theta_1}b(\theta_1,\theta_2)\Big)\chi_1(x_1,\theta_1)\rangle\!\rangle \\ & - \lambda\xi\langle\!\langle g, \Big(\partial_{\theta_1}V(X) + \partial_{\theta_1}b(\theta_1,\theta_2)\Big)\chi_2(x_1,\theta_1)\rangle\!\rangle, \end{aligned} \tag{8.6}$$

where,

$$\psi_2(x_1,\theta_1) = \frac{1}{f(x_1,\theta_1)} \int \Big(g\nabla_{x_2}\Psi\Big)(x_2,\theta_2,\ell_2,x_1,\theta_1,\ell_1)dx_2\frac{d\theta_2}{\pi}d\ell_1 d\ell_2, \tag{8.7}$$

$$\chi_1(x_1,\theta_1) = \frac{1}{f(x_1,\theta_1)} \int \Big(g\partial_{\theta_1}\Psi\Big)(x_1,\theta_1,\ell_1,x_2,\theta_2,\ell_2)dx_2\frac{d\theta_2}{\pi}d\ell_1 d\ell_2, \tag{8.8}$$

$$\chi_2(x_1,\theta_1) = \frac{1}{f(x_1,\theta_1)} \int \Big(g\partial_{\theta_2}\Psi\Big)(x_2,\theta_2,\ell_2,x_1,\theta_1,\ell_1)dx_2\frac{d\theta_2}{\pi}d\ell_1 d\ell_2. \tag{8.9}$$

We introduce the notation $Y_1 = (x_1,\theta_1,\ell_1)$ and $Y_2 = (x_2,\theta_2,\ell_2)$, and prove the following lemma:

**Lemma 8.1.** *For any function* $h(Y_1, Y_2)$*, we have:*

$$\begin{aligned}
\langle\!\langle g, h(Y_1,Y_2)\psi_1(x_1,\theta_1)\rangle\!\rangle &= -\langle\!\langle \nabla_{x_1}\Big(g(X)\frac{F_h(x_1,\theta_1)}{f(x_1,\theta_1)}\Big), \Psi(X)\rangle\!\rangle, \\
\langle\!\langle g, h(Y_1,Y_2)\psi_2(x_1,\theta_1)\rangle\!\rangle &= -\langle\!\langle \nabla_{x_2}\Big(g(X)\frac{F_h(x_2,\theta_2)}{f(x_2,\theta_2)}\Big), \Psi(X)\rangle\!\rangle, \\
\langle\!\langle g, h(Y_1,Y_2)\chi_1(x_1,\theta_1)\rangle\!\rangle &= -\langle\!\langle \partial_{\theta_1}\Big(g(X)\frac{F_h(x_1,\theta_1)}{f(x_1,\theta_1)}\Big), \Psi(X)\rangle\!\rangle, \\
\langle\!\langle g, h(Y_1,Y_2)\chi_2(x_1,\theta_1)\rangle\!\rangle &= -\langle\!\langle \partial_{\theta_2}\Big(g(X)\frac{F_h(x_2,\theta_2)}{f(x_2,\theta_2)}\Big), \Psi(X)\rangle\!\rangle,
\end{aligned} \tag{8.10}$$

*where* $\psi_1$*,* $\psi_2$*,* $\chi_1$ *and* $\chi_2$ *are defined by Eq.* (8.5) *and Eqs.* (8.7)-(8.9)*, and where :*

$$F_h(x_1,\theta_1) = \int (gh)(x_1,\theta_1,\ell_1,x_2,\theta_2,\ell_2)dx_2\frac{d\theta_2}{\pi}d\ell_2 d\ell_1. \tag{8.11}$$

*Proof.* Note that for any function $h(Y_1, Y_2)$, we have:

$$\begin{aligned}
&\langle\!\langle g, h(Y_1,Y_2)\psi_1(x_1,\theta_1)\rangle\!\rangle \\
&= \int \Big(gh\Big)(Y_1,Y_2)\bigg(\frac{1}{f(x_1,\theta_1)}\int (g\nabla_{x_1}\Psi)(x_1,\theta_1,\ell_4,x_3,\theta_3,\ell_3)dx_3\frac{d\theta_3}{\pi}d\ell_4 d\ell_3\bigg)dx_1\frac{d\theta_1}{\pi}d\ell_1 dx_2\frac{d\theta_2}{\pi}d\ell_2 \\
&= \int \bigg(\frac{1}{f(x_1,\theta_1)}\int (gh)(Y_1,Y_2)dx_2\frac{d\theta_2}{\pi}d\ell_2 d\ell_1\bigg)\Big(g\nabla_{x_1}\Psi\Big)(x_1,\theta_1,\ell_4,x_3,\theta_3,\ell_3)dx_1\frac{d\theta_1}{\pi}d\ell_4 dx_3\frac{d\theta_3}{\pi}d\ell_3 \\
&= -\int \nabla_{x_1}\bigg(g(x_1,\theta_1,\ell_4,x_3,\theta_3,\ell_3)\frac{F_h(x_1,\theta_1)}{f(x_1,\theta_1)}\bigg)\Psi(x_1,\theta_1,\ell_4,x_3,\theta_3,\ell_3)dx_1\frac{d\theta_1}{\pi}d\ell_4 dx_3\frac{d\theta_3}{\pi}d\ell_3 \\
&= -\langle\!\langle \nabla_{x_1}\Big(g(X)\frac{F_h(x_1,\theta_1)}{f(x_1,\theta_1)}\Big), \Psi(X)\rangle\!\rangle,
\end{aligned}$$

with $F_h$ defined by (8.11). Similarly, we have:

$$\begin{aligned}
&\langle\!\langle g, h(Y_1,Y_2)\psi_2(x_1,\theta_1)\rangle\!\rangle \\
&= \int \Big(gh\Big)(Y_1,Y_2)\bigg(\frac{1}{f(x_1,\theta_1)}\int (g\nabla_{x_2}\Psi)(x_3,\theta_3,\ell_3,x_1,\theta_1,\ell_4)dx_3\frac{d\theta_3}{\pi}d\ell_4 d\ell_3\bigg)dx_1\frac{d\theta_1}{\pi}d\ell_1 dx_2\frac{d\theta_2}{\pi}d\ell_2 \\
&= \int \bigg(\frac{1}{f(x_1,\theta_1)}\int (gh)(Y_1,Y_2)dx_2\frac{d\theta_2}{\pi}d\ell_2 d\ell_1\bigg)\Big(g\nabla_{x_2}\Psi\Big)(x_3,\theta_3,\ell_3,x_1,\theta_1,\ell_4)dx_1\frac{d\theta_1}{\pi}d\ell_4 dx_3\frac{d\theta_3}{\pi}d\ell_3 \\
&= \int \bigg(\Big(g\nabla_{x_2}\Psi\Big)(Y_1',Y_2')\frac{1}{f(x_2',\theta_2')}\int (gh)(x_2',\theta_2',\ell_4',x_3',\theta_3',\ell_3')dx_3'\frac{d\theta_3'}{\pi}d\ell_3' d\ell_4'\bigg)dx_1'\frac{d\theta_1'}{\pi}d\ell_1' dx_2'\frac{d\theta_2'}{\pi}d\ell_2' \\
&= -\int \nabla_{x_2'}\bigg(g(Y_1',Y_2')\frac{F_h(x_2',\theta_2')}{f(x_2',\theta_2')}\bigg)\Psi(Y_1',Y_2')dx_1'\frac{d\theta_1'}{\pi}d\ell_1' dx_2'\frac{d\theta_2'}{\pi}d\ell_2' \\
&= -\langle\!\langle \nabla_{x_2}\Big(g(X)\frac{F_h(x_2,\theta_2)}{f(x_2,\theta_2)}\Big), \Psi(X)\rangle\!\rangle,
\end{aligned}$$

After the same computations for $\chi_1$ and $\chi_2$, we obtain Eqs. (8.10). ☐

Now, lemma 8.1 allows us to write the formal limit $K, N \to \infty, \frac{K}{N} \to \xi$ of Eq. (8.6) which reads:

$$
\begin{aligned}
\frac{dg}{dt} &- \mu\nabla_{x_1}\cdot\Big(g\nabla_x U(x_1,\theta_1) + \xi\frac{g}{f(x_1,\theta_1)}F_1(x_1,\theta_1)\Big) - \lambda\partial_{\theta_1}(g\partial_\theta U(x_1,\theta_1) + \xi\frac{g}{f(x_1,\theta_1)}F_2(x_1,\theta_1)) \\
&-\mu\nabla_{x_2}\cdot(g\nabla_x U(x_2,\theta_2) + \xi\frac{g}{f(x_2,\theta_2)}F_1(x_2,\theta_2)) - \lambda\partial_{\theta_2}(g\partial_\theta U(x_2,\theta_2) + \xi\frac{g}{f(x_2,\theta_2)}F_2(x_2,\theta_2)) \\
&\quad -d\mu\nabla_{x_1}\cdot(\frac{g}{f(x_1,\theta_1)}\nabla_x f(x_1,\theta_1)) - d\mu\nabla_{x_2}\cdot(\frac{g}{f(x_2,\theta_2)}\nabla_x f(x_2,\theta_2)) \\
&\quad\quad - d\lambda\partial_{\theta_1}(\frac{g}{f(x_1,\theta_1)}\partial_\theta f(x_1,\theta_1)) - d\lambda\partial_{\theta_2}(\frac{g}{f(x_2,\theta_2)}\partial_\theta f(x_2,\theta_2)) = 0,
\end{aligned}
\tag{8.12}
$$

where $F_1$ and $F_2$ read:

$$
\begin{aligned}
F_1(x_1,\theta_1) &= \int \nabla_{x_1}V(x_1,\theta_1,\ell_1,x_2,\theta_2,\ell_2)g(x_1,\theta_1,\ell_1,x_2,\theta_2,\ell_2)dx_2\frac{d\theta_2}{\pi}d\ell_1 d\ell_2, \\
F_2(x_1,\theta_1) &= \int \bigg(g\Big(\partial_{\theta_1}V + \partial_{\theta_1}b\Big)\bigg)(x_1,\theta_1,\ell_1,x_2,\theta_2,\ell_2)dx_2\frac{d\theta_2}{\pi}d\ell_1 d\ell_2.
\end{aligned}
$$

Finally, the link creation/deletion Poisson processes, of frequencies $\nu_f$ and $\nu_d$ respectively, classically lead to a source term $S(g)$ for Eq. (8.12). We recall that a link between two fibers is formed only if the fibers intersect each other, whereas the link deletion process obviously acts on existing links only. This leads to the following source term:

$$
\begin{aligned}
S(g)(x_1,\theta_1,\ell_1,x_2,\theta_2,\ell_2) =& \nu_f f(x_1,\theta_1)f(x_2,\theta_2)\delta(\ell_1,\bar{\ell}(x_1,\theta_1,x_2,\theta_2)\delta(\ell_2,\bar{\ell}(x_2,\theta_2,x_1,\theta_1) \\
&- \nu_d g(x_1,\theta_1,\ell_1,x_2,\theta_2,\ell_2),
\end{aligned}
$$

where the first term corresponds to the link creation process while the second one, to the link deletion process. Here, the quantity $f(x_1,\theta_1)f(x_2,\theta_2)\delta(\ell_1,\bar{\ell}(x_1,\theta_1,x_2,\theta_2)$ $\delta(\ell_2,\bar{\ell}(x_2,\theta_2,x_1,\theta_1)dx_1\frac{d\theta_1}{\pi}dx_2\frac{d\theta_2}{\pi}d\ell_1 d\ell_2$ gives the probability of finding a fiber located within a volume $dx_1\frac{d\theta_1}{\pi}$ about $(x_1,\theta_1)$ and a fiber located within a volume $dx_2\frac{d\theta_2}{\pi}$ about $(x_2,\theta_2)$, such that they intersect with associated lengths within a volume $d\ell_1 d\ell_2$ about $(\ell_1,\ell_2)$. The link creation process generates a new link distribution function proportional to this probability at a rate $\nu_f$. The quantity $-\nu_d g(x_1,\theta_1,\ell_1,x_2,\theta_2,\ell_2)$ corresponds to the decay of the link distribution function with rate $\nu_d$ due to the link deletion process.

# 9 Computation of the non linear term $\int \partial_\theta (G[\rho M]\rho M)\Psi d\theta$

This section is devoted to the computation of the term $X_3$ given by (5.28). For the sake of clarity, the following notations are introduced:

$$M = M_{\theta_0},\ s_0 = \sin 2(\theta - \theta_0),\ c_0 = \cos 2(\theta - \theta_0). \tag{9.13}$$

By symmetry, $\langle h(2(\theta - \theta_0))\rangle = 0$ for all odd functions $h$ on $[-\frac{\pi}{2}, \frac{\pi}{2}]$, where $\langle \cdot \rangle$ is the average defined in Theorem 5.7. We also note from Eq. (4.8), Hypothesis 6.1 and Proposition 5.6 that we have:

$$C_2 = \frac{\alpha L^4 \gamma}{48\eta_f} = \frac{4rdL^2}{\xi 48_r hoc(r)} = \frac{rdL^2}{12\xi\rho c(r)}. \tag{9.14}$$

Using Green's formula, Eqs. (4.7), (5.33) and the same arguments as for $X_2$, we get:

$$\begin{aligned} X_3 &= -\int_{-\frac{\pi}{2}}^{\frac{\pi}{2}} (G[\rho M]\rho M)\partial_\theta \Psi \frac{d\theta}{\pi} \\ &= -C_2 \int_{-\frac{\pi}{2}}^{\frac{\pi}{2}} \left( \int_{-\frac{\pi}{2}}^{\frac{\pi}{2}} \nabla_x^2(\rho M(\theta')) : B(\theta,\theta')\frac{d\theta'}{\pi} \right) \rho M(\theta) \partial_\theta \Psi \frac{d\theta}{\pi} \\ &= -\rho C_2 \int_{-\frac{\pi}{2}}^{\frac{\pi}{2}} \nabla_x^2(\rho M(\theta')) : \left( \int_{-\frac{\pi}{2}}^{\frac{\pi}{2}} B(\theta,\theta') M(\theta)\partial_\theta \Psi \frac{d\theta}{\pi} \right) \frac{d\theta'}{\pi} \\ &= -\frac{\rho C_2}{2r} \int_{-\frac{\pi}{2}}^{\frac{\pi}{2}} \left( \nabla_x^2(\rho M(\theta')) : \int_{-\frac{\pi}{2}}^{\frac{\pi}{2}} B(\theta,\theta')(M(\theta) - \frac{1}{Z^2})\frac{d\theta}{\pi} \right) \frac{d\theta'}{\pi}. \end{aligned}$$

Let us first compute $\nabla_x^2(\rho M)$. We have:

$$\nabla_x^2(\rho M) = M\nabla_x^2 \rho + \nabla_x M \otimes \nabla_x \rho + \nabla_x \rho \otimes \nabla_x M + \rho \nabla_x^2 M,$$

where $\nabla_x M$ is given by (5.30). A direct computation gives:

$$\nabla_x^2 M = 2rM \left[ s_0 \nabla_x^2 \theta_0 + 2\Big(rs_0^2 - c_0\Big) \nabla_x \theta_0 \otimes \nabla_x \theta_0 \right],$$

and thus:

$$\begin{aligned} \nabla_x^2(\rho M) =& M \Big[ \nabla_x^2 \rho + 2\rho r s_0 \nabla_x^2 \theta_0 \\ & + 2rs_0(\nabla_x \theta_0 \otimes \nabla_x \rho + \nabla_x \rho \otimes \nabla_x \theta_0) + 4\rho r(rs_0^2 - c_0)\nabla_x \theta_0 \otimes \nabla_x \theta_0 \Big]. \end{aligned}$$

We now turn towards the computation of

$$\int_{-\frac{\pi}{2}}^{\frac{\pi}{2}} \Big(B(\theta,\theta')M(\theta) - \frac{1}{Z^2}B(\theta,\theta')\Big)\frac{d\theta}{\pi},$$

where $B(\theta,\theta')$ is given by (4.9). For this purpose, we decompose:

$$\omega = (\omega.\omega_0)\omega_0 + (\omega.\omega_0^\perp)\omega_0^\perp = \cos(\theta-\theta_0)\omega_0 + \sin(\theta-\theta_0)\omega_0^\perp,$$

where $\omega_0 = \omega(\theta_0)$ and $\omega_0^\perp$ such that $(\omega_0, \omega_0^\perp)$ is a direct ortho-normal basis of $\mathbb{R}^2$. Using basic trigonometric formulae, one notes that:

$$\begin{aligned}
\omega\otimes\omega &= \frac{1}{2}\Bigg[(1+c_0)(\omega_0\otimes\omega_0) + (1-c_0)\omega_0^\perp\otimes\omega_0^\perp + s_0[\omega_0\otimes\omega_0^\perp + \omega_0^\perp\otimes\omega_0]\Bigg]\\
&= \frac{1}{2}\Bigg[I + c_0[\omega_0\otimes\omega_0 - \omega_0^\perp\otimes\omega_0^\perp] + s_0[\omega_0\otimes\omega_0^\perp + \omega_0^\perp\otimes\omega_0]\Bigg],
\end{aligned}$$

where $I$ is the identity matrix. Denoting $c_0 = c_0(\theta)$, $s_0 = s_0(\theta)$, $c_0' = c_0(\theta')$ and $s_0' = s_0(\theta')$, we get:

$$\begin{aligned}
B(\theta,\theta') &= \sin 2(\theta-\theta')[\omega\otimes\omega + \omega'\otimes\omega']\\
&= \frac{1}{2}[s_0c_0' - s_0'c_0]\Bigg[2I + (c_0+c_0')[\omega_0\otimes\omega_0 - \omega_0^\perp\otimes\omega_0^\perp]\\
&+ (s_0+s_0')[\omega_0\otimes\omega_0^\perp + \omega_0^\perp\otimes\omega_0]\Bigg]\\
&= [s_0c_0' - s_0'c_0]I\\
&+ \frac{1}{2}[c_0s_0c_0' + s_0c_0^2(\theta') - s_0'c_0^2(\theta) - s_0'c_0'c_0][\omega_0\otimes\omega_0 - \omega_0^\perp\otimes\omega_0^\perp]\\
&+ \frac{1}{2}[s_0^2c_0' + s_0s_0'c_0' - s_0'c_0s_0 - s_0'^2c_0][\omega_0\otimes\omega_0^\perp + \omega_0^\perp\otimes\omega_0].
\end{aligned}$$

Note that $B$ is anti-symmetric, i.e. $B(\theta',\theta) = -B(\theta,\theta')$. From the properties of $M$, we get:

$$\int_{-\frac{\pi}{2}}^{\frac{\pi}{2}} B(\theta,\theta')\frac{d\theta}{\pi} = -[\omega_0\otimes\omega_0 - \omega_0^\perp\otimes\omega_0^\perp]\frac{s_0'}{4} + [\omega_0\otimes\omega_0^\perp + \omega_0^\perp\otimes\omega_0]\frac{c_0'}{4},$$

$$\begin{aligned}
\int_{-\frac{\pi}{2}}^{\frac{\pi}{2}} M(\theta)B(\theta,\theta')\frac{d\theta}{\pi} &= -s_0'\langle c_0\rangle I\\
&- \frac{1}{2}[\omega_0\otimes\omega_0 - \omega_0^\perp\otimes\omega_0^\perp](c_0's_0'\langle c_0\rangle + s_0'\langle c_0^2\rangle)\\
&+ \frac{1}{2}[\omega_0\otimes\omega_0^\perp + \omega_0^\perp\otimes\omega_0](c_0'\langle s_0^2\rangle - s_0'^2\langle c_0\rangle).
\end{aligned}$$

Then, we have:

$$\int_{-\frac{\pi}{2}}^{\frac{\pi}{2}} B(\theta,\theta')\Big(M(\theta)-\frac{1}{Z^2}\Big)\frac{d\theta}{\pi} = -s_0'\langle c_0\rangle I + [\omega_0\otimes\omega_0-\omega_0^\perp\otimes\omega_0^\perp]T_1+[\omega_0\otimes\omega_0^\perp+\omega_0^\perp\otimes\omega_0]T_2,$$

with

$$T_1=\frac{s_0'}{4Z^2}-\frac{c_0's_0'\langle c_0\rangle+s_0'\langle c_0^2\rangle}{2},\quad T_2=\frac{c_0'\langle s_0^2\rangle-s_0'^2\langle c_0\rangle}{2}-\frac{c_0'}{4Z^2}.$$

Note that this expression is decomposed into an even function $T_2$ of $\theta'$ and an odd function of $\theta'$ composed of $s_0'\langle c_0\rangle$ and $T_1$. Therefore, $\langle h,T_1\rangle=0$ for all even functions $h$ and $\langle h,T_2\rangle=0$ for all odd functions $h$. Moreover, from integration by parts, the following relations hold:

$$\begin{aligned}\langle s_0^2\rangle &= \frac{\langle c_0\rangle}{r},\\ \langle c_0^2\rangle &= 1-\frac{\langle c_0\rangle}{r},\\ \langle c_0^3\rangle &= \langle c_0\rangle-\frac{1}{r}+2\frac{\langle c_0\rangle}{r^2},\\ \langle c_0^4\rangle &= 1-2\frac{\langle c_0\rangle}{r}+\frac{3}{r^2}-6\frac{\langle c_0\rangle}{r^3},\\ \langle c_0s_0^2\rangle &= \frac{1}{r}(1-2\frac{\langle c_0\rangle}{r}),\\ \langle s_0^4\rangle &= \frac{3}{r^2}(1-2\frac{\langle c_0\rangle}{r}).\end{aligned} \tag{9.15}$$

Then,

$$\begin{aligned}&\int_{-\frac{\pi}{2}}^{\frac{\pi}{2}} \nabla_x^2(\rho M(\theta')) : \Bigg(\int_{-\frac{\pi}{2}}^{\frac{\pi}{2}} (B(\theta,\theta')(M(\theta)-\frac{1}{Z^2}))\frac{d\theta}{\pi}\Bigg)\frac{d\theta'}{\pi}\\ &=\nabla_x^2\rho : [\omega_0\otimes\omega_0^\perp+\omega_0^\perp\otimes\omega_0]\langle T_2\rangle\\ &+4\rho r\nabla_x\theta_0\otimes\nabla_x\theta_0 : [\omega_0\otimes\omega_0^\perp+\omega_0^\perp\otimes\omega_0]\Big(r\langle s_0^2T_2\rangle-\langle c_0T_2\rangle\Big)\\ &+2r(\nabla_x\rho\otimes\nabla_x\theta_0+\nabla_x\theta_0\otimes\nabla_x\rho) : \Big[-\langle c_0\rangle\langle s_0^2\rangle I+[\omega_0\otimes\omega_0-\omega_0^\perp\otimes\omega_0^\perp]\langle s_0T_1\rangle\Big]\\ &+2\rho r\nabla_x(\nabla_x\theta_0) : \Big[-\langle s_0^2\rangle\langle c_0\rangle I+[\omega_0\otimes\omega_0-\omega_0^\perp\otimes\omega_0^\perp]\langle s_0T_1\rangle\Big],\end{aligned} \tag{9.16}$$

where (using Eqs. (9.15) and integration by parts):

$$\begin{aligned}
\langle T_2\rangle &= -\frac{\langle c_0\rangle}{4Z^2},\\
\langle c_0 T_2\rangle &= \frac{\langle c_0\rangle^2}{2r^2} - \frac{1}{4Z^2}(1-\frac{\langle c_0\rangle}{r}),\\
\langle s_0^2 T_2\rangle &= (-\frac{1}{r} + 2\frac{\langle c_0\rangle}{r^2})\frac{1}{4Z^2} + 2\frac{\langle c_0\rangle^2}{r^3} - \frac{\langle c_0\rangle}{r^2},\\
\langle s_0 T_1\rangle &= -\frac{\langle c_0\rangle}{r} + \frac{3\langle c_0\rangle^2}{2r^2} + \frac{\langle c_0\rangle}{4rZ^2},\\
r\langle s_0^2 T_2\rangle - \langle c_0 T_2\rangle &= \frac{\langle c_0\rangle}{r}\Big[\frac{1}{Z^2} - 1 + \frac{3\langle c_0\rangle}{2r}\Big].
\end{aligned}$$

Then, after some computations and using Eq. (9.14), Eq. (9.16) simplifies into:

$$\begin{aligned}
X_3 = &-\frac{dL^2}{24\xi c(r)}\int_{-\frac{\pi}{2}}^{\frac{\pi}{2}} \nabla_x^2(\rho M(\theta')) : \left(\int_{-\frac{\pi}{2}}^{\frac{\pi}{2}} (B(\theta,\theta')(M(\theta) - \frac{1}{Z^2}))\frac{d\theta}{\pi}\right)\frac{d\theta'}{\pi}\\
= &-\frac{dL^2}{24\xi c(r)}\Bigg( - \nabla_x^2\rho : [\omega_0\otimes\omega_0^\perp + \omega_0^\perp\otimes\omega_0]\frac{\langle c_0\rangle}{4Z^2}\\
&+ 4\rho\langle c_0\rangle\nabla_x\theta_0\otimes\nabla_x\theta_0 : [\omega_0\otimes\omega_0^\perp + \omega_0^\perp\otimes\omega_0](\frac{1}{4Z^2} - 1 + \frac{3\langle c_0\rangle}{2r})\\
&+ 2\langle c_0\rangle(\rho\nabla_x\nabla_x\theta_0 + \nabla_x\rho\otimes\nabla_x\theta_0 + \nabla_x\theta_0\otimes\nabla_x\rho) : \Bigg[ - \langle c_0\rangle I\\
&+ [\omega_0\otimes\omega_0 - \omega_0^\perp\otimes\omega_0^\perp](\frac{1}{4Z^2} - 1 + \frac{3\langle c_0\rangle}{2r})\Bigg)\Bigg].
\end{aligned} \tag{9.17}$$

We note that $\langle c_0\rangle = c(r)$. Eq. (9.17) leads to (5.35).

# Chapter 3

# Macroscopic model for linked fibers with alignment interactions: existence theory and numerical simulations

This chapter is about to be submitted.

**Abstract:**

In this paper, we study the macroscopic model of [2] for fibers interacting through linking/unlinking and alignment interactions. As the continuous model has been derived from the particle dynamics, we here aim to (i) gain insight into the properties of the solutions to the macroscopic model and (ii) propose a validation of the macroscopic model via numerical comparison between its solutions and the ones obtained with the particle model. We provide an existence result and perform numerical simulations of the stationary solutions of the macroscopic equation. The numerical simulations of the macroscopic model lead to interesting features such as the emergence of a buckling phenomenon which highlights the physical properties of the macroscopic fiber network. We finally propose a first numerical comparison between the microscopic and macroscopic models. The numerical simulations reveal that the microscopic and macroscopic models are in good agreement, providing we adapt the regime of study.

**keywords:** cross-linked fibers, alignment, individual based model, mean-field limit, macroscopic model, non linear elliptic equation, numerical simulations

**AMS classification:** 35J60, 35Q92, 82C40, 82C22, 82C31, 82C70, 92C10, 92C17

**Acknowledgments:** DP gratefully acknowledges the hospitality of Imperial College London, where part of this research was conducted. DP wishes to gratefully thank Pierre Degond (Imperial College London) for his support and helpful suggestions. DP also thank Fanny Delebecque (IMT, Toulouse), Louis Casteilla (StromaLab, Toulouse) and Anne Lorsignol (StromaLab, Toulouse) for helpful discussions.

## Sommaire

**1 Introduction . . . . . . . . . . . . . . . . . . . . . . . . . . 155**

**2 Microscopic model and mean-field limit . . . . . . . . . 157**

**3 Macroscopic derived model . . . . . . . . . . . . . . . . . 164**

**4 Micro-Macro comparison . . . . . . . . . . . . . . . . . . . 175**

**5 Conclusion . . . . . . . . . . . . . . . . . . . . . . . . . . . 181**

**6 Appendix A . . . . . . . . . . . . . . . . . . . . . . . . . . . 185**

**7 Appendix B . . . . . . . . . . . . . . . . . . . . . . . . . . . 190**

**8 Appendix C . . . . . . . . . . . . . . . . . . . . . . . . . . . 193**

**9 Appendix D . . . . . . . . . . . . . . . . . . . . . . . . . . . 197**

# 1 Introduction

Biological fiber networks such as the Extra-cellular Matrix of adipose tissues are complex cross-linked structures providing internal and external mechanical support to cells, playing major roles in cell and tissue functions [3, 4]. The plasticity of these dynamical networks results from their ability to break and reform cross-links, giving to the tissue the ability to change shape and adapt in response to biological and mechanical stimuli [5, 6]. Because of their vital role in the mechanical behavior of cells and tissues, there is a great deal of interest in understanding such structures. However, they are challenging to model due to the large number of components and the complexity of the interactions within the structure. Several Individual Based Model (IBM) have been proposed to understand the elastic properties of fibrous networks [14, 7, 19, 16], but the computational cost of an IBM tremendously increases with the size of the system. Therefore, IBM for fiber networks remain spatially limited. To model larger systems, some authors treat the network as a continuous medium [21, 20, 22] or couple both particle and continuous visions by homogenization methods to create a less detailed regularly-patterned discrete model [17]. The challenge for these last models is to construct accurate constitutive laws and homogenization techniques to encompass the dynamics of the fiber network, even if it implies a loss of information at the individual level. To overcome this weakness of the macroscopic models, a solution is to derive a macroscopic model from a microscopic one. The macroscopic model will gain in predictability compared to models based on phenomenological considerations [11]. The derivation of macroscopic models from microscopic ones has been intensively studied by many authors, and consists in the large scale limit of a kinetic version of the microscopic model [23]. The kinetic equation of the microscopic model is obtained by considering the limit of a large number of individuals. It describes the evolution of a particle distribution function which is the probability density for a particle to be in a given configuration at a given time. The hydrodynamic limit of this kinetic model is then obtained using conservation properties of the system.

In [2], the authors performed the formal derivation of a kinetic model starting from an individual based model for a dynamical cross-linked network interacting through alignment interactions. The hydrodynamic limit of the kinetic model then leads to a macroscopic model. We here want to provide a first study of the proposed macroscopic model, and compare it to its microscopic version.

The 2D IBM consists of fibers represented as straight lines of fixed length which have the ability to connect and disconnect to their crossing neighbors. Fiber motion is driven by a reaction to an external mechanical potential modeling the action of the cells in the medium (the cells are not modeled as proper agents). Cross-linked fibers are supposed to continuously align together, and we consider small random fiber motion and random fiber reorientation. The maintain of fiber links is modeled through the use of a distance-based potential which cancels when the fiber links are maintained. In [2], it has been shown that such a system leads, at the limit of large number of particles, to a system of two kinetic equations: (i) one for the one-particle distribution function - probability for a fiber to have a given orientation and position-, and (b) one for the two-particle distribution function - probability for two fibers to be in a given configuration in the domain-. The authors show that the system has an intrinsic closure relation and that it can be entirely described by these two distribution functions. Then, in a regime of fast linking/unlinking of fibers, it is shown that the two-particle distribution function reduces to the product of two one-particle distribution functions. This is due to the fact that this scaling hypothesis reduces the action of fiber links and the memory effect of the links is therefore lost. Through the use of the concept of generalized collision invariant introduced in [23], the one-particle distribution function converges towards the equilibria of a collision operator composed of the cross-linked fiber alignment interactions and of the noise intensity. In the hydrodynamic limit, two evolution equations are obtained: (a) for the density function and (b) for the mean local orientation of fibers.

In this paper, we aim to provide a first analysis of the macroscopic model of [2] and to compare the macroscopic model to its microscopic version. In a first part (section 2), we present the microscopic model and show in appendix 6 that the IBM for fiber motion can be seen as a gradient descent for a quadratic penalization of a minimization problem that was proposed in [1]. We then introduce the kinetic equation associated to the IBM and the scaling for the derivation of the macroscopic model. In a second part (section 3), we present the macroscopic model and provide an existence result for the stationary solutions in the case of homogeneous fiber density. Then, we perform numerical simulations for the macroscopic model, and show that interesting physical features appear such as a buckling phenomenon depending upon the model parameters. Finally (section 4), we provide a first numerical comparison between the macroscopic model and the underlying IBM.

# 2 Microscopic model and mean-field limit

## 2.1 Microscopic model

The microscopic 2D model consists of $N$ fibers of uniform and fixed length $L$, described by their center $X_i \in \mathbb{R}^2$ and their orientation angle $\theta_i$. As $\theta_i$ is an angle of line, $\theta_i \in [-\frac{\pi}{2}, \frac{\pi}{2})$. The following biological features are considered: (i) *Fiber growth and elongation:* In order to model fiber growth and elongation, pairs of unlinked intersecting fibers have the possibility to link to each other at random times following a Poisson process. Each link $k$ of the $K$ links at time $t$ is associated to a unique pair of fibers $(i(k), j(k)), i(k) < j(k)$. (ii) *Mechanical external forces:* In order to model the contribution of external elements in the tissue, external mechanical forces are considered. This can model -for instance- the repulsion of fibers by growing confined adipocytes. (iii) *Fiber resistance to bending:* To model fiber resistance to bending, linked fibers are subjected to an alignment potential force at their junction, in order to increase their rigidity. This alignment potential is characterized by a stiffness parameter $\alpha > 0$ playing the role of a flexural modulus. (iv) *Movements of the tissue:* To model tissue movements, we consider random fiber motion and fiber orientation changes of respective amplitude $d_X, d_\theta > 0$.

*Phenomenon (i) : Fiber links.* In order to model long biological fibers as sets of connected segments, intersecting fibers have the ability to link together and linked fibers to unlink at random times, following Poisson processes of frequencies $\nu_f$ and $\nu_d$ respectively. To define the expression of $W_{\text{links}}$, we consider a time at which no linking/unlinking process occurs. Then, the set of links is well-defined and supposed to have $K$ elements. Let $k \in \{1, \dots, K\}$ be a given link and denote by $(i(k), j(k))$ the pair of indices corresponding to the two fibers connected by this link. To make the labeling of the pair unique, we assume without loss of generality that the first element of the linked pair is always the one with lowest index, i.e. $i(k) < j(k)$. The link is supposed to connect two points $X^k_{i(k)}$ and $X^k_{j(k)}$ on fibers $i(k)$ and $j(k)$ respectively. These points are determined by the algebraic distances $\ell^k_{i(k)}$ and $\ell^k_{j(k)}$ to the centers $X_{i(k)}$ and $X_{j(k)}$ of the two fibers respectively; We thus have the relation:

$$X^k_{i(k)} = X_{i(k)} + \ell^k_{i(k)}\omega_{i(k)}, \quad X^k_{j(k)} = X_{j(k)} + \ell^k_{j(k)}\omega_{j(k)},$$

where $\ell^k_{i(k)}$, $\ell^k_{j(k)} \in [-L/2, L/2]$ and where, for any fiber $i$, we let $\omega_i = (\cos\theta_i, \sin\theta_i)$ be the unit vector in the direction of the fiber. All along the link lifetime, the link places a spring-like restoring force that attracts $X_{i(k)}$ back to $X_{j(k)}$ (and vice-versa) as soon as their are displaced one with respect to each other. This restoring force gives rise to a potential energy $V(X_{i(k)}, \theta_{i(k)}, \ell^k_{i(k)}, X_{j(k)}, \theta_{j(k)}, \ell^k_{j(k)})$, with

$$V(X_1, \theta_1, \ell_1, X_2, \theta_2, \ell_2) = \frac{\kappa}{2}|X_1 + \ell_1\omega(\theta_1) - (X_2 + \ell_2\omega(\theta_2))|^2, \tag{2.1}$$

where $\kappa$ is the intensity of the restoring force. Obviously, the larger $\kappa$, the better the maintainance of the link is ensured. The potential $W_{\text{links}}$ is then assumed to be the sum of all the linked fiber spring forces:

$$W_{\text{links}} = \frac{1}{2}\sum_{k=1}^{K} V(X_{i(k)}, \theta_{i(k)}, \ell^k_{i(k)}, X_{j(k)}, \theta_{j(k)}, \ell^k_{j(k)}). \tag{2.2}$$

We stress the fact that the quantities $\ell^k_{i(k)}$ and $\ell^k_{j(k)}$ remain constant throughout the link lifetime. They are determined at the time of the creation of the link.

*Phenomenon (ii): External mechanical forces.* The external potential $W_{ext}$ is supposed to be the sum of potential forces $U(\theta_i)$ acting on each of the $N$ fibers. In this paper, we consider rotation external forces acting on the fiber orientations only and of the form:

$$U(\theta) = c_u \sin^2(\theta - \theta_u), \tag{2.3}$$

where $c_u$ is the intensity of the force and $\theta_u$ a parameter of the model. This potential tends to force the fibers to be oriented with directional angle $\theta_u$. Then, the total external potential is the sum of all the rotation interactions:

$$W_{ext} = \sum_{i=1}^{N} U(\theta_i). \tag{2.4}$$

*Phenomenon (iii): Fiber resistance to bending.* As previously described, linked fibers are submitted to an alignment force at their junction to increase their rigidity. This force tends to align linked fibers $i(k)$ and $j(k)$ and has potential $\mathbf{b}(\theta_{i(k)}, \theta_{j(k)})$ which reads:

$$\mathbf{b}(\theta_1, \theta_2) = \alpha|\sin(\theta_1 - \theta_2)|, \tag{2.5}$$

where $\alpha$ is the flexural modulus. The binary alignment potential depends on the angles $\theta_1$ and $\theta_2$ only, and the total alignment energy $W_{align}$ is supposed to be the sum of all the binary alignment interactions :

$$W_{align} = \frac{1}{2}\sum_{k=1}^{K} \mathbf{b}(\theta_{i(k)}, \theta_{j(k)}). \tag{2.6}$$

*Phenomenon (iv): Tissue movements.* Finally, in order to model random motion of biological elements, fiber positions as well as fiber orientations are submitted random changes supposed to be regular in time. This is modeled by an entropy term $W_{noise}$:

$$W_{noise} = d\sum_{i=1}^{N} \log(\tilde{f})(X_i, \theta_i), \tag{2.7}$$

where $\tilde{f}$ is a 'regularized density' :

$$\tilde{f}(x,\theta) = \frac{1}{N}\sum_{i=1}^{N} \xi^N(x - X_i) \otimes \eta^N(\theta - \theta_i).$$

Here, $\xi^N$ and $\eta^N$ are regularization terms which allow to define the logarithm of $\tilde{f}$. We refer to [2] for the properties of these terms.

The total potential of the system is defined as the sum of all the previously described potentials (Eqs. (2.2),(2.4) (2.6) and (2.7)), and fiber motion follows the steepest descent of the gradient of this potential. Equations for fiber motion and rotation then read:

$$\begin{aligned}
\frac{dX_i}{dt} &= -\mu\nabla_{X_i}\Big(W_{ext} + W_{align} + W_{links} + W_{noise}\Big)\\
\frac{d\theta_i}{dt} &= -\lambda\partial_{\theta_i}\Big(W_{ext} + W_{align} + W_{links} + W_{noise}\Big).
\end{aligned}$$

where $\mu$ and $\lambda$ are mobility coefficients. Using the fact that $W_{align}$ and $W_{ext}$ do not depend on the space variable (see Eqs. (2.6)-(2.4)):

$$\frac{dX_i}{dt} = -\mu\nabla_{X_i}\Big(W_{links} + W_{noise}\Big) \tag{2.8}$$

$$\frac{d\theta_i}{dt} = -\lambda\partial_{\theta_i}\Big(W_{ext} + W_{align} + W_{links} + W_{noise}\Big). \tag{2.9}$$

**Remark** *The IBM defined by Eqs.* (2.8)-(2.9) *corresponds to a gradient descent for a quadratic penalization of a minimization problem related to the model of [1]. These results are shown in Appendix 6, where a numerical comparison between both models is performed.*

We now introduce the mean field kinetic equation which describes the time evolution of the particle system in the limit of a large number of fibers. This is generally performed using the one-particle distribution $f(x, \theta, t)$ which depends on the position $x \in \mathbb{R}^2$, orientation angle $\theta \in [-\frac{\pi}{2}, \frac{\pi}{2})$ and the time $t$. As shown in [2], the presence of fiber links oblige to keep track also of the fiber links distribution function $g(x_1, \theta_1, \ell_1, x_2, \theta_2, \ell_2, t)$ which can be seen as a two-particle distribution function. In [2], we show that the formal limit of Eqs. (2.8), (2.9) for $K, N \to \infty$, $\frac{K}{N} \to \xi$, where $\xi > 0$ is a fixed parameter reads:

$$\frac{df}{dt} - \mu\Big(\xi\nabla_x \cdot F_1 + d\Delta_x f\Big) - \lambda\Big(\partial_\theta((\partial_\theta U)f) + \xi\partial_\theta F_2 + d\partial_\theta^2 f\Big) = 0, \tag{2.10}$$

where

$$\begin{aligned} F_1(x_1, \theta_1) &= \int (g\nabla_{x_1} V)(x_1, \theta_1, \ell_1, x_2, \theta_2, \ell_2) d\ell_1 d\ell_2 \frac{d\theta_2}{\pi} dx_2, \\ F_2(x_1, \theta_1) &= \int \Big(g(\partial_{\theta_1} V + \partial_{\theta_1} b)\Big)(x_1, \theta_1, \ell_1, x_2, \theta_2, \ell_2) d\ell_1 d\ell_2 \frac{d\theta_2}{\pi} dx_2. \end{aligned} \tag{2.11}$$

The two-particle distribution function is described by:

$$\begin{aligned} \frac{dg}{dt} - \mu\Bigg[&\nabla_{x_1}\cdot\Bigg(g\nabla_x U(x_1, \theta_1) + \xi\frac{g}{f(x_1, \theta_1)} F_1(x_1, \theta_1) + d\frac{g}{f(x_1, \theta_1)}\nabla_x f(x_1, \theta_1)\Bigg) \\ &+ \nabla_{x_2}\cdot\Bigg(g\nabla_x U(x_2, \theta_2) + \xi\frac{g}{f(x_2, \theta_2)} F_1(x_2, \theta_2) + d\frac{g}{f(x_2, \theta_2)}\nabla_x f(x_2, \theta_2))\Bigg)\Bigg] \\ -\lambda\Bigg[&\partial_{\theta_1}\Bigg(g\partial_\theta U(x_1, \theta_1) + \xi\frac{g}{f(x_1, \theta_1)} F_2(x_1, \theta_1) + d\frac{g}{f(x_1, \theta_1)}\partial_\theta f(x_1, \theta_1)\Bigg) \\ &+ \partial_{\theta_2}\Bigg(g\partial_\theta U(x_2, \theta_2) + \xi\frac{g}{f(x_2, \theta_2)} F_2(x_2, \theta_2) + d\frac{g}{f(x_2, \theta_2)}\partial_\theta f(x_2, \theta_2)\Bigg)\Bigg] = S(g), \end{aligned} \tag{2.12}$$

where $S(g)$ is the term for creation/deletion of fiber links:

$$S(g) = \nu_f f(x_1, \theta_1) f(x_2, \theta_2) \delta_{\bar{\ell}(x_1, \theta_1, x_2, \theta_2)}(\ell_1) \delta_{\bar{\ell}(x_2, \theta_2, x_1, \theta_1)}(\ell_2) - \nu_d g, \tag{2.13}$$

where $\delta_{\bar{\ell}}(\ell_1)$ denotes the Dirac delta at $\bar{\ell}$, i.e. the distribution acting on test functions $\phi(\ell_1)$ such that $\langle \delta_{\bar{\ell}}(\ell_1), \phi(\ell_1) \rangle = \phi(\bar{\ell})$.

## 2.2 Scaling and kinetic equation

In order to highlight the role of the different variables, we write the system in dimensionless variables. We choose $t_0$ and $x_0$ as units of time and space respectively, and $f_0 = \frac{1}{x_0^2}$, $g_0 = \frac{1}{x_0^6}$ and $U_0 = \frac{x_0^2}{t_0^2}$ for units of distribution functions and energy. The scaling of $f(x, \theta)$ and $g(x_1, \theta_1, \ell_1, x_2, \theta_2, \ell_2)$ comes from the fact that they are probability distribution functions on a 2D domain. The following dimensionless variables are defined:

$$\bar{x} = \frac{x}{x_0},\ \bar{\ell} = \frac{\ell}{x_0},\ \bar{f} = \frac{f}{f_0} = f x_0^2,\ \bar{g} = \frac{g}{g_0} = g x_0^6,\ \bar{U} = \frac{t_0^2 U}{x_0^2}, \tag{2.14}$$

and the following dimensionless parameters are introduced:

$$\mu' = \frac{\mu}{t_0},\ \lambda' = \frac{\lambda x_0^2}{t_0},\ \nu_f' = t_0 \nu_f,\ \nu_d' = t_0 \nu_d, L' = \frac{L}{x_0},\ d' = \frac{d t_0^2}{x_0^2}, \alpha' = \frac{\alpha t_0^2}{x_0^2},\ \kappa' = \kappa t_0^2.$$

Then, as shown in [2], Eq. (2.10) is written in this new set of variables as:

$$\partial_{t'} \bar{f} - \lambda' \partial_\theta (\partial_\theta \bar{U} \bar{f}) - \lambda' \xi \partial_\theta \bar{F}_2 - \mu' \xi \nabla_{\bar{x}} \cdot \bar{F}_1 - d' \lambda' \partial_\theta^2 \bar{f} - d' \mu' \Delta_x \bar{f} = 0,$$

where

$$\bar{F}_1(\bar{x}_1, \theta_1) = \int_{\mathbb{R}^2} \int_{-\frac{\pi}{2}}^{\frac{\pi}{2}} \int_{-L'/2}^{L'/2} \int_{-L'/2}^{L'/2} \nabla_{\bar{x}_1} \bar{V}(\bar{x}_1, \theta_1, \bar{\ell}_1, \bar{x}_2, \theta_2, \bar{\ell}_2) \bar{g}(\bar{x}_1, \theta_1, \bar{\ell}_1, \bar{x}_2, \theta_2, \bar{\ell}_2) d\bar{\ell}_1 d\bar{\ell}_2 \frac{d\theta_2}{\pi} d\bar{x}_2,$$

$$\bar{V}(\bar{x}_1, \theta_1, \bar{\ell}_1, \bar{x}_2, \theta_2, \bar{\ell}_2) = \frac{\kappa'}{2} (\bar{x}_1 + \bar{\ell}_1 \omega(\theta_1) - \bar{x}_2 - \bar{\ell}_2 \omega(\theta_2))^2.$$

and

$$\begin{aligned}
\bar{F}_2(\bar{x}_1, \theta_1) &= \bar{F}_{al}(\bar{x}_1, \theta_1) + \bar{F}_{link}(\bar{x}_1, \theta_1), \\
\bar{F}_{link}(\bar{x}_1, \theta_1) &= \int_{\mathbb{R}^2} \int_{-\frac{\pi}{2}}^{\frac{\pi}{2}} \int_{-L'/2}^{L'/2} \int_{-L'/2}^{L'/2} \Big( \bar{g} \partial_{\theta_1} V \Big)(\bar{x}_1, \theta_1, \bar{\ell}_1, \bar{x}_2, \theta_2, \bar{\ell}_2) d\bar{\ell}_1 d\bar{\ell}_2 \frac{d\theta_2}{\pi} d\bar{x}_2, \\
\bar{F}_{al}(\bar{x}_1, \theta_1) &= \int_{\mathbb{R}^2} \int_{-\frac{\pi}{2}}^{\frac{\pi}{2}} \int_{-L'/2}^{L'/2} \int_{-L'/2}^{L'/2} \Big( \bar{g} \partial_{\theta_1} \bar{\mathbf{b}} \Big)(\bar{x}_1, \theta_1, \bar{\ell}_1, \bar{x}_2, \theta_2, \bar{\ell}_2) d\bar{\ell}_1 d\bar{\ell}_2 \frac{d\theta_2}{\pi} d\bar{x}_2,
\end{aligned}$$

and where $\bar{\mathbf{b}}(\theta_1, \theta_2) = \alpha' |\sin(\theta_1 - \theta_2)|$. In [2], we set the time and space scale such that $\lambda' = \mu' = 1$. In order to keep a degree of freedom, we here chose $t_0$ and $x_0$ such that $\lambda' = 1$ and let $\mu'$ as a free parameter. To this aim, we consider only the case where $\lambda = \frac{t_0}{x_0^2}$. Therefore, the scaled version of the kinetic model reads (dropping the tildes and primes for the sake of clarity):

$$\partial_t f - \partial_\theta(\partial_\theta U f) - \xi \partial_\theta F_2 - \mu\xi \nabla_x \cdot F_1 - d\partial_\theta^2 f - d\mu\Delta_x f = 0. \tag{2.15}$$

We now define the regime of interest. We use the same scaling as for [2]:a small parameter $\varepsilon \ll 1$ is introduced and the space and time units are set to $\tilde{x_0} = \varepsilon^{-1/2} x_0$, $\tilde{t_0} = \varepsilon^{-1} t_0$. The fiber length measured at scale $x_0$ is supposed to stay of order 1 as $\varepsilon \to 0$, i.e. $L = O(1)$. The variables $x$, $t$, $\ell$ and unknowns $f$ and $g$ are then correspondingly changed to $\tilde{x} = \sqrt{\varepsilon} x$, $\tilde{t} = \varepsilon t$, $\tilde{\ell} = \sqrt{\varepsilon}\ell$, $\tilde{f}(\bar{x}, \theta) = \varepsilon^{-1} f(x, \theta)$ and $\tilde{g}(\tilde{x}_1, \theta_1, \tilde{\ell}_1, \tilde{x}_2, \theta_2, \tilde{\ell}_2) = \varepsilon^{-3} g(x_1, \theta_1, \ell_1, x_2, \theta_2, \ell_2)$. The external potential is supposed to be of order $\varepsilon$: $U^1 = O(\varepsilon)$, i.e. $\tilde{U}^1 = \varepsilon^{-1} U^1$ with $\tilde{U}^1 = O(1)$. The strength of the alignment potential is supposed to be large $\alpha = O(\varepsilon^{-1})$, i.e. $\tilde{\alpha} = \varepsilon\alpha$ with $\tilde{\alpha} = O(1)$. The intensity of the alignment potential between linked fibers is supposed to be small $\kappa = O(\varepsilon)$, i.e. $\tilde{\kappa} = \varepsilon^{-1}\kappa$ with $\tilde{\kappa} = O(1)$ and the diffusion coefficient and parameter $\xi$ are supposed to stay of order 1: $d, \xi = O(1)$. In order to simplify the analysis of the system, the process of linking/unlinking is supposed to occur at a very fast time scale, i.e. $\tilde{\nu}_f = \varepsilon^2 \nu_f$ and $\tilde{\nu}_d = \varepsilon^2 \nu_d$, with $\tilde{\nu}_f$, $\tilde{\nu}_d = O(1)$. In this paper, we chose to consider that $\mu$ is of order 1:$\mu = O(1)$. As shown in [2], the macroscopic version of Eqs. (2.15) reads:

$$-\xi\partial_{\theta_1}\tilde{F}_{al} - \varepsilon\left(\xi\partial_\theta \tilde{F}_{link} + d\partial_\theta^2 \tilde{f}\right) + \varepsilon^2\left(\partial_t \tilde{f} - \partial_\theta(\partial_\theta \tilde{U}\tilde{f}) - \xi\mu\nabla_{\tilde{x}} \cdot \tilde{F}_1 - d\mu\Delta_{\tilde{x}}\tilde{f}\right) = 0. \tag{2.16}$$

where:

$$\begin{aligned}
\tilde{F}_1 &= \int_{L^\varepsilon} \nabla_{\tilde{x}_1} \tilde{V}(\tilde{x}_1, \theta_1, \tilde{\ell}_1, \tilde{x}_2, \theta_2, \tilde{\ell}_2)\varepsilon^3 \tilde{g}(\tilde{x}_1, \theta_1, \tilde{\ell}_1, \tilde{x}_2, \theta_2, \tilde{\ell}_2) d\tilde{x}_2 \frac{d\theta_2}{\pi} d\tilde{\ell}_1 d\tilde{\ell}_2 \\
&= \frac{1}{\varepsilon^2} F_1 = O(\varepsilon^3), \\
\tilde{F}_{link} &= \int_{L^\varepsilon} \partial_{\theta_1} \tilde{V}(\tilde{x}_1, \theta_1, \tilde{\ell}_1, \tilde{x}_2, \theta_2, \tilde{\ell}_2)\varepsilon^3 \tilde{g}(\tilde{x}_1, \theta_1, \tilde{\ell}_1, \tilde{x}_2, \theta_2, \tilde{\ell}_2) d\tilde{x}_2 \frac{d\theta_2}{\pi} d\tilde{\ell}_1 d\tilde{\ell}_2 \\
&= \frac{1}{\varepsilon^2} \varepsilon F_{link}(x_1, \theta_1) = O(\varepsilon^3) \\
\tilde{F}_{al} &= \int_{L^\varepsilon} \partial_{\theta_1} \tilde{b}(\theta_1, \theta_2)\varepsilon^3 \tilde{g}(\tilde{x}_1, \theta_1, \tilde{\ell}_1, \tilde{x}_2, \theta_2, \tilde{\ell}_2) d\tilde{x}_2 \frac{d\theta_2}{\pi} d\tilde{\ell}_1 d\tilde{\ell}_2 = F_{al}(x_1, \theta_1) \\
&= \varepsilon\partial_{\theta_1}\Phi[f^\varepsilon](x_1, \theta_1) + \varepsilon^2 G[f^\varepsilon](x_1, \theta_1) + O(\varepsilon^3),
\end{aligned}$$

and where $L^\varepsilon = \mathbb{R}^2 \times [-\frac{\pi}{2}, \frac{\pi}{2}] \times [-\frac{\sqrt{\varepsilon}L}{2}, \frac{\sqrt{\varepsilon}L}{2}]^2$. Finally,

$$\tilde{g} = \frac{\tilde{\nu_f}}{\tilde{\nu_d}} \tilde{f}(\tilde{x}_1, \theta_1)\tilde{f}(\tilde{x}_2, \theta_2)\delta_{\bar{\ell}(\tilde{x}_1, \theta_1, \tilde{x}_2, \theta_2)}(\tilde{\ell}_1)\delta_{\bar{\ell}(\tilde{x}_2, \theta_2, \tilde{x}_1, \theta_1)}(\tilde{\ell}_2) + O(\varepsilon^2), \tag{2.17}$$

We now aim to apply this scaling to the microscopic model (2.8)-(2.9).

## 2.3 Scaled microscopic model

Using the scaling of previous section, we have:

$$\tilde{X}_i = \sqrt{\varepsilon} X_i, \quad \frac{d\tilde{X}_i}{d\tilde{t}} = \frac{1}{\sqrt{\varepsilon}} \frac{dX_i}{dt}.$$

From Eq. (2.1), (2.5) and (2.3), the scaled expressions of the potentials read:

$$\begin{aligned} \tilde{V}(\tilde{x}_1, \theta_1, \tilde{\ell}_1, \tilde{x}_2, \theta_2, \tilde{\ell}_2) &= \frac{\tilde{\kappa}}{2} |\tilde{x}_1 + \tilde{\ell}_1 \omega(\theta_1) - \tilde{x}_2 - \tilde{\ell}_2 \omega(\theta_2)|^2 = V(x_1, \theta_1, \ell_1, x_2, \theta_2, \ell_2), \\ \tilde{\mathbf{b}}(\theta_1, \theta_2) &= \tilde{\alpha} |\sin(\theta_1 - \theta_2)| = \varepsilon \mathbf{b}(\theta_1, \theta_2). \end{aligned}$$

Using these expressions together with Eqs. (2.2), (2.4), (2.7) and (2.6) we have

$$\tilde{W}_{links} = W_{links}, \tilde{W}_{ext} = \frac{W_{ext}}{\varepsilon}, \tilde{W}_{noise} = W_{noise}, \tilde{W}_{align} = \varepsilon W_{align}. \tag{2.18}$$

Introducing these expressions in (2.8)-(2.9), the scaled version of the microscopic model reads (dropping the tildes):

$$\frac{dX_i}{dt} = -\mu \nabla_{X_i} \Big( W_{links} + W_{noise} \Big) \tag{2.19}$$

$$\frac{d\theta_i}{dt} = -\frac{1}{\varepsilon^2} \partial_{\theta_i} \Big( \varepsilon^2 W_{ext} + W_{align} + \varepsilon W_{links} + \varepsilon W_{noise} \Big). \tag{2.20}$$

Note that system (2.19)-(2.20) can be recovered from Eq. (2.16). Indeed, letting $f$ and $g$ be the one and two-particle distribution functions:

$$\begin{aligned} f(x, \theta, t) =& \frac{1}{N} \sum_{i=1}^{N} \delta_{(X_i(t), \theta_i(t))}(x, \theta), \\ g(x_1, \theta_1, \ell_1, x_2, \theta_2, \ell_2, t) =& \frac{1}{2K} \sum_{k=1}^{K} \delta_{(X_{i(k)}, \theta_{i(k)}, \ell^k_{i(k)}, X_{j(k)}, \theta_{j(k)}, \ell^k_{j(k)})}(x_1, \theta_1, \ell_1, x_2, \theta_2, \ell_2) \\ &+ \delta_{(X_{j(k)}, \theta_{j(k)}, \ell^k_{j(k)}, X_{i(k)}, \theta_{i(k)}, \ell^k_{i(k)})}(x_1, \theta_1, \ell_1, x_2, \theta_2, \ell_2), \end{aligned}$$

where $\delta_{(X_i(t), \theta_i(t))}(x, \theta)$ denotes the Dirac delta located at $(X_i(t), \theta_i(t)$, we cant write for instance:

$$\begin{aligned} F_1(x_1, \theta_1) &= \int (g \nabla_{x_1} V)(x_1, \theta_1, \ell_1, x_2, \theta_2, \ell_2) d\ell_1 d\ell_2 \frac{d\theta_2}{\pi} dx_2 \\ &= \frac{1}{2K} \sum_{k=1}^{K} \nabla_{x_1} V(X_{i(k)}, \theta_{i(k)}, \ell^k_{i(k)}, X_{j(k)}, \theta_{j(k)}, \ell^k_{j(k)}) = \nabla_{X_i} W_{links}. \end{aligned}$$

With the same treatment for the other terms, we obtain that $F_{al}$ is the continuous counterpart of $W_{align}$, $F_{link}$ the continuous counterpart of $W_{links}$ for fiber rotation, $d\partial_\theta f$ and $d\mu\nabla_x f$ the continuous counterparts of $W_{noise}$ for fiber rotation and motion respectively, and $\partial_\theta U f$ the counterpart of the external potential $W_{ext}$. System (2.19)-(2.20) shows, in accordance with Eq. (2.16), that the restoring potential $W_{links}$ and the noise $W_{noise}$ act at the same order for fiber motion, and that fiber rotation is mainly driven by the alignment potential between linked fibers $W_{align}$ which acts at leading order in $O(\frac{1}{\varepsilon^2})$. For fiber rotation, the restoring potential and the noise act at the same order $O(\frac{1}{\varepsilon})$ and the external potential $W_{ext}$ is of order $O(1)$. Therefore, the two scaled models are in good agreement. We recall however that the rigorous convergence of the particle system to the kinetic equation (2.16) is still an open problem.

# 3 Macroscopic derived model

In the regime previously defined, as shown in [2] and restoring the parameter $\mu$, we obtain that $f^\varepsilon$ and $g^\varepsilon$ formally satisfy:

$$\begin{aligned} &-\xi\partial_\theta\left(\partial_\theta\Phi[f^\varepsilon](x,\theta)f^\varepsilon\right) - d\partial_\theta^2 f^\varepsilon \\ &\qquad + \varepsilon\left[\partial_t f^\varepsilon - \partial_\theta\left(\left[\partial_\theta U^1 + \xi G[f^\varepsilon](x,\theta)\right]f^\varepsilon\right) - d\mu\Delta_x f^\varepsilon\right] = O(\varepsilon^2), \end{aligned} \tag{3.21}$$

with

$$\Phi[f^\varepsilon](x_1,\theta_1) = C_1\int_{-\frac{\pi}{2}}^{\frac{\pi}{2}} \sin^2(\theta-\theta_2) f^\varepsilon(x_1,\theta_2)\frac{d\theta_2}{\pi} \tag{3.22}$$

$$G[f^\varepsilon](x_1,\theta_1) = C_2\sum_{i,j=1}^{2}\frac{\partial^2}{\partial x_i\partial x_j}\int_{-\frac{\pi}{2}}^{\frac{\pi}{2}} f^\varepsilon(x_1,\theta_2)B_{ij}(\theta_1,\theta_2)\frac{d\theta_2}{\pi}, \tag{3.23}$$

$$C_1 = \frac{\alpha L^2\nu_f}{2\nu_d}\ ,\ C_2 = \frac{\alpha L^4\nu_f}{48\nu_d}, \tag{3.24}$$

and

$$B(\theta_1,\theta_2) = \sin 2(\theta_1-\theta_2)[\omega(\theta_1)\otimes\omega(\theta_1)+\omega(\theta_2)\otimes\omega(\theta_2)] = \Big(B_{ij}(\theta_1,\theta_2)\Big)_{i,j=1,2}. \tag{3.25}$$

Finally, neglecting the terms in $O(\varepsilon^2)$ and defining the collision operator $Q(f^\varepsilon)$ such that:

$$Q(f) = d\partial_\theta^2 f + \xi\partial_\theta(\partial_\theta\Phi[f])f), \tag{3.26}$$

we obtain:

$$\varepsilon\left[\partial_t f^\varepsilon - \partial_\theta\left(\left[\partial_\theta U^1 + \xi G[f^\varepsilon](x,\theta)\right]f^\varepsilon\right) - d\mu\Delta_x f^\varepsilon\right] = Q(f^\varepsilon). \tag{3.27}$$

Like many macroscopic models, the derivation of the macroscopic equations is based on the convergence of the particle distribution function to local equilibrium at large scales in space and time. In [2], it is shown that the microscopic fiber distribution function $f^\varepsilon$ converges as $\varepsilon \to 0$ to a Von Mises distribution $f(x,\theta,t)$:

$$\begin{aligned} f(x,\theta,t) &= \rho(x,t) M_{\theta_0(x,t)}(\theta) \\ M_{\theta_0(x,t)}(\theta) &= \frac{e^{r\cos 2(\theta-\theta_0(x,t))}}{\int_{-\frac{\pi}{2}}^{\frac{\pi}{2}} e^{r\cos 2\theta}\frac{d\theta}{\pi}}, \end{aligned} \tag{3.28}$$

where $r$ is the order parameter given by:

$$r = \frac{\xi \alpha L^2 \rho(x,t) c(r) \nu_f}{4d\nu_d},$$

and $c(r)$ does not depend on $\theta_0$ and reads:

$$c(r) = \int_{-\frac{\pi}{2}}^{\frac{\pi}{2}} \cos 2(\theta) M_0(\theta) \frac{d\theta}{\pi}. \tag{3.29}$$

In the case of a homogeneous fiber distribution $\rho(x,t) = \rho_0$, the local fiber orientation $\theta_0(x,t)$ solves:

$$\partial_t \theta_0 - \sum_{i,j=1}^{2} \partial_{x_i}\Big(a_{ij}(\theta_0)\partial_{x_j}\theta_0\Big) + \alpha_5 h(\theta_0) = 0, \tag{3.30}$$

where $a_{ij} \in \mathbb{R}$ for $i,j = 1,2$ are the coefficients of a $2\times 2$ matrix $A$ such that:

$$A(\theta) = \begin{pmatrix} \alpha_2 - \alpha_3\cos 2\theta & -\alpha_3 \sin 2\theta \\ -\alpha_3\sin 2\theta & \alpha_2 + \alpha_3\cos 2\theta \end{pmatrix}.$$

Finally, the function $h$ is the macroscopic counterpart of the external potential $U$ and reads:

$$h(\theta_0) = \int_{-\frac{\pi}{2}}^{\frac{\pi}{2}} U'(\theta) M_{\theta_0}(\theta) \frac{d\theta}{\pi}. \tag{3.31}$$

The coefficients $\alpha_1, \alpha_2, \alpha_3$ and $\alpha_5$ are fully determined by parameters $r$, $d$ and $L$ and their expression can be found in appendix 8. Note that from (2.3), we have:

$$U'(\theta) = c_u \sin 2(\theta - \theta_u),$$

and thus:

$$\int_{-\frac{\pi}{2}}^{\frac{\pi}{2}} U'(\theta) M_{\theta_0}(\theta)\frac{d\theta}{\pi} = c_u \sin 2(\theta_0 - \theta_u) c(r), \tag{3.32}$$

## 3.1 Theoretical analysis of the macroscopic model

In this section, we are interested in the existence of stationary solutions to Eq. (3.30), i.e we study the following quasi linear partial differential equation:

$$\sum_{i,j=1}^{2}\Big(a_{ij}(\theta)\partial_{ij}\theta\Big)+\sum_{i,j=1}^{2}\Big(b_{ij}(\theta)\partial_i\theta\partial_j\theta\Big)-h(\theta)=0. \tag{3.33}$$

Here, $b_{ij}\in\mathbb{R}$ for $i,j=1,2$ are the coefficients of the following $2\times 2$ matrix $B$:

$$B(\theta)=2\alpha_3\begin{pmatrix}\sin 2\theta & -\cos 2\theta\\ -\cos 2\theta & -\sin 2\theta\end{pmatrix}.$$

Note that $b_{ij}(\xi)=a'_{ij}(\xi)$ for all $i,j=1,2$. Let us denote by $F:C^\infty(\Omega)\to C^\infty(\Omega)$ the non linear differential operator defined by the left hand side of Eq. (3.33):

$$F(\theta)=\sum_{i,j=1}^{2}\Big(a_{ij}(\theta)\partial_{ij}\theta\Big)+\sum_{i,j=1}^{2}\Big(b_{ij}(\theta)\partial_i\theta\partial_j\theta\Big)-h(\theta). \tag{3.34}$$

We consider Dirichlet boundary conditions $\theta=\phi$ on $\partial\Omega$ and we aim to prove the following theorem:

**Theorem 3.1.** *Let $\Omega$ be a bounded domain in $\mathbb{R}^n$ with boundary $\partial\Omega\in C^{2,\gamma}(\bar\Omega)$. Suppose that there exists $M>0$ such that:*

$$\begin{aligned} h(z)&\ge 0 \qquad z\ge M\\ h(z)&\le 0 \qquad z\le -M.\end{aligned} \tag{3.35}$$

*Then, if $\phi\in C^{2,\gamma}(\bar\Omega)$, there exists a solution $\theta\in C^{2,\gamma}(\bar\Omega)$ of the Dirichlet problem $F(\theta)=0$ in $\Omega$, $\theta=\phi$ on $\partial\Omega$ where $F(\theta)$ is defined by* (3.34).

*Proof.* We first give some definitions and arguments to show that Eq. (3.33) for $F$ given by (3.34) is a quasi linear elliptic equation. Let $DF(\theta_0)$ be the linearization of $F$ at $\theta_0$:

$$DF(\theta_0)v=\frac{\partial}{\partial s}F(\theta_0+sv)|_{s=0}=\sum_{i,j=1}^{2}\Big(a_{ij}(\theta_0)\partial_{ij}v\Big)+Lv,$$

where $L$ is a linear differential operator of order 1 which coefficients depend on $D^1\theta_0$:

$$\begin{aligned} Lv=&\sum_{i,j=1}^{2}\Big(a'_{ij}(\theta_0)(\partial_i\theta_0\partial_j v+\partial_i v\partial_j\theta_0)\Big)\\ &+\sum_{i,j=1}^{2}\Big(a''_{ij}(\theta_0)\partial_i\theta_0\partial_j\theta_0+a'_{ij}(\theta_1)\partial_{x_ix_j}\theta_0-h'(\theta_0)\Big)v,\end{aligned} \tag{3.36}$$

Thus, the linearization at $\theta_0$ is elliptic provided the matrix $A(\theta_0)$ is definite positive. As shown in [2], this condition is ensured for all model parameters, independently of $\theta_0$.

To obtain existence of solutions to equation (3.33), we consider the following operator $Q : C^2(\Omega) \to C(\Omega)$:

$$Qu = \sum_{i,j=1}^{2} a_{ij}(x,u)\partial_{ij}u + \mathbf{g}(x,u,Du), \tag{3.37}$$

Note that $F$ coincides with $Q$ if:

$$\mathbf{g}(x,u,Du) = \sum_{i,j=1}^{2} \left( b_{ij}(u)\partial_i u \partial_j u \right) - h(u). \tag{3.38}$$

We first obtain existence provided the solutions of a related family of problems are uniformly bounded in $\Omega$, thanks to the following fundamental existence theorem:

**Theorem 3.2.** *([25], chap 12) Let $\Omega$ be a bounded domain in $\mathbb{R}^n$ and suppose that the operator $Q$ is elliptic in $\bar{\Omega}$ with coefficients*

$$a_{ij} \in C^1(\bar{\Omega} \times \mathbb{R}), \quad \mathbf{g} \in C^\gamma(\bar{\Omega} \times \mathbb{R} \times \mathbb{R}^n), \quad 0 < \gamma < 1,$$

*Let $\partial\Omega \in C^{2,\gamma}$ and $\phi \in C^{2,\gamma}(\bar{\Omega})$. Then, if there exists a constant $M$, independent of $u$ and $\tau$, such that every $C^{2,\gamma}(\bar{\Omega})$ solution of the Dirichlet problems*

$$\begin{aligned} Q_\tau u &= a_{ij}(x,u,Du)D_{ij}u + \tau \mathbf{g}(x,u,Du) \;\; in \Omega \\ u &= \tau\phi \;\; on \partial\Omega, \;\; 0 \le \tau \le 1 \end{aligned} \tag{3.39}$$

*satisfies*

$$||u||_{C^1(\bar{\Omega})} = \sup_\Omega |u| + \sup_\Omega |Du| < M,$$

*it follows that the Dirichlet problem $Qu = 0$ in $\Omega$, $u = \phi$ on $\partial\Omega$ is solvable in $C^{2,\gamma}(\bar{\Omega})$.*

The existence of solutions for the Dirichlet problem with such an elliptic operator thus depends upon the existence of a uniform bound for solutions of related problems. As shown in [25], a priori estimates for the gradient of $C^2(\Omega)$ solutions can be obtained in terms of the gradients on the boundary $\delta\Omega$ and the magnitudes of solutions, and there exist a variety of hypothesis that guarantee a boundary gradient estimate for solutions to such problems. Altogether, solutions to the Dirichlet problem $Qu = 0$ in $\Omega$, $u = \phi$ on $\partial\Omega$ can be obtained using the following hypothesis:

**Hypothesis 3.1.** *Suppose that there exist positive constants* $\mu_1$ *and* $\mu_2$ *such that*

$$\frac{\mathbf{g}(x,z,p)\, sign\ z}{\lambda(x,z,p)} \leq \mu_1|p| + \mu_2 \qquad \forall (x,z,p) \in \Omega \times \mathbb{R} - \{0\} \times \mathbb{R}^n$$

*where* $\lambda(x,z,p)$ *is the smallest eigenvalue of matrix* $A = (a_{ij})_{i,j=1,2}$*.*

**Hypothesis 3.2.** *Suppose that there exists a constant* $M$ *such that*

$$z\mathbf{g}(x,z,0) \leq 0 \qquad \textit{for } x \in \Omega, |z| \geq M$$

And the following theorem ensures existence of solutions under structural conditions for function $g$ and smoothness of the boundary $\partial\Omega$:

**Theorem 3.3.** *([25], chap 14) Let* $\Omega$ *be a bounded domain in* $\mathbb{R}^n$ *and suppose that the operator* $Q$ *is elliptic in* $\bar{\Omega}$ *with coefficients*

$$a_{ij} \in C^1(\bar{\Omega} \times \mathbb{R}), \;\; \mathbf{g} \in C^{\gamma}(\bar{\Omega} \times \mathbb{R} \times \mathbb{R}^n), \;\; 0 < \gamma < 1,$$

*satisfying* $\mathbf{g} = \mathcal{O}(|p|^2)$ *as* $|p| \to \infty$*, uniformly for* $x \in \Omega$ *and bounded* $z$*, together with hypothesis 3.1, or 3.2. Then, if* $\partial\Omega \in C^{2,\gamma}$ *and* $\phi \in C^{2,\gamma}(\bar{\Omega})$*, there exists a solution* $u \in C^{2,\gamma}(\bar{\Omega})$ *of the Dirichlet problem* $Qu = 0$ *in* $\Omega$*,* $u = \phi$ *on* $\partial\Omega$*.*

Therefore, the existence of solutions to (3.33)-(3.41) is ensured provided we have 3.1 (or 3.2), $b = \mathcal{O}(|p|^2)$ as $p \to \infty$, a smooth boundary $\partial\Omega$ and $\phi \in C^{2,\gamma}$. We now aim to explicit these conditions.

Since the coefficients $b_{ij}(z)$ are bounded by $2\alpha_3$ for all $i,j = 1,2$ and all $\theta$, for $p \to \infty$, using Eq. (3.38):

$$\mathbf{g}(x,z,p) \leq \mu(z)|p|^2$$

where $\mu(z)$ is a function which depends on $z$ only. Therefore, we obtain $b = \mathcal{O}(|p|^2)$ as $p \to \infty$ for bounded $z$. Moreover, we have:

$$z\mathbf{g}(x,z,0) = -zh(z)$$

Therefore, Hyp. 3.2 reduces to a condition for function $h(z)$: there exist $M$ such that

$$\begin{aligned} h(z) &\geq 0 \qquad z \geq M \\ h(z) &\leq 0 \qquad z \leq -M. \end{aligned} \tag{3.40}$$

Altogether, if the external potential $U$ is such that (3.40) is satisfied, the Dirichlet problem $F(\theta) = 0$ on $\Omega$, $\theta = \phi$ in $\partial\Omega$ has a solution $\theta \in C^{2,\gamma}(\bar{\Omega})$. If we do not assume Hypotheses 3.1 or 3.2 (i.e (3.40)), the Dirichlet problem $Qu = 0$ in $\Omega$, $u = \phi$ on $\partial\Omega$ is solvable provided the solutions of a related family of problems such as (3.39) are uniformly bounded on $\Omega$ (theorem 3.2).

□

In order to gain insight into the properties of the solutions to the macroscopic model, we provide in next section a numerical study of this model.

## 3.2 Numerical simulations of the macroscopic model

Here, we aim to study numerically the macroscopic equation in the case of a homogeneous fiber density $\rho$. We first write Eq. (3.42) in a semi conservative form, and test the proposed numerical method. We then present the numerical profiles of the solutions as functions of the model parameters.

### 3.2.1 Semi-conservative form of the macroscopic equation

As for the microscopic model, we consider a 2D square domain of side length $2S$, $\Omega = [-S, S] \times [-S, S]$, with periodic boundary conditions on the top and bottom and Dirichlet boundary conditions $\theta_1$ and $\theta_2$ on the left and right sides of the domain:

$$\begin{aligned} \theta(x,-S) &= \theta(x,S) \ \forall \ x \in [-S,S] \\ \partial_y\theta(x,-S) &= \partial_y\theta(x,S) \ \forall \ x \in [-S,S], \\ \theta &= \theta_1 \ \text{ on } \Gamma_L, \\ \theta &= \theta_2 \ \text{ on } \Gamma_R. \end{aligned} \tag{3.41}$$

The stationary solutions $\theta(x)$ of Eq. (3.30) solve:

$$\begin{aligned} \alpha^-(\theta)\partial_{xx}\theta + \alpha^+(\theta)\partial_{yy}\theta + 2\alpha_3 \sin(2\theta)((\partial_x\theta)^2 - (\partial_y\theta)^2 - \partial_{xy}\theta), \\ -4\alpha_3\cos(2\theta)\partial_x\theta\partial_y\theta - h(\theta) = 0 \qquad\qquad \text{in } \Omega, \end{aligned} \tag{3.42}$$

where $\alpha^\pm(\theta) = \alpha_2 \pm \alpha_3\cos(2\theta)$. In order to introduce the numerical scheme, we aim to write Eq. (3.42) in a semi conservative form. For this purpose, we note that:

$$\begin{aligned} \cos 2\theta\partial_{xx}\theta - 2\sin 2\theta(\partial_x\theta)^2 &= \partial_x\Big(\cos 2\theta\partial_x\theta\Big) = \frac{1}{2}\partial_{xx}\sin 2\theta, \\ \cos 2\theta\partial_{yy}\theta - 2\sin 2\theta(\partial_y\theta)^2 &= \frac{1}{2}\partial_{yy}\sin 2\theta, \\ \sin 2\theta\partial_{xy}\theta + 2\cos 2\theta\partial_x\theta\partial_y\theta &= \partial_x(\sin 2\theta\partial_y\theta) = -\frac{1}{2}\partial_{xy}\cos 2\theta. \end{aligned}$$

Then, Eq. (3.42) can be written:

$$\alpha_2\Big(\partial_{xx}\theta + \partial_{yy}\theta\Big) - \alpha_3\left(\frac{1}{2}\partial_{xx}\sin 2\theta - \frac{1}{2}\partial_{yy}\sin 2\theta - \partial_{xy}\cos 2\theta\right) - h(\theta) = 0 \quad \text{in } \Omega \tag{3.43}$$

The numerical scheme used to solve Eqs. (3.43) with boundary conditions (3.41) can be found in appendix 6.3. As this equation contains non linear terms, we discretize the equation with simple finite differences and apply a Newton algorithm. As Newton solutions are sensitive to initial conditions, we proceed by continuation on a set of sub-problems, the solution of the first one being known.

### 3.2.2 Comparison with exact solutions

Here, we aim to validate the numerical method proposed in Appendix (6.3) by comparing its solutions to exact solutions.

**Test case I:** We first aim to test our numerical scheme on the following test case:

$$\begin{aligned}\Delta\theta + \frac{\pi^2\theta}{S^2} &= \sin(\pi\frac{y}{S}) + \frac{\pi^2}{S^2}\Big(\frac{\theta_2-\theta_1}{2S}(x-S)+\theta_2\Big)\\ \theta &= \theta_1 \ \text{ on } \Gamma_L\\ \theta &= \theta_2 \ \text{ on } \Gamma_R\end{aligned}$$

for which the exact solutions $\theta_{ex}$ read:

$$\theta_{ex}(x,y) = \sin(\pi\frac{y}{S})\frac{x^2-S^2}{2} + \frac{\theta_2-\theta_1}{2S}(x-S)+\theta_2. \tag{3.44}$$

Note that this equation can be obtained using (3.43) with $\alpha_2 = 1, \alpha_3 = 0$ and

$$h(x,y,\theta) = \frac{\pi^2\theta}{S^2} - \sin(\pi\frac{y}{S}) - \frac{\pi^2}{S^2}\Big(\frac{\theta_2-\theta_1}{2S}(x-S)+\theta_2\Big). \tag{3.45}$$

Therefore, we can apply the numerical method proposed in 6 with $\alpha_3 = 0$ and using

$$\frac{\partial h(x,y,\theta)}{\partial\theta} = \frac{\pi^2}{S^2}.$$

To validate the numerical scheme, we investigate the convergence when the space step $(\Delta x, \Delta y)$ tends to $(0,0)$. For this purpose, we use $\Delta x = \Delta y = \frac{0.1}{2^n}$ for $n$ from 0 to 5 and compute the $L^2$ norm of the error between the numerical solution $\theta$ and the exact solution $\theta_{ex}$ (see Eq. (3.44)). Fig. 3.1 shows the error curve plotted as function of $\Delta x$ in log log scale.

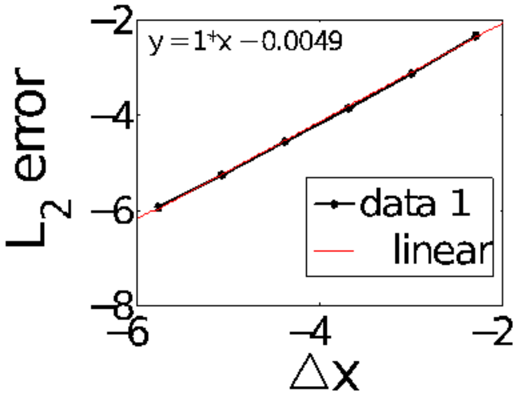

Figure 3.1: $L^2$ error for the orientation $\theta$ as function of $\Delta x$ in log log scale. Red curve: linear fit (the equation of the linear fit is indicated on the graph). The scheme is numerically of order 1.

As shown by Fig. 3.1, the log of the error linearly increases as function of the log of the space step $\Delta x$, with slope 1. This shows that the numerical scheme is of order 1.

**test case II** In the case $\alpha_3 \neq 0$ and for $h(\theta) = 0$, the solutions $\theta(x, y)$ of (3.43) can be written as solutions of the following fixed-point problem for all $(x, y) \in [-S, S]^2$:

$$\theta(x, y) = g(\theta(x, y)),$$

where $g : \mathbb{R} \to \mathbb{R}$ is such that

$$\begin{aligned} g(\xi) &= \frac{\alpha_3}{2\alpha_2} \sin 2\xi + ax + b \\ a &= \frac{1}{2S}\Big(\frac{\alpha_3}{2\alpha_2}(\sin 2\theta_1 - \sin 2\theta_2) + \theta_2 - \theta_1\Big) \\ b &= \theta_1 - \frac{\alpha_3}{2\alpha_2} \sin 2\theta_1 + aS \end{aligned} \tag{3.46}$$

Note that $\theta(x, y) = \theta(x)$ for all $y \in [-S, S]$ in this case. Figs. 3.2 show the profile of the solutions to (3.43) for $h(\theta) = 0$, $\alpha_2 = 1$ and $\alpha_3 = -1$ (A) or $\alpha_3 = 1$ (B). The profiles of the numerical solutions (which do not depend on $y$) are plotted as functions of $x$ for $y = -0.2$ for these two $\alpha_3$. The error between the numerical solution $\theta$ and its corresponding value $g(\theta)$ in log log scale is of order $10^{-15}$ whatever the mesh size $\Delta x$.

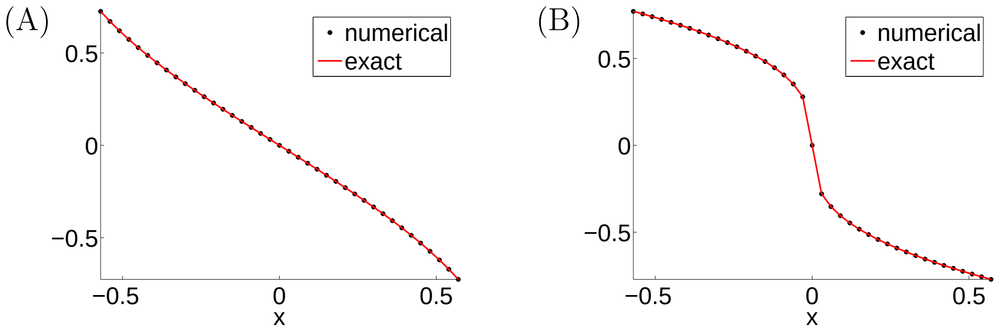

Figure 3.2: Black dots: Numerical solution $\theta(x,-0.2)$ of (3.43) for $\alpha_2 = 1$ and $h(\theta) = 0$, as function of $x$, red curve: function $g(\theta(x,-0.2))$. (A): for $\alpha_3 = -1$, (B): for $\alpha_3 = 1$.

Figs. 3.2 (A) and (B) show that the numerical solutions $\theta(x,y)$ of (3.43) (black dots) match the values of $g(\theta(x,y))$ (red curve) for all $x \in [-S,S]$ and a given $y$. As shown by Fig. 3.2 (C), the $L^1$ error between the numerical values of $\theta$ and $g(\theta)$ is of order $10^{-15}$ for all $\Delta x$. Therefore, the numerical solutions of (3.43) are solutions to the fixed point problem $\xi = g(\xi)$ for all $(x,y) \in \Omega$. This tends to validate the numerical method of 6 when $\alpha_3 \neq 0$.

It is noteworthy that the non linear term have a non negligible impact on the profile of the solutions. Indeed, for $\alpha_3 = 0$ and no external forces ($h(\theta) = 0$), the solution is linear in $x$. The deformation from this linear profile is stronger for $\alpha_3 = 1$ (Fig. 3.2 (B)) than for $\alpha_3 = -1$ (Fig. 3.2 (A)). This is due to the fact that the non linear terms are the macroscopic counterpart of the alignment potential between cross-linked fibers (note that in [2], it is shown that physically-relevant values for the model parameters lead to $\alpha_3 \leq 0$). As shown by the profile of Fig. 3.2 (A), this leads to a diffusion of the orientations from the center of the domain (where fibers are oriented horizontally), while $\alpha_3 > 0$ leads to a propagation of the orientations from the borders of the domain (where the Dirichlet conditions impose an orientation towards $\pm\frac{\pi}{4}$).

### 3.2.3 A buckling phenomenon induced by the rotation potential

Here, we study the influence of the rotation potential contained in the term $h(\theta)$ of Eq. (3.43) on the profile of the solutions. Fiber orientations are initially set to, for all $(x,y) \in \Omega$:

$$\theta(x,y) = \theta_1 + (\theta_2 - \theta_1)x, \tag{3.47}$$

which is compatible with the boundary conditions (3.41). Figs. 3.3- 3.5 show the profiles of the solutions as functions of $x$ for $y = -0.2$, $\alpha_2 = 0.1$ and three different values of $\alpha_3 \leq 0$: $\alpha_3 = 0$ (A), $\alpha_3 = -10^{-3}$ (B) and $\alpha_3 = -0.01$ (C). For each, the rotation potential intensity $c_u$ (see (2.3)) varies from $c_u = 0$ (black dots), $c_u = 1$ (red curve) and $c_u = 10$ (green curve). The boundary conditions (3.41) are chosen with $\theta_1 = \frac{\pi}{4}$ and $\theta_2 = -\frac{\pi}{4}$ (symmetric) for Fig. 3.3, while we have perturbed $\theta_1$ of a small quantity for Fig. 3.4 ($\theta_1 = 0.98\frac{\pi}{4}$) and $\theta_2$ for Fig. 3.5 ( $\theta_2 = -0.98\frac{\pi}{4}$).

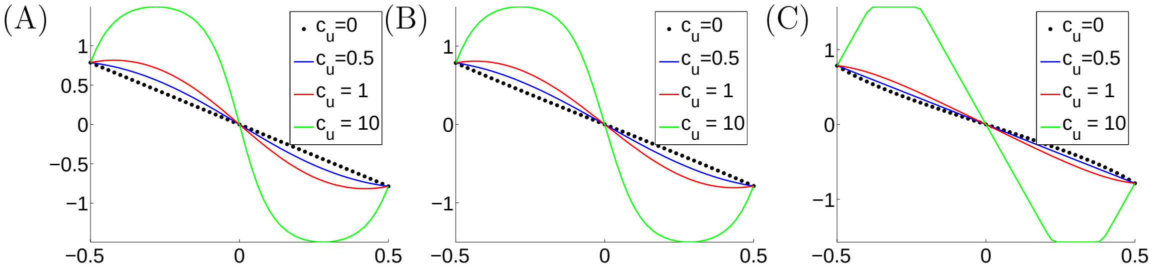

Figure 3.3: Profiles of the solutions to (3.43)-(3.41) for $\alpha_2 = 0.1$, $\theta_1 = -\theta_2 = \frac{\pi}{4}$ (symmetric boundary conditions). Black dots: $c_u = 0$, red curve: $c_u = 1$, green curve: $c_u = 10$. (A) $\alpha_3 = 0$, (B) $\alpha_3 = -0.05$, (C) $\alpha_3 = -0.1$.

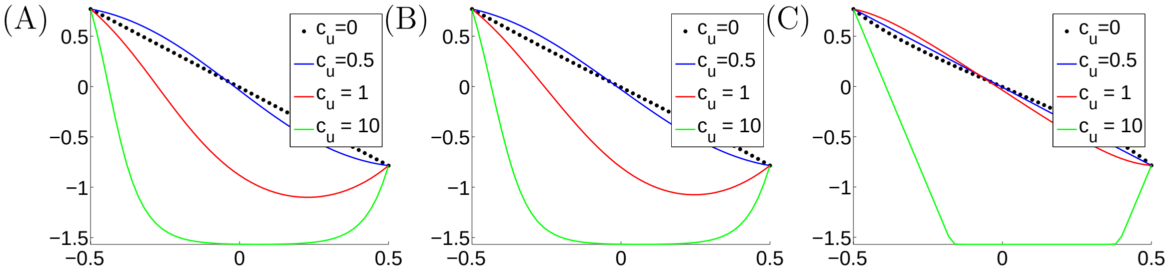

Figure 3.4: Profiles of the solutions to (3.43)-(3.41) for $\alpha_2 = 0.1$, $\theta_1 = 0.98\frac{\pi}{4}$, $\theta_2 = -\frac{\pi}{4}$ (assymmetric boundary conditions). Black dots: $c_u = 0$, red curve: $c_u = 1$, green curve: $c_u = 10$. (A) $\alpha_3 = 0$, (B) $\alpha_3 = -0.05$, (C) $\alpha_3 = -0.1$.

As shown by Figs. 3.3-3.5, three stationnary states are obtained when introducing the rotation potential (2.3): (i) a symmetric state in which fibers of the left side of the domain are oriented in $\frac{\pi}{2}$ and fibers of the right side in $-\frac{\pi}{2}$ (Fig. 3.3), (ii) an asymmetric state in which all the fibers are oriented in $\frac{\pi}{2}$ (Fig. 3.4) and (iii) an asymmetric state in which all the fibers are oriented in $-\frac{\pi}{2}$ (Fig. 3.5). These plots show that there exists a critical $c_u$ for which the solutions are in the unstable configuration (i): a slight increase of $c_u$ will lead the solution to buckle and change for configurations (ii) or (iii). The boundary conditions determine the mode of bending (i.e the passage (i) - (ii) or (i) - (iii)). The critical $c_u$ depends upon the value of the parameter $\alpha_3$, which plays the role of an elastic modulus. Indeed, for

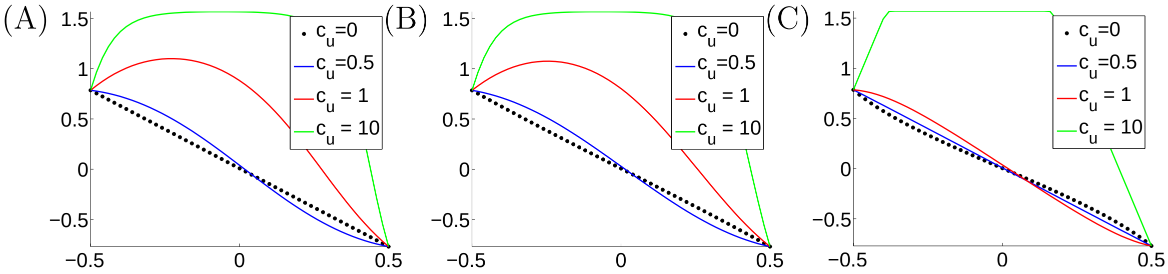

Figure 3.5: Profiles of the solutions to (3.43)-(3.41) for $\alpha_2 = 0.1$, $\theta_1 = \frac{\pi}{4}$, $\theta_2 = -0.98\frac{\pi}{4}$ (assymmetric boundary conditions). Black dots: $c_u = 0$, red curve: $c_u = 1$, green curve: $c_u = 10$. (A) $\alpha_3 = 0$, (B) $\alpha_3 = -0.05$, (C) $\alpha_3 = -0.1$.

$\alpha_3 = 0.1$ (Figs. 3.3-3.5 (C)), the buckling phenomenon appears between $c_u = 1$ and $c_u = 10$ while smaller values of $\alpha_3$ leads to buckled situations for $c_u$ between 0.5 and 1.

These observations enable us to gain insight into the physical meaning of parameters $\alpha_2$ and $\alpha_3$ for the macroscopic model. It tends to show that the whole fiber structure could be seen as an elastic material. In this case, its elastic modulus is linked to parameters $\alpha_2$ and $\alpha_3$. In this configuration, the external potential contained in the term $h(\theta)$ could be seen as a force generating compressing stress.

To continue our analysis of the macroscopic model, a natural approach is to numerically compare its solutions to the ones obtained with its microscopic corresponding model. In the next section, we present a first step towards the comparison between the macroscopic system of equations and the microscopic dynamics.

# 4 Comparison between the macroscopic model and the particle dynamics

In this section, we perform numerical simulations of the microscopic scaled equations and compare numerically the obtained solutions to the ones of the macroscopic model.

## 4.1 Equilibria

We first compare the distribution of the fiber orientations $\theta_i$ with the theoretical distribution $M_{\theta_0(x)}$ given by (3.28). For the microscopic simulations, the noise $d_X$ on the fiber space motion is fixed and chosen such that the fiber density is homogeneous and constant in time. As explained in appendix 7, this is performed by adapting the value of the free parameter $\mu$. As the macroscopic fiber distribution does not depend on $y$ (because of the boundary and initial conditions which do not depend on $y$), the mean orientation $\theta_0(x)$ for $x = (x_1, x_2) \in \mathbb{R}^2$ of the fibers of the microscopic model is computed as the circular mean of the fiber orientations, over all the fibers such that the $x$-coordinate of their center is contained in a neighborhood of $x_1$. More explicitly, for each $x \in [-S + s_D/2, S + s_D/2] \times [-S, S]$:

$$\theta_0(x) = \frac{1}{2} \arg \left( \sum_{i \in \mathcal{I}(x)} e^{2i\theta_i} \right)$$

where $\mathcal{I}(x)$ is the set of fibers the center of which has $x$ coordinate near $x_1$: $\mathcal{I}(x) = \{i \mid x_i \in [x_1 - \frac{s_D}{2}, x_1 + \frac{s_D}{2}[\}$, $x_i$ being the $x$-coordinate of fiber $i$ center. In order to reduce the noise in the representation, we average the observables over 10 simulations.

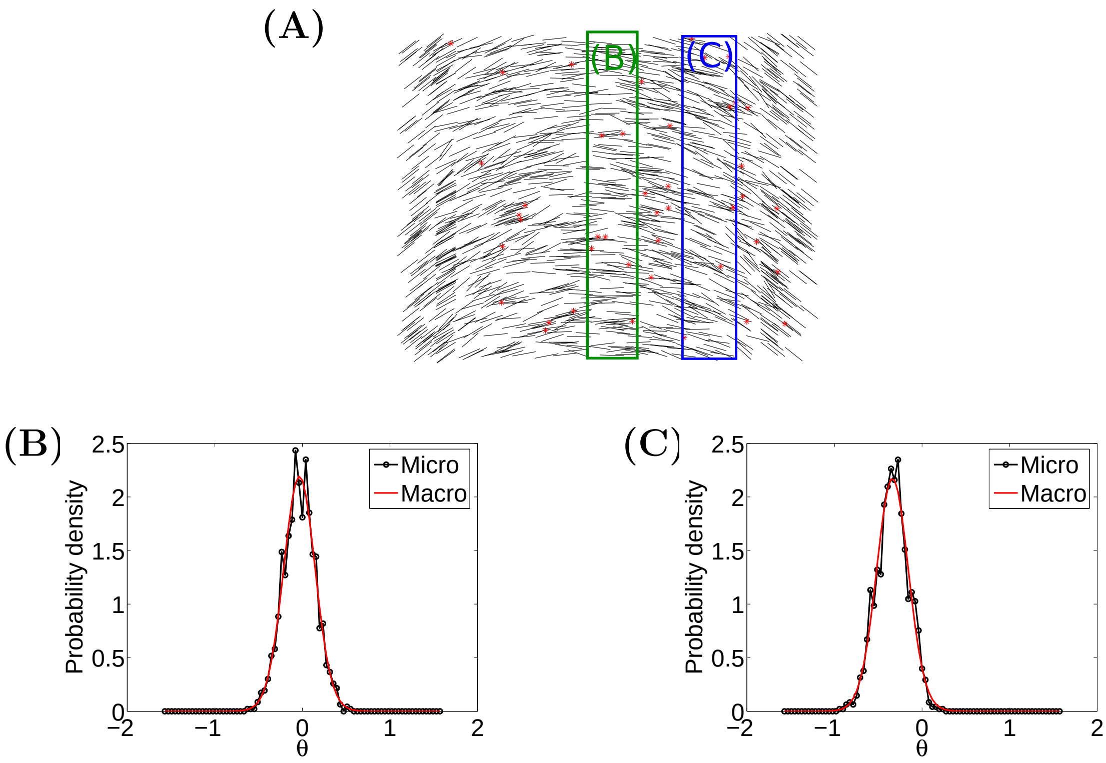

Figure 3.6: (A) Particle simulation $N = 1500$, $\theta_1 = -\theta_2 = \frac{\pi}{4}$, $\varepsilon = 0.1$, $\alpha = 0.1$, $c_u = 0$, $d = 1e - 5$, $\nu_f = 0.1$, $\chi = \frac{\nu_f}{\nu_d} = 0.1$. Zones of the domain for the computation of $r$ in Figs. (B) and (C) are indicated as green and blue rectangles respectively. (B) Distribution of the circular mean of the orientation angles $\theta_i$ for fibers the center of which is close to $x = 0.2$ (red), compared to its theoretical distribution (black), averaged over 10 simulations. (C) Distribution of the circular mean of the orientation angles $\theta_i$ for fibers which the center of which is close to $x = 0$ (red) compared to its theoretical distribution (black), averaged over 10 simulations.

As shown in Fig. 3.6, the theoretical distribution of orientations and the microscopic one are in good agreement for a fitted value of $r$. We find the same order parameter $r \approx 7.5$ for fibers in a neighborhood of the center of the domain $x = 0$ as well as for $x = 0.2$, for this set of parameter. This tends to show that the order is conserved in the whole domain. In appendix 9, we show that the order parameter does not depend on the size $s_D$ of the numerical boxes used to compute its value.

## 4.2 Order parameter

We now want to study how the order parameter $r$ depends upon the model parameters. The order parameter fitted from the simulations of the microscopic model as previously explained is referred to as $r_{fit}$, and $r_{nfit}$ denotes its value normalized by function $c$, i.e $r_{nfit} = \frac{r_{fit}}{c(r_{fit})}$. We denote by $r_{nth}$ its expected value from the macroscopic model:

$$r_{nth} = \frac{r_{th}}{c(r_{th})} = \frac{\xi \alpha L^2 \nu_f \rho}{4d\nu_d} = \frac{\xi \alpha L^2 \chi \rho}{4d}, \tag{4.48}$$

where $\chi = \frac{\nu_f}{\nu_d}$ is the ratio between the fiber linking and unlinking frequencies. Note that the macroscopic order parameter $r$ depends upon the model parameters but also on the quantity $\xi$ (ratio between the number of fiber links and total number of fibers). If the values of the model parameters are well determined for the microscopic and macroscopic models, the relation between the microscopic value of $\xi$ and its macroscopic one is more difficult to obtain. In order to highlight this phenomenon, we show in Fig. 3.7 (A) the value of $r_{nfit}$ as function of the noise intensity $d$, for $\chi = 0.1$ and $\chi = 1$. Note that $r_{nfit}$ decreases as function of $d$. In Fig. 3.7 (B), we show the logarithm of $r_{nfit}$ as function of the logarithm of $d$ (green and blue curves for $\chi = 0.1$ and $\chi = 1$ respectively), and their corresponding linear fits (black and red curves). We obtain slopes of $-0.2$ for $\chi = 0.1$ and $-0.1$ for $\chi = 1$. This suggests that $\xi$ depends non trivially upon $d$ and $\chi$.

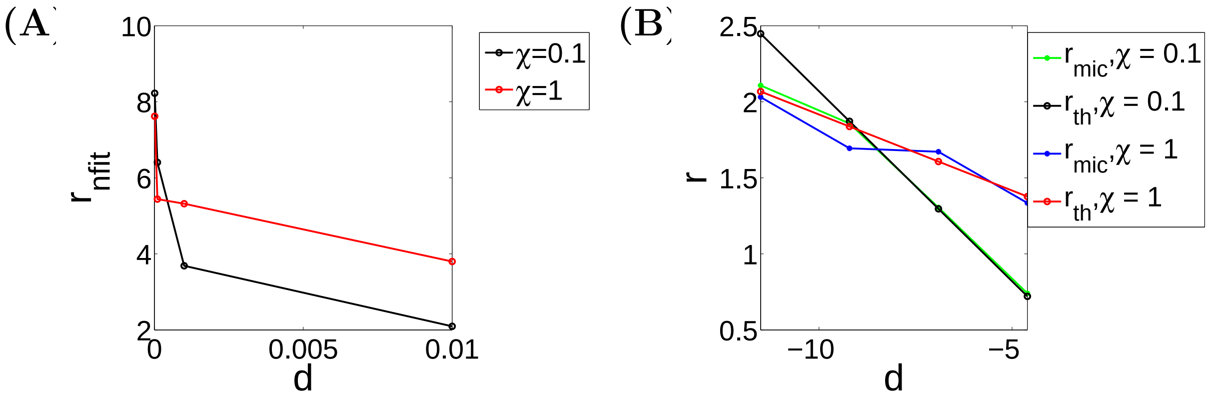

Figure 3.7: (A): values of $r_{nfit}$ as function of the noise $d$ for $\chi = 0.1$ (black curve) and $\chi = 1$ (red curve). (B): values of $r_{nfit}$ as function of the noise $d$ in loglog scale for $\chi = 0.1$ (green curve) and $\chi = 1$ (blue curve) and their respective fit (black and red curve).

As a first validation, we would like to compare the profiles of the solutions for the macroscopic and microscopic models. This is performed next section.

## 4.3 Profiles of the solutions

Here, we use the order parameter fitted in the microscopic simulations to compute the solutions of the macroscopic model for the same set of parameters. As explained in Appendix 7, simulations are performed on the same square domain for the microscopic and macroscopic model: $[-S, S] \times [-S, S]$ with side length $2S$ for $S = 0.5$. The numerical grid for the macroscopic simulations is such that $\Delta x = \Delta y = 0.025$ and the time step respect the CFL condition (see appendix 7) with $\delta_f = \frac{L}{2}$. If not differently stated, the macroscopic values of the model parameters are chosen such that:

$$\nu_f = \nu_d = 0.1, \quad c_u = 0.1, \quad \alpha = 0.1, \quad \kappa = 0.1, \quad d_X = 5e^{-5}, \quad N = 1500, \quad L = 0.2,$$

and $\varepsilon = 0.1$. Fig. 3.8 shows the simulations performed for $\chi = 0.1$ and different values of the noise intensity $d$ and for external potential $c_u = 0.01$ (A) and $c_u = 0.1$ (B). We recall that the noise in the space variables is fixed, i.e $\mu$ is chosen such that $d\mu = d_X = 5e^{-5}$. As highlighten by the study of the macroscopic model (see section 3.2.3), buckled solutions are obtained for a certain set of parameters. Due to the randomness of the phenomena of the microscopic model (random noise, fiber linking unlinking, random initial configurations), the final solutions of the microscopic model will converge randomly to one of the buckled situations, with no preference for one or the other. Therefore, in order to enable the comparison between the microscopic and macroscopic buckled situations, we use the symmetry of the buckled situations and study the absolute value of the fiber orientations $|\theta(x)|$. Fig. 3.8 shows simulations for different noise parameter $d$ as well as different external potential forces $c_u$. For each set of parameter, we show the profiles of $\theta(x)$ for both microscopic and macroscopic models in unbuckled situations, and $|\theta(x)|$ for both models in case of buckled situations. Red curves correspond to the solutions of the macroscopic model, black curves to the solutions of the microscopic one. As shown by Fig. 3.8, we obtain a very good agreement between the solutions of the microscopic and macroscopic models in the case $\chi = 0.1$ (small amount of fiber links).

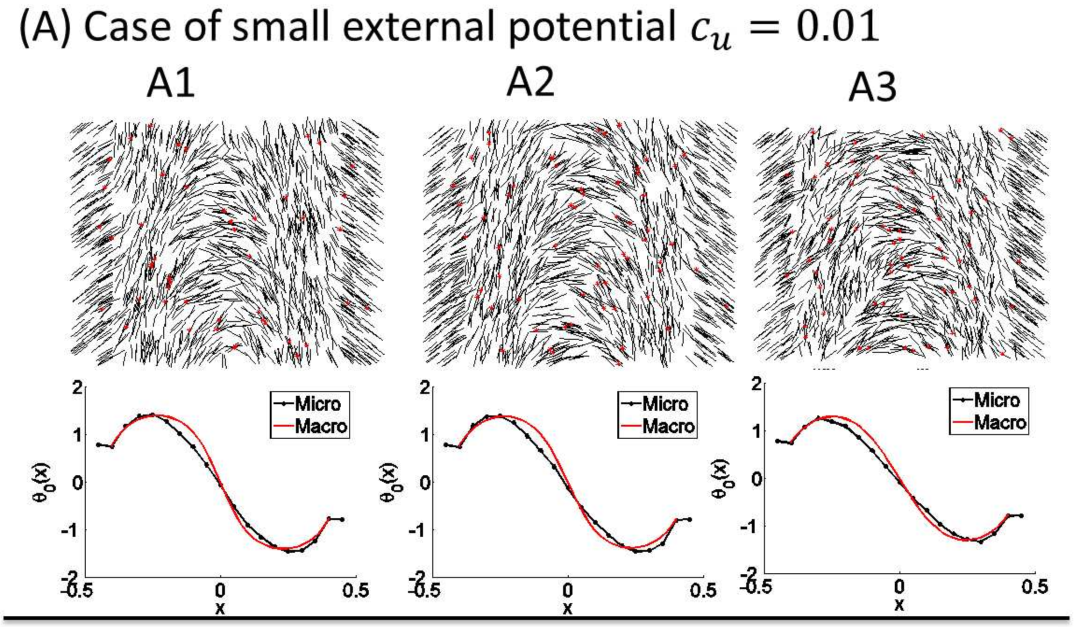
(A) Case of small external potential $c_u = 0.01$

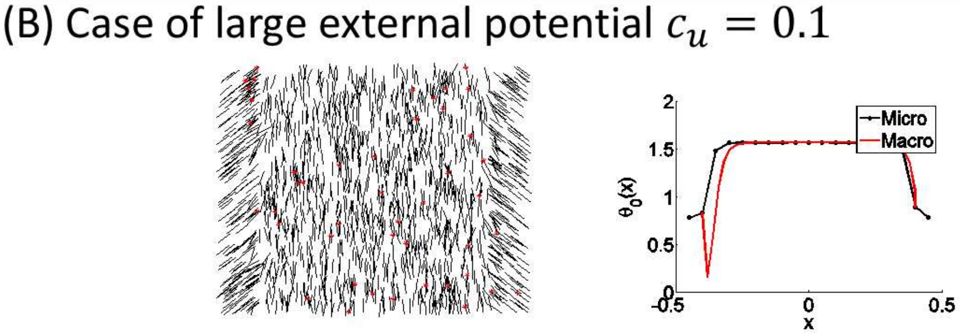
(B) Case of large external potential $c_u = 0.1$

Figure 3.8: (A) Simulations of the microscopic model with $\varepsilon = 0.1$, external potential $c_u = 0.01$ and fiber linking/unlinking frequencies such that $\chi = 0.1$ (first line). From A1 to A3: for increasing values of the microscopic noise $d$: $d = 10^{-5}$, $d = 10^{-4}$ and $d = 10^{-3}$. For each, we show the profiles of the solutions averaged over the $y$ direction and over 10 simulations for the microscopic model (black curves, second line). For each set of parameters, we superimpose the profiles of the solutions to the macroscopic model (red curve). For small $d$ and small external potential $c_u = 0.01$ (A1,A2), fiber orientation angles reach $\frac{\pi}{2}$ and $-\frac{\pi}{2}$ on the left and right hand sides of the domain, with a zone of quasi horizontal fibers in the middle, as predicted by the macroscopic model. For increasing $d$ (A3), the profile flattens and fibers no longer reach the orientation angles $\frac{\pi}{2}$. The macroscopic model captures the same features for the same parameters. (B) Case $c_u = 0.1$. In this case, all fibers reach orientation $\pm\frac{\pi}{2}$ due to the large intensity of the external potential for both the microscopic and macroscopic model.

As shown by Fig. 3.8 (A), for small noise intensity $d$ and small external potential $c_u = 0.01$, fibers reach $\frac{\pi}{2}$ and $-\frac{\pi}{2}$ on the left and right hand side of the domain, while fibers in the middle are quasi horizontally disposed, as predicted by the macroscopic model (Figs. 3.8 (A1-A2)). For increasing $d$, the profile of the fiber orientation flattens and fibers no longer reach the orientation angles $\frac{\pi}{2}$ (Fig. 3.8 (A3)). The macroscopic model captures the same features for the same parameters. In the case of a larger external potential, all the fibers are vertically disposed in the domain (except on the boundaries because of the Dirichlet conditions, see Fig. 3.8 (B)). This is also predicted by the macroscopic model. This tends to show that the macroscopic model captures the same features as the microscopic model in case of a small value of $\chi$. However, different solutions are obtained when comparing both models for $\chi = 1$. As shown in Fig. 3.9, for the same parameters, the profile of the solution of the microscopic model is much more flattened than for the macroscopic model with $\chi = 1$.

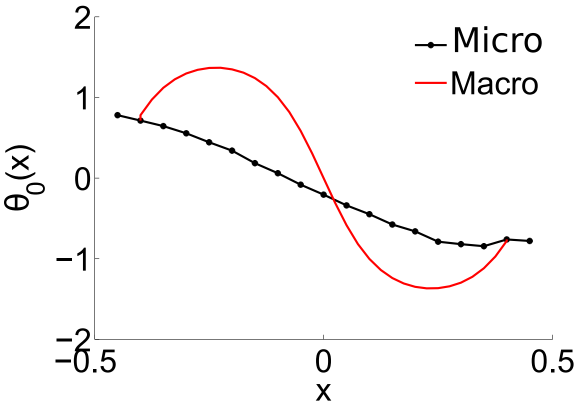

Figure 3.9: Simulation of the microscopic model with $\varepsilon = 0.1$, external potential $c_u = 0.01$, $d = 10^{-4}$ and fiber linking/unlinking frequencies such that $\chi = 1$. For the same parameters and $\chi = 1$, the profile of the solution of the microscopic model (black curve) is much more flattened than for the macroscopic model (red curve).

This suggests that the noise must be much larger in the macroscopic model for both profiles to correspond. From this observation, we deduce that the amount of fiber links has a strong effect on the 'temperature' of the system. This is due to the fact that fibers have a finite length in the microscopic model, whereas the large scale limit supposes that fiber length tends to 0. To highlight this phenomenon, we plot (in loglog scale) in Fig. 3.10 the $L^2$ norm of the difference between the solution of the microscopic model and the one of the macroscopic model, as function of the fiber length $L$. We explore the fiber lengths $L \approx 0.16$, $L \approx 0.2$ and $L \approx 0.22$ (respective microscopic values: 0.05,0.06 and 0.07), and the respective number of fibers are chosen to $N_f = 1800$, $N_f = 1500$ and $N_f = 1250$. For each, three different noise intensities are tested $d = 10^{-5}, 10^{-4}$ and $d = 10^{-3}$. Figs. 3.10 (A) and (B) are obtained for $\chi = 0.1$ and $\chi = 1$ respectively. The external potential is $c_u = 0.01$.

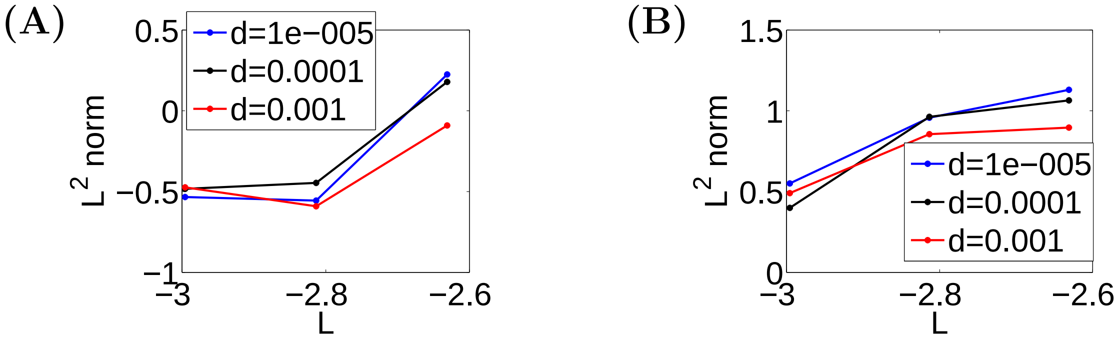

Figure 3.10: (A) $L^2$-norm of the difference between the microscopic fiber orientation and the macroscopic one for $c_u = 0.01$, $\chi = 0.1$, plotted in loglog scale as function of the (microscopic) fiber length $L$ for three different values of the noise intensity $d$: $d = 10^{-5}$ (blue curve), $d = 10^{-4}$ (black curve) and $d = 10^{-3}$. (B) Same plots in the case $\chi = 1$.

As shown by Fig. 3.10, the difference between the microscopic and macroscopic profiles decreases when the fiber length decreases. For $\chi = 0.1$, we obtain a small error of order 0.6 whereas for $\chi = 1$ the error is 1.64 for the smallest fiber length considered. These results are a first step towards the numerical proof of convergence of the microscopic model to the macroscopic one as the fiber length goes to zero.

# 5 Conclusion

In this paper, we have analyzed the macroscopic model derived from a microscopic model for fibers interacting through linking and unlinking interactions, alignment between cross-linked fibers and external rotation potential. We have shown that the starting Individual based dynamics can be written in form of a minimization problem under a given regime, showing the analogy between the models of [1] and [2]. Under some regularity assumptions for the external potential, we were able to obtain existence of stationary solutions to the macroscopic derived model. The numerical simulations of the macroscopic model showed the apparition of a buckling phenomenon, giving a first insight into the mechanical properties of the system. We showed that the distribution of fiber mean local orientation of the microscopic model were in good agreement with the predictions of the macroscopic model and we were able to compute the order parameter of the microscopic model. The numerical simulations of the microscopic model showed that in a well chosen regime, the microscopic and macroscopic models were in good agreement. We finally gave a first numerical analysis towards the proof of the convergence of the microscopic model to the macroscopic one.

We have seen that the fiber links density have a strong impact on the final structures that the macroscopic model does not capture. This is due to the fact that the scaling suppose that the linking/unlinking process is quasi instantaneous. This assumption makes the action of the links vanish in the macroscopic model, and no memory effect of the fiber cross-links remain. Works are in progress to better understand the effects of the links on the temperature of the system. Further perspectives of this model include numerical simulations of the complete kinetic model, or the establishment of a hydrodynamic scaling based on a more realistic assumption for fiber linking/unlinking dynamics.

Many questions remain open concerning the macroscopic model. On an analytical viewpoint, unicity results for the stationary solutions of the macroscopic model are the subject of future work. On a numerical viewpoint, we plan to develop numerical techniques to enable the microscopic simulations to be performed under the kinetic regime. An other direct perspective of this work is to consider non homogeneous density. As shown in [2], this leads to a much more complex system of two coupled highly non linear equations requiring advanced numerical methods.

# Bibliography

[1] D. Peurichard et al. *Simple mechanical cues could explain adipose tissue morphology*, submitted

[2] D. Peurichard, F. Delebecque, P. Degond *Continuum model for linked fibers with alignment interactions*, submitted

[3] D. Boal (2002), *Mechanics of the Cell*, Cambridge University Press, New York.

[4] P. Friedl, E.B.Brocker, (2000) *The biology of cell locomotion within three dimensional extracellular matrix*, Cell Mol. Life Sci, 51:595-615.

[5] O. Chaudury, S. H. Parekh, D. A. Fletcher (2007) *Reversible stress softening of actin networks*, Nature, 445:295-298.

[6] O. Lieleg, J. Kayser, G. Brambilla, L. Cipelletti and A. R. Bausch (2011) *Complex Slow Dynamics in Bundled Cytoskeletal Networks*, Nature Materials, 10:236-242.

[7] B.A. DiDonna, A. J. Levine (2006) *Filamin cross-linked semiflexible networks: Fragility under strain*, Phys Rev Lett. 97(6):068104

[8] D. Manoussaki, S. R. Lubkin, R. B. Vemon, J. D. Murray, (1996) *A mechanical model for the formation of vascular networks in vitro*, Acta Biotheoretica, 44(3-4):271-282

[9] A. Tosin, D. Ambrosi, L. Preziosi (2006),*Mechanics, chemotaxis in the morphogenesis of vascular networks*, Bull. Math. Biol., 68:1819-1836

[10] A. Chauviere, T. Hillen, L. Preziosi, (2007) *Continuum model for mesenchymal motion in a fibrous network*, Networks, Heterogeneous Media, 2:333-357

[11] T. Hillen, (2006), *M5 mesoscopic and macroscopic models for mesenchymal motion*, J. Math. Biol. 53:585-616.

[12] W. Alt, M. Dembo, (1999)*Cytoplasm dynamics, cell motion: two phase flow models*,Mathematical Biosciences, 156(1):207-228

[13] R.B. Dickinson,(2000) *A generalized transport model for biased cell migration in an anisotropic environment*,J. Math. Biol., 40:97-135

[14] R. Alonso, J. Young, Y. Cheng, (2014) *A particle interaction model for the simulation of biological, cross-linked fibers inspired from flocking theory*, Cell. mol. bioeng., 7(1):58-72

[15] C.P. Broedersz et al,(2010)*Cross-link governed dynamics of biopolymer networks*, PRL 105, 238101

[16] J.A Astrom, P.B.S Kumar, I. Vattulaine, M. Karttunen (2005)*Strain hardening in dense actin networks*, Phy. Rev. E. 71:050901

[17] I. Pivkin, G. Karniadakis. (2008) *Accurate coarse-grained modeling of red blood cells.* Phys. Rev. Lett. 101(11):118105.

[18] G.A. Buxton, N. Clarke, P.J. Hussey (2009)*Actin dynamics, the elasticity of cytoskeletal networks*, Express Polymer Letters, 3(9):579-587.

[19] D.A Head, A.J. Levine, F.C MacKintosh,(2003) *Distinct regimes of elastic response, deformation modes of cross-linked cytoskeletal, semiflexible polymer networks*, Phys. Rev. E. 68:061907

[20] H. Krasher, J. Lammerding, H. Huang, R.T. Lee, R.D. Kamm (2003) *A three-dimensional viscoelastic model for cell deformation with experimental verification*, Biophys. J. ,85(5):3336-49

[21] L.A. Tabler, Y. Shi, L. Yang, P.V. Bayly (2011)*A poroelastic model for cell crawling including mechanical coupling between cytoskeletal contraction, actin polymerization*, J. Mech. Mat. Struct., 6:569-589

[22] J.F. Joanny, F. Jlicher, K. Kruse, J. Prost (2007)*Hydrodynamic Theory for Multi-Component Active Polar Gels*, New J. Phys. 9 442

[23] P. Degond, S. Motsch, (2008) *Continuum limit of self-driven particles with orientation interaction*, Math. Mod. Meth. App. S. 18:1193-1215

[24] M.E. Taylor, *Partial Differential Equations III*, App. Maths. Sc., vol 117

[25] D. Gilbarg, N.S. Trudinger, (1977)*Elliptic Partial Differential Equations of Second Order*, Springer-Verlag

# 6 The microscopic model as a penalization method of a minimization problem

In this appendix, we aim to compare the microscopic model (2.8)-(2.9) with the model proposed in [1]. In [1], we developed an IBM for a fiber network with the same characteristics as the one described in section 2. Contrary to the IBM of this paper, in [1], the maintain of fiber links is modeled as a constraint and at each time step, fibers seek to minimize their mechanical interaction energy resulting from the total potential of the system, under the linkeage constraint between linked fibers. From now on, we will refer to as model I for the model of this paper (Eqs. (2.8)-(2.9)) and as model II for the model of [1]. In a first section, we present the main features of model II, and its numerical scheme is detailed in section 6.2. Section 6.3 is devoted to the numerical scheme for model I and shows the analogy between the two formulations. Finally, numerical simulations to compare models I and II are presented in section 6.4.

## 6.1 Individual Based Model of [1]

The total mechanical potential of the system is defined as a sum of the contributions of phenomena (ii) and (iii) (see section 2.1):

$$W_{tot} = W_{ext} + W_{align}. \tag{6.1}$$

All along the link life, linked fibers must remain attached. The maintain of the link is modeled as an equality constraint $\vec{V}_{i(k)j(k)} = 0$, where $\vec{V}_{i(k),j(k)}(X,\theta)$ is defined by Eq. (2.1).

During the simulation, fibers are submitted to random motion (phenomenon (iv)), new fiber links can appear and existing links can disappear (phenomenon (i)). These phenomena disrupt the mechanical equilibrium and force the fibers to move in order to restore the equilibrium. This can be written in form of a minimization problem. For this purpose, we consider a time discretization $t^n = n\Delta t$, $\Delta t \in \mathbb{R}$, $n \in \mathbb{N}$. At each time $t^n$, fiber positions and orientation angles solve:

$$(X^n, \theta^n) = \underset{(X,\theta)\in C}{\operatorname{argmin}}\, W_{tot}(X,\theta) \tag{6.2}$$

where $C = \{(X,\theta) \mid \vec{V}_{i(k),j(k)}(X,\theta) = 0 \;\forall\, k \in [1,K]\}$. In [1], tissue movements are modeled as time regular random changes, i.e fiber positions $X_i$ and orientations $\theta_i$ are actualized between time steps $t^n$ and $t^{n+1}$ as follows for all $i \in [1,N]$:

$$X_i^{n+1/2} = X_i^n + \eta_1\sqrt{2d_X\Delta t}, \theta_i^{n+1/2} = \theta_i^n + \eta_2\sqrt{2d_\theta\Delta t}, \tag{6.3}$$

where $\eta_1$ and $\eta_2$ are random numbers chosen from a Gaussian distribution and $d_X$ and $d_\theta$ are the respective amplitudes of fiber random motion and rotation.

## 6.2 Numerical scheme for the minimization problem

We propose to solve the minimization problem (6.2) by an Uzawa type algorithm. For this purpose, we define the Lagrangian $\mathcal{L}$ of the system:

$$\begin{aligned} \mathcal{L}(X,\theta) &= W_{tot} + \sum_{k=1}^{K} \vec{\lambda}_{i(k),j(k)} \vec{V}_{i(k),j(k)}(X,\theta) \\ &= \sum_{i=1}^{N} U(\theta_i) + \sum_{k=1}^{K} \Bigg( \sin(\theta_{i(k)} - \theta_{j(k)}) + \vec{\lambda}_{i(k),j(k)}.\vec{V}_{i(k),j(k)}(X,\theta) \Bigg). \end{aligned} \tag{6.4}$$

Given an initial configuration $(X^{n+1/2}, \theta^{n+1/2})$, the configuration $(X^n, \theta^n)$ at time $t^n$ is defined as the limit as $p \to \infty$ of the iterative sequence $(X^p, \theta^p)$ where $(X^p, \theta^p, \vec{\lambda}^p)$ is defined for all $i \in [1, N]$, $k \in [1, K]$ by:

$$\begin{aligned} X_i^{p+1} &= X_i^p - \alpha_X^i \nabla_{X_i} \mathcal{L}(X^p, \theta^p, \lambda^p) \\ \theta_i^{p+1} &= \theta_i^p - \alpha_\theta^i \partial_{\theta_i} \mathcal{L}(X^p, \theta^p, \lambda^p) \\ \vec{\lambda}_{i(k)j(k)}^{p+1} &= \vec{\lambda}_{i(k)j(k)}^{p} + \lambda \vec{V}_{i(k)j(k)}(X^{p+1}, \theta^{p+1})). \end{aligned} \tag{6.5}$$

with initial condition $(X^0, \theta^0, \vec{\lambda}^0) = (X^{n+1/2}, \theta^{n+1/2}, \vec{\lambda}^0)$ and $\vec{\lambda}_{i(k)j(k)}^0 = 0$, for all $(k) \in [1, K]$. The parameter $\lambda$ controls the actualization of the constraints and is further described. The minimization steps $\alpha_X$, $\alpha_\theta$ control fiber $i$ elementary motion and rotation respectively and their actualization is further described. The convergence test of the algorithm reads:

$$|\frac{\mathcal{L}^{p+1} - \mathcal{L}^p}{\mathcal{L}^p}| \leq \varepsilon_r, \tag{6.6}$$

for a chosen $\varepsilon_r > 0$. Here, $\mathcal{L}^p$ is the value of the Lagrangian at iteration $p$. Because of the non convexity of the minimization problem, the uniqueness of the solution to (6.2) is not ensured and a configuration at each time step corresponds to a local minimum of the minimization problem. The numerical parameters $\alpha_X^i$ and $\alpha_\theta^i$ are chosen such that the amplitude of the change of each variable remains controlled. Given the bounds $\delta_X$ and $\delta_\theta$, the goal is to ensure $|X_i^{p+1} - X_i^p| \leq \delta_X$ and $|\theta_i^{p+1} - \theta_i^p| \leq \delta_\theta$, for each fiber $i$. Using (6.4) and (6.5), the following expressions hold:

$$\begin{aligned} |X_i^{p+1} - X_i^p| &= \alpha_a^i |\nabla_{X_i} W_{tot} + \nabla_{X_i} \vec{V}_{\vec{\lambda}}| \\ |\theta_i^{p+1} - \theta_i^p| &= \alpha_\theta^k |\partial_{\Theta_k} W_{tot} + \partial_{\Theta_k} \vec{V}_{\vec{\lambda}}|. \end{aligned}$$

The parameters $\alpha_a^i$, $\alpha_f^k$ and $\alpha_\theta^k$ are consequently set such that:

$$\begin{aligned} \alpha_a^i &= \frac{\delta_X}{2} \min(\frac{1}{|\nabla_{X_i} W_{tot}|}, \frac{1}{|\nabla_{X_i} \vec{V}_{\vec{\lambda}}|}) \\ \alpha_\theta^i &= \frac{\delta_\theta}{2} \min(\frac{1}{|\partial_{\Theta_k} W_{tot}|}, \frac{1}{|\partial_{\Theta_k} \vec{V}_{\vec{\lambda}}|}. \end{aligned} \tag{6.7}$$

The gradient bounds are estimated at each iteration of the minimization algorithm and are included into Eqs. (6.7) to compute the values of the numerical steps. We refer to [1] for more details on the calibration of the numerical parameters.
For fiber linking/unlinking, we define $p_k^t$ the coefficients such that $p_k^t = 1$ if the pair of fibers $(i(k), j(k))$ are linked at time $t$, $p_k^t = 0$ otherwise. The time evolution of this coefficient between $t$ and $t+\Delta t$ reads, using the fact that $\nu'_f = \varepsilon^2\nu_f$, $\nu'_d = \varepsilon^2\nu_d$:

$$\begin{aligned}
\mathbb{P}(p_k^{t+\Delta t} = 1 \mid p_k^t = 0) =& 1 - e^{-\nu'_f\Delta t} && \text{if } \max(\ell_{i(k),j(k)}, \ell_{j(k),i(k)}) \leq \frac{L}{2} \\
=& 0 && \text{otherwise} \\
\mathbb{P}(p_k^{t+\Delta t} = 0 \mid p_k^t = 1) =& 1 - e^{-\nu'_d\Delta t}
\end{aligned}$$

where $\ell_{i(k)j(k)} = \bar{\ell}(X_{i(k)}, \theta_{i(k)}, X_{j(k)}, \theta_{j(k)})$ such that:

$$\bar{\ell}(X_{i(k)}, \theta_{i(k)}, X_{j(k)}, \theta_{j(k)}) = \frac{(x_{j(k)} - x_{i(k)})\sin\theta_{j(k)} - (y_{j(k)} - y_{i(k)})\cos\theta_{j(k)}}{\sin(\theta_{j(k)} - \theta_{i(k)})}, \quad (6.8)$$

where $X_{i(k)} = (x_{i(k)}, y_{i(k)})$ are the coordinates of the center of fiber $i(k)$. Finally, $\nu_f$ and $\nu_d$ are the macroscopic frequencies of the linking and unlinking processes, respectively.

## 6.3 Link between the model of section 2.1 and its numerical scheme

Coming back to the model of this paper, if we perform an explicit Euler scheme of (2.8)-(2.9) at discrete times $t^k = k\Delta t$, and splitting the random motion part, we can write for all $i \in [1, N]$:

$$X_i^{k+1/2} = X_i^k + \eta_1\sqrt{2d\Delta t}, \theta_i^{k+1/2} = \theta_i^k + \eta_2\sqrt{2d\Delta t}, \quad (6.9)$$

$$X_i^{k+1} = X_i^{k+1/2} - \mu\Delta t\nabla_{X_i}\Big(W_{tot} + W_{links}\Big)(X^{k+1/2}, \theta^{k+1/2}) \quad (6.10)$$

$$\theta_i^{k+1} = \theta_i^{k+1/2} - \lambda\Delta t\partial_{\theta_i}\Big(W_{tot} + W_{links}\Big)(X^{k+1/2}, \theta^{k+1/2}), \quad (6.11)$$

where $\eta_1$ and $\eta_2$ are random numbers chosen from a gaussian distribution and from a uniform one respectively. Note that the random motion has been here approximated by Gaussian noises on the fiber positions and orientations. From (2.2), it is clear that iterations (6.10)-(6.11) correspond to a gradient descent for a quadratic penalization of the minimization problem (6.2), with penalization factor $\kappa$. Then, as we will show in next section, the solutions of (6.2) at each time $t^n$ match the solutions of (6.10)-(6.11) for large $k$ if the penalization factor $\kappa$ is well chosen and if we consider fiber alignment and external potential only. Therefore, these two different formulations model the same dynamics at two different time scales. However, random fiber motion and reorientation as well as fiber linking/unlinking must be carrefully fitted if one wants to compare the two models. Indeed, each configuration at time $t^n$ of model I corresponds to a converged configuration of model II between two linking/unlinking events, or two significant fiber random motion and reorientation. The model parameters of model II ($\alpha$, $c_u$, $\kappa$, $d$, $\nu_f$, $\nu_d$) act at the same time scale whereas for model I, the time scale of $\nu_f, \nu_d$ and $d$ are much larger than the ones of $\alpha$, $c_u$.

In order to bound the maximal motion for fibers by $\delta_f$, we use the following CFL condition in the numerical simulations:

$$\Delta t = \frac{\delta_f}{\max(c_u, \kappa, \alpha L)}.$$

Finally, the fiber linking/unlinking process is treated as for model II (see 6.2).

## 6.4 Comparison of the microscopic models I and II

We consider a 2D square domain $[-S, S] \times [-S, S]$, with periodic boundary conditions at the top and bottom and Dirichlet boundary conditions for fiber positions and orientations at the right and left sides of the domain. Fibers are thus fixed at the left and right sides and have orientations $\theta_1$ and $\theta_2$, for chosen $(\theta_1, \theta_2) \in (-\frac{\pi}{2}, \frac{\pi}{2}]$. These conditions are modeled at the individual level as zones $\Gamma_L = [-S, -S + s_D] \times [-S, S]$ (left side of the domain) and $\Gamma_R = [S - s_D, S] \times [-S, S]$ (right side of the domain), where $s_D$ is the size of these zones. We refer to $\Gamma_D = \Gamma_L \cup \Gamma_R$ as the 'Dirichlet zone', for which the positions and orientations of the fibers in this zone are fixed. We initialize the system by randomly inserting $N$ fibers in the domain. We decompose the domain in the $x$ direction into $N_s + 1$ points distant of $s_D$, and fiber orientations are initially set to, for all $i \in [1, N]$:

$$\theta_i = \theta_1 + (\theta_2 - \theta_1)\frac{k_i}{N_s}, \tag{6.12}$$

where $k_i \in [0, N_s]$ is such that the interval $[-S + k_i s_D, -S + (k_i + 1)s_D]$ contains the $x$ coordinate of fiber $i$ center. Note that fibers of center in $\Gamma_R$ have orientation $\theta_2$, and fiber of center in $\Gamma_L$ have orientation $\theta_1$. Fig. 3.11 shows simulations at equilibrium for model I and II, without random noise ($d_X = d_\theta = 0$). The simulations are performed for $S = 0.6$ and for $N = 400$ fibers of length $L = 0.2$, initially linked to each of its intersecting neighbors. Figs. 3.11 (A) and (B) are performed without fiber linking/unlinking for models I and II respectively. For Figs. 3.11 (C) and (D), fiber linking/unlinking is activated with frequencies $\nu_f = \nu_d = 10$ for the two models. The rotation external potential is supposed to act on linked

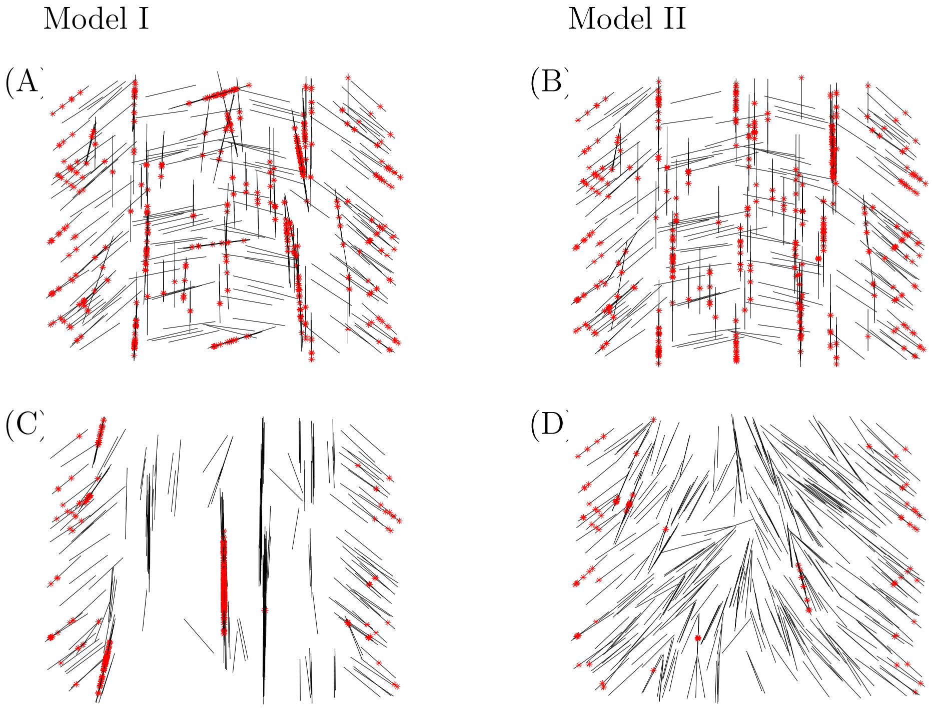

Figure 3.11: Model parameters $\alpha = 1$, $u = 1$. (A) Stationary solutions of model II for $\nu_f = \nu_d = 0$, $\Delta t = 0.1$. (B) Stationary solutions of model I for $\nu_f = \nu_d = 0$ and $\kappa = 10$, $\Delta t_2 = 0.01$. (C): Stationary solutions of model II for $\Delta t = 0.1$ and linking/unlinking $\nu_f = \nu_d = 10$. (D): stationary solutions of model I for $\Delta t_2 = 0.01$, $\kappa = 10$ and linking/unlinking $\nu_f = \nu_d = 10$, $\mu = \lambda = 1$

fibers only. As shown by Figs. 3.11 (A) and (B), the two models produce the same structures when no linking/unlinking is introduced and for a penalization parameter $\kappa = 10$ for model I. However, for the same linking/unlinking frequencies (Figs. 3.11 (C) and (D)), the two models produce very different structures. For this fiber linking/unlinking dynamics, model II creates localized and aligned fiber clusters while model I does not generate fiber clustering. This is due to the fact that fiber linking/unlinking does not act at the same scale for the two models. For model II, the fiber cross-links are necessarily maintained throughout motion (motion induced by the alignment force between cross-links and by the external potential), which gives to the system a memory of the cross-links. During fiber alignment and rotation, the pair of linked fibers remain attached and recruit neighboring fibers thanks to the linking process. For model I, fiber cross-links are modeled as forces between fibers. Therefore, there is a competition between rotation, alignment, and retraction potential between fibers of a linked pair. With this model, the attachment sites on linked fibers can be distant from each other during fiber motion.

At the time fibers are detached by the unlinking process, they are not necessarily crossed, preventing them to be reattached by the linking process.

To sum up, the two models show a good correspondence for fixed fiber links with no fiber linking/unlinking. This confirms that model I can be viewed as a gradient descent for a quadratic penalization of model II. However, when the same dynamical linking/unlinking is considered for both models, model II can generate fiber patterns which are not observed with model I. The major difference between both models is that alignment, rotation and retraction potential between fiber cross-links acts at the same time scale for model I, while the retraction is much larger in model II (because it is seen as a constraint). For the two models to be equivalent with dynamical fiber linking/unlinking, the frequencies of these processes must be fitted with the rotation and alignment potentials. Either smaller linking/unlinking frequencies for model I (compared to model I), either smaller rotation and alignment potential intensities for model II compared to model I lead to the same structures.

**Remark:** *The choice of model I as a starting point for the derivation of a macroscopic model was motivated by two reasons. First of all, a minimization algorithm is by nature a discrete method whereas we needed a continuous description of the motion for the derivation. Moreover, the macroscopic equation is obtained in the limit of large linking/unlinking frequencies. By construction, model II intrinsically have a memory of the links and is not suited to this scaling limit.*

# 7 Numerical algorithm for the particle dynamics

Here, we propose a numerical scheme for the scaled version of the IBM of section 2.1. The numerical scheme for model (2.8)-(2.9) can be found in appendix 6.3

**Scaling** Following Section 2.2, we set:

$$\tilde{X}_i = \sqrt{\varepsilon} X_i \; , \tilde{L}_i = L_i, \;\; \tilde{\theta}_i = \theta_i, \Delta\tilde{t} = \varepsilon \Delta t \; .$$

Inserting these expressions into Eq. (6.9), we obtain:

$$\tilde{X}_i^{k+1/2} = \tilde{X}_i^k + \eta_1 \sqrt{2d'\mu'\Delta\tilde{t}}, \;\; \tilde{\theta}_i^{k+1/2} = \tilde{\theta}_i^k + \eta_2 \sqrt{2\frac{d'}{\varepsilon}\Delta\tilde{t}}. \tag{7.1}$$

where $\eta_1$ and $\eta_2$ are random numbers chosen from Gaussian distributions and $d'$ is the macroscopic noise on fiber random motion and rotation. With the same treatment for the other terms (using Eqs. (2.18) together with Eqs. (6.10),(6.11)), fiber motion and rotation between time steps $\tilde{t}^k$ and $\tilde{t}^{k+1}$ are such that:

$$\tilde{X}_i^{k+1} = \tilde{X}_i^{k+1/2} - \mu'\Delta\tilde{t}\nabla_{\tilde{X}_i}\tilde{W}_{links}(\tilde{X}^{k+1/2}, \theta^{k+1/2})$$

$$\theta_i^{k+1} = \theta_i^{k+1/2} - \frac{\Delta\tilde{t}}{\varepsilon^2}\partial_{\theta_i}\Big(\varepsilon^2\tilde{W}_{ext} + \tilde{W}_{align} + \varepsilon\tilde{W}_{links}\Big)(\tilde{X}^{k+1/2}, \theta^{k+1/2}).$$

Note that the CFL condition becomes:

$$\Delta\tilde{t} = \frac{\varepsilon^2 \delta_f}{\max(c_u, \kappa, \alpha L)}.$$

The numerical scheme obtained is thus in agreement with the microscopic scaled equations (2.19)-(2.20).

For fiber linking/unlinking, we define $p_k^{\tilde{t}}$ the coefficients such that $p_k^{\tilde{t}} = 1$ if the pair of fibers $(i(k), j(k))$ are linked at time $\tilde{t}$, $p_k^{\tilde{t}} = 0$ otherwise. The time evolution of this coefficient between $\tilde{t}$ and $\tilde{t} + \Delta\tilde{t}$ reads, using the fact that $\nu_f' = \varepsilon^2 \nu_f$, $\nu_d' = \varepsilon^2 \nu_d$:

$$\begin{aligned}
\mathbb{P}(p_k^{\tilde{t}+\Delta\tilde{t}} = 1 \mid p_k^{\tilde{t}} = 0) =& 1 - e^{-\frac{\nu_f'}{\varepsilon^2}\Delta\tilde{t}} && \text{if } \max(\ell_{i(k),j(k)}, \ell_{j(k),i(k)}) \leq \frac{L}{2} \\
=& 0 && \text{otherwise} \\
\mathbb{P}(p_k^{\tilde{t}+\Delta\tilde{t}} = 0 \mid p_k^{\tilde{t}} = 1) =& 1 - e^{-\frac{\nu_d'}{\varepsilon^2}\Delta\tilde{t}}
\end{aligned}$$

where $\nu_f$ and $\nu_d$ are the macroscopic frequencies of the linking and unlinking processes, respectively.

## 7.1 Initialization and model parameters

**Model parameters** The previous scaling obliges us to work on larger domains as $\varepsilon$ becomes smaller. For convenience, we rather want to perform the simulations with fixing the space domain $\Omega$, i.e making it independent of $\varepsilon$. Note that this amounts to consider that the space scale is such that $\tilde{\tilde{x}}_0 = x_0$ instead of $\tilde{x}_0 = \varepsilon^{-1/2} x_0$ as before. All the variables with a space dimension are thus adapted in this new scaling such that (using (2.14)):

$$\tilde{\tilde{\lambda}} = \frac{\lambda}{\varepsilon} = \frac{1}{\varepsilon}\ , \quad \tilde{\tilde{L}} = \sqrt{\varepsilon} L\ , \quad \tilde{\tilde{d}} = \varepsilon d\ , \quad \tilde{\tilde{\alpha}} = \varepsilon \alpha\ ,$$

and the other ones remain unchanged. In this new set of variables, equations for fiber motion and rotation read:

$$\tilde{X}_i^{k+1/2} = \tilde{X}_i^k + \eta_1 \sqrt{2\tilde{\tilde{d}}\varepsilon\mu'\Delta\tilde{t}}, \quad \tilde{\theta}_i^{k+1/2} = \tilde{\theta}_i^k + \eta_2 \sqrt{2\frac{\tilde{\tilde{d}}}{\varepsilon}\Delta\tilde{t}}. \tag{7.2}$$

and

$$\begin{aligned}
X_i^{k+1} &= X_i^{k+1/2} - \mu'\varepsilon\Delta\tilde{t}\nabla_{X_i}\tilde{\tilde{W}}_{links}(X^{k+1/2}, \theta^{k+1/2}) \\
\theta_i^{k+1} &= \theta_i^{k+1/2} - \frac{\Delta\tilde{t}}{\varepsilon^2}\partial_{\theta_i}\Big(\varepsilon^2\tilde{\tilde{W}}_{ext} + \tilde{\tilde{W}}_{align} + \varepsilon\tilde{\tilde{W}}_{links}\Big)(X^{k+1/2}, \theta^{k+1/2}).
\end{aligned}$$

Note that fiber rotation remains unchanged while fiber motion acts at lower order $O(\varepsilon)$. This is expected results since in this new scaling, fibers smaller than before are considered. Finally, in order to control the amplitude of fiber random motion, the parameter $\mu$ is chosen such that $d\mu$ is a constant $d_X$. To this aim, for each value of the noise $d$, we set:

$$\mu = \frac{d_X}{d}.$$

**Initialization** We consider a 2D square domain with periodic boundary conditions at the top and bottom and Dirichlet boundary conditions $\theta_1$ and $\theta_2$ at the right and left sides of the domain, for chosen $(\theta_1, \theta_2) \in (-\frac{\pi}{2}, \frac{\pi}{2}]$. These conditions are modeled at the individual level as zones $\Gamma_L = [-S, -S+s_D] \times [-S, S]$ (left side of the domain) and $\Gamma_R = [S - s_D, S] \times [-S, S]$ (right side of the domain), where $s_D$ is the size of these zones. We refer to $\Gamma_D = \Gamma_L \cup \Gamma_R$ as the 'Dirichlet zone', for which the positions and orientations of the fibers in this zone are fixed. We initialize the system by randomly inserting $N$ fibers in the domain. We decompose the domain in the $x$ direction into $N_s + 1$ points $s_D$ apart, and fiber orientations are initially set to, for all $i \in [1, N]$:

$$\theta_i = \theta_1 + (\theta_2 - \theta_1)\frac{k_i}{N_s}, \tag{7.3}$$

where $k_i \in [0, N_s]$ is such that the interval $[-S + k_i s_D, -S + (k_i + 1)s_D]$ contains the $x$ coordinate of fiber $i$ center. Note that fibers of center in $\Gamma_R$ have orientation $\theta_2$, and fiber of center in $\Gamma_L$ have orientation $\theta_1$.

# 8 Numerical scheme for the macroscopic model

## 8.1 Coefficients of the macroscopic model

Here, we give the details of the coefficients $\alpha_1, \alpha_2, \alpha_3, \alpha_4, \alpha_5$ of Eq. (3.30) (see [2] and restoring the $\mu$):

$$\begin{aligned}
\alpha_1 &= 1 - \frac{1}{Z^2} \\
\alpha_2 &= \frac{d}{\alpha_1}(\mu\alpha_1 + \frac{\xi\alpha L^4\gamma c(r)}{24}) \\
\alpha_3 &= \frac{\xi\alpha L^4\gamma}{24\alpha_1}(\frac{1}{4Z^2} - 1 + \frac{6dc(r)}{\xi\alpha L^2\gamma}) \\
\alpha_5 &= \frac{1}{\alpha_1},
\end{aligned} \tag{8.1}$$

where we recall that $\alpha$ is the intensity of the alignment potential between cross-linked fibers, $d$ the noise intensity, $\xi$ the ratio between the numebr of fiber links and the total number of fibers, $L$ the fiber length, $r$ the order parameter and:

$$Z = \int_{-\frac{\pi}{2}}^{\frac{\pi}{2}} e^{r\cos 2\theta} \frac{d\theta}{\pi}.$$

Next section is devoted to the numerical method used for numerically computing the solutions of the macroscopic model written in a semi conservative form given by Eq. (3.43).

## 8.2 Numerical method

First, the square space domain $\Omega$ is discretized into $N_x$ (resp $N_y$) points in $x$ (resp $y$) direction, such that $x_j = -S + j\Delta x$, $y_i = -S + (i-1)\Delta y$ for all $(j,i) \in [1, N_x] \times [1, N_y]$. We refer to the discretized domain as $\Omega^N = \{(x_j, y_i), (i,j) = [1, N_x] \times [1, N_y]\}$. Eq. (3.43) is discretized with simple centered finite differences. For this purpose, we define $\Theta$ as the $N_xN_y$ vector such that $\Theta_k = \theta(x_j, y_i)$, where $k = j + (i-1)N_x, k \in [1, N_xN_y]$. Note that $\theta(x_{j+1}, y_i) = \Theta_{k+1}$, $\theta(x_j, y_{i+1}) = \theta_{k+N_x}$. We use trapezoidal method for computing the values of the integrals contained in the terms $Z$ and $c(r)$ of the coefficients $\alpha_1, \alpha_2$ and $\alpha_3$. For this purpose, $[0, 2\pi]$ is discretized into $N' + 1$ points $\xi_i = (i-1)\frac{2\pi}{N'}$ and the integral of a function $f(\theta)$ is approximated by:

$$\int_{[0,2\pi]} f(\theta)\frac{d\theta}{2\pi} = \sum_{i=1}^{N'} \frac{(\xi_{i+1} - \xi_i)(f(\xi_i) + f(\xi_{i+1}))}{4\pi}.$$

By the use of centered finite differences of order 2, Eq. (3.43) can be written

$$F(\Theta) = \mathcal{O}(\Delta x^2 + \Delta y^2 + \Delta x \Delta y), \tag{8.2}$$

where $F$ is a $N_x N_y$ vector such that for all $k \in [1, N_x] \times [1, N_y]$

$$F_k(\Theta) = \alpha_2 (D^k_{xx}\Theta + D^k_{yy}\Theta) - \frac{\alpha_3}{2}\Big(D^k_{xx}\mathcal{S} - D^k_{yy}\mathcal{S} - 2D^k_{xy}\mathcal{C}\Big) - h(\Theta_k).$$

Here, $\mathcal{S}, \mathcal{C}$ are $N_x N_y$ vectors such that $\mathcal{S}_k = \sin 2\Theta_k, \mathcal{C}_k = \cos 2\Theta_k$ for all $k$ and $D^k_{xx}\Theta, D^k_{yy}\Theta$ and $D^k_{xy}\Theta$ (resp. $D^k_{xx}\mathcal{S}, D^k_{yy}\mathcal{S}$ and $D^k_{xy}\mathcal{S}$ and similarly for $\mathcal{C}$) are the approximations of the second order derivatives of $\theta$ (resp. $\sin 2\theta$ and $\cos 2\theta$) evaluated at point $(x_i, y_j)$ ($k = j + (i-1)N_x$). For a given vector $G \in \mathbb{R}^{N_x N_y}$:

$$D^k_{xx}G = \frac{G^R_k - 2G_k + G^L_k}{\Delta x^2}, D^k_{yy}G = \frac{G^T_k - 2G_k + G^B_k}{\Delta y^2} D^k_{xy}G = \frac{G^{RT}_k - G^{RB}_k - G^{LT}_k + G^{LB}_k}{4\Delta x \Delta y}$$

where $G^R_k, G^L_k, G^T_k, G^B_k$ are the values of vector $G$ on the right (R), left (L), top (T) and bottom (B) numerical grid points of point $k$ respectively (same principle for RT,RB,LT and LB). We recall that each $k$ is associated to a unique $(i, j)$ such that $k = j + (i-1)N_x$. The left side of the domain corresponds to $j = N_x$, the right side to $j = 1$, the top to $i = N_y$ and the bottom to $i = 1$. For implementing Dirichlet boundary conditions on the right side for instance, we consider that the left neighbor $G_{k+1}$ of $G_k$ is such that $G_{k+1} = G_2$ for the $k$ such that $j = N_x$ (for instance $\Theta_{k+1} = \theta_2$ if $G$ is the fiber orientation). For periodic boundary conditions, we simply connect the top and bottom of the domain. If $k$ is such that $i = N_y$ (top), then $G_{k+N_x}$ (top neighbor) becomes $G_{k-N_x(N_y-2)}$, its symmetric point (regarding $y$ direction) located at the bottom of the domain. Altogether,

$G_k^R, G_k^L, G_k^T, G_k^B$ are computed thanks to:

$$
\begin{aligned}
G_k^R = & G_{k+1} && (1 \leq j \leq N_x - 1), (1 \leq i \leq N_y) \\
& G_2 && j = N_x, (1 \leq i \leq N_y) \\
G_k^L = & G_{k-1} && (2 \leq j \leq N_x), (1 \leq i \leq N_y) \\
& G_1 && j = 1, (1 \leq i \leq N_y) \\
G_k^T = & G_{k+N_x} && (1 \leq i \leq N_y - 1), (1 \leq j \leq N_x) \\
& G_{k-Nx(Ny-2)} && i = N_y, (1 \leq j \leq N_x) \\
G_k^B = & G_{k-N_x} && (2 \leq i \leq N_y), (1 \leq j \leq N_x) \\
& G_{k+Nx(Ny-2)} && i = 1, (1 \leq j \leq N_x) \\
G_k^{RT} = & G_{k+N_x+1} && (1 \leq i \leq N_y - 1), (1 \leq j \leq N_x - 1) \\
& G_2 && j = N_x, (1 \leq i \leq N_y) \\
& G_{k-Nx(Ny-2)+1} && i = N_y, (1 \leq j \leq N_x - 1) \\
G_k^{LT} = & G_{k+N_x-1} && (1 \leq i \leq N_y - 1), (2 \leq j \leq N_x) \\
& G_{k-Nx(Ny-2)+1} && i = N_y, (1 \leq j \leq N_x - 1) \\
& G_1 && j = 1, (1 \leq i \leq N_y) \\
G_k^{RB} = & G_{k-N_x+1} && (2 \leq i \leq N_y), (1 \leq j \leq N_x - 1) \\
& G_2 && j = N_x, (1 \leq i \leq N_y) \\
& G_{k+Nx(Ny-2)+1} && i = 1, (1 \leq j \leq N_x - 1) \\
G_k^{LB} = & G_{k-N_x-1} && (2 \leq i \leq N_y), (2 \leq j \leq N_x) \\
& G_1 && j = 1, (1 \leq i \leq N_y) \\
& G_{k+Nx(Ny-2)-1} && i = 1, (1 \leq j \leq N_x - 1),
\end{aligned}
$$

for $G_1$ and $G_2$ given by the Dirichlet boundary conditions as previously explained. We now aim to apply a Newton algorithm to Eq. (8.2). For this purpose, we compute the $N_x N_y \times N_x N_y$ jacobian matrix $F'$ of function $F : \Omega^N \to \Omega^N$. Given an initial configuration $\theta^0$, the solution $\theta$ of Eq. (8.2) corresponds to the convergence in $k$ of the sequence:

$$F'(\theta^k)(\theta^{k+1} - \theta^k) = -F(\theta^k). \tag{8.3}$$

The jacobian $F'(\Theta)$ of $F(\Theta)$ is such that $F'_{kl}(\Theta) = \frac{\partial F_k(\Theta)}{\partial \Theta_l}$ for all $(k,l) \in [1, N_x N_y]^2$ and reads:

$$
\begin{aligned}
F'_{k,k} &= -\alpha_2(\frac{2}{\Delta x^2} + \frac{2}{\Delta y^2}) - \alpha_3(-\frac{2\mathcal{C}_k}{\Delta x^2} + \frac{2\mathcal{C}_k}{\Delta y^2}) - h'(\Theta_k) && (1 \leq j \leq N_x), (1 \leq i \leq N_y) \\
F'_{k,k+1} &= \alpha_2 \frac{1}{\Delta x^2} - \alpha_3 \frac{\mathcal{C}_{k+1}}{\Delta x^2} && (1 \leq j \leq N_x - 1), (1 \leq i \leq N_y) \\
F'_{k,k-1} &= \alpha_2 \frac{1}{\Delta x^2} - \alpha_3 \frac{\mathcal{C}_{k-1}}{\Delta x^2} && (2 \leq j \leq N_x), (1 \leq i \leq N_y) \\
F'_{k,k+N_x} &= \alpha_2 \frac{1}{\Delta y^2} + \alpha_3 \frac{\mathcal{C}_{k+N_x}}{\Delta y^2} && (1 \leq j \leq N_x - 1), (1 \leq i \leq N_y - 1) \\
F'_{k,k-N_x} &= \alpha_2 \frac{1}{\Delta y^2} + \alpha_3 \frac{\mathcal{C}_{k-N_x}}{\Delta y^2} && (1 \leq j \leq N_x - 1), (2 \leq i \leq N_y) \\
F'_{k,k-Nx(Ny-2)} &= \alpha_2 \frac{1}{\Delta y^2} + \alpha_3 \frac{\mathcal{C}_{k-Nx(Ny-2)}}{\Delta y^2} && (1 \leq j \leq N_x - 1), i = N_y \\
F'_{k,k+Nx(Ny-2)} &= \alpha_2 \frac{1}{\Delta y^2} + \alpha_3 \frac{\mathcal{C}_{k+Nx(Ny-2)}}{\Delta y^2} && (1 \leq j \leq N_x - 1), i = 1 \\
F'_{k,k+N_x+1} &= -\alpha_3 \frac{\mathcal{S}_{k+N_x+1}}{2\Delta x \Delta y} && (1 \leq j \leq N_x - 1), (1 \leq i \leq N_y - 1) \\
F'_{k,k-Nx(Ny-2)+1} &= -\alpha_3 \frac{\mathcal{S}_{k-Nx(Ny-2)+1}}{2\Delta x \Delta y} && (1 \leq j \leq N_x - 1), i = N_y \\
F'_{k,k-N_x-1} &= -\alpha_3 \frac{\mathcal{S}_{k-N_x-1}}{2\Delta x \Delta y} && (2 \leq j \leq N_x), (2 \leq i \leq N_y) \\
F'_{k,k+Nx(Ny-2)-1} &= -\alpha_3 \frac{\mathcal{S}_{k+Nx(Ny-2)-1}}{2\Delta x \Delta y} && (2 \leq j \leq N_x), i = 1 \\
F'_{k,k-N_x+1} &= \alpha_3 \frac{\mathcal{S}_{k-N_x+1}}{2\Delta x \Delta y} && (1 \leq j \leq N_x - 1), (2 \leq i \leq N_y) \\
F'_{k,k+Nx(Ny-2)+1} &= \alpha_3 \frac{\mathcal{S}_{k+Nx(Ny-2)+1}}{2\Delta x \Delta y} && (1 \leq j \leq N_x - 1), i = 1 \\
F'_{k,k+N_x-1} &= \alpha_3 \frac{\mathcal{S}_{k+N_x-1}}{2\Delta x \Delta y} && (2 \leq j \leq N_x), (1 \leq i \leq N_y - 1) \\
F'_{k,k-Nx(Ny-2)-1} &= \alpha_3 \frac{\mathcal{S}_{k-Nx(Ny-2)+1}}{2\Delta x \Delta y} && (2 \leq j \leq N_x), i = N_y
\end{aligned}
$$

## 8.3 Continuation method

As Newton's method strongly depends on the initial conditions, we proceed by continuation. For this purpose, we introduce a numerical parameter $\tau$ into the boundary conditions as well as in front of the external potential $h$ and apply the previous algorithm on the following set of sub-problems:

$$F_{\tau,k}(\Theta) = \alpha_2(D^k_{\tau,xx}\Theta + D^k_{\tau,yy}\Theta) - \frac{\alpha_3}{2}\Big(D^k_{\tau,xx}\mathcal{S} - D^k_{\tau,yy}\mathcal{S} - 2D^k_{\tau,xy}\mathcal{C}\Big) - \tau h(\Theta_k),$$

for boundary conditions:

$$\begin{aligned} \theta &= \theta_1 \quad \text{on } \Gamma_L \\ \theta &= \tau\theta_2 \quad \text{on } \Gamma_R. \end{aligned}$$

Note that $\Theta = \theta_1$ is solution to these sub-problems for $\tau = 0$, and that we recover the full system for $\tau = 1$. We then discretize the interval $[0, 1]$ into $P$ points. Given the initial configuration for $\tau = 0$, the final solution $\theta$ of the full system is given by the $P$ iteration of the sequences $\theta_{\tau_p}$ such that each $\theta_{\tau_p}$ is the converged solution of Eq. (8.3) for initial configuration $\theta_{\tau_{p-1}}$.

# 9 Order Parameter

In this section, we study how the order parameter depends on the size $s_D$ of the numerical boxes used to average the orientations of the fibers. Fig. 3.12 (A) shows the values of $r$ as function of $s_D$ averaged over 20 simulations for $c_u = 0$ and for two different points of the domain: around $x = 0$ (black curve) and around $x = 0.2$ (green curve). Figs. 3.12 (B) and (C) show the values (averaged over 20 simulations) of the mean orientation $\theta_0$ and density $\rho$ as function of $x$. For each, we used $s_D = 0.02$ (black curve) and $s_D = 0.05$.

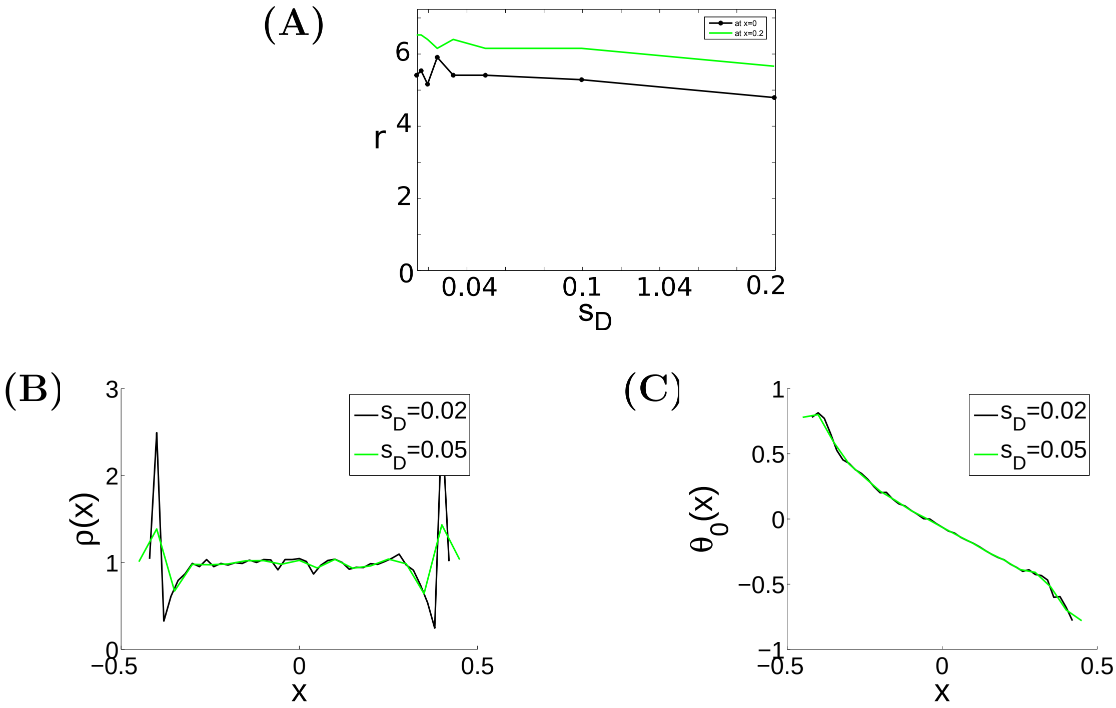

Figure 3.12: Parameter $r$ for $x = 0$ (black curve) and $x = 0.2$ (green curve), averaged over 20 numerical simulations and plotted as function of $s_D$. Numerical parameters for the simulations: $N = 1500$, $\theta_1 = -\theta_2 = \frac{\pi}{4}$, $\varepsilon = 0.1$, $\alpha = 0.1$, $c_u = 0$, $d_\theta = 5e - 5$

Fig. 3.12 (A) shows that for $c_u = 0$ the parameter $r$ which corresponds to the distribution of fiber orientations is almost constant as function of the size $s_D$. We choose $s_D = 0.05$ for the rest of the simulations. Figs. 3.12 (B) and (C) reveal that the mean orientation (B) and fiber density (C) for $c_u = 0$ do not depend upon the size of the numerical boxes used to compute their value. With no external potential, the microscopic distribution of fibers varies linearly from $\theta_0(-S) = \theta_1$ to $\theta_0(S) = \theta_2$ as expected. The fiber density is homogeneous and equal to 1, except close to the Dirichlet zone where the fibers accumulate. This is due to the way of implementing the Dirichlet conditions at the individual level, but this effect is neglected here.

# Chapter 4

# Large-scale dynamics of short-range repulsion and cell division

This chapter is a work in collaboration with S. Motsch

---

**Abstract** Non overlapping constraints arise naturally in the study of incompressible fluids and in biological/social systems. It consists in considering that the density of individuals cannot exceed a maximal density threshold corresponding to jamming. In this work, we explore the effects of density congestion at the macroscopic level. At the individual scale, the particles are modeled as 2D spheres which move in order to be in non-overlapping configuration. We derive a macroscopic model starting from the mean-field description of the particle model, and show that it leads to a porous media equation. The solutions of the macroscopic equation show different features compared to its underlying agent-based model, and this is due to the fact that Dirac masses are unstable for the macroscopic model. We propose a modified version of the macroscopic equation and numerically validate the new formulation by comparison with the particle model.

## Sommaire

1 **Introduction** . . . . . . . . . . . . . . . . . . . . . . . . . . **200**
2 **Short range repulsion: I** . . . . . . . . . . . . . . . . . . . . **201**
3 **Short range repulsion: II** . . . . . . . . . . . . . . . . . . . . **208**
4 **Repulsion and cell division** . . . . . . . . . . . . . . . . . . **213**
5 **Conclusion** . . . . . . . . . . . . . . . . . . . . . . . . . . **213**
6 **Appendix A** . . . . . . . . . . . . . . . . . . . . . . . . . . **220**
7 **Appendix B** . . . . . . . . . . . . . . . . . . . . . . . . . . **221**

# 1 Introduction

One of the main difficulties in the modeling of complex systems such as fish schooling or tumor growth is the lack of fundamental laws. However, there is always one rule that agents have to satisfy: two agents cannot occupy the same space at the same time. Despite the simplicity of the rule, this constraint has several intriguing effects (non-convex problems). The goal of this work is to explore how this constraint manifests itself at large-scales both analytically and numerically using a generic model of short-range repulsion as a starting point.

In the literature, the problem of non-overlapping is ubiquitous in the modeling of collective behavior. When pedestrians are crossing [26, 35, 33] or when birds flock together [4], avoidance of neighbors is always necessary. Usually, this rule is modeled by a repulsion interaction [1, 41, 18]. At the macroscopic scale, the density constraint is a key factor and is responsible for instance in the formation of car traffic jam [7, 8, 6]. The effect of congestion leads to numerous challenging mathematical models such as non-linear diffusion [14, 15] and two-phase flows [9, 21]. More generally density constraints have been studied for fluid models in [5, 19, 28, 10, 37, 22, 20]. Incompressibility constraints have also been analyzed using optimal transport theory [32]. Finally, the derivation of macroscopic equations from microscopic dynamics have been extensively studied in the case of repulsion interaction [13, 34, 36, 27] and in case of volume exclusion [11, 12].

In the understanding of cancer development, mathematical modeling now complements experimental and clinical studies. Models for tumor growth present several levels of complexity, at the biomedical level as well as at the mathematical level [23]. The simplest models contain competition for space using fluid mechanical concepts [30], and become more complex when studying the role of nutrient supplies. When coupling growth and diffusion, one common dynamics used is the so-called KKP equations [25, 42]. The density constraint is 'implicit' in a source term as cells die if a threshold is reached. However, a drawback of this approach is that dead cells should not 'vanish'. In practical case, the so-called Swanson's model is used without density threshold and therefore the density keeps increasing. Other models have been proposed in which growth is limited by the competition for space [39, 38, 40]. In this approach, tumor growth with nutrients is modeled through a Hele-Shaw model which lead to traveling wave solutions. If microscopic models for tumor growth were proposed in [29, 20], the majority of models of interest are macroscopic ones and describe the evolution of the density of particles. In this paper, we want to link as rigorously as possible the macroscopic dynamics to the microscopic one.

The focus of this paper is to explore the effects of density constraint in a simple model of tumor growth. Starting from an agent-based model with short-range repulsion, we are interested in the large scale behavior of the dynamics using partial differential equations. In a first attempt, we derive a macroscopic model using the weak equation satisfied by the so-called empirical distribution. We observe that micro- and macro- dynamics have drastically different behaviors: the microscopic solutions converge to a stationary state, whereas the macroscopic solutions keep spreading in space. Here, as we are interesting in the long time behavior, there is no guarantee that both micro- and macro- dynamics remain close, even if the number of particles $N$ is large. Moreover, for short range repulsion, Dirac masses are not stable [3] which also explains why the macroscopic dynamics diverges from the particle simulations.

The difficulty comes from the 'local' range of interaction: repulsion should only apply when particles are 'close enough'. But this notion of *closeness* is lost when looking at the density distribution $\rho(x)$. For this reason, we modify in a second step the dynamics at the macroscopic level to *de-activate* repulsion at low-density. Such modifications allows to retrieve the same dynamics as observed in the microscopic description.

Finally, we combine short-range repulsion and 'growth' to deduce new types of solutions. In this dynamics, the solution first increases on his support until it reaches a density threshold, then the solution starts to spread. But in contrast to the Swanson's model, the spread actually propagates exponentially fast in time.

# 2 Short range repulsion: I

## 2.1 Agent-based models

In this section, we introduce a dynamics of short range repulsion of $N$ particles $\{x_i\}_o$ moving in $\mathbb{R}^2$. All the particles have the same size $R > 0$ and their evolution is governed by the following system of equations:

$$\dot{x}_i = -\sum_{j=1, j\neq i}^{N} \phi_{ij}(x_j - x_i), \qquad \text{with} \quad \phi_{ij} = \phi\left(\left|\frac{x_j - x_i}{2R}\right|^2\right). \tag{2.1}$$

where $\phi \geq 0$ is the interaction function. As we intend to model short-range repulsion, $\phi$ is defined such that:

$$\phi(s) = \begin{cases} |1 - s^{\alpha}| & \text{, if } 0 < s \leq 1 \\ 0 & \text{, otherwise.} \end{cases} \tag{2.2}$$

Of particular interest will be the two cases: $\alpha = 1$ and $\alpha = -1$. Repulsion is only active when two particles are at a distance smaller than $2R$ from each other.

There is an energy associated with this dynamics, namely:

$$\mathcal{E}(\{x_i\}) = -\frac{1}{2}\sum_{i\neq j} \Phi\left(\left|\frac{x_j - x_i}{2R}\right|^2\right), \tag{2.3}$$

with $\Phi$ an anti-derivative of $\phi$. The functional $\mathcal{E}$ is decaying along the solutions $\{x_i(t)\}_i$ of (2.1). More precisely, using that $\dot{x}_i = -\frac{1}{4R^2}\nabla_{x_i}\mathcal{E}$, we find:

$$\frac{\mathrm{d}}{\mathrm{d}t}\mathcal{E}(\{x_i(t)\}) = \sum_i \nabla_{x_i}\mathcal{E} \cdot \dot{x}_i = -\frac{1}{4R^2}\sum_i |\dot{x}_i|^2 \quad \leq \quad 0.$$

This property is used to build an adapted numerical scheme (see appendix), the time step $\Delta t$ is chosen such that the energy is always decaying numerically.

As in an illustration of the dynamics, we propose in figure 4.13 four snapshots of a simulation run with $N = 100$ particles. We observe that the dynamics converges to a stationary state with a 'hexagonal lattice' structure. Each particle is separated from the others by a distance of at least $2R$. In other words, the stationary state belongs to the set:

$$\mathcal{C} = \Big\{\{x_i\}_i \ : \ |x_i - x_j| \geq 2R\Big\}.$$

Thus, the evolution equation (2.1) can be seen as a penalizing method to enforce a non-overlapping constraint $|x_i - x_j| \geq 2R$ for all $i, j$. We notice that a direct implementation of such non-overlapping constraint would be challenging since the set $\mathcal{C}$ is non-convex [31, 33].

We can even estimate the radius $L$ of the disc surrounding the whole structure of particles, is we suppose that they are in a configuration of optimal arrangement. Indeed in 2D, the highest density among all the possible packing arrangements for circles of constant radius is $\pi/2\sqrt{3}$. This result, due to the works of Gauss [24], corresponds to an hexagonal lattice. Thus, in this simulation, the radius can be computed with:

$$L = \sqrt{N \cdot \frac{2\sqrt{3}}{\pi}} \cdot R \approx 2.1$$

since we use $N = 100$ particles with radius $R = .2$ space units.

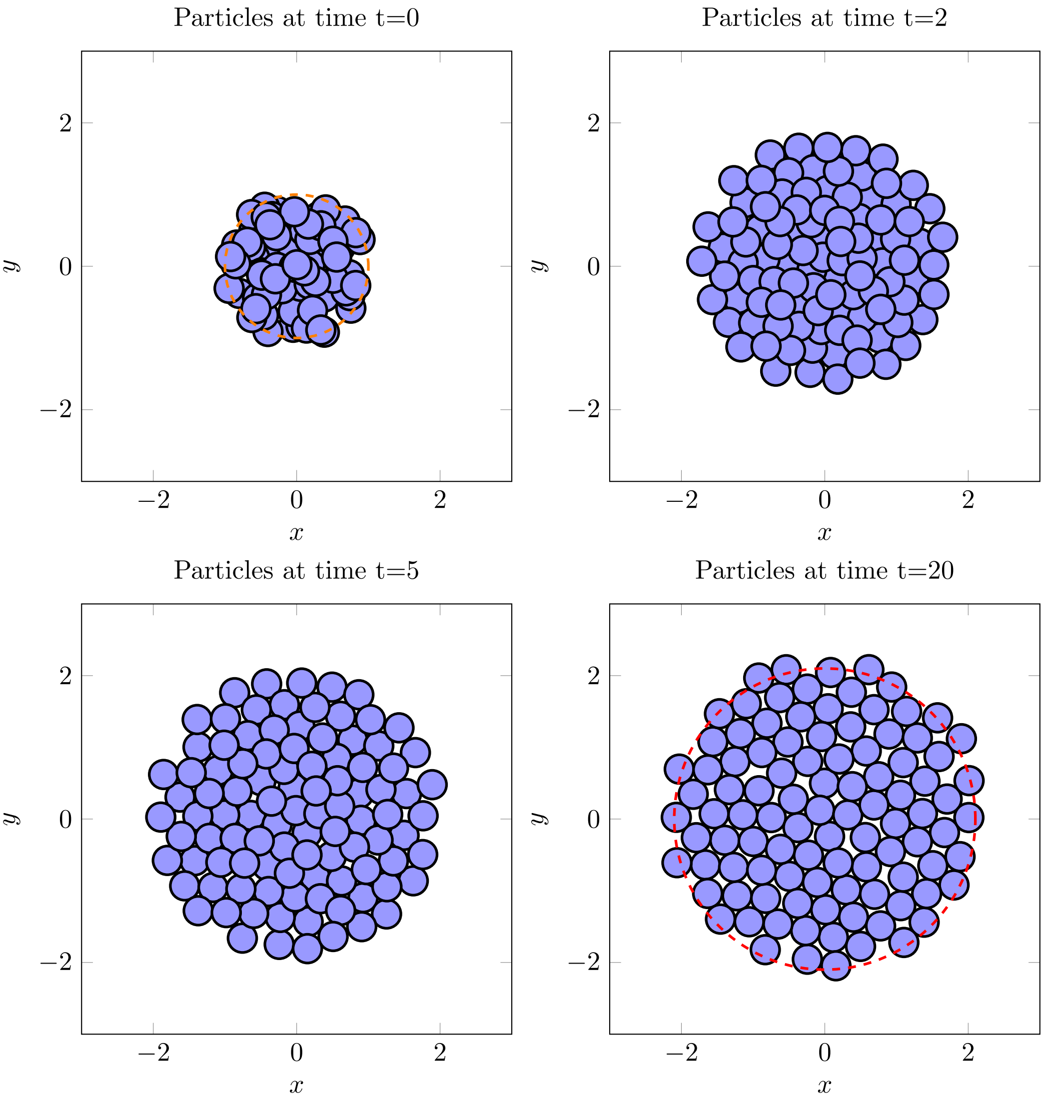

Figure 4.13: Evolution of the positions of the particles following the dynamics (2.1). Initially (top-left), the cells are distributed in the unit circle (draw in orange) . Then, the cells spread over time ($t = 2, 5$ time units) until reaching an equilibrium at $t = 20$ time units (bottom-right). We draw in red the diameter circle predicted by the maximum packing number of circles.. Parameters: $N = 100$ cells, radius $R = .2$, $\alpha = -1$, $\Delta t = 10^{-1}$.

## 2.2 Macroscopic dynamics

We would like to analyze the *microscopic* dynamics (2.1) from a macroscopic point of view. With this aim, we introduce the so-called empirical distribution:

$$\rho(x,t) = \sum_i \delta(x - x_i(t)), \tag{2.4}$$

where $\{x_i(t)\}_i$ are solution of the dynamical system (2.1). To find the equation satisfied by the empirical distribution $\rho$, we integrate $\rho$ against a test function $\varphi$ and take the time derivative. One deduces that $\rho$ satisfies (weakly) the following PDE:

$$\partial_t \rho + \nabla_x \cdot (G[\rho]\rho) = 0, \tag{2.5}$$

with

$$G[\rho](x) = -\int_{y\in\mathbb{R}^2} \phi\left(\left|\frac{x-y}{2R}\right|^2\right)(y-x)\rho(y)\,\mathrm{d}y. \tag{2.6}$$

We refer to equations (2.5)(2.6) as the *macroscopic* dynamics associated with the *microscopic* dynamics (2.1).

Similar to the microscopic dynamics, there is an energy associated with this dynamics:

$$\mathcal{E}(\rho) = -\frac{1}{2}\int_{x,y\in\mathbb{R}^2} \Phi\left(\left|\frac{x-y}{2R}\right|^2\right)\rho(x)\rho(y)\,\mathrm{d}x\mathrm{d}y, \tag{2.7}$$

where $\Phi$ is an antiderivative of $\phi$. The energy satisfies:

$$\frac{\mathrm{d}}{\mathrm{d}t}\mathcal{E}(\rho) = -\frac{1}{2R^2}\int_{x\in\mathbb{R}^2} \Big(G[\rho](x)\Big)^2 \rho(x)\,\mathrm{d}x \quad \leq \quad 0.$$

**Remark 2.1.** *We do not normalize the empirical distribution* (2.4) *by* $1/N$ *in order to keep the information of the number of particles. The total mass is essential at the particle level to determine the size of the support of the stationary state. If one would like to study the asymptotic limit* $N \to \infty$*, one would have to normalize by* $N$ *and investigate a limit* $R \to 0$*.*

As an illustration of the macroscopic dynamics, we perform a numerical simulation in a similar situation as the microscopic dynamics. We initiate the density $\rho_0$ with 100 particles distributed in the unit circle:

$$\rho_0(x) = \begin{cases} \frac{100}{\pi} & \text{if } |x| \leq 1 \\ 0 & \text{if } |x| > 1 \end{cases} \tag{2.8}$$

We plot in figure 4.14 the density $\rho(x,t)$ at $t = 1$ and $t = 5$ time units. We observe that the distribution is spreading and does not seem to converge to a stationary

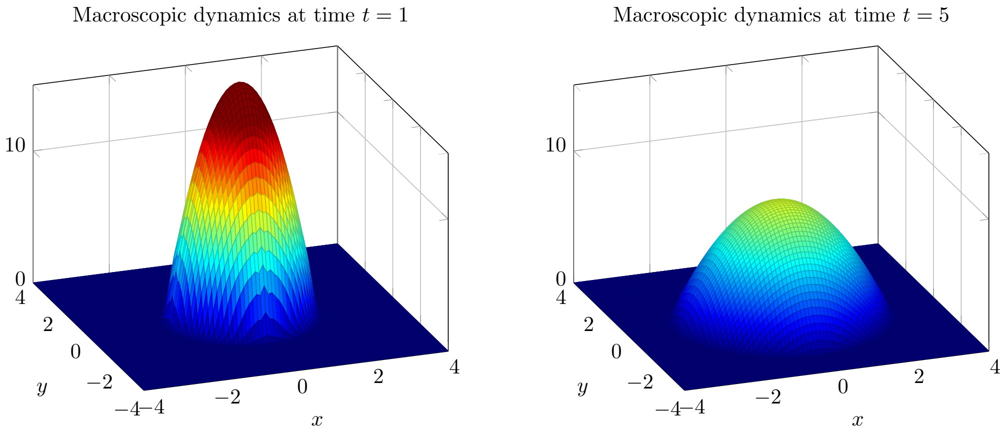

Figure 4.14: The solution $\rho(x,t)$ of the macroscopic dynamics (2.5)(2.6) with initial condition (4) at $t = 1$ and $t = 5$ unit times. The density keeps spreading in space. Parameters: $\Delta x = \Delta y = 10^{-1}$, $\Delta t = 2.5 \cdot 10^{-2}$. Total density is 100 with $R = .2$, CFL $= .75$.

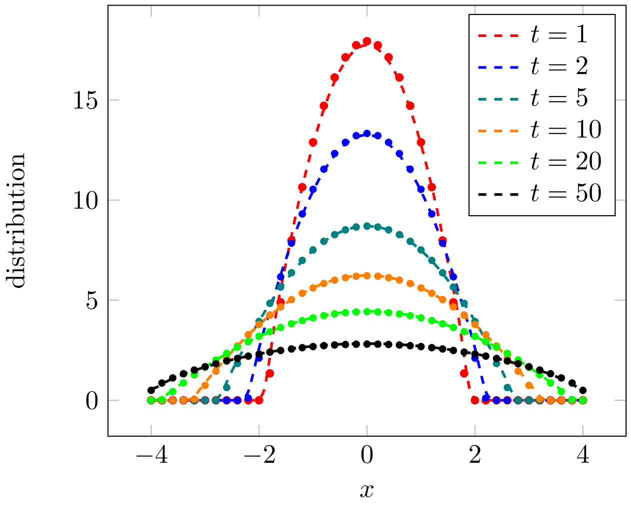

Figure 4.15: Solutions of the macroscopic dynamics on the line $(x, 0)$: solving the convolution equation (2.5)(2.6) (dashed line) and solving the porous media equation (2.9) (dotted). Both simulations are in perfect agreement with small discrepancy at the boundary of the support of $\rho(x,t)$. Parameters of the simulations: $R = .2$, total density $\int_x \rho_0(x)\,\mathrm{d}x = 100$, $\Delta x = \Delta y = 10^{-1}$. Due to CFL condition, we use $\Delta t = 2.5 \cdot 10^{-2}$ to solve (2.5)(2.6) (dashed line) and $\Delta t = 2 \cdot 10^{-3}$ to solve (2.9) (dotted).

state as the microscopic dynamics (fig. 4.13). A more detailed comparison will be performed later on.

As the radius of the particle $R$ is expected to be small compared to the spatial length of the dynamics, we would like to investigate the asymptotic behavior of the macroscopic dynamics (2.5)(2.6) as $R$ tends to zero. Formally, we have:

$$\begin{aligned} G[\rho](x) &= -(2R)^3 \int_{z\in\mathbb{R}^2} \phi(|z|^2) z \rho(x+2Rz)\,\mathrm{d}z \\ &= -(2R)^4 \left(\int_{z\in\mathbb{R}^2} \phi(|z|^2) z\otimes z\,\mathrm{d}z\right) \nabla_x \rho(x) + O(R^6), \end{aligned}$$

by symmetry of $\phi(|z|)$. Polar coordinates yields:

$$G[\rho](x) = -(2R)^4 \int_{r\geq 0} \phi(|r|^2) r^3\,\mathrm{d}r \begin{bmatrix} \pi & 0 \\ 0 & \pi \end{bmatrix} \nabla_x \rho(x) + O(R^6) = -\alpha_R \nabla_x \rho(x) + O(R^6),$$

with $\alpha_R = \pi(2R)^4 \int_{r\geq 0} \phi(|r|^2) r^3\,\mathrm{d}r$. From the expression of $\phi$ (2.2), $\alpha_R$ is finite if $\alpha > -2$. Thus, neglecting the higher order term, we deduce that the model (2.5) (2.6) reduces to the porous media equation:

$$\partial_t \rho = \alpha_R \nabla_x \cdot \Big(\rho \nabla_x \rho\Big), \tag{2.9}$$

with

$$\alpha_R = \pi(2R)^4 \int_{r\geq 0} \phi(|r|^2) r^3 \mathrm{d}r. \tag{2.10}$$

In contrast to a diffusion equation, the support of the solution to the porous media equation remains compact. Still, as we observe in figure 4.15, the solution spreads until it eventually becomes flat.

## 2.3 Microscopic versus macroscopic

From the figures 4.14 and 4.15, we observe that the simulations of both *macroscopic* dynamics (2.5) and (2.9) do not reflect the simulations of the *microscopic* dynamics (2.1) (figure 4.13). The stationary state predicted by the microscopic dynamics consists in the whole mass of cells uniformly distributed on a disk. Whereas for the macroscopic dynamics, the density keeps spreading overtime.

To better illustrate this observations, we perform a comparison of the radial distribution of the density for both *micro*- and *macro* equations overtime starting from an uniform distribution in the unit disc. In figure 4.16, we plot the evolution of the radial distribution at different times for both dynamics with an average of 100 realizations for the microscopic dynamics to reduce the fluctuations (due to the randomness of the initial configurations in the microscopic model). In both figures, we observe a spread of the distribution initially. But in the microscopic dynamics, the spread stops around $T \approx 20$ time units, whereas in the macroscopic dynamics, the distribution keeps spreading. Thus, the microscopic dynamics converges to a stationary state supported on a compact domain, whereas the macroscopic dynamics will continue spreading.

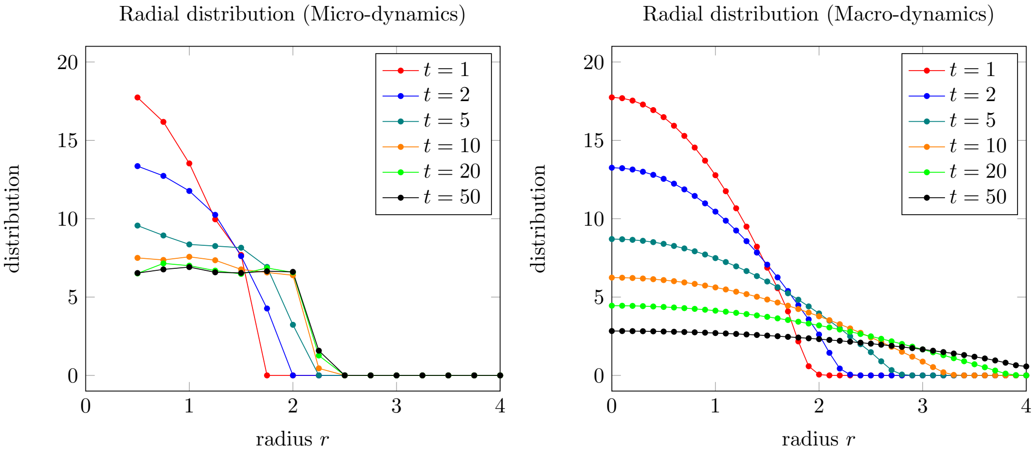

Figure 4.16: Evolution of the radial distributions over time. We observe that in the microscopic dynamics (left), the distribution converges to a stationary distribution (constant on a compact set). In contrast, the distribution of the macroscopic dynamics (right) keeps spreading and does not reach an equilibrium. Parameters: see figures 4.13 and 4.14. An average of 100 simulations have been done for the microscopic dynamics to remove fluctuation.

Since the macroscopic dynamics (2.5)-(2.6) is derived from the microscopic dynamics (2.1), the discrepancies between the two dynamics require some explanations. There are two factors to take into account. First, the correspondence between the dynamics can only be proven as the number of particles $N$ tends to infinity. Here, we have fixed the number of particles equal to $N = 100$. Secondly, we have investigated the large time behavior of the dynamics (i.e. $t \to \infty$), and since there is no 'uniform' bounds in time between microscopic and macroscopic dynamics, one cannot guarantee that the two solutions will remain close.

Now concerning our specific dynamics of short-range repulsion, there is one key observations: Dirac masses are not stable for the macroscopic dynamics. Starting from $\rho_0(x)$ a perturbation of a Dirac mass in equation (2.5)-(2.6), the solutions $\rho(x,t)$ will diffuse in space and thus departs from the Dirac distribution. A more detailed analysis of the stability of 'shell solutions' is provided in [3]. Therefore, even though the macroscopic dynamics have formally as a solution the empirical distribution (2.4), this solution is unstable. Thus, it will not be observed numerically. Notice that in the case of an attractive potential, a Dirac distribution would have been stable.

# 3 Short range repulsion: II

## 3.1 Introduction

As we have shown previously, the simulations of the macroscopic dynamics (2.5)-(2.6) do not match the solutions of the microscopic dynamics (2.1). One explanation is that Dirac masses are not stable solution for the dynamics. In this section, we would like to propose another PDE to describe the particle dynamics.

The main idea is as follows: particles stop interacting once they are at a distance greater than $2R$. Unfortunately, the information of inter-particle distance is lost when we describe a system by a density distribution $\rho(x)$. To overcome this problem, let assume that particles are actually discs of size $R$. Then particles interact only when they overlap (see figure 4.17). Thus, if we describe the dynamical system by the *modified* empirical distribution:

$$\widetilde{\rho}(x,t) = \frac{1}{\pi R^2}\sum_{i=1}^{N} \mathbf{1}_{B(x_i(t),R)}(x),$$

interaction occurs only in the region when $\{\widetilde{\rho} > \rho_*\}$ where $\rho_* = \frac{1}{\pi R^2}$.

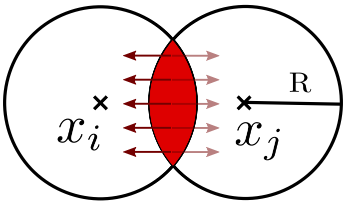

Figure 4.17: The two particles located at $x_i$ and $x_j$ interact when they are at a distance less than $2R$ from each other. On this region, the modified empirical distribution $\widetilde{\rho}$ is larger than the threshold $\rho_* = \frac{1}{\pi R^2}$.

## 3.2 Modified macroscopic dynamics

We propose to modify the macroscopic dynamics (2.5)(2.6) *only* in the region of low density. With this aim, we fix a threshold $\rho_*$ and identify the region of low density as $\{\rho < \rho_*\}$. Then, we propose the following dynamics:

$$\partial_t \rho + \nabla_x \cdot (\overline{G}[\rho]\rho) = 0, \tag{3.1}$$

with

$$\overline{G}[\rho](x) = -\int_{y\in\mathbb{R}^2} \phi\left(\left|\frac{x-y}{2R}\right|^2\right)(y-x)\mathbf{h}(\rho(y))\,\mathrm{d}y, \tag{3.2}$$

and (see figure 4.19):

$$\mathbf{h}(\rho) = \begin{cases} 0 & \text{if } \rho < \rho_*, \\ \rho - \rho_* & \text{if } \rho \geq \rho_*. \end{cases} \tag{3.3}$$

If there is no low density region (i.e. $\rho(x) > \rho_*$ for all $x$), then:

$$\begin{aligned} \overline{G}[\rho](x) &= -\int_{y\in\mathbb{R}^2} \phi\left(\left|\frac{x-y}{2R}\right|^2\right)(y-x)\Big(\rho(y)-\rho_*\Big)\,\mathrm{d}y \\ &= G[\rho](x), \end{aligned}$$

by symmetry. Therefore, the dynamics (3.1)-(3.3) only modifies the previous dynamics (2.5)-(2.6) inside and nearby the low density region.

The proposed dynamics (3.1)-(3.2) shares similarities with Hele-Shaw type models [39, 16] where a pressure law is modified to distinguish low and large density. In our approach, the modification is in the estimation of the density.

We illustrate the dynamics using the same initial condition $\rho_0$ (4) in figure 4.18 with the threshold $\rho_* = \frac{c}{\pi R^2}$ where $c = \pi/2\sqrt{3} \approx .907$ is the 'packing number' of circles in 2D. In contrast to figure 4.14, the solution is converging to a stationary state compactly supported.

As in the previous section, we can once again derive the asymptotic equation as the radius of the particle tends to zero (i.e., $R \to 0$). Following the same calculation, we find:

$$\begin{aligned} \overline{G}[\rho](x) &= -(2R)^3 \int_{z\in\mathbb{R}^2} \phi(|z|^2) z\mathbf{h}\Big(\rho(x+2Rz)\Big)\,\mathrm{d}z \\ &= -\alpha_R \mathbf{h}'(\rho(x))\,\nabla_x\rho(x) + O(R^6), \end{aligned}$$

with $\alpha_R$ given by (2.10). We deduce formally the following modified porous media equation:

$$\partial_t\rho = \alpha_R \nabla_x \cdot \Big(\mathbf{h}'(\rho)\rho\nabla_x\rho\Big). \tag{3.4}$$

This equation does not have classical solution as $\mathbf{h}'$ is a discontinuous function at $\rho = \rho_*$. To avoid this discontinuity, one can 'smooth' the function $\mathbf{h}$ near $\rho_*$ such that $\mathbf{h}'$ becomes continuous. Moreover, we can introduce the function $H$ satisfying:

$$H'(\rho^2) = \mathbf{h}'(\rho). \tag{3.5}$$

For the function $\mathbf{h}$ given by eq. (3.3), we obtain: $H(s) = (s-\rho_*^2)^+$. The equation (3.4) becomes:

$$\partial_t\rho = \frac{\alpha_R}{2}\Delta_x H(\rho^2). \tag{3.6}$$

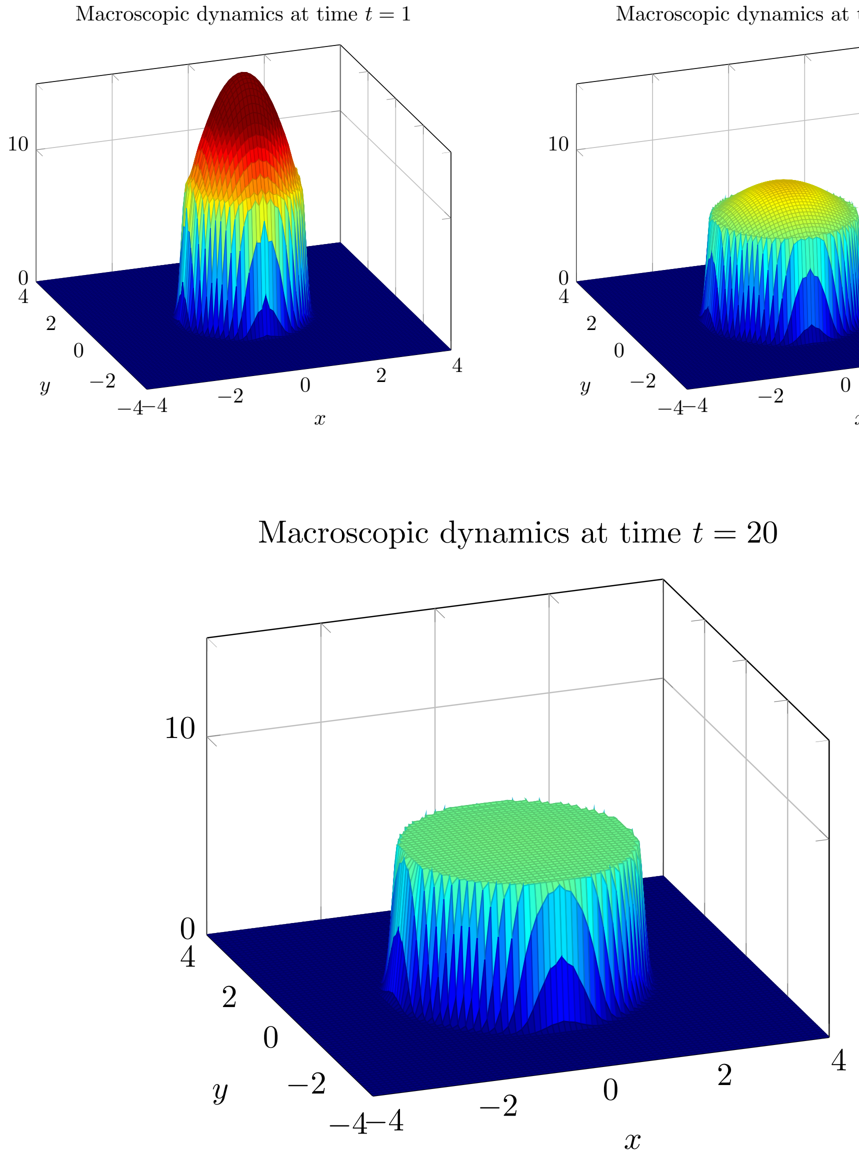
Macroscopic dynamics at time $t = 1$

Macroscopic dynamics at time $t = 5$

Macroscopic dynamics at time $t = 20$

Figure 4.18: Simulation of the macroscopic dynamics (3.1)-(3.3) with the initial condition (4) at $t = 1$, 5 and 20 unit times. The solution converges to a stationary state uniformly distributed on a disc. Parameters: see figure 4.14.

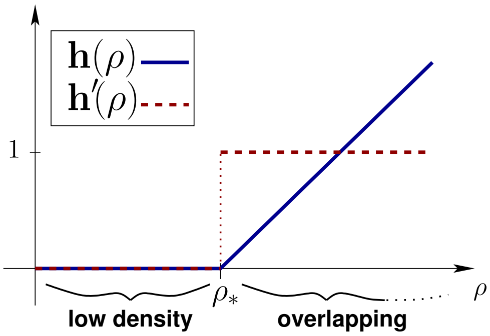

Figure 4.19: Example of function $\mathbf{h}(\rho) = (\rho - \rho_*)^+$ used to modify the dynamics in low density region.

To compare the modified macroscopic dynamics (3.1)-(3.3) and its asymptotic limit (3.4), we run two simulations with the same initial condition as in figure 4.15. We observe in figure 4.20 that both simulations are in excellent agreement with each other.

## 3.3 Microscopic versus macroscopic

Thanks to the modification of the dynamics in the low density in (3.2), we have observed that the dynamics stops spreading at low density and eventually converges to stationary states (Fig. 4.18). We would like now to make a more detailed comparison with the microscopic dynamics.

To this aim, we once again perform a comparison between the radial distribution of the micro- and *modified* macro- dynamics (resp. (2.1) and (3.1)). In figure 4.21, we observe that the distribution are in fairly good agreement. There are some discrepancy at the transition of zero density ($r \approx 2$ space unit), the macroscopic dynamics give a sharper transition. Moreover, the microscopic dynamics spread slightly more. This can be explained by the underlying hypothesis for estimating the equivalent radius, *i.e* cells are not necessarily in a configuration of optimal packing (see Fig. 4.13).

In appendix, we run a second comparison between microscopic and macroscopic dynamics where we divide the radius of particles by 2: $R = .1$ and multiply the number of particles by 4 ($N = 400$). We find once again that both simulations are in excellent agreement, the microscopic still have a tendency to spread slightly more.

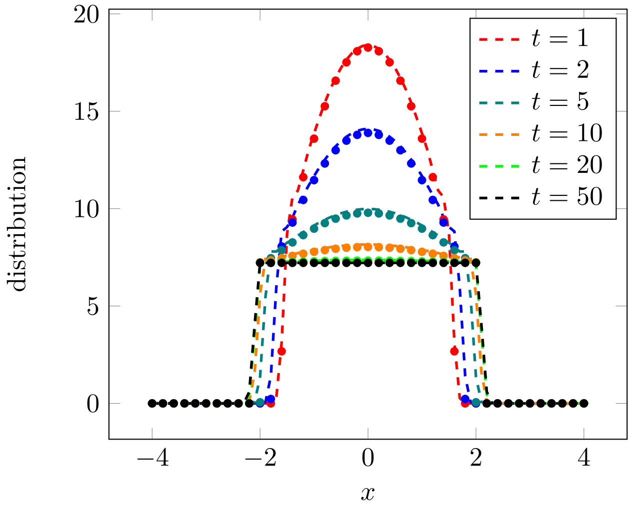

Figure 4.20: Simulations of the modified dynamics (3.1)-(3.3) (dashed line) and (3.6) (dotted). See fig. 4.15 for the parameters.

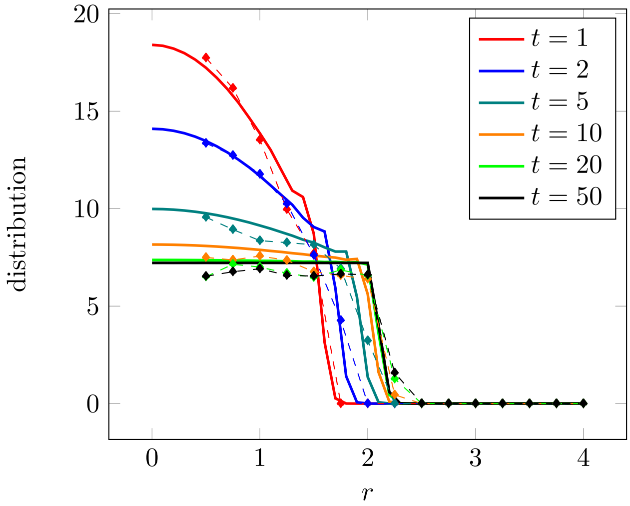

Figure 4.21: Evolution of the radial distributions for the microscopic dynamics (diamond) and macroscopic dynamics (3.1) (line). Both curves are in good agreements except that the microscopic dynamics spreads slightly more. Parameters: see figures 4.13 and 4.14. An average of 100 simulations have been done for the microscopic dynamics to remove fluctuation.

# 4 Repulsion and cell division

We would like to explore the combination of short-range repulsion dynamics with *cell division*. Thanks to our previous investigation, we can use the description of short-range repulsion using the porous media equation (3.6). In its simplest form, cell division at a constant rate $\mu$ modifies the dynamics in the following way:

$$\partial_t \rho = \frac{\alpha_R}{2} \Delta_x H(\rho^2) + \mu \rho. \tag{4.7}$$

We would like to observe what is the large time behavior of solutions.

With this aim, we explore numerically the solution for initial condition:

$$\rho_0(x) = \left\{ \begin{array}{ll} \frac{10}{\pi} & \text{if } |x| \leq 1 \\ 0 & \text{if } |x| > 1 \end{array} \right.$$

corresponding to $N = 10$ particles uniformly distributed on the unit circle. We run a simulation with the *seeding* parameter $\mu = .05$. In figure 4.22, we plot the distribution on the x-axis for different times. We observe two phases: first the distribution is only increasing on its support without spatial diffusion. This phase corresponds that the density constraint has not been reached on the unit circle. After around $t = 20$ time units, the density $\rho(x,t)$ has reached the density $\rho_*$ is therefore short-range repulsion starts to have an effect. As a result, the density $\rho$ starts to spread in space. But in contrast to the classical Fisher's equation, the density is actually spreading exponentially fast.

To better observe this property, we plot in Fig. 4.23 the position of the front of the density (estimated using the level curves of $\rho(x,t)$). From $t = 0$ to $t = 20$ time units, the front remains close to 1 (corresponding to the initial condition distributed on the unit circle). Then, the position of the front starts to increase rapidly in time. An exponential fit is provided in green.

This result can be put in perspective with recent work on tumor cancer of glioma [30]. Experimentally, it has been shown that the tumor of glioma cells have different phases of growth corresponding to different level of congestion.

# 5 Conclusion

In this work, we provided a first step towards the understanding of how cell-cell non overlapping interactions impact the propagation properties of a growing mass of cells. Starting from a simple agent-based model for cells interacting through repulsion interactions (with no diffusion), we showed that the derived macroscopic model did not capture the same features as predicted by the microscopic dynamics. Indeed, the solutions of the microscopic model converge in time to a compact

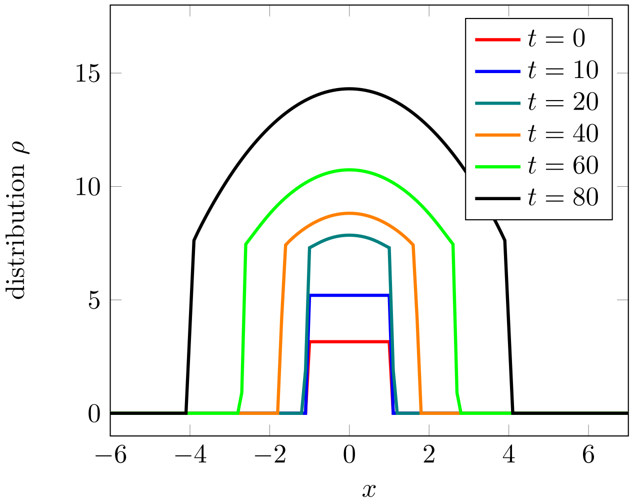

Figure 4.22: Short-range repulsion and cell division. Solution of (4.7) for $\mu = .05$. We observe two phases of growth, before and after $t = 20$ time units.

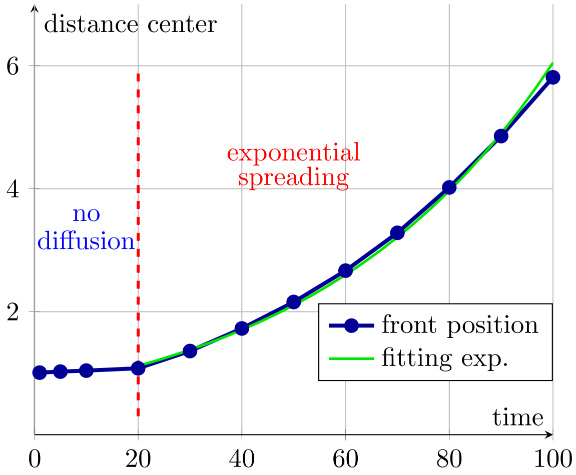

Figure 4.23: Position of the front of the density plotted in figure 4.22. The front the density is propagating exponentially fast once the density has reached the threshold $\rho_*$ at $t = 20$ time units.

supported spherical structure of a given size, while the solutions of the macroscopic model keep spreading. We showed that this is due to the fact that Dirac masses are unstable for the macroscopic equation. The slightest perturbation of a Dirac mass in the macroscopic model will cause the cell structure to start spreading. In order to obtain a macroscopic model in accordance to the microscopic dynamics, we proposed a modified version of the macroscopic equation. The idea was to introduce congestion features in the interacting kernel. We showed that this model led to a modified porous media equation in the limit of small number of particles, where the diffusion is only active in regions of large enough density. We obtained a good agreement between the numerical solutions of the microscopic and modified macroscopic model. This confirmed the relevance of the proposed model. By introducing cell division into the macroscopic model, we observed traveling wave type solutions spreading exponentially fast.

Many questions remain open with this work. On a mathematical viewpoint, the rigorous derivation of the macroscopic model from its underlying particle model is still an open question. The instability of the Dirac masses for the macroscopic model remains to be theoretically demonstrated. Further numerical tests will be perform to deeper understand the propagation properties of the model with source term. On a biological viewpoint, this model will be used to explore the mechanisms of glioma formation.

# Bibliography

[1] I. Aoki. A simulation study on the schooling mechanism in fish. *Bulletin of the Japanese Society of Scientific Fisheries (Japan)*, 1982.

[2] D. Balagué, J. A. Carrillo, T. Laurent, and G. Raoul. Dimensionality of Local Minimizers of the Interaction Energy. *Archive for Rational Mechanics and Analysis*, 209(3):1055–1088, May 2013.

[3] D. Balagué, J. A. Carrillo, T. Laurent, and G. Raoul. Nonlocal interactions by repulsive–attractive potentials: Radial ins/stability. *Physica D: Nonlinear Phenomena*, 260:5–25, October 2013.

[4] M. Ballerini, N. Cabibbo, R. Candelier, A. Cavagna, E. Cisbani, I. Giardina, A. Orlandi, G. Parisi, A. Procaccini, and M. Viale. Empirical investigation of starling flocks: a benchmark study in collective animal behaviour. *Animal Behaviour*, 76(1):201–215, 2008.

[5] F. Berthelin. Existence and weak stability for a pressureless model with unilateral constraint. *Mathematical Models and Methods in Applied Sciences*, 12(02):249–272, 2002.

[6] F. Berthelin and D. Broizat. A model for the evolution of traffic jams in multi-lane. *Kinetic and Related Models*, 5(4):697–728, 2012.

[7] F. Berthelin, P. Degond, M. Delitala, and M. Rascle. A model for the formation and evolution of traffic jams. *Archive for Rational Mechanics and Analysis*, 187(2):185–220, 2008.

[8] F. Berthelin, P. Degond, V. Le Blanc, S. Moutari, M. Rascle, and J. Royer. A traffic-flow model with constraints for the modeling of traffic jams. *Mathematical Models and Methods in Applied Sciences*, 18(supp01):1269–1298, 2008.

[9] F. Bouchut, Y. Brenier, J. Cortes, and J.-F. Ripoll. A hierarchy of models for two-phase flows. *Journal of NonLinear Science*, 10(6):639–660, 2000.

[10] D. Bresch, C. Perrin, and E. Zatorska. Singular limit of a Navier–Stokes system leading to a free/congested zones two-phase model. *Comptes Rendus Mathematique*, 352(9):685–690, 2014.

[11] M. Bruna and S. Chapman. Excluded-volume effects in the diffusion of hard spheres. *Physical Review E*, 85(1):011103, 2012.

[12] M. Bruna and S. Chapman. Diffusion of finite-size particles in confined geometries. *Bulletin of mathematical biology*, 76(4):947–982, 2014.

[13] M. Burger, V. Capasso, and D. Morale. On an aggregation model with long and short range interactions. *Nonlinear Analysis: Real World Applications*, 8(3):939–958, July 2007.

[14] M. Burger, M. Di Francesco, J-F. Pietschmann, and B. Schlake. Nonlinear cross-diffusion with size exclusion. *SIAM Journal on Mathematical Analysis*, 42(6):2842–2871, 2010.

[15] M. Burger, R. Fetecau, and Y. Huang. Stationary states and asymptotic behavior of aggregation models with nonlinear local repulsion. *SIAM Journal on Applied Dynamical Systems*, 13(1):397–424, 2014.

[16] Helen Byrne and Dirk Drasdo. Individual-based and continuum models of growing cell populations: a comparison. *Journal of mathematical biology*, 58(4-5):657–687, 2009.

[17] J. Carrillo, A. Chertock, and Y. Huang. A finite-volume method for nonlinear nonlocal equations with a gradient flow structure. *Communications in Computational Physics*, 17(01):233–258, 2015.

[18] I. D Couzin, J. Krause, R. James, G. D Ruxton, and N. R Franks. Collective Memory and Spatial Sorting in Animal Groups. *Journal of Theoretical Biology*, 218(1):1–11, 2002.

[19] G. Degond, J. Hua, and L. Navoret. Numerical simulations of the Euler system with congestion constraint. *Journal of Computational Physics*, 230(22):8057–8088, 2011.

[20] P. Degond, G. Dimarco, T. Mac, and N. Wang. Macroscopic models of collective motion with repulsion. *arXiv preprint arXiv:1404.4886*, 2014.

[21] P. Degond and J. Hua. Self-Organized Hydrodynamics with congestion and path formation in crowds. *Journal of Computational Physics*, 237:299–319, 2013.

[22] P. Degond, L. Navoret, R. Bon, and D. Sanchez. Congestion in a macroscopic model of self-driven particles modeling gregariousness. *Journal of Statistical Physics*, 138(1-3):85–125, 2010.

[23] T. Deisboeck and I. D Couzin. Collective behavior in cancer cell populations. *Bioessays*, 31(1):190–197, 2009.

[24] Carl Friedrich Gau\s s. Besprechung des Buchs von LA Seeber: Intersuchungen über die Eigenschaften der positiven ternären quadratischen Formen usw. *Göttingsche Gelehrte Anzeigen*, 2:188–196, 1831.

[25] H. Harpold, E. Alvord, and K. Swanson. The Evolution of Mathematical Modeling of Glioma Proliferation and Invasion:. *Journal of Neuropathology and Experimental Neurology*, 66(1):1–9, January 2007.

[26] D. Helbing and P. Molnar. Social force model for pedestrian dynamics. *Math. Comput. Simul Phys Rev E*, 51:4282, 1985.

[27] C. Kipnis, S. Olla, and S. R. S. Varadhan. Hydrodynamics and large deviation for simple exclusion processes. *Communications on Pure and Applied Mathematics*, 42(2):115–137, 1989.

[28] S. Labbé and E. Maitre. A free boundary model for Korteweg fluids as a limit of barotropic compressible Navier-Stokes equations. *Methods and Applications of Analysis*, 20(2):165–178, 2013.

[29] M. Leroy Leretre. *Etude de la croissance tumorale via la mod\ 'elisation agent-centr\ 'e du comportement collectif des cellules au sein d\ ' une population cellulaire.* PhD thesis, Univ. Paul Sabatier, Toulouse, 2014.

[30] J. Lowengrub, H. Frieboes, F. Jin, Y-L. Chuang, X. Li, P. Macklin, S. Wise, and V. Cristini. Nonlinear modelling of cancer: bridging the gap between cells and tumours. *Nonlinearity*, 23(1):R1–R91, January 2010.

[31] B. Maury. A time-stepping scheme for inelastic collisions. *Numerische Mathematik*, 102(4):649–679, January 2006.

[32] B. Maury, A. Roudneff-Chupin, and F. Santambrogio. A macroscopic crowd motion model of gradient flow type. *Mathematical Models and Methods in Applied Sciences*, 20(10):1787–1821, 2010.

[33] B. Maury and J. Venel. A discrete contact model for crowd motion. *ESAIM: Mathematical Modelling and Numerical Analysis*, 45(01):145–168, January 2011.

[34] D. Morale, V. Capasso, and K. Oelschläger. An interacting particle system modelling aggregation behavior: from individuals to populations. *Journal of Mathematical Biology*, 50(1):49–66, January 2005.

[35] M. Moussaïd, E. Guillot, M. Moreau, J. Fehrenbach, O. Chabiron, S. Lemercier, J. Pettré, C. Appert-Rolland, P. Degond, and G. Theraulaz. Traffic Instabilities in Self-Organized Pedestrian Crowds. *PLoS Comput Biol*, 8(3):e1002442, March 2012.

[36] K. Oelschläger. Large systems of interacting particles and the porous medium equation. *Journal of Differential Equations*, 88(2):294–346, 1990.

[37] C. Perrin and E. Zatorska. Free/Congested Two-Phase Model from Weak Solutions to Multi-Dimensional Compressible Navier-Stokes Equations. *accepted in Communications in Partial Differential Equations*, 2015.

[38] B. Perthame, F. Quirós, M. Tang, and N. Vauchelet. Derivation of a Hele-Shaw type system from a cell model with active motion. *Interfaces and Free Boundaries*, 16:489–508, 2014.

[39] B. Perthame, F. Quirós, and J. Vázquez. The Hele–Shaw Asymptotics for Mechanical Models of Tumor Growth. *Archive for Rational Mechanics and Analysis*, 212(1):93–127, 2014.

[40] B. Perthame, M. Tang, and N. Vauchelet. Traveling wave solution of the Hele–Shaw model of tumor growth with nutrient. *Mathematical Models and Methods in Applied Sciences*, 24(13):2601–2626, 2014.

[41] C. W Reynolds. Flocks, herds and schools: A distributed behavioral model. In *ACM SIGGRAPH Computer Graphics*, volume 21, pages 25–34, 1987.

[42] K. Swanson, C. Bridge, J. D. Murray, and E. Alvord Jr. Virtual and real brain tumors: using mathematical modeling to quantify glioma growth and invasion. *Journal of the Neurological Sciences*, 216(1):1–10, December 2003.

# 6 Numerical schemes

## 6.1 Particle dynamics

To discretize the particle dynamics (2.1), we use an Euler method with an adaptive time step $\Delta t$ to ensure that the energy (2.3) is decaying:

1) Let $\{x_i(t_n)\}_i$, $\mathcal{E}(t_n)$ the corresponding energy and a time step $\Delta t$

2) For all $i \in \{1, N\}$, compute:

$$x_i(t_{n+1}) = x_i(t_n) - \Delta t \sum_{j=1, j\neq i}^{N} \phi_{ij} \cdot \Big(x_j(t_n) - x_i(t_n)\Big)$$

   Deduce the corresponding energy $\mathcal{E}(t_{n+1})$.

3) If $\mathcal{E}(t_{n+1}) > \mathcal{E}(t_n)$, go back to 2) with $\widetilde{\Delta t} = \Delta t/2$.
   Otherwise update $t_n$ to $t_{n+1}$.

## 6.2 PDE dynamics

We use an upwind-method to solve equation (2.5)-(2.6). To simplify the notation, we illustrate the method in 1D. We use a uniform grid in space and time and denote: $\rho_i^n = \rho(x_i, t^n)$ with $x_i = i\Delta x$ and $t^n = n\Delta t$. The scheme is based on the following discretization:

$$\frac{\rho_i^{n+1} - \rho_i^n}{\Delta t} + \frac{(\rho G)_{i+1/2} - (\rho G)_{i-1/2}}{\Delta x} = 0,$$

where $(\rho G)_{i+1/2}$ is the value of $\rho(x)G[\rho](x)$ at the interface $x_{i+1/2}$. To estimate this value, we first estimate the 'velocity' at the interface $x_{i+1/2}$: $G_{i+1/2} = \frac{G_i + G_{i+1}}{2}$. Then, we decentralize:

$$(\rho G)_{i+1/2} = \begin{cases} (\rho G)_i & \text{if } G_{i+1/2} > 0, \\ (\rho G)_{i+1} & \text{if } G_{i+1/2} < 0. \end{cases}$$

The CFL condition associated with this scheme is given by $\lambda \Delta t/\Delta x$ where $\lambda = 2 \max |G|$.

For the porous media equation (2.9), we use the formulation (in 1D) $\partial_t \rho = \alpha_R \partial_{xx}(\rho^2)/2$ to deduce

$$\frac{\rho_i^{n+1} - \rho_i^n}{\Delta t} = \frac{\alpha_R}{2} \frac{(\rho_{i+1}^n)^2 - 2(\rho_i^n)^2 + (\rho_{i-1}^n)^2}{\Delta x^2}.$$

In our all simulations, we have verified that both positivity and energy decaying were satisfied. A more sophisticated scheme has been proposed in [17] that can guarantee both properties.

# 7 Micro- and macro- dynamics ($R = .1$, $N = 400$)

We propose to conduct similar numerical simulations as in section 3.3 for a different setting. We multiply the number of particles by 4 and divide the radius of the particles by 2. The positions of the particles and the density distribution at $t = 20$ time units are plotted in figure 4.24 (resp. top-left and top-right). An average of 100 realization is performed to estimate the radial distribution of particles over time in figure 4.24 (bottom).

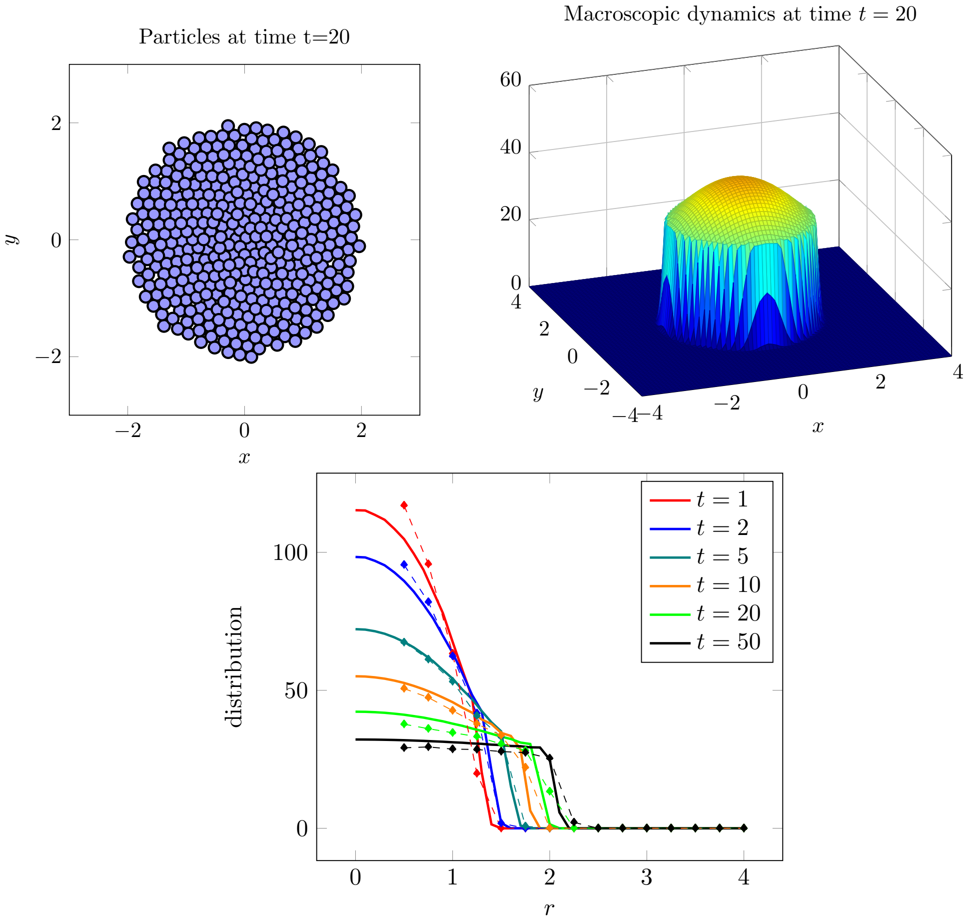

Figure 4.24: **Top-left**: positions of the particles after $t = 20$ unit time running the microscopic dynamics (2.1). Parameters: $N = 400$ particles, $R = .1$, $\alpha = -1$, $\Delta t = 10^{-1}$. **Top-right**: density $\rho(x,t)$ solution of the macroscopic dynamics (3.1). **Bottom**: radial distributions for the micro- and macro- dynamics (resp. diamond and plain).

# Chapter 5

# Extensions of the works

In this chapter, we present two works in progress which are built using the concept developed for the individual based model for adipose tissues (Chap I). The first work (with P. Degond and B. Aymard) is a hybrid model for vasculogenesis, the second one (with P. Degond, M. Feireira and S. Motsch) aims at modeling the mechanisms of ballistic aggregation.

### Sommaire

**1 A model for vasculogenesis . . . . . . . . . . . . . . . . . . 222**

**2 A model for ballistic aggregation . . . . . . . . . . . . . 230**

## 1 A model for vasculogenesis

In this section, we present the preliminary works of [19]. In this study, we aim at understanding the emergence of a vascular network in a porous media flow. In a first section, we present the main features of the model and in section 1.2 we show the first numerical simulations. Section 1.3 highlights some conclusions and perspectives of this preliminary work.

### 1.1 Model

A vascular network is a complex system which involves transition phases between porous media flow and network flow. Here, four major actors are considered: capillaries, blood, oxygen and tissue. The capillaries are modeled as tubes of fixed length which are supposed to be created and deleted according to the needs of the tissue. In order to model the influence of oxygen on the capillary distribution [18], the new capillaries are supposed to be oriented towards the gradient of oxygen. The local porosity of the tissue is supposed to be directly linked to the local amount of capillaries. The blood is modeled through its speed and pressure, and is supposed to follow Darcy's law. Finally, oxygen is modeled through its density distribution $\rho$ and is supposed to be (i) convected by the blood flow, (ii) diffused in the tissue and (iii) consumed by the elements of the tissue. The next paragraphs provide the details of each element of the model.

**Capillary network** The capillary network is modeled as a set of $K$ elementary capillaries. They are modeled as tubes of fixed length described by a position vector $X_k = (x_k, y_k) \in \mathbb{R}^2$ of their center and an orientation vector $\omega_k = (\cos\theta_k, \sin\theta_k) \in \mathbb{S}^1$. The orientation angle $\theta_k$ is defined modulo $\pi$ to model the isotropy of the blood flow. Each capillary unit located at point $X$ is supposed to generate an elementary porosity matrix $K_k(X)$ and an elementary diffusion matrix $D_k(X)$:

$$\begin{cases} \mathbf{K}_k(\mathbf{X}) = \kappa\,(\boldsymbol{\omega}_k \otimes \boldsymbol{\omega}_k)\,\delta_{\mathbf{X}_k}(\mathbf{X}), \\ \mathbf{D}_k(\mathbf{X}) = d\,(\boldsymbol{\omega}_k \otimes \boldsymbol{\omega}_k)\,\delta_{\mathbf{X}_k}(\mathbf{X}), \end{cases}$$

where $\delta_x(X)$ is the Dirac function, and $\kappa, d$ real positive constants. These elementary porosity and diffusion matrices are supposed to participate into the global porosity and diffusion properties of the medium (further described). In order to model apparition and destruction of capillaries according to the needs of the tissue, capillary units are created and deleted with (random) Poisson processes of frequencies $\nu_c$ and $\nu_r$ respectively. The rate of creation is supposed to depend upon the local density $\rho$, and reads:

$$\nu_c(X) = \nu_c^* \psi\left(\frac{g(\rho(X), \nabla\rho(X)) - g_c}{h_c}\right) S(\rho(X)), \tag{1.1}$$

with

$$\begin{cases} \psi(x) = \frac{1}{2}(1 + \tanh(x)), \\ g(\rho, \nabla\rho) = L_0 \frac{||\nabla\rho(\mathbf{X})||}{\rho(\mathbf{X}) + \rho^*}, \\ S(\rho) = \left(\frac{sup_X||\rho|| - \rho}{sup_X||\rho||}\right), \end{cases}$$

where $\nu_c^*$, $g_c$, $h_c$, $L_0$, $\rho^*$ real positive constants. If a capillary is created at a point $\mathbf{X}$, then its direction is defined by

$$\boldsymbol{\omega} = \frac{\nabla\rho(\mathbf{X})}{||\nabla\rho(\mathbf{X})||}. \tag{1.2}$$

We assume that $n_k$ new capillaries are created at each time step. The removal of capillaries is also modeled as a Poisson 's process of frequency depending upon the density $\rho$:

$$\nu_r(X) = \nu_r^* \psi\left(\frac{g_r - g(\rho(X), \nabla\rho(X))}{h_r}\right) \left(1 - S(\rho(X))\right), \tag{1.3}$$

where $\nu_r^*$, $g_r$ and $h_r$ are real positive constants. It is also assumed that at initial time $t = 0$, there is no capillary in the tissue.

**Tissue (Porous medium)** The tissue is a porous medium modeled by a porosity matrix $\mathbf{K}$ and a diffusion matrix $\mathbf{D}$. As previously explained, the capillaries participate into the global porosity and diffusion of the medium: the global porosity matrix $\mathbf{K}$ and the global diffusion matrix $\mathbf{D}$ are defined by:

$$\begin{cases} \mathbf{K}(\mathbf{X}) = k_h \mathbf{I}_2 + \displaystyle\sum_{k\, s.t. ||\mathbf{X}_k - \mathbf{X}|| \leq R} \kappa\, (\boldsymbol{\omega}_k \otimes \boldsymbol{\omega}_k), \\ \mathbf{D}(\mathbf{X}) = d_h \mathbf{I}_2 + \displaystyle\sum_{k\, s.t. ||\mathbf{X}_k - \mathbf{X}|| \leq R} d\, (\boldsymbol{\omega}_k \otimes \boldsymbol{\omega}_k), \end{cases} \tag{1.4}$$

where $\mathbf{I}_2$ is the $2 \times 2$ identity matrix, $k_h$, $d_h$ and $R$ real positive constants. For each, the first term models a homogeneous medium, and the second term models the network of capillaries. For the sake of consistency with the model of capillary network, the following compatibility condition is considered:

$$R = L_c.$$

**Blood flow** The blood flow through the porous medium of porosity matrix $\mathbf{K}$ is supposed to be described by Darcy's system:

$$\begin{cases} \mathbf{u} = -\mathbf{K}\nabla p \\ -\mathrm{div}(\mathbf{K}\nabla p) = 0 \end{cases} \tag{1.5}$$

where $p$ is the blood pressure and $\mathbf{u}$ the blood velocity. In order to close the problem, the following boundary conditions are considered: (i) The pressure is known at the left and the right border of the domain (see ). (ii) For the sake of simplicity, periodic boundary conditions are set at the top and the bottom of the domain:

$$\begin{cases} p(0, y) = p_L \\ p(L_x, y) = p_R \\ p(x, L_y) = p(x, 0) \end{cases} \tag{1.6}$$

The length of the domain ($L_x$,$L_y$) is taken of the order of $1000[\mu m]$. Artery blood pressure entering the capillaries is approximately $37.7[mmHg]$, while exiting blood pressure is of the order of $19.6[mmHg]$ (see [12]). The blood velocity in the capillaries is of the order of $400[\frac{\mu m}{s}]$ (see [12]).

**Oxygen** Oxygen is described by a density function $\rho$. Oxygen motion is supposed to be driven by three different phenomena: (i) it is convected by the blood, (ii) diffused through the tissue and (iii) consumed by the tissue by cell breathing phenomena. For the sake of simplicity, the rate of oxygen consumption is supposed to be constant and measured by $\beta$ in this preliminary work. The summary of these 3 rules leads to the following convection-diffusion equation with a source term:

$$\partial_t\rho + \nabla.(\rho\mathbf{u}) - \nabla.(\rho\mathbf{D}\nabla\rho) = -\beta\rho, \tag{1.7}$$

where $\mathbf{D}$ is the diffusion matrix previously described. Note that oxygen consumption is generally not homogeneous due to the different types of cells in the medium, such as stem cells, differentiated cells *etc* which consume oxygen at different rates and in different zones in the domain. This could be taken into account in this model by considering a non constant rate $\beta$. At initial time $t = 0$ the oxygen rate is supposed to be maximal:

$$\rho(x, y, 0) = \rho_{\max}.$$

As previously mentioned, an artery brings oxygenated blood at the left part of the domain, and a vein pumps out the blood on the right part. Periodic boundary condition are assumed on $y$-axis. This leads to the following set of boundary conditions:

$$\begin{cases} \rho(0, y, t) = \rho_0, \\ \partial_x\rho(L_x, y, t) = 0, \\ \rho(x, L_y, t) = \rho(x, 0, t). \end{cases}$$

**Summary of the model**
The full system writes:

$$\begin{cases} \text{Blood flow} \\ \qquad \begin{cases} \mathbf{u} = -\mathbf{K}\nabla p \\ \operatorname{div}(\mathbf{u}) = 0 \end{cases} \\ \text{Oxygen convection/diffusion/consumption} \\ \qquad \left\{ \partial_t\rho + \nabla.(\rho\mathbf{u}) - \nabla.(\rho\mathbf{D}\nabla\rho) = -\beta\rho \right. \\ \text{Capillary network, creation and removal} \\ \qquad \begin{cases} (\mathbf{X}_k, \boldsymbol{\omega}_k)_{k=1,\ldots,N(t)} \\ \text{Creation: Poisson 's process of frequency } \nu_c \\ \text{Removal: Poisson 's process of frequency } \nu_r \end{cases} \\ \text{Tissue (porosity matrix and diffusion matrix)} \\ \qquad \begin{cases} \mathbf{K}(\mathbf{X}) = k_h\mathbf{I}_d + \displaystyle\sum_{k\,s.t.||\mathbf{X}_k-\mathbf{X}||\leq R} \kappa\,(\boldsymbol{\omega}_k \otimes \boldsymbol{\omega}_k) \\ \mathbf{D}(\mathbf{X}) = d_h\mathbf{I}_d + \displaystyle\sum_{k\,s.t.||\mathbf{X}_k-\mathbf{X}||\leq R} d\,(\boldsymbol{\omega}_k \otimes \boldsymbol{\omega}_k) \end{cases} \end{cases}$$

with the following boundary conditions:

$$\begin{cases}\text{Left boundary: artery} \\ \quad \begin{cases} p(0,y) = p_0 \\ \rho(0,y,t) = \rho_0 \end{cases} \\ \text{Right boundary: vein} \\ \quad \begin{cases} p(L_x,y) = p_1 \\ \partial_x \rho(L_x,y,t) = 0 \end{cases} \\ \text{Top and bottom boundaries: periodicity} \\ \quad \begin{cases} \mathbf{u}(x,L_y,t) = \mathbf{u}(x,0,t) \\ p(x,L_y,t) = p(x,0,t) \\ \rho(x,L_y,t) = \rho(x,0,t) \end{cases} \end{cases}$$

and the following initial conditions:

$$\begin{cases}\text{Maximal oxygen rate at initial time} \\ \quad \rho(x,y,0) = \rho_{\max} \\ \text{No capillary at initial time} \\ \text{Tissue (porosity matrix and diffusion matrix) at initial time} \\ \quad \begin{cases} \mathbf{K}(\mathbf{X}) = k_h \mathbf{I}_d(\mathbf{X}) \\ \mathbf{D}(\mathbf{X}) = d_h \mathbf{I}_d(\mathbf{X}) \end{cases} \end{cases}$$

## 1.2 Numerical simulations - capillary network

In this section, numerical simulations for the capillary network are presented. The goal is to study how a capillary network self-organizes given an initial $O_2$ density $\rho$ without blood flow. Simulations are performed on a domain $\Omega = [0, L_x] \times [0, L_y]$. In the following, different initial $O_2$ densities are considered.

**Test case 1** In this paragraph, the initial density $\rho$ is of the form (see Fig. 5.25):

$$\rho(x,y) = 100 \times \left( \frac{1 + \cos(Ax)\cos(By)}{2} \right)$$

with:

$$A = \frac{2\pi}{L_x}\,, \qquad B = \frac{2\pi}{L_y}.$$

Note that in this case, the oxygen gradient reads:

$$\nabla \rho(x,y) = \begin{pmatrix} (-50A)\sin(Ax)\cos(By) \\ (-50B)\cos(Ax)\sin(By) \end{pmatrix}$$

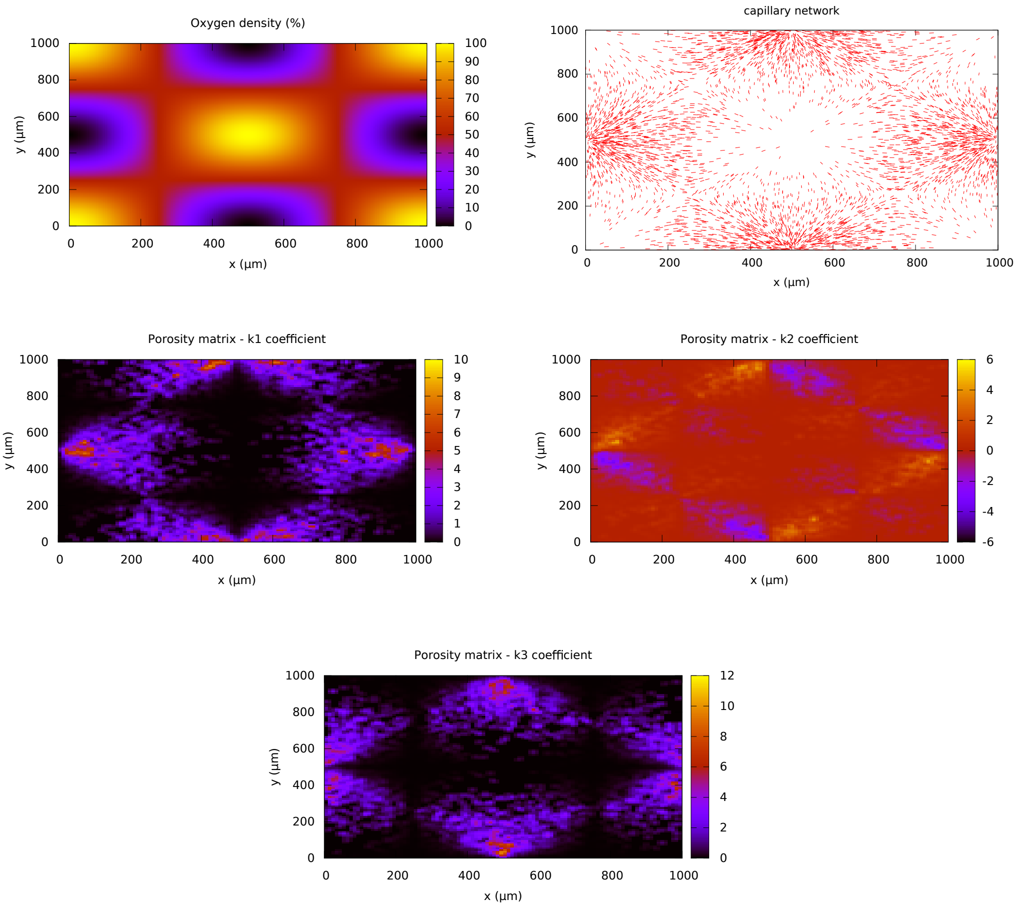

Figure 5.25: *Test case 1: Top line oxygen density and capillary network. Bottom line: Coefficients* $k_1$*,* $k_2$ *and* $k_3$ *of porosity matrix* $K$

As shown by Fig. 5.25, a good correspondence between the capillary network and the oxygen density is obtained. At equilibrium, the capillary density is directly connected to the oxygen density. This is due to the fact that the Poisson process for creating/removing elementary capillaries are functions of the oxygen density. Moreover and as expected, the capillaries are oriented towards the gradient of oxygen. This results in the creation of a connected network denser in poorly oxygenated regions. In Fig. 5.25, using the symmetry of the porosity matrix defined by (1.4), the three coefficients $\mathbf{K}_{11}$, $\mathbf{K}_{22}$ and $\mathbf{K}_{12}$ of matrix $\mathbf{K}$ are shown. Note that $\mathbf{K}$ is the projection matrix of the mean orientation of capillaries. Therefore, $\mathbf{K}_{11}$ is maximal if all the capillaries are horizontally disposed, and $\mathbf{K}_{22}$ if their orientation is vertical. This figure shows the good agreement between the distribution of the capillary orientations and the oxygen gradient. A blood flow in such porous medium is therefore expected to be convected from one highly oxygenated region to another following the gradient of the oxygen. This is the subject of future work.

**Test case 2** Here, the oxygen density $\rho$ is of the same form as previously, but the number of maxima in the domain is increased (see Fig. 5.26). As shown by this figure, the resulting capillary network is again in good agreement with the oxygen density distribution, and the capillary orientations seems to follow the gradient of the oxygen density.

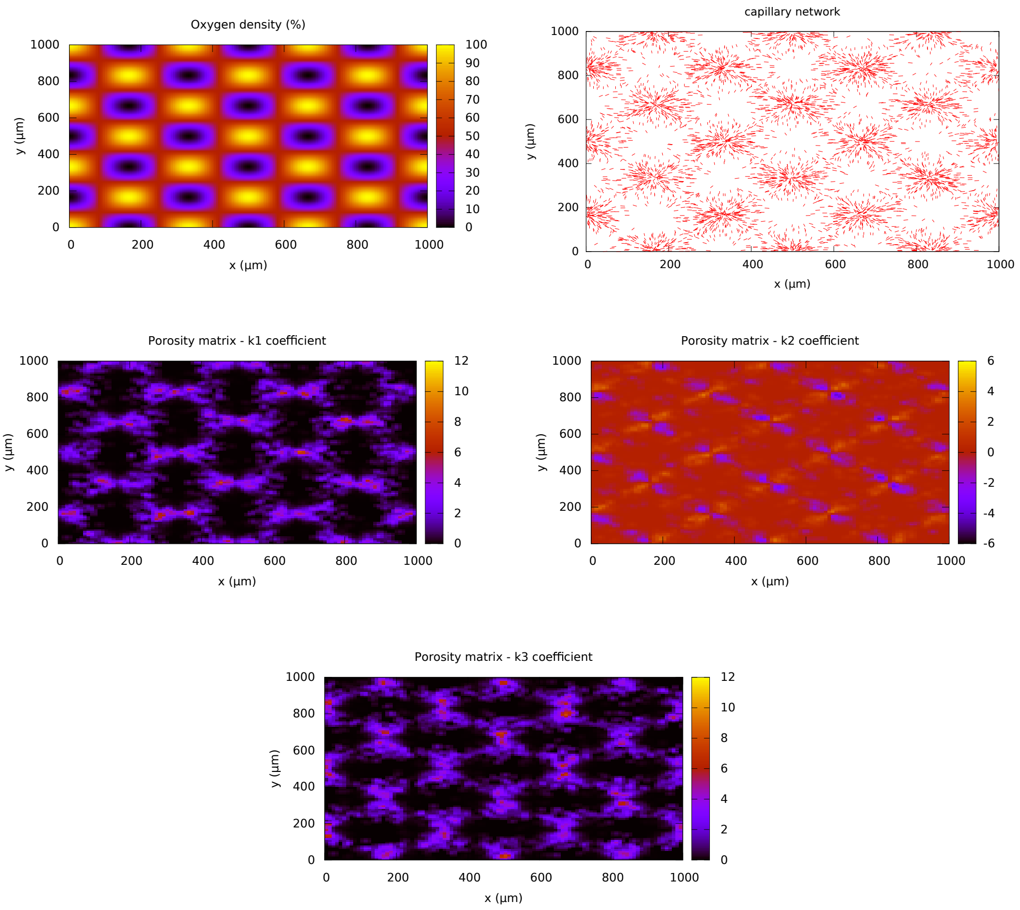

Figure 5.26: *Test case 2: top line: oxygen density and capillary network. Bottom: Coefficients* $k_1$*,* $k_2$ *and* $k_3$ *of porosity matrix* $K$*.*

These results show that given a fixed oxygen distribution, a capillary network with specific properties emerges. This network is denser in less oxygenated zones and the capillaries are oriented towards the gradient of the oxygen density.

## 1.3 First conlusions

These first simulations tend to validate the numerical method for building a capillary network given a fixed oxygen distribution. The perspective of this preliminary work is the introduction of a blood flow following Darcy's law to study how such a porous medium will transport a fluid. Further perspectives are the exploration of a dynamical oxygen density $\rho$. Such a study will aim to answer the question of how the capillary network reorganizes if the oxygen is convected by the blood. More specifically, some properties on the speed, form *etc* of the capillary network are expected to be deduced. The final full model is expected to bring new perspectives on the understanding of how the complex coupled organization of capillaries, blood flow and oxygen can lead to the emergence of an organized and stable vascular network.

## 1.4 References

1. D. Peurichard, F. Delebecque, A. Lorsignol, C. Barreau, J. Rouquette, X. Descombes, L. Casteilla and P. Degond *Modelling tissue homeostasis*, submitted to Proceedings of the National Academy of Sciences of the United States of America, 2014.
2. E. Boissard, P. Degond, S. Motsch, *Trail formation based on directed pheromon deposition*, Journal of Mathematical Biology, 2013, pp. 1267-1301.
3. L.B. Lucy, *A numerical approach to the testing of the fission hypothesis*, The astronomical journal, 1977.
4. R.A. Gingold, J.J. Monaghan, *Smoothed particle hydrodynamics: theory and application to non-spherical stars*, Mon Not Royal Astronomical Society, 1977.
5. J.J. Monaghan, *Smoothed particle hydrodynamics*, Annual Review of Astronomy and Astrophysics, 1992.
6. M. Muller, D. Charypar, M. Gross, *Particle based fluid simulation for interactive applications*, Eurographics/SIGGRAPH Symposium on Computer Animation, 2003
7. F. Collin, R. Egli, F.Y. Lin, *Computing a null divergence velocity field using smoothed particle hydrodynamics*, Journal of Computational Physics, 2006.
8. M. Ihmsem, J. Orthmann, B. Solenthaler, A. Kolb, M. Teschner, *SPH fluids in computer graphics*, Eurographics, 2014

9. G. Duvaut, *Mécanique des Milieux Continus*, Masson, 1990
10. F. Vergnet, *Self Organization of high density suspensions of swimming agents*, Master thesis, 2014

11. R. Sepulchre, *Cours: Introduction au génie biomédical*, Institut Montefiore,

Université de Liege, 2010.
12. B. Teisseire, *Eléments majeurs de la perfusion microcirculatoire*, ”Société Française de Perfusion” congress
(available online: http://www.sofraperf.fr/documentation/congres/tours/98-112bis.htm).
13. S.A. Williams, S. Wasserman, D.W. Rawlinson, R.I. Kitney, L.H. Smaje, J.E. Tooke, *Dynamic measurement of human capillary blood pressure*, Clinical Science, London, 1988.
14.N. Kielbasiewicz, *Aide mémoire Gnuplot 4.0*, Ecole Nationale Supérieure des Techniques Avancées, 2008
15.Kirk Levin, ”Relationship between blood flow, vascular resistance and blood pressure”.
16.M.R. Pinsky, L. Brochard, J. Mancebo, M. Antonelli, ”Applied physiology in intensive care medicine 2”, Physiological reviews and editorial, Springer.
17. Maxime Nicolas, ”Ecoulement dans les milieux poreux”, DEA Mécanique Energétique, Provence University, Marseilles.
18. Lennart Lindbom, Ronald F. Tuma, Karl-E. Arfors, Influence of oxygen on perfused capillary density and capillary red cell velocity in rabbit skeletal muscle
19. Benjamin Aymard, Pierre Degond, Self Organization of vascularization: from porous media flow to network flow, 2015, in preparation

# 2 A model for ballistic aggregation

In this section, we present the preliminary works of [1], where we aim at understanding the mechanisms of ballistic aggregation. Epithelial cells are bound together in sheets of tissue called epithelia. The cells are held together through several types of interactions. The goal of the project is to build a mathematical model which can take into account different geometries for the cells. The idea is to model a cell as a set of connected elementary units of simple geometry such as 2D spheres. Here, we present the main features of a preliminary work which serves as a starting point for cell aggregation.

## 2.1 Introduction

As a starting point, a model for self-propelled particle which attach together throughout motion is being developed. In this model, cells move with a constant velocity in a given direction as long as they don’t collide. When two cells collide, they link together and remain attached during motion afterwards: they keep moving together with the same velocity. In order to avoid cell overlapping, a minimization method is used during each collision. By this mean, the colliding cells will rearrange to be in a non overlapping configuration which minimizes their distance. The main steps are represented in Fig. 5.27.

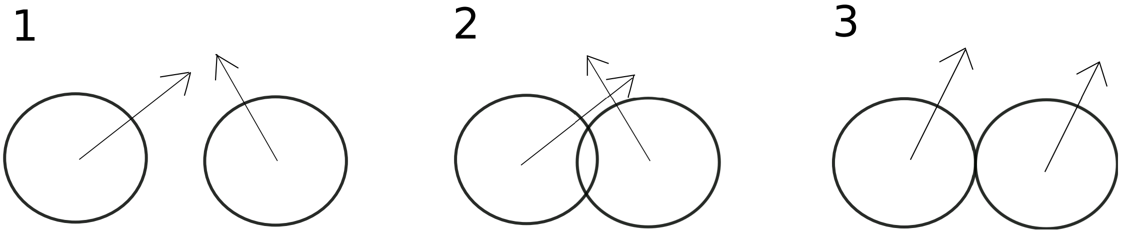

Figure 5.27: Steps for cell motion. 1: self-propelled cells with proper velocity vectors. 2: Collision 3: motion after rearrangement and actualization of the velocities.

More precisely, the $N$ cells are modeled by $N$ non-overlapping spheres in $\mathbb{R}^2$, with radius $R_i > 0$ and center $X_i = (x_{i_1}, x_{i_2}),\ i = 1, ..., N$ denoted by $s_i,\ i = 1, ..., N$. Suppose each cell $i$ moves with constant velocity $V_i = (v_{1,i}, v_{2,i})$ as long as it doesn't collide with any cell. The respective positions of the $N$ cells, before any collision is therefore guided by the following system of $N$ ODEs :

$$\frac{dX_i}{dt}(t) = V_i,\ t \geq 0,\quad X_i(0) = X_i^0. \tag{2.8}$$

When they collide, cells are supposed to rearrange to be in non-overlapping configuration. In that prospect, we define the following constraints :

$$\forall i, j = 1, ..., N | i \neq j,\ \|X_i - X_j\| > R_i + R_j,$$

where $\|\|$ demotes the Euclidian norm.

When two 2D-spheres $s_i$ and $s_j$ (for $i \neq j$ of course) collide, they bind and stay together as a "2-bodies cell" with new velocity $(V_i + V_j)/2$. More generally, if a cluster of $k$ spheres "encounters" a cluster of $m$ cells, they bind, giving rise to a new cluster of $m + n$ cells with a velocity that is the arithmetic mean of the previous velocities of each cell constituting the new cluster.

The goal is to investigate the dynamics behind this phenomenon until all the spheres are connected, namely, how long does this process take, which kind of structures can arise at the end and what is the relation with the velocity a priori defined.

## 2.2 Individual based model for cell aggregation

In order to gain some insight about the phenomenon of the aggregation of $N$ spheres without overlapping, a numerical approach is proposed through the development of an individual based model. The computational domain is a square

$A = [0, L] \times [0, L]$ with periodic boundary conditions. The distance $d$ between two spheres corresponds to the Euclidean distance on a torus surface, *i.e.* for $X_i,\ X_j \in A$,

$$d(X_i, X_j)^2 = \min\{|x_{i_1} - x_{j_1}|, L - |x_{i_1} - x_{j_1}|\}^2 + \min\{|x_{i_2} - x_{j_2}|, L - |x_{i_2} - x_{j_2}|\}^2.$$

The dynamics is discrete in time, with time-step $\delta_t$. Consider the initial conditions $(X_i^0)_{i=1,\dots,N}$ and $(V_i^0)_{i=1,\dots,N}$, in order to define the dynamics of center of cell $i$, Eq. (2.8) is discretized with a Euler-Explicit discretization scheme. Then, in case of overlapping situations, the positions are reajusted such that the binded cells stay close but do not overlap. This amount to solve a minimization under constraints problem. Indeed, if cells $i$ and $j$ collide, then $d(X_i, X_j)^2$ is defined as the global to-be-minimized potential. The minimization of the global potential therefore tends to keep touching cells binder, under non-overlapping constraints. Finally the velocity of each sphere is actualized. The process ends when there is just one cluster left.

More precisely, the full algorithm reads:

- First step: free motion.

$$\forall i = 1 \dots N, \quad \hat{X}_i^n = X_i^{n-1} + \delta_t V_i^{n-1} \mod L.$$

- Second step: Readjustment by minimization
  Define, for $(X_i, X_j) \in A \times A$,

$$\phi_\varepsilon(X_i, X_j) = (R_i + R_j + \varepsilon \min\{R_i, R_j\})^2 - d(X_i, X_j)^2$$

  and $S_\varepsilon$ the set of the pairs of quasi-touching spheres :

$$S_\varepsilon = \{(i, j) \in \{1 \dots N\} \mid \phi_\varepsilon(X_i, X_j) \geq 0\}.$$

  Consider the following potential :

$$W(X_1, ..., X_N) = \frac{1}{2} \sum_{(i,j) \in S_0} d(X_i, X_j)^2;$$

  the adjustment is then made by solving locally the minimization problem

$$(X_1^n, ..., X_N^n) = \underset{\phi_0(X_i, X_j) < 0,\ i,j=1,\dots,N}{\operatorname{argmin}} W(X_1, ..., X_N),$$

  starting with $(\hat{X}_1^n, ..., \hat{X}_N^n)$.

- Third step: Actualization of the velocity;
  after identifying the clusters, $C_1^n, ..., C_{M_n}^n$, actualization of the velocity of each sphere

$$\forall k = 1, ..., M_n,\ \forall i \in C_k^n, \quad V_i^n = \frac{\sum_{j \in C_k^n} V_j^{n-1}}{\operatorname{card}(C_k^n)}.$$

## 2.3 Minimization algorithm

The constrained non-linear minimization problem arising on the second step can be solved by a modification of the Arrow-Hurwicz-Uzawa algorithm as described in the following. Since the potential $W$ is not strictly convex, the solution to this problem is not unique.

The algorithm includes two loops: an outer and an inner loop. The inner loop stands for the minimization algorithm itself and is described later on. Let $S_{m-1}$ be the set of pairs of overlapping spheres at the $(m-1)th$ iteration of the outer loop. At the $mth$ iteration, $S_{m-1}$ is first actualized to $S_m$. Secondly, if there was no change, i.e if $S_{m-1} = S_m$, the outer loop stops, otherwise the minimization algorithm is performed for the set of spheres defined by $S_m$ only. The aim of using these two loops is to avoid the undesired recruitment of spheres to a cluster due do numerical oscillations.

The Lagrangian of the system reads:

$$\begin{aligned} L(X_1,...,X_N,\lambda) &= W(X_1,...,X_N) + \Phi(X_1,...,X_N,\lambda), \\ \Phi(X_1,...,X_N,\lambda) &= \sum_{i,j=1,...,N} \lambda_{i,j}\phi(X_i,X_j), \end{aligned}$$

where $\lambda = (\lambda_{i,j})_{i,j=1,...,N}$, with $\lambda_{i,j} \geq 0$ for $(i,j) \in S$ and $\lambda_{i,j} = 0$ otherwise, is the set of Lagrange multipliers of the constraints. Denoting $\lambda_S = (\lambda_{i,j})_{(i,j)\in S}$, $L$ can be rewritten such as

$$\begin{aligned} L(X_1,...,X_N,\lambda_S) &= \sum_{(i,j)\in S} \left[\frac{1}{2} d(X_i,X_j)^2 + \lambda_{i,j}\phi(X_i,X_j)\right] \\ &= \sum_{(i,j)\in S} \left[\frac{1}{2} d(X_i,X_j)^2 + \lambda_{i,j}((R_i+R_j)^2 - d(X_i,X_j)^2)\right] \\ &= \sum_{(i,j)\in S} \left[\lambda_{i,j}(R_i+R_j)^2 + d(X_i,X_j)^2\left(\frac{1}{2} - \lambda_{i,j}\right)\right]. \end{aligned}$$

and therefore:

$$\begin{aligned} \nabla_{X_i} L(X_1,..,X_N,\lambda_S) &= 2\sum_{j|(i,j)\in S} \left(\frac{1}{2} - \lambda_{i,j}\right)(X_i - X_j) - 2\sum_{j|(i,j)\in S} \left(\frac{1}{2} - \lambda_{j,i}\right)(X_j - X_i) \\ &= 2\sum_{j|(i,j)\in S} (1 - 2\lambda_{i,j})(X_i - X_j), \qquad i = 1,...,N \end{aligned}$$

Let an initial configuration $(X_1^0,...,X_N^0)$ and initial values for the multipliers $\lambda_{i,j}^0,\ i,j = 1,...,N$ be given, such that $\lambda_{i,j}^0 \geq 0$, for $(i,j) \in S$ and 0 otherwise. A local minimizer of $W$, $(X_1^\infty,...,X_N^\infty)$, satisfying $\phi(X_i^\infty, X_j^\infty) < 0,\ i,j = 1,...,N,$

corresponds to the convergence in $p$ of the sequence $(X_1^p, ..., X_N^p)_{p\in\mathbb{N}}$, which is defined recursively by

$$\begin{aligned} X_i^{p+1} &= (X_i^p - \alpha_i \nabla_{X_i} L(X_1^p, ..., X_N^p, \lambda_S^p))(modL), \quad i = 1, ..., N \\ \lambda_{i,j}^{p+1} &= max(0, \lambda_{i,j}^p(1-2c_{i,j}) + \beta\phi(X_i^{p+1}, X_j^{p+1}) + c_{i,j}), \quad (i,j) \in S \end{aligned} \tag{2.9}$$

where $\beta$ is a numerical parameter controlling the actualization of the constraints, $\alpha_i$ is the minimization step which controls the motion of each elementary sphere $i, i = 1, ..., N$ and $c_{i,j} = (R_i + R_j)\sqrt{(\alpha_i + \alpha_j)\beta}$ further described.

The convergence test of the minimization algorithm reads

$$\left|\frac{L^{p+1} - L^p}{L^p}\right| \le \epsilon_L, \quad \max_{i=1,...,N} \frac{|X_i^{p+1} - X_i^p|}{R_i} \le \epsilon_X,$$

for chosen small positive constants $\epsilon_L$ and $\epsilon_X$, where $L^p = L(X_1^p, ..., X_N^p, \lambda_S^p)$. As the minimization problem is not convex, it is noteworthy that the uniqueness of a minimum is not ensured. Moreover, the Uzawa algorithm as previously defined can lead to oscillations around the minima. To avoid this phenomenon, next sections aim at presenting a modified version of the Uzawa algorithm which proves more efficient for our problem.

## 2.4 Modified Uzawa algorithm

In this section, we aim to modify the Uzawa algorithm of previous section to avoid oscillations around the solutions. We consider the Lagrangian in the general case:

$$\mathcal{L}(X_1, \ldots, X_N, \lambda_1, \ldots \lambda_M) = W(X_1, \ldots, X_N) + \sum_{j=1}^{M} \lambda_j \Phi_j(X_1, \ldots, X_N).$$

The constraints are

$$\Phi_j(X_1, \ldots, X_N) \le 0, \quad \forall j = 1, \ldots, M,$$

and consequently:

$$\lambda_j \ge 0, \quad \forall j = 1, \ldots, M.$$

Then, the Uzawa algorithm is written:

$$X_i^{p+1} = X_i^p - \alpha[\partial_{X_i} W(X^p) + \sum_{j=1}^{M} \lambda_j^p \partial_{X_i}\Phi_j(X^p)], \tag{2.10}$$

$$\lambda_j^{p+1} = \max\{0, \lambda_j^p + \beta\Phi_j(X^p)\}. \tag{2.11}$$

The first equation, upon dividing by $\Delta t$ and adjusting the $\alpha$ (namely changing $\alpha$ in $\tilde{\alpha}\Delta t$) is a discretized form of the differential equation

$$\dot{X}_i = -\tilde{\alpha}[\partial_{X_i} W(X) + \sum_{j=1}^{M} \lambda_j \partial_{X_i} \Phi_j(X)].$$

The problem is that the second equation cannot easily be put in the form of a differential equation because of the max.

But we can try ... We get (with $\beta = \tilde{\beta}\Delta t$):

$$\begin{aligned} & \lambda_j^{p+1} = \max\{0, \lambda_j^p + \beta\Phi_j(X^p)\} \\ \Leftrightarrow\quad & 0 = \max\{-\lambda_j^{p+1}, -\lambda_j^{p+1} + \lambda_j^p + \beta\Phi_j(X^p)\} \\ \Leftrightarrow\quad & 0 = \max\{-\frac{\lambda_j^{p+1}}{\Delta t}, \frac{-\lambda_j^{p+1} + \lambda_j^p}{\Delta t} + \tilde{\beta}\Phi_j(X^p)\} \\ \Leftrightarrow\quad & 0 = \min\{\frac{\lambda_j^{p+1}}{\Delta t}, \frac{\lambda_j^{p+1} - \lambda_j^p}{\Delta t} - \tilde{\beta}\Phi_j(X^p)\} \end{aligned}$$

Now, we disassociate the $\Delta t$ on the left and the right arguments of the max and we call $\tau$ the first $\Delta t$. We get in the limit $\Delta t \to 0$, keeping $\tau$ fixed:

$$\min\{\frac{\lambda_j}{\tau}, \dot{\lambda}_j - \tilde{\beta}\Phi_j(X)\} = 0$$

with is equivalent to the following alternative (we disregad the equality case for simplicity):

- either $\frac{\lambda_j}{\tau} < \dot{\lambda}_j - \tilde{\beta}\Phi_j(X)$, then $\lambda_j = 0$ and $\dot{\lambda}_j > \tilde{\beta}\Phi_j(X)$,
- or $\frac{\lambda_j}{\tau} > \dot{\lambda}_j - \tilde{\beta}\Phi_j(X)$, then $\dot{\lambda}_j = \tilde{\beta}\Phi_j(X)$ and $\lambda_j > 0$.

We see that

$$\lambda_j \equiv 0 \text{ on an interval of time } \Rightarrow \Phi_j(X) < 0 \text{ on this interval.}$$

Therefore, the differential analog of (2.11) is:

$$\begin{cases} \dot{\lambda}_j = \tilde{\beta}\Phi_j(X), \text{ if } \lambda_j > 0 \\ \lambda_j = 0 \text{ and } \Phi_j(X) < 0, \text{ otherwise.} \end{cases}$$

We note that the particular choice of $\tau$ is irrelevant in the final result. We see also that the signal for $\lambda_j$ to start to become $> 0$ is that $\Phi_j(X) > 0$.

The differential system is written (dropping the tildes):

$$\dot{X}_i = -\alpha[\partial_{X_i} W(X) + \sum_{j=1}^{M} \lambda_j \partial_{X_i} \Phi_j(X)], \tag{2.12}$$

$$\begin{cases} \dot{\lambda}_j = \beta \Phi_j(X), \text{ if } \lambda_j > 0 \\ \lambda_j = 0 \text{ and } \Phi_j(X) < 0, \text{ otherwise.} \end{cases} \tag{2.13}$$

Now, we take the second order version of (2.12). This gives:

$$\ddot{X}_i = -\alpha \sum_{k=1}^{N} \partial_{X_k} \Big[\partial_{X_i} W(X) + \sum_{j=1}^{M} \lambda_j \partial_{X_i} \Phi_j(X)\Big] \dot{X}_k - \alpha \sum_{j=1}^{M} \dot{\lambda}_j \partial_{X_i} \Phi_j(X). \tag{2.14}$$

Using (2.13), we can replace $\dot{\lambda}_j$ in (2.14) by $\beta \Phi_j(X) H(\lambda_j)$, where $H$ is the Heaviside function. It also proves more efficient to modify it by replacing $H(\lambda_j)$ by $\lambda_j H(\lambda_j)$. We get:

$$\ddot{X}_i = -\alpha \sum_{k=1}^{N} \partial_{X_k} \Big[\partial_{X_i} W(X) + \sum_{j=1}^{M} \lambda_j \partial_{X_i} \Phi_j(X)\Big] \dot{X}_k \\ -\alpha\beta \sum_{j=1}^{M} \Phi_j(X) H(\lambda_j) \lambda_j \partial_{X_i} \Phi_j(X), \tag{2.15}$$

It turns out that passing to second order introduces exponentially growing modes. To remove them, we replace the complicated expression

$$\alpha \sum_{k=1}^{N} \partial_{X_k} \Big[\partial_{X_i} W(X) + \sum_{j=1}^{M} \lambda_j \partial_{X_i} \Phi_j(X)\Big] \dot{X}_k,$$

by a simple second order dynamics in the force field given by the right hand side of (2.12). We get:

$$\ddot{X}_i = -\alpha^2[\partial_{X_i} W(X) + \sum_{j=1}^{M} \lambda_j \partial_{X_i} \Phi_j(X)] - \alpha\beta \sum_{j=1}^{M} \Phi_j(X) H(\lambda_j) \lambda_j \partial_{X_i} \Phi_j(X), \tag{2.16}$$

Now, we just add a velocity damping term in the form of $-C\dot{X}_i$ and we finally obtain:

$$\ddot{X}_i = -\alpha^2[\partial_{X_i} W(X) + \sum_{j=1}^{M} \lambda_j \partial_{X_i} \Phi_j(X)] - \alpha\beta \sum_{j=1}^{M} \Phi_j(X) H(\lambda_j) \lambda_j \partial_{X_i} \Phi_j(X) - C\dot{X}_i, \tag{2.17}$$

We end up with the final system:

$$\ddot{X}_i = -\alpha^2[\partial_{X_i} W(X) + \sum_{j=1}^{M} \lambda_j \partial_{X_i} \Phi_j(X)] - \alpha\beta \sum_{j=1}^{M} \Phi_j(X) H(\lambda_j) \lambda_j \partial_{X_i} \Phi_j(X) - C\dot{X}_i, \tag{2.18}$$

$$\begin{cases} \dot{\lambda}_j = \beta \Phi_j(X), \text{ if } \lambda_j > 0 \\ \lambda_j = 0 \text{ and } \Phi_j(X) < 0, \text{ otherwise.} \end{cases} \tag{2.19}$$

We now consider the equilibria of this system. If $(X_i)_{i=1,\dots,N}$, $(\lambda_j)_{j=1,\dots,M}$ is an equilibrium, then the $\lambda$'s are equilibria of the first order system (2.12), (2.13) because we have not modified the equations for $\lambda$. Furthermore, note that we get $\Phi_j \le 0$, $\lambda_j \ge 0$, and $\lambda_j > 0 \Rightarrow \Phi_j = 0$. So, we get $\lambda_j \Phi_j = 0$. We also get $\dot{X}_i = 0$. So, the equilibria of (2.18) are such that

$$\partial_{X_i} W(X) + \sum_{j=1}^{M} \lambda_j \partial_{X_i} \Phi_j(X) = 0, \quad \forall i = 1, \dots, N.$$

which defines the equilibria or the first order system.

## 2.5 Special case

We now specialize with

$$\begin{aligned} W(X_1, \dots, X_N) &= \frac{1}{2} \sum_{1 \le i < j \le N} |X_i - X_j|^2 \\ \Phi_{ij}(X_1, \dots, X_N) &= d^2 - |X_i - X_j|^2, \end{aligned}$$

and the unknowns are $(X_i)_{i=1,\dots,N}$ and $(\lambda_{ij})_{1 \le i < j \le N}$. For simplicity, we define $\lambda_{ij} = \lambda_{ji}$ when $j < i$.

Now, we compute:

$$\partial_{X_i} W(X_1, \dots, X_N) = \sum_{j \ne i} (X_i - X_j)$$

$$\partial_{X_k} \Phi_{ij}(X_1, \dots, X_N) = \begin{cases} 0 & \text{if} \quad k \ne (i \text{ or } j) \\ -2(X_i - X_j) & \text{if} \quad k = i \\ -2(X_j - X_i) & \text{if} \quad k = j \end{cases}$$

Then, the first order model is written:

$$\dot{X}_i = -\alpha[\partial_{X_i} W(X) + \sum_{1 \le k < \ell \le N} \lambda_{k\ell} \partial_{X_i} \Phi_{k\ell}(X)], \tag{2.1}$$

$$\begin{cases} \dot{\lambda}_{k\ell} = \beta \Phi_{k\ell}(X), \text{ if } \lambda_{k\ell} > 0 \\ \lambda_{k\ell} = 0 \text{ and } \Phi_{k\ell}(X) < 0, \text{ otherwise.} \end{cases} \tag{2.2}$$

And the second order model with damping is written:

$$\begin{aligned} \ddot{X}_i = -\alpha^2[\partial_{X_i} W(X) + \sum_{1 \le k < \ell \le N} \lambda_{k\ell} \partial_{X_i} \Phi_{k\ell}(X)] \\ -\alpha\beta \sum_{1 \le k < \ell \le N} \Phi_{k\ell}(X) H(\lambda_{k\ell}) \lambda_{k\ell} \partial_{X_i} \Phi_{k\ell}(X) - C\dot{X}_i, \end{aligned} \tag{2.3}$$

$$\begin{cases} \dot{\lambda}_{k\ell} = \beta \Phi_{k\ell}(X), \text{ if } \lambda_{k\ell} > 0 \\ \lambda_{k\ell} = 0 \text{ and } \Phi_{k\ell}(X) < 0, \text{ otherwise.} \end{cases} \tag{2.4}$$

Now, we replace the derivatives of $W$ and $\Phi_{k\ell}$ by the expressions computed above and we find for the first order model:

$$\dot{X}_i = -\alpha \sum_{j \neq i} (1 - 2\lambda_{ij})(X_i - X_j), \tag{2.5}$$

$$\begin{cases} \dot{\lambda}_{k\ell} = \beta(d^2 - |X_k - X_\ell|^2), \text{ if } \lambda_{k\ell} > 0 \\ \lambda_{k\ell} = 0 \text{ and } d^2 - |X_k - X_\ell|^2 < 0, \text{ otherwise.} \end{cases} \tag{2.6}$$

For the second order model, we find:

$$\begin{aligned} \ddot{X}_i = {} & -\alpha^2 \sum_{k \neq i} (1 - 2\lambda_{ik})(X_i - X_k) \\ & -2\alpha\beta \sum_{k \neq i} (d^2 - |X_i - X_k|^2)(X_k - X_i)\lambda_{ik} H(\lambda_{ik}) - C\dot{X}_i, \end{aligned} \tag{2.7}$$

$$\begin{cases} \dot{\lambda}_{k\ell} = \beta(d^2 - |X_k - X_\ell|^2), \text{ if } \lambda_{k\ell} > 0 \\ \lambda_{k\ell} = 0 \text{ and } d^2 - |X_k - X_\ell|^2 < 0, \text{ otherwise.} \end{cases} \tag{2.8}$$

## 2.6 Discretization

We discretize (2.7) in a centered way with explicit treatment of the first order differential term. We keep the $\Delta t$ although when writing the Uzawa algorithm, it is better to set $\Delta t = 1$ and to find the best set of parameters $\alpha$, $\beta$:

$$\begin{aligned} \frac{X_i^{n+1} - X_i^n + X_i^{n-1}}{\Delta t^2} = {} & -\alpha^2 \sum_{k \neq i} (1 - 2\lambda_{ik}^n)(X_i^n - X_k^n) \\ -2\alpha\beta \sum_{k \neq i} (d^2 - |X_i^n - X_k^n|^2)(X_k^n - X_i^n)\lambda_{ik}^n H(\lambda_{ik}^n) & - C\frac{X_i^{n+1} - X_i^{n-1}}{2\Delta t}, \end{aligned} \tag{2.1}$$

$$\lambda_{k\ell}^{n+1} = \max\{\lambda_{k\ell}^n + \Delta t\, \beta(d^2 - |X_k^n - X_\ell^n|^2), 0\}. \tag{2.2}$$

In practice, we will choose $C$ close to the critical damping

$$C = 4d\sqrt{\alpha\beta}.$$

## 2.7 Conclusion

Numerical simulations will be performed to validate the numerical method proposed for this model of aggregating spheres. Such a preliminary work is expected to explain how self-propelled particles aggregate when they collide. More precisely, properties such as the speed, form and mean velocity of the global cell structure are expected to be deduced with this model. The final goal of the project is to use the minimization approach to model a cell of complex geometry as a set of connected aggregated elements remaining attached throughout motion.

## 2.8 References

1. P. Degond, M. Ferreira, Modelling the aggregation of $N$ spheres over time, in preparation
2. Uzawa H Arrow HJ, Hurwicz L. Studies in linear and nonlinear programming. Stanford University Press, 1958.

# Conclusion

In this thesis, we studied theoretically and numerically models of complex systems coming from the biology. Of particular interest was the modeling of adipose tissue morphogenesis and homeostasis. We first developed an individual-based model for adipose tissues in which the motion of adipocytes and collagen fibers was mainly driven by simple mechanical cues. An in-depth parametric analysis of this model was performed to explore different scenarios and biological phenomena. We developed numerical segmentation techniques on the biological images in order to enable the quantitative comparison between the model results and the experiments. As a validation, the model results showed a quantitative agreement with the experiments on real tissues. Then (Chap II and III), we derived a macroscopic model for a fiber network as characterized by the IBM of chapter I. The kinetic model associated to the IBM for fibers is the first example of a model closed at the level of the two-particle distribution function. In a hydrodynamic regime, we obtained a macroscopic model and proposed its first theoretical and numerical study. We were able to obtain existence of stationary solutions under some hypothesis, and the numerical simulations highlighted physical properties of the macroscopic equation. A first numerical comparison with the underlying IBM offered promising prospects towards the validation of the macroscopic model.

If Chap V gives the first prolongations of this PhD work, there are numerous other directions in which the work can be extended. On a biological viewpoint, the IBM of Chap. I could be used to understand the mechanisms of adipose tissue homeostasis disruption, and therefore could help understanding the processes of wound healing, obesity *etc.*. This model could also be extended in 3D. Through an in-depth analysis of the macroscopic model (started in Chap III), we expect to show the relevance of this model by comparison to its underlying IBM. On a mathematical viewpoint, the rigorous derivation of the macroscopic equation from its underlying IBM is still an open question. Future works will deeper investigate the unicity of solutions to the macroscopic equation in case of a homogeneous fiber density. The theoretical and numerical study of the case of a non homogeneous fiber density is the subject of future works. Finally, further perspectives are the removal of the fast fiber linking/unlinking hypothesis, in order to understand how a finite lifetime of the cross-links affects the macroscopic dynamics.